

MAGNESIUM BORON OXIDE TUNNEL BARRIERS

A Dissertation

Presented to the Faculty of the Graduate School

of Cornell University

in Partial Fulfillment of the Requirements for the Degree of

Doctor of Philosophy

by

John Creighton Read

May 2009

© 2009 John Creighton Read
ALL RIGHTS RESERVED

MAGNESIUM BORON OXIDE TUNNEL BARRIERS

John Creighton Read, Ph.D.

Cornell University 2009

In this dissertation I investigate the materials physics of thin film growth processes for magnetic tunnel junctions (MTJs) and Josephson junctions (JJs). The studies I present focus primarily on the chemical, electronic, and structural properties of the tunnel barriers and their interfaces with the adjacent electrodes. I developed a growth process for making MgO (MgBO)-based MTJs, studied this film stack in detail, and also examined the materials properties of MgB₂ oxidation processes and AlN tunnel barrier formation for JJ development.

I conducted x-ray photoelectron spectroscopy (XPS) studies on CoFeB / MgO bilayers to explore the MgO growth process. MgO that is rf sputtered directly on CoFeB or on a thin Mg protective layer forms MgBO with promising physical and chemical properties. Post-growth annealing reduces Fe and Co oxides formed in the deposition process through a reaction of B from the electrode with O in the transition metal oxides. Annealing also causes an atomic rearrangement of the Mg, B, and O species in these barriers. In sputtered MTJs with thin barriers, reaction between B from the electrode and sputter deposited MgO is an inherent part of the formation of MgO-based MTJs.

I studied the correlated results of scanning tunneling electron microscopy (STEM) utilizing electron energy-loss spectroscopy (EELS), scanning tunneling spectroscopy (STS), current-in-plane tunneling (CIPT), and magnetometry studies. These investigations show that MgBO barriers have fewer low energy defect states than MgO barriers and comparison of MTJs with MgBO barriers with MTJs

with Mg/MgO bilayer barriers shows that MgBO barriers yield higher TMR values and lower RA values than MgO barriers of comparable thickness. MgBO MTJs are also compatible with permalloy-B (PyB) free electrodes that show desirable magnetic characteristics. The electrode B content is important for the formation of low defect MgBO barriers and for the use of superior Py-based electrode materials for spin torque magnetic random access memory (MRAM) and magnetic sensor applications.

I also studied MgBO barriers in an exploration of the oxidation of MgB₂ thin films. The oxidation of the MgB₂ film surface forms MgBO that is chemically similar to the MgBO materials formed in MTJ structures. Exposure to N₂ or O₂ promotes formation of MgO on the MgB₂ film surface which becomes completely composed of MgO if the oxidation process is carried out at elevated temperatures for an extended time. Lower temperatures form oxides similar to the native surface oxide, and promote formation of elemental B, and B sub-oxide near the film surface. These B species are likely to effect JJs made with these barrier formation processes. These chemical studies provide insights into optimal MgBO barrier formation techniques for future MgB₂-based JJ devices.

Finally, I started developing growth processes for AlN tunnel barriers formed both by N beam exposure of Al films and by reactive rf sputtering of AlN in either Ar or N₂ for use in Nb / AlN / Nb JJs. Both AlN growth processes introduce O into the AlN film, which could possibly be controlled with the use of a getter material during barrier deposition. These XPS studies show that when a pure N₂ atmosphere is used for reactive rf sputtering of AlN, the film growth nitridizes the underlying Nb film, similar to the way MgO oxidizes CoFeB. These studies provide some insights as to optimal AlN barrier formation for JJ structures that can now be further developed.

BIOGRAPHICAL SKETCH

John Read was born in Richmond, Virginia, but his family moved to the small town of Lexington soon after his birth and he spent the next seventeen years of his life there. In high school he developed a love for music, painting, and sculpting, and after graduating attended the Maryland Institute College of Art in Baltimore, MD from 1992-1996, where he majored in painting with a minor in art history. He was fortunate to have the opportunity to work as an intern at the Office of Exhibits Central, the primary exhibit fabrication shop for the Smithsonian Institution in Washington, D.C., during the summer after his Sophomore year and eventually was able to gain a short contract position as a fabricator there. During this time he learned the basics of woodworking and cabinetmaking which greatly formed the next few years of his life. During his last two years in art school, he became very interested in artists who embraced science and nature as their primary conceptual focus for artworks which motivated him to seek out a more scientific education.

After completing his art degree, he enrolled at Catonsville Community College, just outside of Baltimore, where he took classes at night for two years, catching up on the math courses he missed in high school and college. During this time he worked at a lumberyard, then with an interior architect and furniture maker, Tom Swift Studios, in the D.C. area, and finally as a fabricator and glazer at Kensington Glass Arts. In the fall of 1998 he enrolled at the University of Maryland in the physics department and began taking undergraduate math and physics courses. Two years later he was lucky enough to earn an undergraduate research position in the lab of Professor Ichiro Takeuchi. There he learned the basics of high vacuum technique, thin film deposition, combinatorial synthesis, device fabrication, and device measurement. After graduating with a degree in physics in 2001, he stayed on in the Takeuchi lab for another semester before moving to the cold north to

attend Cornell University for graduate school.

After his first year at Cornell, he somehow convinced Professor Robert Buhrman to allow him to spend the summer working in the D7 lab. He began working on BEEM and XPS experiments on thin film device layers and oxide tunnel barriers and managed to earn a spot in the group. During the years that followed he attempted experiments in molecular electronics but eventually settled back into thin film growth and characterization for tunnel junction device development. In his last two years of graduate school, he worked primarily on MgO MTJs, with side projects on MgB₂ and AlN, and helped start a new phase of research exploring MTJs made at Cornell.

For my Family and Friends

ACKNOWLEDGEMENTS

Over the last six and a half years I have met and worked with a number of amazing people and have drawn strength from friends and family alike. I owe thanks to many people for their support, friendship, guidance, and collaboration. These next paragraphs are an attempt to pay tribute to each of these people who played a role in the creation of the research I present here. I am very grateful to them all.

Without the guidance and support, resources and input of Bob Buhrman, none of the work in this dissertation would have ever happened. Bob is a great man. He is a brilliant scientist, a progressive thinker, and an excellent person. In the course of composing this dissertation I've gone back through all of my work from these past years and it is very clear to me how much influence he has had on the way I think about experiments. He has taught me everything I know about science and physics and his example is an inspiration to me. I first encountered Bob at the Fall MRS conference in Boston in 2000. He presented some of the first spin transfer work and I was totally amazed, not only by the science, but also by his personality and presentation style. I was applying to graduate schools at that time, and although I was not considering Cornell and did not think of myself as an Ivy Leaguer, I decided to take a shot in the dark with the hope of getting to work for Bob. To my surprise, I was accepted and decided to try it out. This is the single best decision I made in graduate school and I was lucky enough to land a spot in Bob's lab after my first year. Bob has made it possible for me to collaborate with excellent researchers throughout the country, and I have little doubt that the only reason the community paid any attention to my work is because his name is on everything I've done. Because of Bob I got to visit Japan and to attend a policy meeting in Washington, DC on the impact of science and technology graduate students on American society. Bob truly deserves the bulk of

the credit for whatever contributions our work makes to the physics community. It has been an honor to work with him.

I wish to express my sincere thanks to Dan Ralph and Piet Brouwer who both served on my committee. During our IRG meetings I came to more fully appreciate the incredible intellect of these men and their ability to simplify complicated problems. In terms of content and clarity, Dan Ralph is the best speaker I have ever seen. His brilliance routinely shines through in the way he presents results and models. He is a constant reminder that smart people ask questions and the depth of his understanding of physics and his undying curiosity about how nature works are inspiring. Dan provided me with a great deal of feedback in the writing of this dissertation and helped me clarify many of the more subtle ideas that are discussed in the chapters about MTJs. I owe Dan many thanks for his input on my work over these past few years. Piet Brouwer is my favorite theorist. He presents extraordinary and complicated ideas in a way that even I can understand and digest, which clearly shows just how well he grasps the physics. I deeply appreciate his enthusiasm for science and his friendly nature. He has always made time for me when I stopped by his office and he always asks probing physics questions that have helped guide me towards reasonable explanations of the data I've collected. He has been an extremely helpful resource for gauging the impact of the research I've worked on and I deeply appreciate his input.

In my early days in the Buhrman group I collaborated with Prof. Hector Abruña on attempts to make BEEM measurements on self assembled monolayers of molecules. Prof. Abruña is the single most inspiring researcher I have ever met and every time I interact with him I feel more excited about doing science. His love for science and his love for living are contagious and it is always a pleasure to chat with and learn from him. Viva Abruña!

When I joined the Buhrman group I was lucky to have three mentors: Andrew Perrella, Phil Mather, and Eileen Tan. Andrew and Phil taught me film growth techniques, how to take good data with the STM/BEEM systems, and all the complicated operations and maintenance issues related to keeping the D7 lab up and running. Andrew and Phil were both excellent teachers and had very different styles in the lab. I benefitted greatly from having a broad range of training and ideas to draw from. Sadly, Andrew passed away and the world lost a great scientist and an amazing person. Andrew is probably the strongest person I have ever known and I will never forget his excellence and his example of grace under pressure. He was the best of us, may he rest in peace. Phil continues to produce excellent research at Everspin and gave me some great advice and help when I first started making MTJ layers for CIPT studies. Aside from being brilliant, Phil is one of the most genuine people I have ever worked with. He helped me in a great many ways and I will never forget my time with him in D7. Eileen taught me how to use the XPS system which became the workhorse for much of my research. Her research guided a lot of my studies and I always enjoyed working with her and talking with her. Eileen had great ideas and always had a smile and a funny story to share. She continues to research magnetism at the Data Storage Institute in her native Singapore and I imagine she would chuckle if she could see the XPS system now.

Ilya Krivorotov is a force of nature. I have never seen such a combination of complete brilliance, extraordinary work ethic, talent, and humility. I got to know Ilya when he was a post-doc in the Buhrman and Ralph groups. He taught me a lot about spin transfer and how to do good experiments, and he has been a great friend over the years. I always enjoy a chance to chat with Ilya and I thank him very much for all that he has done for me. Ozhan Ozatay is another good friend from my early days in the Buhrman group. Ozhan is an excellent scientist in

addition to being extraordinarily hard working. Ozhan has amazing determination as well as being a man of great faith. I sincerely appreciate his help with letting me use his Van der Pauw dipper to measure film sheet resistance values. I enjoyed our conversations about science and religion and wish him continued success in his career and life. Another friend from my early days in the group is Nathan Emley. Nate truly set the standard for hard work and excellent results. He is an amazing fabricator, scientist, and guitar player and I hope his career and life continue to bring him happiness and success. Eric Ryan has also been a good friend over the years I've spent in Clark Hall. Eric has an extremely broad knowledge base and I have always enjoyed our conversations about a great many topics. Usually I lost our political arguments, which means I learned something. I appreciate his friendship and I wish him well in his life and career.

Burak Ulgut was my collaborator for the BEEM studies on molecules and in the process of this work he became a good friend. Buruk is brilliant and creative and without his help I would not have made much progress on the experiments. Although it was a difficult set of experiments, the enthusiasm that Buruk brought to the lab helped push me through the many failures. I also got to enjoy learning more about Turkish culture from Buruk and I very much appreciate his friendship, encouragement, and advice over the years. I wish Buruk nothing but happiness and success in his life. Daniel Estrada was the first REU student that I worked with, back in the days when I was trying BEEM experiments on molecules. I appreciate his willingness to try out the difficult experiments we were developing and also the new music that he introduced me to. Daniel was a great addition to the lab and I very much enjoyed our conversations about art and music. I also wish to thank Yi Cui, Ke Chen, and Xiaying Xi of Penn. State and Brian Moeckly of Superconductor Technologies for collaborating with me on the MgB₂ experiments.

These excellent researchers made all the films I studied and experimented with the various oxidation processes used to form oxide tunnel barriers. This started as a small side project and kept growing until it reached what I present in chapter 5. I hope that the work we have done helps them with future experiments and I thank them for all their contributions to our efforts at Cornell.

About two years ago I began working with Judy Cha on the MgBO MTJ project. Judy was kind enough to study my samples with TEM, STEM, and EELS and generated amazing, beautiful data that helped to explain many details of the growth process. Since that time I had the good fortune to get to know her better, both as a collaborator and as a friend. Judy is an extremely talented scientist and a fascinating person with great strength of character. She always has a good perspective on research and continually impresses me with how much information she yields from her data. I enjoyed working with Judy and I wish her well as she moves on to her next adventure. During the past few years I also had the privilege of working with David Muller on the MgBO MTJ project. David has an extraordinary grasp of how experiments impact technology and an incredibly deep and broad knowledge of physics. His suggestions about research directions are always helpful as is his input in understanding the results we obtained. I sincerely appreciate David's help, guidance, and perspective on my research. Luqiao Liu spent a lot of time working with me in the D7 lab when he first joined the Buhrman group and he helped me out a great deal with XRD and AFM studies of seed layers for what became the MgBO MTJ project. Luqiao has extraordinarily high intelligence and he is very driven. These attributes will carry him far and are certain to help him continue to produce excellent science for the duration of his career.

Since they joined the group and began working with me, both Hsin-Wei (Mark) Tseng and Yun Li have been sources of great joy. The best part of every work day for me was spending time with them. Whether discussing experiments, trying to teach me some Mandarin phrases, or working together in the lab, Mark and Yun always bring intelligence, happiness, kindness, and good feeling to the lab. I have had the privilege of getting to know them also as friends and I count them among my favorite people. Both of them have helped me in more ways than they even realize and I look forward to watching them develop into even better scientists over the next few years. I have no doubt that they will continue to produce great work. Mark is an excellent fabricator with a strong work ethic and a high degree of organization. His careful approach and capable nature are sure to help him achieve greatness. Yun is one of the smartest people I have ever met. She is focused, determined, hard working, and fearless. These attributes will help her achieve greatness. These highly capable people now run D7 and I have the highest degree of confidence that they will push the science coming out of D7 into new and interesting directions. Pinshane Huang joined our D7 team as a summer REU student and quickly impressed me with her high level of motivation and work ethic. She put in very long hours, working like a senior graduate student, and produced excellent results. She also became a good friend and I enjoyed our talks about a great many topics over the years. She is extremely talented and I look forward to seeing her achieve great things in her time at Cornell.

Bill Egelhoff made it possible for me to complete my goal of measuring TMR in MTJ structures made at Cornell. His willingness to work with me, first by having his staff measure my samples, and then by letting me use his system myself, made it possible for me to make several iterations of samples until I had a big pile of data. Without Bill's help I would not have nearly as much progress in figuring

out how to grow MTJ layers incorporating MgO barriers. Bill is a remarkably enthusiastic researcher with great ideas and an extraordinarily generous nature. I have known few people who enjoy doing science more and who are more interested in getting to the bottom of things than Bill. I look forward to working with him for the next few years at NIST.

In the past year I had the pleasure of working with Derek Stewart on some of the theoretical considerations for the MgBO MTJ project. I enjoyed my interactions with Derek and I learned a lot from him with regards to the theories behind MgO MTJs. Derek is a gifted, generous person who showed me a great deal of patience when explaining his work. I thoroughly enjoyed working with Derek on this project, as well as getting to know him a little, and I wish him continued success and happiness.

More recently I have gotten to know Praveen Gowtham. I have encountered few people who have more fun doing physics than Praveen and his enthusiasm is contagious. He has an amazing attitude about living and has been a good friend to me. He has a deep understanding of physics, a strong drive to learn more through experiments, and truly enjoys figuring things out. These attributes are certain to help him continue to produce excellent science. I am also thankful to several other Buhrman group members from whom I learned many things, both in group meeting and in the lab. Juting Zhai, Andrei Garcia, Preeti Chalsani, Greg Fuchs, Vlad Pribiag, Oukjae Lee, Zhipan Li, and Takahiro Moriyama have all been great resources and co-workers and I wish them all continued success.

I owe many thanks to Chris Lobb, who remained a source of encouragement for me throughout my time in graduate school. He greatly helped me get in, helped me find the will to stay, and I deeply appreciate all of his encouragement. I also thank Ichiro Takeuchi, who gave me my start in research and whose recommendation no

doubt played a major part in getting me into Cornell, for his continued support during my time in Ithaca.

I am deeply indebted to the staff of the LASSP machine shop in Clark Hall not only for their help with research problems, but also for their willingness to spend time chatting with me about a great many topics. Stan Carpenter, Rodney Bowman, Chris Cowulich, Jeff Koski, Stan McFall, and Bob Tillotson, have bailed me out of many challenging fabrication and mechanical issues that arose while keeping D7 running. They also provided some of the best humor one can find in the building, if not the world, and were a constant source of excellent stories. I also thank them for attending my "shop appreciation days," which were really just an excuse to make them hang out with me. The machine shop also throws the single best party of the year, the Christmas party, which has always been my favorite day in Clark Hall for the years I've worked in the basement. Thanks for making my time in Clark Hall better. I also want to thank Bob "Sned" Snedeker, who ran the student shop when I joined the ranks of the Clark Hall basement. Sned taught me how to use the machine shop and helped me out with many fabrication issues. Sned was a good teacher and I always enjoyed a hearty chat with him.

The research services team is also full of friends who have helped me out a great deal over the years. Whether figuring out how to move a vacuum chamber, controlling the humidity in the lab, shipping pumps for repairs, or generally maintaining the equipment in D7, the guys in research services have provided a lot of support and I am very grateful for their help. When I first started, Win Tanner was the supervisor, but sadly he passed away a few years ago. Win was a fantastic, extremely helpful person who always had a smile and a solution. Bob Kenyon now runs the show and over the years has become a great friend. Bob has kept me up to date about construction issues that might effect the working condition of the lab

and he always had time to help with whatever situations arose that needed fixing to maintain the lab. Bob is an extraordinarily generous man who has extended me many favors and shared many stories with me. I owe Bob a great many thanks. Dan Sheerer joined the team more recently and has become a good friend over the past few years. Dan has always made time to help me out with whatever I've asked for help with. As a fellow music lover, Dan and I have shared many stories about folk music and guitar playing and we even got to see Kelly Joe Phelps together – front row seats. Dan is also one of the funniest people I have ever know and I appreciate his humor, especially on those days when nothing was going right, and its ability to lift me up. Leonard Frelove (Clark Hall's Santa) and David Bowman helped me out with making sure packages got to D7, with a variety of installations in the lab, and with many pleasant conversations. Thanks guys.

Jon Shu has been a great help to me over the years with XPS-related science. Jon is an extremely talented and highly capable researcher and I enjoyed collaborating with him. Jon gave me a lot of helpful advice over the years and I greatly value his friendship. There is no doubt that Jon helped improve my quality of life and I always enjoyed our conversations. I thank him for all of his help. Ron Kemp is a fantastic resource for thin film growth and processing, in addition to being a good man. He has given me very helpful advice over the years with film growth techniques and vacuum chamber modifications. I always enjoyed talking with Ron and I sincerely appreciate that he was always so willing to help me out with whatever project I brought to him.

Rosemary French in the physics department has been a great friend to me over the years, from the time I started out until the present day. Rosemary has always helped me find the bright side of grad school life and her kind, genuine nature has helped me maintain perspective. I wish her happiness and satisfaction in the

coming years. Cathy Wetterer and Debbie Sladich helped me out a lot over the years, both at CNS and at CCMR, with ordering equipment, getting reimbursed for travel expenses, borrowing projectors, and setting up talks. I have really enjoyed getting to know both of these ladies and I so enjoyed stopping by to chat with them from time to time. They are wonderful, helpful, and cheerful, and I thank them both for all their help.

I deeply appreciate the encouragement and support of Yuanjia Zhang. Yuanjia is a dear friend and a constant source of strength for me. She is extremely intelligent, patient, kind, and genuine and I so value her friendship. Yuanjia is an excellent researcher and a fantastic person and I wish her continued success and happiness.

Jun Zhu was a great friend to me while she was a post-doc in the McEuen lab. Our conversations were always interesting and I enjoyed getting to know her. Jun helped me find confidence in myself during my difficult transition to taking sole responsibility for the operation of D7. I deeply appreciate all of her help and I wish her continued success and happiness in her life. Jing Jin has also been a very good friend to me over the years. Jing is one of the first people I met in Ithaca and I have enjoyed getting to know her better over the years. I wish her well as she moves towards her next adventure and I thank her for her friendship. Jon McCoy has also been a good friend. I enjoyed our 2-3 AM conversations about movies, art, politics, music, religion, dating, and all the other topics we worked through. Jon is a great example for living well and I appreciate his advice and friendship.

Michael Thomas has been a constant voice in my head during my time in grad school. Michael is the person who taught me cabinetmaking years ago and his teaching style had a strong influence on me. In my teaching in the lab I try to think back to how Michael taught me and then proceed accordingly. Michael

always made me feel appreciated and that my contributions were important. It has always been my goal to operate in a similar fashion, and if I have achieved this goal, it is because of his excellent training. Bow and Dolores Davis have also been great friends to me. I deeply appreciate and value their encouragement and support during my time in Ithaca. My friend Pete Davis has helped me navigate many difficult aspects of my life during grad school. Our hikes through the woods near Lexington have always helped me regain center and remember where I came from. I deeply appreciate Pete's support and encouragement while I fought my way up the grad school hill.

Jacob Grose is an incredible friend. Jacob changed the way I think about doing science and deeply influenced how I see the scientific world. Jacob is brilliant and talented and I am certain he will continue to shape the world around him no matter his setting. I enjoyed our late night conversations about so many topics; we usually ran through all of them in each conversation, and I deeply value his continued friendship. Steve Biller has been a wonderful friend to me over these past years. I met Steve in the physics department at Maryland and he has been extremely good to me ever since. He has helped me maintain perspective on my past while encouraging me to live in the present and look optimistically to the future. I am very grateful for Steve's friendship over the years. Nathan Ellis has been an extraordinarily good friend to me during my time in Ithaca. Nate has helped me figure out how to fabricate several pieces of lab equipment and helped me solve many mechanical problems in D7 over the years. He has also gone way above and beyond by helping me fix my truck, helping me move, and generally listening to my problems as I waded my way through research. I am very thankful for his help, advice, and friendship.

I owe a great deal to my dear friend Pat Braganca. Our conversations about experiments are always stimulating and I learn so much from him. Pat is my window into the spin transfer device world and his input and advice helped guide my work towards materials studies that device fabricators and measurement specialists find useful. Pat is an extraordinary scientist with a remarkable set of skills. He is also a fantastic person with a huge heart and he deserves only happiness in his life. Pat is a man of great faith and our late night conversations about religion are some of my fondest memories of my time in Ithaca. I completely enjoyed being Pat's housemate and groupmate over these past years and I look forward to watching him achieve all his goals in life.

Andrew Noble is like a brother to me. I met Andrew the first week I moved to Ithaca and I have valued his friendship ever since. We have been through many ups and downs together, and over the years I have been deeply moved by his kindness, compassion, and generosity through all of it. I feel blessed to have such a friend.

I thank my grandfather, Robert Irons, and the memory of my grandmother, Caroline Irons, for their love and support while I worked my way through school. I am sorry that I placed so much importance on my work that I missed seeing them more over the years I spent in Ithaca. They have made my time in Ithaca, and my time on this earth, much richer.

I also wish to thank my aunt Peggy Deberry and my uncle Jim Deberry for their encouragement and support during my time in Ithaca. Peggy and Jim have shown me so much love and support during my years in Ithaca and they are both great sources of inspiration for me in terms of doing science, math, and engineering. They are truly wonderful people and they have been extraordinary advisors and friends over the years.

My sister, Julie Avera, has been a remarkable source of strength for me over the years. Her faith and love have helped me through my darkest moments and elevated my brightest moments. Her example is deeply moving to me and she is a constant reminder of my past and always knows exactly what I need to hear and when I need to hear it. Julie has kept me grounded in reality and has been a constant reminder of what things are truly important in life. My brother-in-law, Vance Avera, has also been an amazingly kind friend to me over the years. Vance has always treated me like family and has shown me nothing but love and support during my years in Ithaca. Julie and Vance are people of great faith who have given my life so much richness, and getting to know their daughters Mary Elizabeth, Kate, and Caroline, is one of the greatest gifts I have ever been given.

I owe everything in my life to my mother, Betty Read. Her patience with me over the years has been extraordinary. Her examples of selfless living and love for all are just two of the many reasons that she is the most amazing person that I know. The way that she lives is both inspiring and motivating and demonstrates the depth of her faith. She has never shown me anything but love, compassion, and kindness, and there is nothing in my life that I am more proud of than the fact that I am her son.

TABLE OF CONTENTS

Biographical Sketch	iii
Dedication	v
Acknowledgements	vi
Table of Contents	xix
List of Tables	xxii
List of Figures	xxiii
1 Introduction	1
REFERENCES	8
REFERENCES	8
2 Background	9
2.1 Magnetoresistance and Magnetic Tunnel Junctions	9
2.1.1 Hard Disk Drive Read Heads and Magnetic Random Access Memory	32
2.2 Thin Film Growth	38
2.2.1 Growth Process for MgBO MTJ Thin Film Stacks	41
2.3 Summary	52
REFERENCES	53
REFERENCES	53
3 X-ray Photoelectron Spectroscopy Studies of CoFeB / MgO Bi- layers	58
3.1 Introduction	58
3.2 Sample Preparation	60
3.3 Spectra Peak Fitting	63
3.4 Oxidation of CoFeB Thin Films	68
3.5 Plasma and Thermal Oxidation of CoFeB / Mg Bilayers	74
3.6 Electron Beam Evaporated MgO Layers on CoFeB electrodes	78
3.7 Radio Frequency Sputtered MgO Layers on CoFeB electrodes	82
3.8 Sputtered Mg / MgO Bilayers on CoFeB electrodes	91
3.8.1 Use of a Ta getter During rf Sputtering	93
3.9 Summary	95
REFERENCES	99
REFERENCES	99
4 Chemical, Electronic, Structural, and Magnetic Investigation of MgBO Based MTJs	102
4.1 Motivation	102
4.2 Introduction	103

4.3	Experimental Techniques	105
4.4	Electron Energy-Loss Spectroscopy Data from a Single Interface Sample	108
4.5	Electron Energy-Loss Spectroscopy Data from MgBO MTJs	111
4.6	Scanning Tunneling Spectroscopy Data	117
4.7	Comparison of MgBO and Mg/MgO MTJs	121
4.8	CIPT Studies	128
4.8.1	Discussion of RA vs. t Plots	133
4.9	TEM images of Ni-Fe-B Free Electrode Layers	137
4.10	M_S and H_C measurements	141
4.11	Free Layer Coupling	145
4.12	Summary and Conclusions	149
	REFERENCES	151

REFERENCES 151

5	X-ray Photoelectron Spectroscopy Studies of the Oxidation of MgB₂ Thin Films	156
5.1	Introduction	156
5.2	Experimental Details	159
5.3	Spectral Peak Identification in Control Samples	163
5.4	Annealed and Oxidized HPCVD MgB ₂ Films	174
5.5	Oxidized RE MgB ₂ Films of Different Thicknesses	179
5.6	Effects of Ion Milling on the MgB ₂ Thin Film Surface	190
5.7	Effects of Etching the MgB ₂ Thin Film Surface with Water	195
5.8	Discussion and Conclusions	199
	REFERENCES	204

REFERENCES 204

6	XPS Studies of AlN Tunnel Barriers	209
6.1	Introduction	209
6.2	Experimental Details	210
6.3	Nitrogen Beam Exposed Aluminum Films	212
6.4	RF Sputtered AlN Films	218
6.5	STM/STS Measurements of Nitrogen Beam Exposed Aluminum Films	225
6.6	Summary	230
	REFERENCES	231

REFERENCES 231

7	Follow-Up Experiments, Future Directions, and Dissertation Summary	234
7.1	MgBO Tunnel Barrier Growth	234
7.1.1	MgO Sputtering Power, Chamber Pressure, and Getter Use	236

7.1.2	MgBO Target Sputtering	238
7.2	Glassy Magnetic Electrodes	239
7.2.1	New B-based Alloys	239
7.2.2	Out of Plane Magnetized Free Layers	240
7.3	MTJ Device Fabrication and Transport Measurements	240
7.3.1	MTJ Transport Measurements	241
7.3.2	STT MTJs and FIB EELS Studies	243
7.3.3	Double Barrier Junctions	244
7.4	MgB ₂ / MgBO / MgB ₂ Josephson Junction Development	246
7.4.1	MgB ₂ / MgBO Annealing Studies	246
7.4.2	MgB ₂ / MgBO Barrier Thickness Studies	247
7.5	Nb / AlN / Nb and Nb / NbN / AlN / NbN / Nb Josephson Junction Growth	248
7.6	Hybrid Magnetic Tunnel Junction - Josephson Junction Film Layer Growth	249
7.7	Dissertation Summary	252
	REFERENCES	256

REFERENCES

256

LIST OF TABLES

5.1	Estimated HPCVD MgB ₂ film stoichiometries	202
5.2	Estimated RE MgB ₂ film stoichiometries	203

LIST OF FIGURES

1.1	Plot of TMR versus RA for MgO MTJs made by the Canon Anelva corporation and how these values relate to read head sensors and hard drive density (data from ref [1,2]).	2
1.2	Progression of magnetoresistance (data from ref [1,2]).	3
2.1	TMR and magnetization data as a function of applied field in a Ni / NiO / Co MTJ (from ref[2]).	10
2.2	Schematic of densities of states for a normal metal and for a ferromagnet.	12
2.3	Schematic of a MTJ device and ideal plots of TMR and magnetization as a function of applied field.	13
2.4	Schematic of tunnel for the parallel and antiparallel states for an MTJ device.	15
2.5	Normalized conductivity data and schematic of densities of states for an Al / AlO _x / Ni tunnel junction (from ref[9]).	17
2.6	GMR data from a Fe / Cr / Fe spin valve at 300 K (from ref[12]) and from various Fe /Cr superlattices at 4.2 K (from ref[13]). . . .	18
2.7	Two-resistor (Valet-Fert) model of GMR (from ref[14]).	20
2.8	TMR measurements in AlO _x -based MTJs at room temperature (from ref[15] and ref[16]).	22
2.9	TEM images and TMR measurements of MgO-based MTJs (from ref[18] and ref[19]).	23
2.10	Theoretical depiction of coherent tunneling in an ideal Fe / MgO / Fe MTJ (from ref [20]).	25
2.11	Theoretical results showing different decay rates through the MgO barrier for electrode wavefunctions of different symmetries in an ideal Fe / MgO / Fe MTJ (from ref [20]). Also shown is the spin-split band structure for bcc Fe showing which Bloch states populate E _F (from ref[5]).	27
2.12	Studies of various CoFeB alloy electrodes and their effect on TMR in MgO MTJs (from ref[24] and [25]).	29
2.13	Studies of RA product reduction for different MgO barrier deposition techniques. The data in the top panel (from ref[26]) is labeled differently from how the authors of the paper label them, as described in the text. The data in the bottom panel (from ref[27]) compares MgO barriers deposited with an without a Ta getter. . .	31
2.14	Schematic of a MRAM array using MTJs as the memory element (bit).	34
2.15	Comparison of MRAM cell size for toggle and STT MRAM (from ref[44]).	36
2.16	AutoCAD renderings of the seventh gun installation for the AJA system.	40

2.17	Schematic of CIPT measurement (from ref[46] and [47]).	43
2.18	TEM images of typical MgO MTJ CIPT structure grown in the AJA system (data courtesy of J. Cha).	45
3.1	Description of the thin film structures investigated using XPS that are discussed in this chapter.	62
3.2	XPS peak fitting scheme for the B 1s, (Mg 2p, Co 3p, and Fe 3p), O 1s, Fe 2p, and Co 2p spectral regions for data taken from a 20 nm $\text{Co}_{60}\text{Fe}_{20}\text{B}_{20}$ /2 nm eb evaporated MgO sample.	64
3.3	B 1s and O 1s spectra from B_2O_3 thin films grown on Ta (from ref. [11]).	66
3.4	Mg 2p and O 1s spectra from thermally oxidized Mg thin films grown on Mo (from ref. [14]).	67
3.5	Co 2p and O 1s spectra from Co_3O_4 thin films grown on CoO (from ref. [16]).	69
3.6	Fe 2p and O 1s spectra from various Fe oxide films grown on MgO or Al_2O_3 (from ref. [17]).	70
3.7	XPS data from lightly ($\sim 10^{-4}$ Torr-second O_2 dose) and significantly (~ 15 Torr-second O_2 dose) oxidized 20 nm $\text{Co}_{60}\text{Fe}_{20}\text{B}_{20}$ films.	72
3.8	XPS data from lightly ($\sim 10^{-4}$ Torr-second O_2 dose) and significantly (~ 15 Torr-second O_2 dose) oxidized 20 nm $\text{Fe}_{60}\text{Co}_{20}\text{B}_{20}$ films before and after annealing.	75
3.9	XPS data from plasma oxidized 1.4 nm thick Mg thin films deposited on 20 nm thick CFB base electrodes before and after annealing.	76
3.10	XPS data from thermally oxidized 1.0 and 1.4 nm thick Mg thin films deposited on 6 nm thick CFB base electrodes before and after annealing.	79
3.11	XPS data from 1.0 and 2.0 nm thick electron beam evaporated Mg layers grown on CFB electrodes before and after annealing	81
3.12	XPS data from 1.0 and 2.0 nm thick electron beam evaporated MgO layers grown on FCB electrodes before and after annealing.	83
3.13	XPS data from 1.0 and 2.0 nm thick rf sputtered MgO layers (1 mTorr) grown on CFB electrodes before and after annealing.	85
3.14	XPS data from 1.0 and 2.0 nm thick rf sputtered MgO layers (10 mTorr) grown on CFB electrodes before and after annealing.	88
3.15	XPS data from 1.0 and 2.0 nm thick rf sputtered MgO layers (1 mTorr) grown on FCB electrodes before and after annealing.	89
3.16	XPS depth profiling data from CoFeB/MgO/Ta and CoFeB/MgO/CoFeB/Ta structures before and after annealing (from ref [23]).	90
3.17	XPS data from sputtered Mg / MgO bilayers grown on CFB electrodes before and after annealing.	92

3.18	XPS data from sputtered Mg / MgO bilayers grown on CFB electrodes before and after annealing.	94
3.19	Comparison of XPS data from sputtered MgO barrier layers grown with or without the use of a Ta getter (adapted from ref[26]). The Ta getter process reduces but does not eliminate the formation of MgBO, as shown by the intensities of the peak at ~ 532 eV.	96
4.1	Spectroscopic images from an annealed IrMn / CFB / MgO(10 nm) / Ta structure (Figure courtesy of J. Cha).	110
4.2	Individual EELS data from the MgBO and MgO regions of the annealed IrMn / CFB / MgO(10 nm) / Ta structure (Figure courtesy of J. Cha).	111
4.3	EELS data from as-grown and annealed CFB / 1.1nm MgBO / Py ₉₅ B ₅ and FCB / 1.1nm MgBO / Py ₈₀ B ₂₀ MTJ samples (data courtesy of J. Cha).	113
4.4	Multiple EELS data taken sequentially from one electrode to the other for as-grown and annealed versions of a CFB / 1.6nm MgBO / CFB MTJ (data courtesy of J. Cha).	114
4.5	3DAP studies of MgO MTJ structures showing B diffusion and segregation (from ref [25]).	116
4.6	STS data taken from ebd grown MgO, sputtered bilayer Mg/MgO, and rf sputtered MgBO materials on CFB electrodes.	119
4.7	STS data taken from ebd grown MgO and sputtered bilayer Mg/MgO barriers on Fe electrodes (from ref[34]).	120
4.8	Comparative CIPT data from as-grown MgBO MTJs with different electrode combinations and from MTJs with MgBO and Mg/MgO tunnel barriers of similar thickness.	123
4.9	Transport data from ref [11] (upper panel) and ref [12] (lower panel) comparing various barrier deposition methods.	124
4.10	Transport data showing TMR response to annealing for different thickness Mg seed layers and X-ray absorption data from ref [23].	126
4.11	STEM images of a CFB/1.6nm MgBO/CFB MTJ structure before and after annealing (data courtesy of J. Cha).	127
4.12	STEM images of a CFB/1nm Mg/1nm MgO/CFB MTJ structure before and after annealing (data courtesy of J. Cha).	129
4.13	CIPT data from MgBO-MTJs with various electrode combinations and barrier thicknesses.	130
4.14	Summary of CIPT data from MgBO-MTJs with various electrode combinations, barrier thicknesses, and getter processes used during deposition.	132
4.15	Semi-log plots of the data from Fig. 4.13 showing RA product as a function of tunnel barrier thickness.	134
4.16	Schematic of an ideal tunnel barrier.	135

4.17	TEM images and CBED patterns (insets) of as-grown (AG) and annealed (A) MgBO MTJs using different PyB free electrode layers. (Figure courtesy of J. Cha).	139
4.18	Measurements of free layer M_S values for MTJs with various electrode combinations as a function of annealing temperature.	140
4.19	Measurements of free layer H_C values for MTJs with various electrode combinations as a function of annealing temperature.	144
4.20	Schematic of orange peel coupling in an MTJ (from ref[44]).	145
4.21	Magnetization loops of $\text{Py}_{80}\text{B}_{20}$ free layers as a function of MgBO barrier thickness and annealing temperature.	146
4.22	Free layer coupling field measurements of MTJs as a function of MgBO barrier thickness (1.1-1.7 nm) and annealing temperature.	148
5.1	Proposed process of oxidation of the MgB_2 thin film surface.	158
5.2	Normalized angle-dependent XPS data from a control HPCVD MgB_2 thin film sample.	161
5.3	Normalized angle-dependent XPS data from a control RE MgB_2 thin film sample.	162
5.4	XPS data from RE deposited MgB_2 thin films grown on a variety of substrates.	164
5.5	XPS data from a PLD-deposited MgB_2 thin film sample, from ref[25].	166
5.6	The MgB_2 crystal structure.	167
5.7	XPS data from a pressed MgB_2 pellet that has been scraped and ion milled in-situ, from ref[26]. The labels in red are due to the authors.	168
5.8	XPS data from various B and B oxide samples, from ref[32].	169
5.9	Conductance data from point contact and heterostructure measurements incorporating MgB_2 thin films with native surface oxide barriers, from ref [35] and ref [22].	171
5.10	XPS data from an HPCVD MgB_2 thin film treated with post-growth annealing in Mg vapor.	176
5.11	XPS data from an HPCVD MgB_2 thin film exposed to UHP N_2 after growth for 90 seconds at a sample temperature of 400°C	178
5.12	Comparison of XPS data from MgB_2 thin films exposed to UHP N_2 for 30 minutes at a sample temperature of 200°C (upper panel) or 400°C (lower panel).	180
5.13	XPS data from a 150 nm thick RE MgB_2 thin film.	182
5.14	XPS data from a 500 nm thick RE MgB_2 thin film.	184
5.15	XPS data from a 150 nm thick RE MgB_2 thin film exposed to O_2 at a sample temperature of 240°C	186
5.16	XPS data from a 500 nm thick RE MgB_2 thin film exposed to O_2 at a sample temperature of 240°C	187
5.17	XPS data from a 150 nm thick RE MgB_2 thin film exposed to O_2 at a sample temperature of 400°C	189

5.18	XPS data from a 500 nm thick RE MgB ₂ thin film exposed to O ₂ at a sample temperature of 400°C.	191
5.19	AFM scans from the surfaces of 150 nm and 500 nm thick RE MgB ₂ thin films exposed to O ₂ at a sample temperature of 400°C.	192
5.20	B 1s spectra from four experimental investigations, (a) ref [26], (b) ref [41], and (c) ref [42], (d) ref [43], all of which modify the MgB ₂ surface with Ar ion milling.	194
5.21	XPS data from an RE film, after a year of storage in a dessiccator, and after Ar ion milling.	196
5.22	XPS data from control RE and HPCVD films etched in water.	198
5.23	XPS data from oxidized HPCVD films etched in water.	200
6.1	XPS data from Nb / Al films exposed to a N beam after in-situ vacuum transfer.	211
6.2	XPS data from sputter-etched, air-exposed PSMBE AlN films (from ref [19]).	213
6.3	XPS data from abrasively polished oxidized AlN films (from ref [20]).	215
6.4	XPS data from air-exposed AlN powder from ref [21].	217
6.5	XPS data from Nb / Al films exposed to a N beam at high power before and after vacuum annealing.	219
6.6	XPS data from AlN films rf sputtered on Nb in Ar or N ₂ before and after vacuum annealing.	220
6.7	Nb 3d XPS data from AlN films rf sputtered on Nb in Ar or N ₂ before and after vacuum annealing.	222
6.8	Nb 3d XPS data reactively dc sputtered NbN film using progressively higher N concentration in Ar/N ₂ process gas (from ref[24]).	224
6.9	XPS data from 1-2 nm thick AlN films rf sputtered on Nb in N ₂ before and after vacuum annealing.	226
6.10	XPS data from 2-3 nm thick AlN films rf sputtered on Nb in N ₂ before and after vacuum annealing.	227
6.11	Topography of the surface of an Al film exposed to a beam of atomic N at 400 W for 20 minutes.	228
6.12	STS data from an Al film exposed to a beam of atomic N at 400 W for 20 minutes. The data in each panel were averaged from within two different 25 nm ² film areas.	229
7.1	Cartoon of a double barrier junction incorporating MgBO barriers and a PyB free layer.	245
7.2	Cartoon of hybrid MTJ - JJ device film layers. The dashed lines indicate breaks in the deposition when the wafer is removed from vacuum and placed in a different deposition chamber.	250

CHAPTER 1

INTRODUCTION

The current Information Age and the Internet exist in large part due to the exponential growth rate in ultrahigh-density data-storage capacity over the past three decades. If ways are found to continue such growth rates, great benefits to society will occur through the evolution of even more powerful information technology. For the past few years, successful miniaturization and implementation of the magnetic tunnel junction (MTJ) has been crucial to maintaining growth in information storage technology. These thin-film structures emerged as the central device for next-generation magnetic random access memory (MRAM) and magnetic sensor applications, and are already in use in hard disk drive read heads. However, unless creative ways evolve to further optimize MTJs, highly attractive prospects for applications such as MRAM will go unrealized.

The remarkable improvements in both tunneling magnetoresistance (TMR) and junction resistance area (RA) product in MgO-based MTJs have pushed the capabilities of the MgO MTJ as a read head sensor in the hard disk drive sector as shown in Fig. 1.1. In addition, the MgO MTJ is at the forefront of emerging device applications including spin transfer MRAM and microwave oscillators (see Fig. 1.2). [1, 2] The MgO-based MTJ is a system wherein the correct choice of materials makes all the difference with regards to device performance. The research presented in this dissertation aims to unravel some of the important effects in both fabricating and optimizing MgO MTJs with an eye towards additional modifications that promote future device structures.

In chapter 2 I give a brief discussion of the historical development of MTJs accompanied by a simple theoretical explanation for the essential physics that

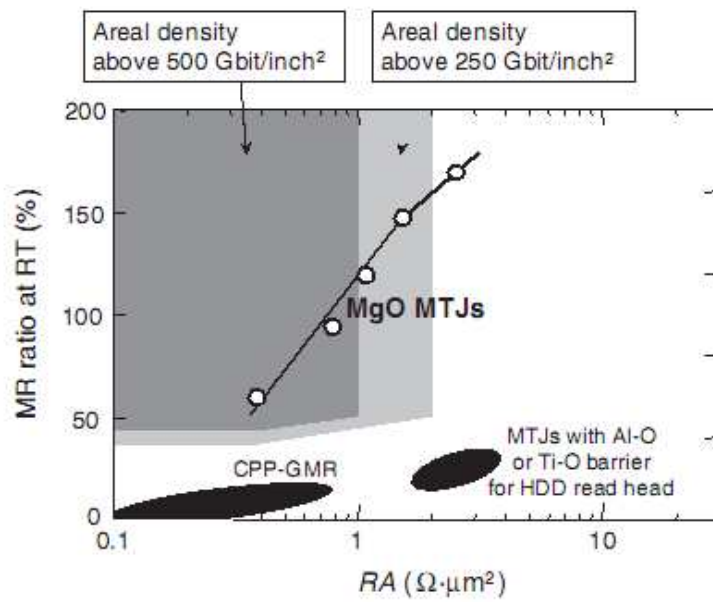


Figure 1.1: Plot of TMR versus RA for MgO MTJs made by the Canon Anelva corporation and how these values relate to read head sensors and hard drive density (data from ref [1,2]).

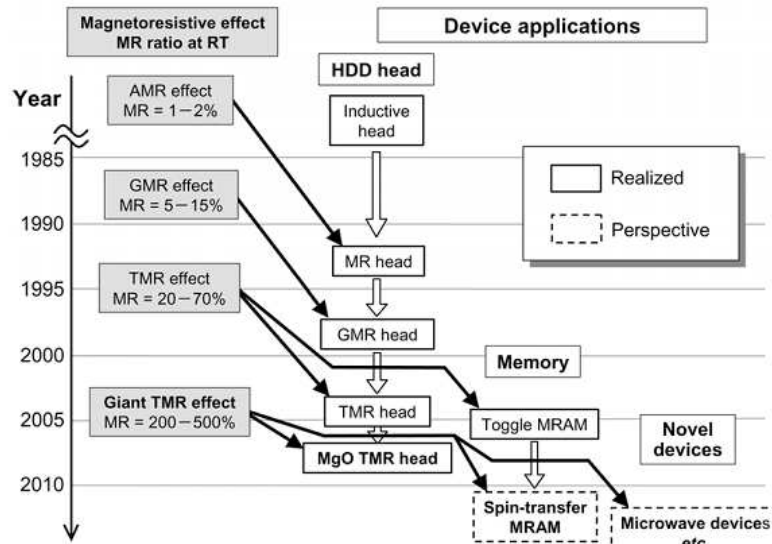


Figure 1.2: Progression of magnetoresistance (data from ref [1,2]).

governs MTJs with amorphous (AlO_x) and crystalline (MgO) barrier materials. Here there is a discussion of some of the most important discoveries related to magnetoresistance research. I track the development of the MTJ leading up to the discovery and enhancement of MgO -based MTJs. I discuss the research of the last 5-7 years on MgO MTJs in some detail with a focus placed on the interplay of materials and device performance. In the second part of chapter 2 I discuss the growth procedures that I developed for making MgBO -MTJs.

In chapter 3 I discuss the results of x-ray photoelectron spectroscopy (XPS) studies on $\text{CoFeB} / \text{MgO}$ bilayer samples. I investigate the growth of several types of MgO on CoFeB alloy electrodes and study the formation of B, Fe, and Co oxides as a function of MgO deposition technique and post-growth annealing. Plasma oxidation and thermal oxidation of a sufficiently thick Mg layer do not substantially oxidize the electrode and form relatively stoichiometric MgO . However, if the Mg layer is not thick enough, then B within the electrode diffuses out of the electrode and reacts with surface oxygen to form a MgBO surface layer. Electron beam evaporation of MgO also forms stoichiometric MgO on CoFeB without the formation of significant electrode oxides. Substantial electrode oxidation occurs during the growth of rf sputtered MgO layers. Thicker MgO layers and layers grown at higher sputtering pressures form greater amounts of B, Fe, and Co oxides. The rf sputtering process acts to plasma oxidize the electrode, and although annealing reduces the Fe and Co oxides, B oxide remains in the MgO barrier. There is an atomic rearrangement of the Mg, B, and O species during annealing which suggests a change in the chemical environment of the MgBO surface oxide. Insertion of an Mg layer between the CoFeB electrode and the MgO barrier is successful in reducing the electrode oxidation, but Mg/MgO bilayer barriers still allow B oxide incorporation into the MgO barrier during annealing if the Mg layer is thinner than

1.4 nm. The increased control over the barrier composition achieved by inclusion of an Mg layer or through use of gettering materials during the MgO deposition is due to the capture of oxygen liberated from the MgO target in the early stages of sputtering. However, reaction between B from the electrode and sputter deposited MgO appears to be an inherent part of the formation of rf sputtered MgO-based MTJs. These XPS studies explore the chemistry of the tunnel barriers that can form in different MgO growth processes. When correlated with the results of the next chapter, it becomes clear that the formation of MgBO barrier materials have significant benefits in making robust MTJ structures.

In chapter 4, I discuss the correlated results of several studies which show that the slight oxidation of B-alloyed bottom electrode materials during rf sputtering of an MgO target has several advantageous effects on the properties of the subsequently formed tunnel barrier material. Scanning transmission electron microscopy (STEM) / electron energy-loss spectroscopy (EELS) studies provide clear evidence that B oxide is present in the MgBO tunnel barrier in both the as-grown and annealed states. Scanning tunneling spectroscopy (STS) measurements show that as-grown MgBO barriers have fewer low energy defect states than MgO barriers and that there is no substantial increase in these defect states after annealing. Comparison of MTJs with MgBO barriers with MTJs with Mg/MgO bilayer barriers of comparable thickness shows that MgBO barriers yield higher TMR values and lower RA values. This chapter also addresses work on the use of B-alloyed permalloy (Py, Ni₈₁Fe₁₉) top electrodes. Transmission electron microscopy (TEM) measurements correlated with current-in-plane Tunneling (CIPT) measurements show that Py₈₀B₂₀ alloys are highly effective in forming MgBO MTJs with high TMR (~ 150 %) and low RA ($\sim 15 \Omega(\mu\text{m})^2$) values after annealing. These MTJs also show desirable magnetic behavior, low saturation magnetization (M_S) and

coercivity (H_C), and the dipolar coupling of the free layers decreases significantly after annealing. The work in this chapter shows that B is not only important for the formation of ultra-thin, low-resistance tunnel barriers, but is also the crucial component for enabling the use of superior ferromagnetic electrode materials (PyB alloys) for spin torque MRAM and magnetic sensor applications.

The XPS studies of the oxidation of MgB_2 thin films discussed in Chapter 5 show that the highly reactive nature of Mg dominates the oxidation of the film surface, but that surface oxide is composed of both Mg and B components. Exposure to N_2 or O_2 oxidizes the film, promoting the formation of MgO on the MgB_2 film surface and the surface becomes completely composed of MgO if the oxidation process is carried out at elevated temperature ($400^\circ C$) for extended time. However, if the oxidation occurs at lower temperature ($200^\circ C$), then the surface oxide formed is a mixed MgBO, similar to the native oxide. The oxidation process depletes the film surface of Mg, forming MgO_x , and promotes development of elemental B, and B sub-oxide near the film surface. The degree of formation of the elemental B, and B sub-oxide species is dependent upon the method of delivery of O to the film surface as well as the sample temperature during oxidation. The presence of semi-metallic elemental B and semi-conducting B sub-oxide could indicate other current paths exist in such oxide tunnel barriers that are likely to be a source of electronic noise as well as potentially detrimental to the superconducting electronic device behavior. Etching experiments show that oxygen delivered using different mechanisms (exposure to atmosphere, N_2 or O_2 exposure at elevated temperatures, ion milling, and water exposure) alters the MgB_2 film surface in similar ways to different extents. O incorporation into the MgB_2 film and formation of elemental B and B suboxide during the film oxidation could influence tunneling transport and degrade device performance, but the studies presented in this chapter provide

insights into optimal barrier formation techniques for JJ device development.

Chapter 6 discusses XPS studies of AlN tunnel barriers formed both by N beam exposure of Al films and by reactive rf sputtering of AlN in either Ar or N₂ process gas. Both film growth processes introduce O into the AlN film. When a pure N₂ atmosphere is used for reactive rf sputtering of AlN, the film growth nitridizes the underlying Nb film, similar to the way MgO oxidizes CoFeB. These studies provide some insights as to optimal AlN barrier formation for Josephson Junction structures.

I outline several experiments that are presented as extensions of the research discussed in this dissertation in Chapter 7 and I also provide a summary of the most significant results of my work.

REFERENCES

- [1] S. Yuasa, and D. D. Djayaprawira, Giant tunnel magnetoresistance in magnetic tunnel junctions with a crystalline MgO(0 0 1) barrier, *J. Phys. D: Appl. Phys.* **40**, R337 (2007).
- [2] S. Yuasa, Giant Tunneling Magnetoresistance in MgO-based Magnetic Tunnel Junctions, *J. Phys. Soc. Jpn.* **77**, 031001 (2008).

CHAPTER 2

BACKGROUND

The experiments described in this dissertation focus primarily on the growth and characterization of electrode and tunnel barrier materials for two specific electronic devices that are similar in structure but have significantly different uses. The essential part of both magnetic tunnel junctions (MTJs) and Josephson junctions (JJs) is composed of thin film electrode / tunnel barrier / electrode trilayers. In both systems the materials properties of the tunnel barrier and the electrode / barrier interfaces can substantially effect device performance. The first sections of this chapter describe the historical development and basic physics of MTJs and the final sections outline the growth process for MgBO-based MTJs that I developed.

2.1 Magnetoresistance and Magnetic Tunnel Junctions

The fundamental principle of magnetic memory, storage, and sensing is magnetoresistance (MR). Early magnetic field sensors used anisotropic MR (AMR), where the electrical resistance of a ferromagnetic material changes if the direction of an applied magnetic field is moved from parallel to perpendicular to the direction of current flow. The resistance change of AMR, on the order of 1%, is due to an increase in electron scattering in the parallel field-current configuration in comparison to the perpendicular field-current configuration. This MR effect is useful for measuring the amount of current flowing in a wire and is also used in magnetic compasses. Although the AMR effect is small, it points to a fundamental relationship between electron scattering and magnetic field.

In 1975 Julliere observed a difference in the resistance of Fe / Ge / Co mul-

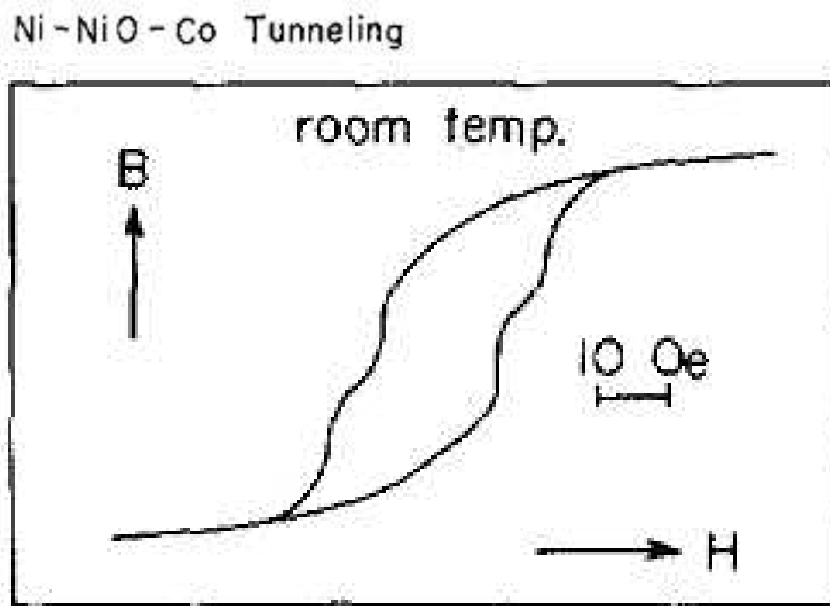
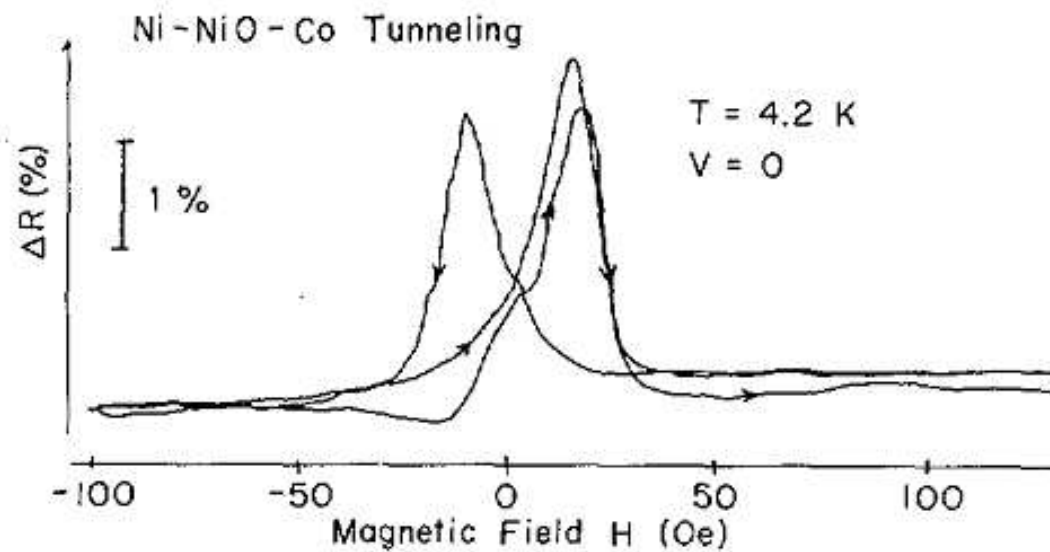


Figure 2.1: TMR and magnetization data as a function of applied field in a Ni / NiO / Co MTJ (from ref[2]).

tilayers as a function of the relative orientation of the ferromagnetic electrode magnetizations (parallel (P) or antiparallel (AP)) in an applied magnetic field on the order of 14% at 4.2 K. [1] He attributed this effect to spin-dependent electron tunneling through the Ge layer. A few years later, Maekawa and Gafvert observed a similar effect in thin film stacks of Ni / NiO / Ni, Ni / NiO / Fe, and Ni / NiO / Co (see Fig. 2.1). [2] These initial experimental observations of tunneling magnetoresistance (TMR) were described by the Julliere model, where TMR is defined in terms of the spin polarization (P) of the individual ferromagnetic electrodes.

$$TMR = \frac{\Delta R}{R} = \frac{R_{AP} - R_P}{R_P} = \frac{2P_1P_2}{1 - P_1P_2} \quad (2.1)$$

$$P = \frac{n_{\uparrow}(E_F) - n_{\downarrow}(E_F)}{n_{\uparrow}(E_F) + n_{\downarrow}(E_F)} \quad (2.2)$$

In this equation for P, $n_{\uparrow}(E_F)$ and $n_{\downarrow}(E_F)$ are the majority (spin up) and minority (spin down) densities of states for the electrode material at the Fermi level (E_F). It is important to note that for this definition of TMR the maximum value is infinite, provided both electrode P values are equal to 1. However, in practice most materials have $P < 1$. TMR does not become larger than 100 % until the electrode P values approach 0.6, which suggests that other mechanisms effect MTJs that exhibit TMR values above $\sim 100\%$.

Simple cartoons of the density of electron states for a normal metal and for a ferromagnet are shown in Fig. 2.2. A typical ferromagnet has an asymmetric density of states such that there is a greater density of one spin state (majority) than the other (minority). [3, 4] TMR can either be positive or negative and some materials even exhibit a density of states such that there is only one kind of spin

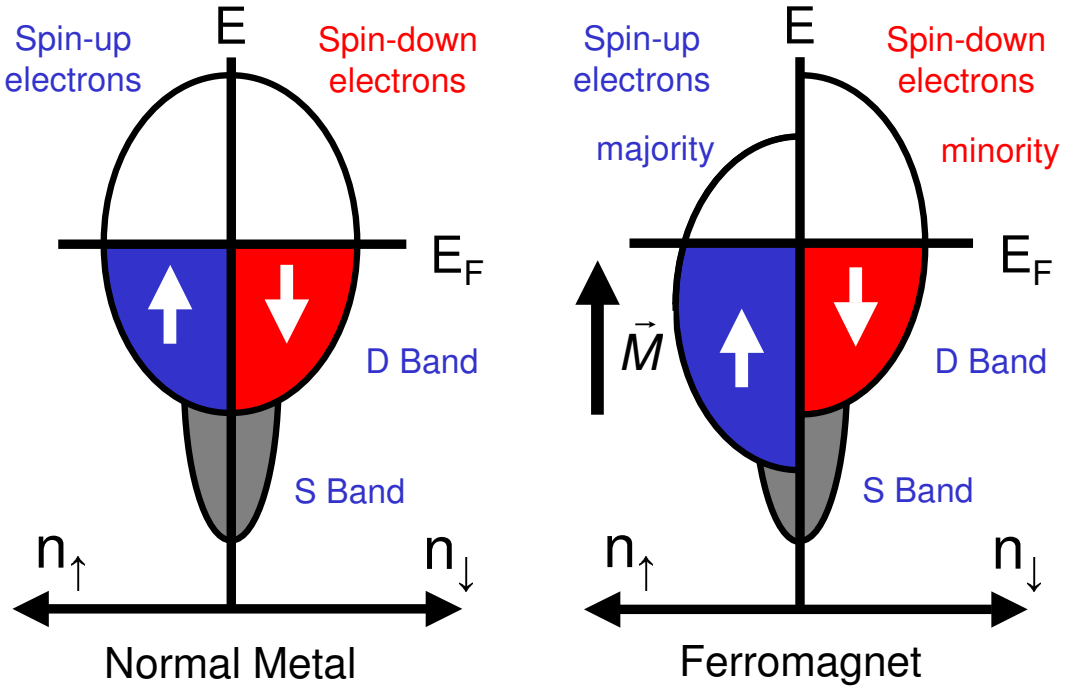


Figure 2.2: Schematic of densities of states for a normal metal and for a ferromagnet.

state available at E_F , which means they have $P = 1$. [3, 4] These half-metals are of great interest for enhancement of TMR, however extraordinary control of the crystal structure of these materials in an MTJ structure is required to achieve half metallic behavior.

A schematic of an idealized MTJ is shown in Fig. 2.3 with depictions of the ideal behavior of TMR (or ΔR) and magnetization as a function of applied field which help to understand the data displayed in Fig. 2.1. The MTJ consists of a thin ($\sim 1-2$ nm) insulating layer sandwiched between two ferromagnetic layers. The insulating layer, or tunnel barrier, is so thin that electrons can quantum mechanically tunnel from one electrode to the other. In order for a MTJ to exhibit features such as these, the two electrode materials must have different values of coercivity (H_C) which is the magnetic field strength required to flip the electrode

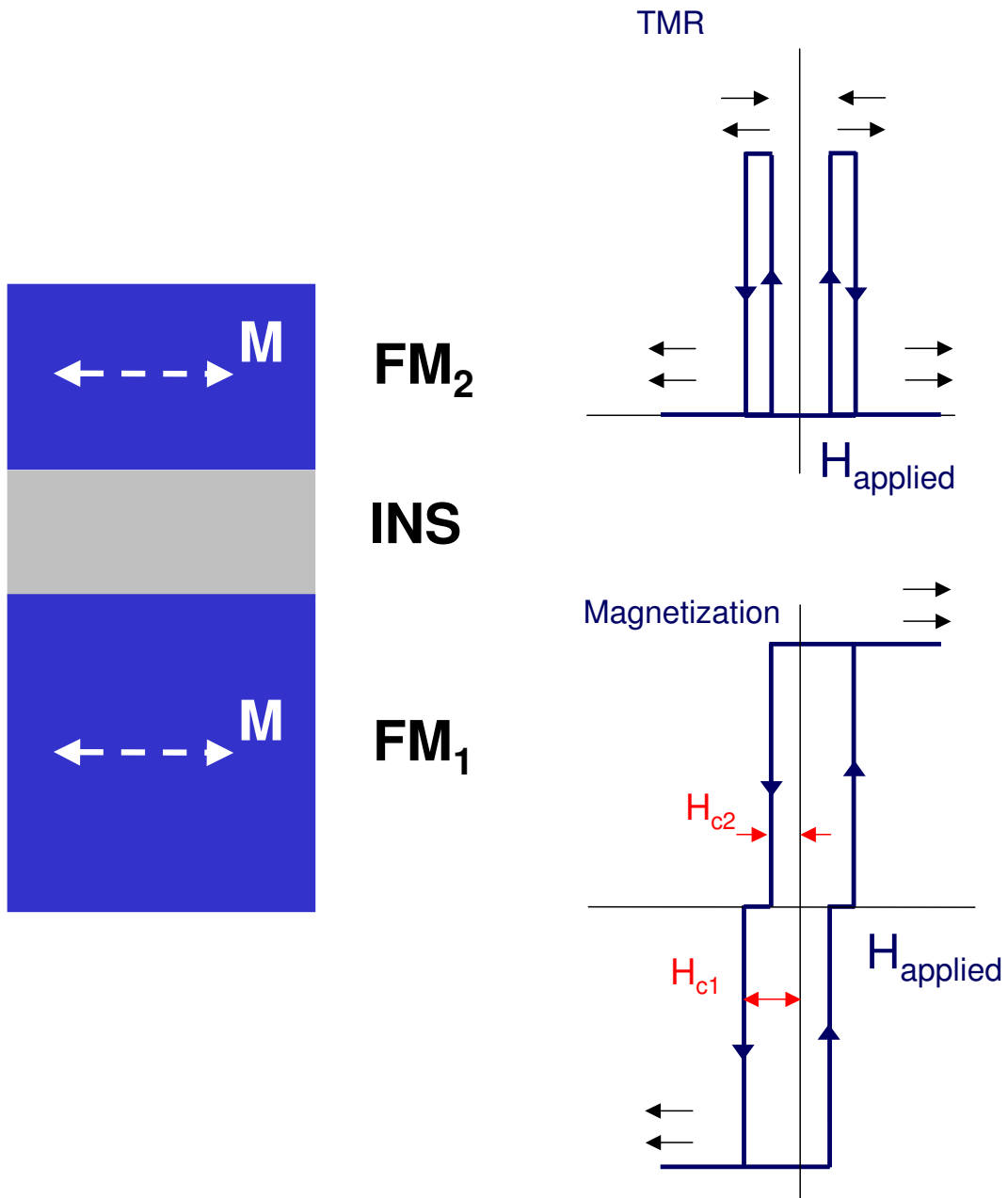


Figure 2.3: Schematic of a MTJ device and ideal plots of TMR and magnetization as a function of applied field.

magnetization. In a typical MTJ, different H_C values are achieved by either using two different materials or by using the same material but forming electrode layers of different thicknesses. The arrows on the idealized "data" in Fig. 2.3 show the direction of field sweep, and the black arrow pairs show the relative electrode magnetization configuration for the various field values. So, in this picture when the electrode magnetizations are parallel to one another the resistance state of the MTJ is low. However, when the applied magnetic field strength is between the values of the electrode coercivities ($H_{c2} < H_{applied} < H_{c1}$) then the MTJ is in state such that the electrode magnetizations are antiparallel to one another and the junction resistance is at its maximum value. [5–7]

A deeper understanding of the electrode transport taking place in this system is illustrated in Fig. 2.4. These idealized cartoons show the electrode densities of states for the parallel and antiparallel orientations. In the parallel state, the occupied and available electrode states for both majority and minority electrons are nominally identical. Provided the tunnel barrier is thin enough to allow electron tunneling, both up and down electron spins tunnel from the occupied (biased) electrode to the unoccupied (unbiased) electrode, the probability for electron tunneling is maximized, and the MTJ is at its lowest resistance value. However, the situation is quite different when the MTJ is in the antiparallel state. In this condition, the occupied and available electrode states are not the same. There are a large number of occupied majority spin states, but significantly fewer available majority spin states. Similarly, there are few occupied minority spin states and a large number of available minority spin states. These conditions do allow for tunneling, but do to the large differences in occupied and available spin states, tunneling is minimized and the MTJ is at its highest resistance value. This picture of tunneling in an MTJ is reasonable for disordered barrier materials like aluminum oxide (AlO_x). How-

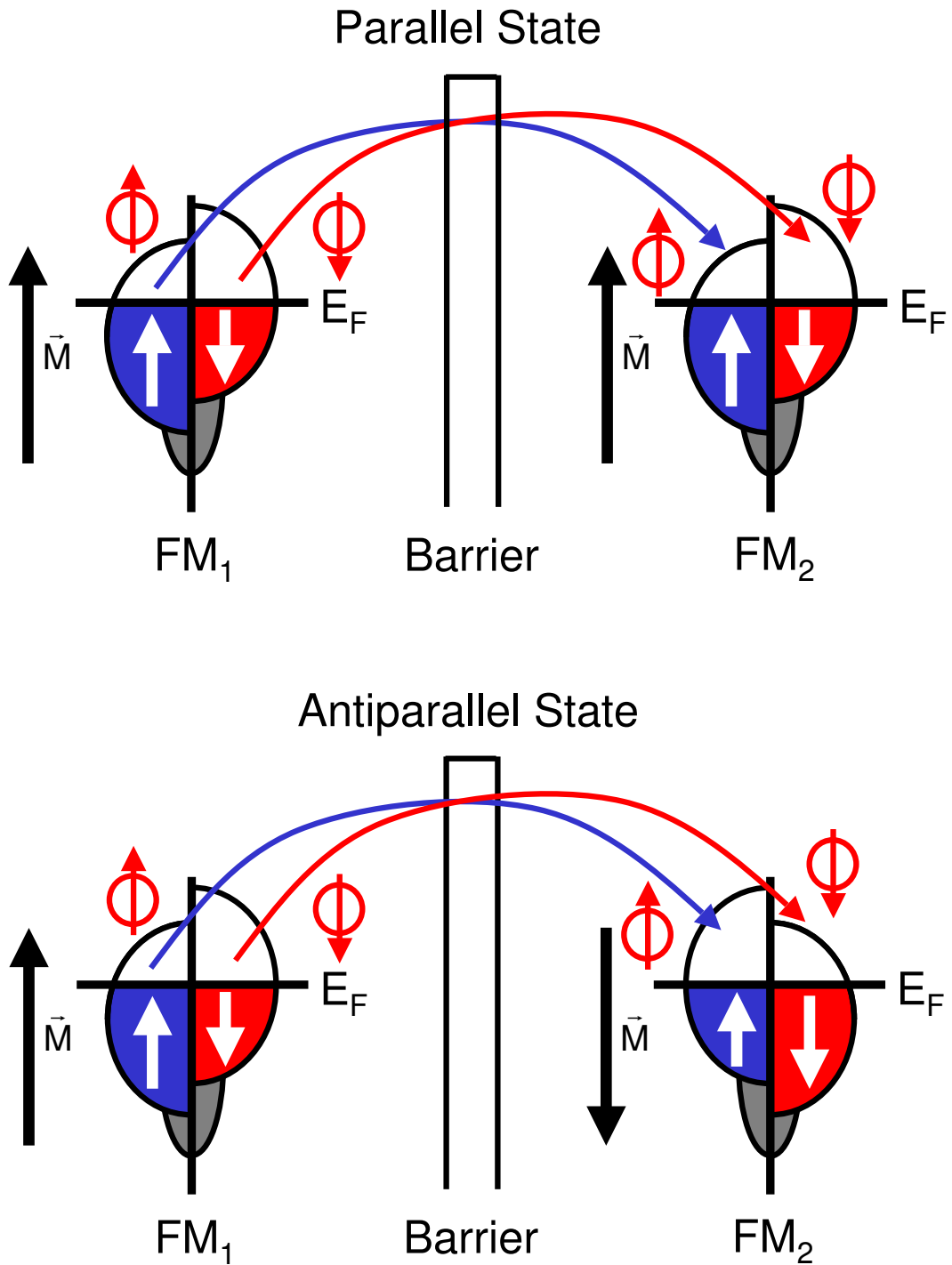


Figure 2.4: Schematic of tunnel for the parallel and antiparallel states for an MTJ device.

ever, when crystalline MTJs with the correct combination of barrier and electrode materials are formed, different mechanisms govern electron tunneling. [5–7]

Related experiments in tunneling between a superconductor and a ferromagnet through an insulator performed by Tedrow and Meservey provided a means to directly measure the spin polarization of ferromagnetic materials at low temperature (~ 0.4 K). The base electrode of these structures is an Al layer ($T_C \sim 1.2$ K) that was thermally oxidized to form a thin AlO_x tunnel barrier. On top of this was deposited a thin film of a Ferromagnetic material (Fe, Ni, Co, or Gd in the early experiments). The essential principle of the measurements is illustrated in both the data and the schematic shown in Fig. 2.5. Under the application of a large magnetic field the quasiparticle energies in the superconducting Al layer are split by $\pm \mu H$, where μ is the magnitude of the electron magnetic moment and H is the applied magnetic field. [8] The schematic of the experiment shows the Al density of states for $H = 0$ (solid lines) and for $H \neq 0$. When H is applied, spin-split peaks appear in the Al density of states at $\pm \Delta \pm \mu H$, where 2Δ is the superconducting energy gap in Al. In the experiment, as the bias voltage (V) is swept, peaks appear in the normalized conductance ($(dI/dV_s)/(dI/dV_n)$), where the subscripts s and n respectively refer to the superconducting ($T \leq T_C$) and normal ($T > T_C$) state). Using the schematic as a guide to the physics, the peaks occur at $V = \pm \frac{1}{e}(\Delta \pm \mu H)$. [8] Carefully taking the ratios of the conductivities for the various spin-split peaks yields the spin polarization of the material. [8, 9]

With the development of high precision deposition tools the ability to more carefully control thin film interfaces led to discoveries regarding magnetic coupling between thin film layers. Using light scattering of Fe / Cr / Fe and Fe / Au / Fe trilayers, Grünberg and co-workers demonstrated that the Fe layers are antifer-

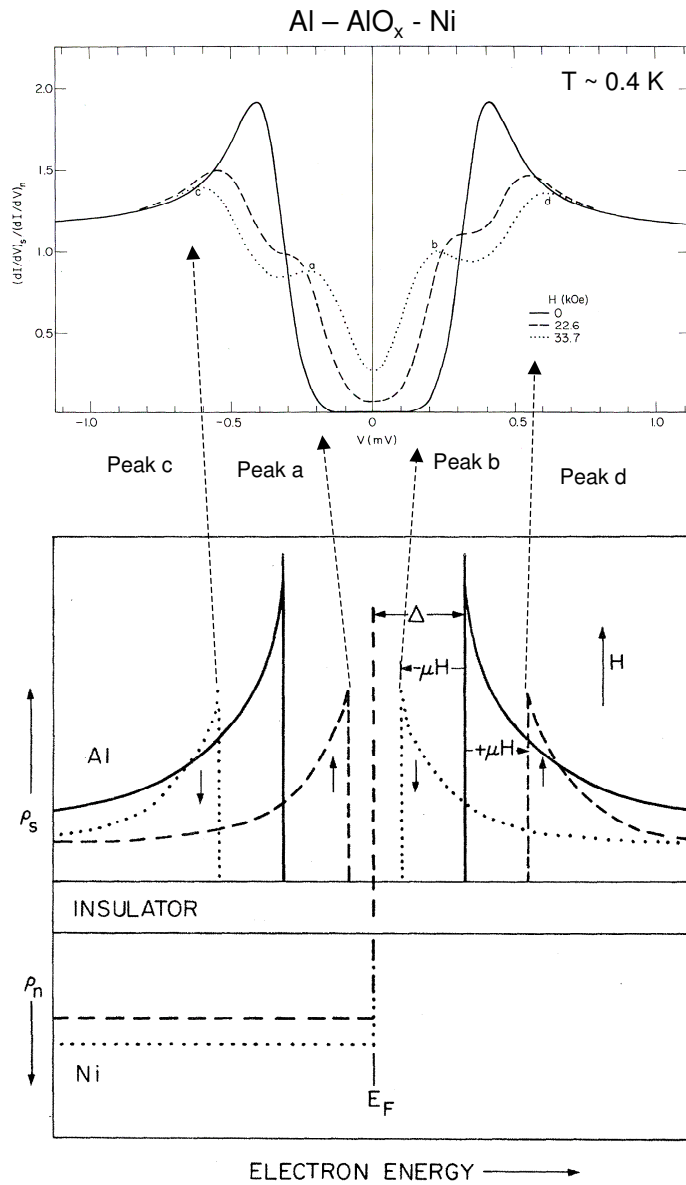


Figure 2.5: Normalized conductivity data and schematic of densities of states for an Al / AlO_x / Ni tunnel junction (from ref[9]).

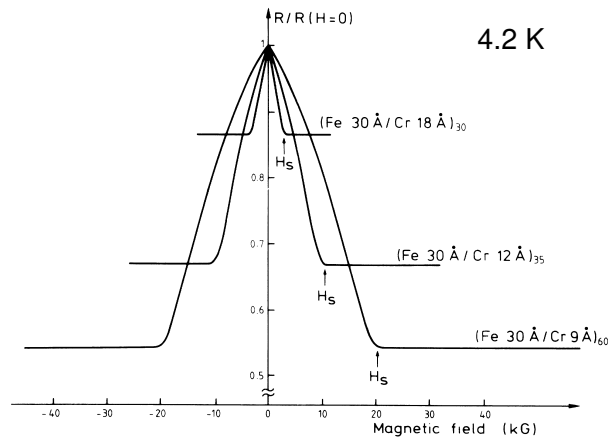
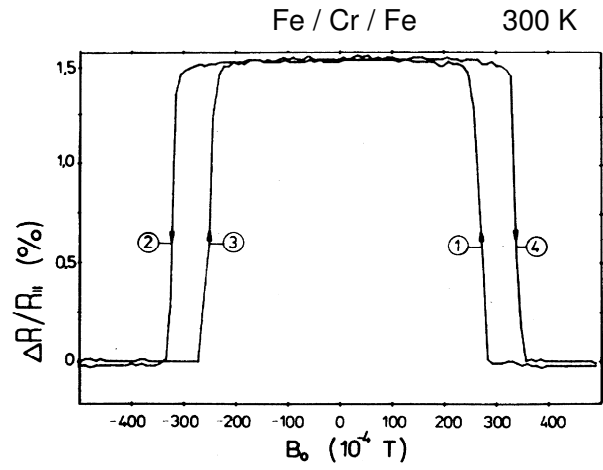


Figure 2.6: GMR data from a Fe / Cr / Fe spin valve at 300 K (from ref[12]) and from various Fe /Cr superlattices at 4.2 K (from ref[13]).

romagnetically coupled to one another when a Cr spacer layer is used. [10] This research ultimately led to the demonstration of giant MR (GMR) on the order of 10% in Fe / Cr / Fe by Binasch and co-workers (Grünberg group) [11] and on the order of 30-50% in Fe / Cr superlattices by Baibich and co-workers (Fert group) [12] (see Fig. 2.6). The discovery of GMR sparked a revolution in the MR research world which defined the modern hard disk drive industry.

Valet and Fert provided a model for the physics principles that govern GMR, which is summarized visually in Fig. 2.7 and commonly referred to as the 2-resistor model of GMR. [13] A simple picture for GMR is that ferromagnetic materials filter electrons that pass through them with regards to spin. An electron that scatters through a ferromagnet will emerge on the other side in an angular momentum state that is parallel to the magnetization of the ferromagnet. This means that if an electron moves through a ferromagnet / normal metal / ferromagnet trilayer where the ferromagnet magnetizations are parallel to one another, then there will be few scattering events for the conducting electrons with spin states that are parallel to the electrode magnetizations. Electrons in spin states that are antiparallel will scatter significantly more, but there still exists one low resistance conductance channel and so the parallel magnetization state is a low resistance state. If the ferromagnet magnetizations are antiparallel to one another then both spin up and spin down conducting electrons will scatter as they pass through the spin valve. So both conductance channels are equally resistive and high relative to the low resistance state. These measurements and the explanation of the underlying principles of spin-dependent scattering that govern GMR, won Grünberg and Fert the 2007 Nobel Prize in Physics.

The demonstration of GMR revitalized the MR community and generated a

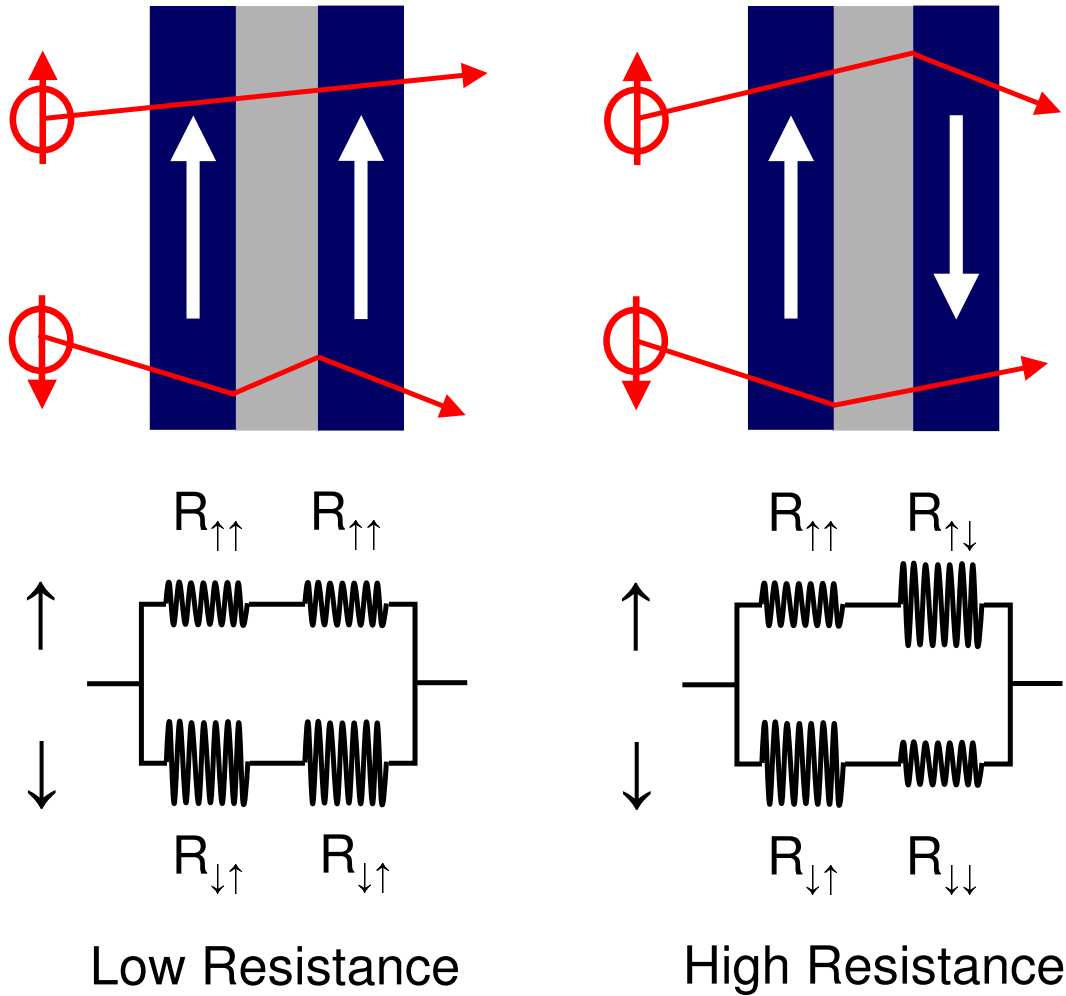


Figure 2.7: Two-resistor (Valet-Fert) model of GMR (from ref[14]).

great deal of interest in the previous work on tunnel junctions described above. After Moodera and co-workers [14] and Miyazaki and co-workers [15] showed in 1995 that TMR can be achieved in AlO_x -based MTJs at room temperature (see Fig. 2.8), research on MTJs rose steadily. As the need for greater sensitivity arose in the disk drive industry as recording media sizes shrank, the superior performance of MTJs made them the sensor of choice for next-generation hard drive read heads. The AlO_x -based MTJs of Moodera and Miyazaki exhibited TMR on the order of 10-20% and the highest reported values for TMR in an AlO_x -based MTJ come from NVE. Wang and co-workers achieved $\sim 70\%$ TMR through impressive device

engineering, specifically by incorporating glassy magnetic electrodes that allow for smoother electrode-barrier interfaces. [16]

Although the work of the NVE team represented significant progress in AlO_x -based MTJs, that same year Parkin and co-workers [17] and Yuasa and co-workers [18] published groundbreaking results from MgO-based MTJs showing remarkable TMR around 200% after annealing (see Fig. 2.9). Such high TMR had been previously predicted by Butler and co-workers [19] and by Mathon and co-workers [20] who independently explained the enhancement in TMR as being due to coherent tunneling in the Fe / MgO / Fe system and vastly different decay rates for majority and minority spin electrode Bloch states of different symmetries as they couple through the MgO barrier. Figure 2.10 shows calculations from ref[20] for the transmission probability of majority and minority spin electrons with regard to crystal momentum. The calculations show that, unlike the Julliere model, majority and minority spin electrons tunnel differently through a crystalline MgO barrier. The Julliere model assumes that all majority and minority spin Bloch states have the same spin polarization and therefore tunnel with the same efficiency leading to completely incoherent tunneling. However, in the calculations for the Fe / MgO / Fe system it is clear that majority and minority Bloch states do not tunnel the same way. The majority Bloch states are almost entirely forward focused (zone centered) while the minority Bloch states are off-center. The enhancement of transmission at these off-center sites is due to resonant tunneling through interfacial surface states, and these locations are referred to as hot-spots.

More detail regarding the tunneling in Fe / MgO / Fe MTJs can be found in the calculations of densities of states for the parallel and antiparallel MTJ states shown in Fig. 2.11. It is clear from these calculations that Bloch states with different

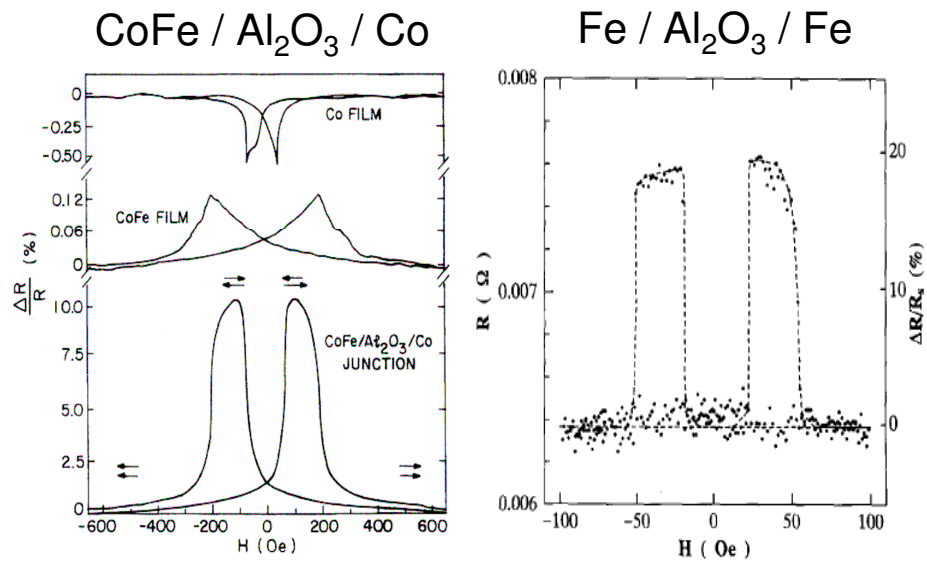


Figure 2.8: TMR measurements in AlO_x-based MTJs at room temperature (from ref[15] and ref[16]).

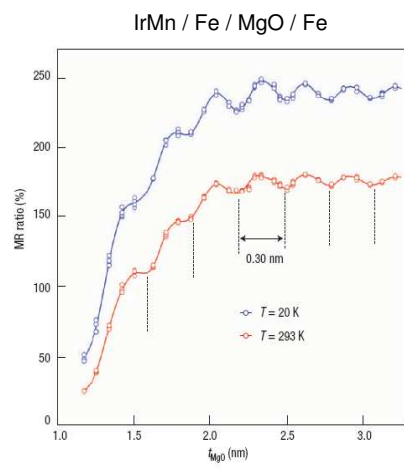
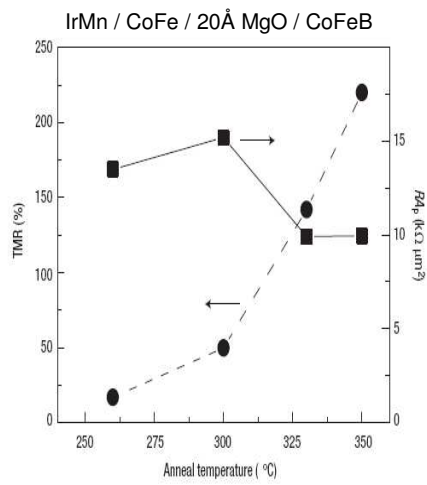
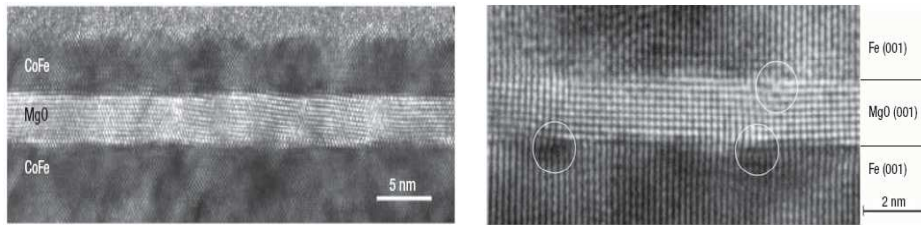
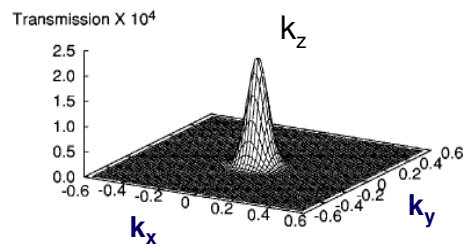


Figure 2.9: TEM images and TMR measurements of MgO-based MTJs (from ref[18] and ref[19]).

orbital symmetry couple into the MgO tunneling states with different efficiency. The s-like Δ_1 majority Bloch state decays very slowly through the MgO, but the p-like Δ_5 and d-like $\Delta_{2'}$ Bloch states decay much more rapidly. Therefore, as the MgO barrier gets thicker, the majority electrons that are most likely to tunnel to the counter electrode have s-like Δ_1 symmetry. In the case of minority spin states, p-like Δ_5 Bloch states decay more slowly than d-like Δ_2 and $\Delta_{2'}$ Bloch states. So, the minority electrons that are likely to tunnel through a thick MgO barrier have p-like Δ_5 symmetry. Although these p-like Δ_5 minority Bloch states tunnel the most efficiently of the minority states, they decay far more rapidly in the MgO barrier than the majority s-like Δ_1 states. The result is a very large spin-filtering effect from the MgO barrier that creates a substantially smaller minority spin tunnel current in comparison to the majority spin tunnel current. The large difference in these tunnel currents is the primary reason for the extraordinarily high TMR in Fe / MgO / Fe MTJs.

The initial measurements of large TMR in MgO-MTJs [17, 18] demonstrate that the behavior of TMR as a function of barrier thickness depends somewhat upon the barrier growth method and that annealing the structures is crucial to achieving large TMR values. The data of Parkin and co-workers shows very clearly that TMR increases with annealing temperature (up to a point – annealing begins to degrade performance at $\sim 425^\circ\text{C}$ in these junctions). Yuasa and co-workers published earlier that same year showing high TMR of about 88% ($P_{\text{tunneling}} \sim 0.55$) in Fe / MgO / Fe MTJs. [21] Careful inspection of the methods section of their Nature Materials publication which demonstrates $\sim 188\%$ TMR ($P_{\text{tunneling}} \sim 0.70$) explains the difference in the structures. The higher TMR structure was annealed half-way through growth. After the MgO barrier was deposited, the sample temperature was increased. This drives surface oxygen (chemisorbed oxygen)

Majority Transmission for 8 MgO Layers



Minority Transmission for 8 MgO Layers

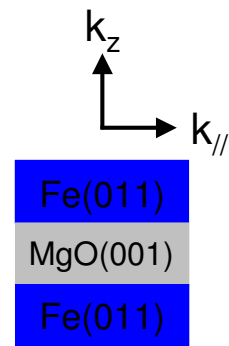
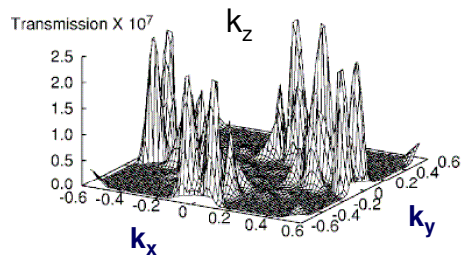


Figure 2.10: Theoretical depiction of coherent tunneling in an ideal Fe / MgO / Fe MTJ (from ref [20]).

into the barrier or evaporates it off of the barrier surface leaving a far less reactive MgO surface for the top Fe electrode to be grown on. In the case of the work of Parkin and co-workers annealing likely reduces interfacial electrode oxides and also improves the crystalline coherency of the electrode - MgO interfaces and the MgO barrier itself.

Parkin mentions that the IBM samples show no strong dependence of TMR on barrier thickness while Yuasa shows a clear increase in TMR with barrier thickness as predicted by Butler and co-workers and Mathon and co-workers. This discrepancy leads one to question whether barrier deposition and electrode materials influence the TMR dependence upon thickness. The IBM samples were probably grown using techniques developed by Mauri [22] using a three step process of depositing a Mg layer, then a MgO layer, and then oxidizing the entire stack. However, the IBM team may have used one of several MgO deposition techniques, most likely either an ion-beam deposition of MgO or a reactive sputtering deposition of Mg in Ar/O. In contrast, the highly crystalline, epitaxial Fe / MgO / Fe MTJs grown with molecular beam epitaxy (Fe electrodes) and electron beam evaporation (MgO) of Yuasa and co-workers exhibit a clear thickness dependence of TMR, which suggests that in terms of making high TMR MTJs with thin barriers, approaches other than e-beam evaporation will work best.

Shortly after these initial demonstrations, the team at Canon Anelva demonstrated high TMR of 230% ($P_{tunneling} \sim 0.73$) in CoFeB / MgO / CoFeB MTJs that were entirely sputtered and annealed post-growth. [23] This began the ongoing race to high TMR in MgO MTJs that rapidly ascended from 355% ($P_{tunneling} \sim 0.80$) [24] to 500% ($P_{tunneling} \sim 0.85$) [25] to the current high TMR mark of 600% ($P_{tunneling} \sim 0.87$) [26]. All of these high TMR values were first reported by

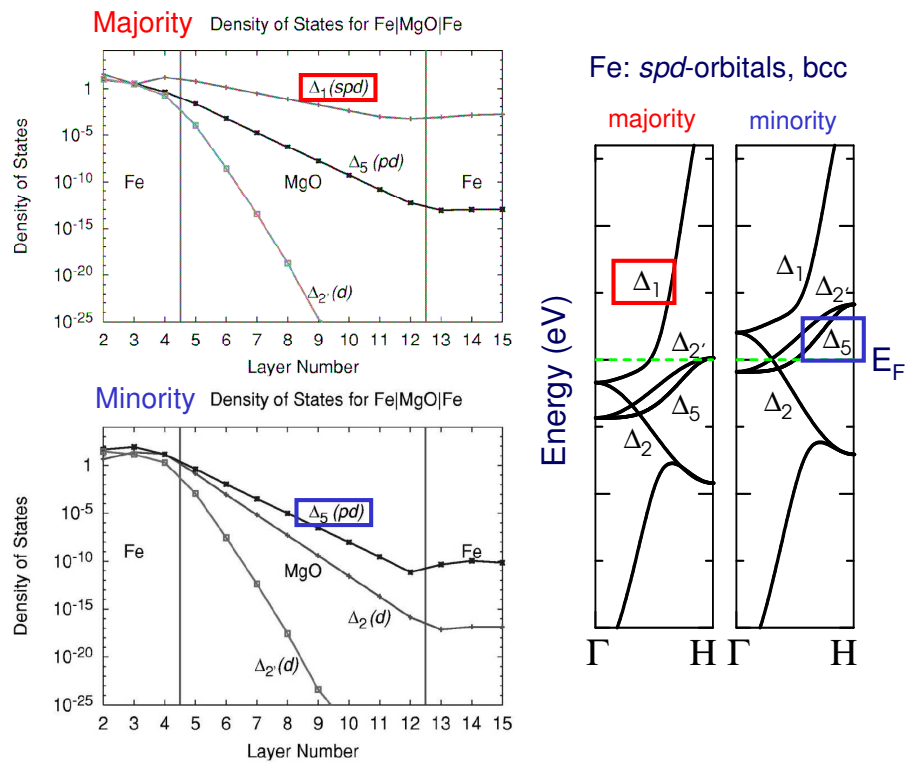


Figure 2.11: Theoretical results showing different decay rates through the MgO barrier for electrode wavefunctions of different symmetries in an ideal Fe / MgO / Fe MTJ (from ref [20]). Also shown is the spin-split band structure for bcc Fe showing which Bloch states populate E_F (from ref[5]).

the team of Ohno at Tohoku University in Japan, but Parkin's team has been able to reach the 300-350% ($P_{tunneling} \sim 0.77 - 0.80$) range. [5] The work of the Tohoku team rests on two significant discoveries besides whatever magical techniques they may use to grow such nice MgO barriers. First, they have used Co-Fe-B alloys of different compositions, showing that $Co_{20}Fe_{60}B_{20}$ gives the best results. Second, they have removed the antiferromagnetic pinning layer to allow extremely high temperature annealing of upwards of $\sim 500^{\circ}C$ which promotes coherent junction crystallinity (See Fig. 2.12).

While the Ohno group was raising the bar regarding TMR, the team at Anelva was working to push down the junction resistance while maintaining as high a TMR as possible. The typical figure of merit used to compare junctions is the junction specific resistance or resistance area (RA) product, simply the junction area times the junction resistance. The Anelva team made remarkable headway, first achieving $\sim 2.4 \Omega(\mu m)^2$ and 138% TMR with a Mg / MgO barrier deposition process [27] and then $\sim 0.4 \Omega(\mu m)^2$ and 50% TMR by using a Ta getter before direct MgO deposition (see Fig. 2.13). [28] However, the article of Tsunekawa and co-workers [27] is a bit confusing. The authors present TMR and RA data as a function of barrier thickness for Mg/MgO and MgO barriers which appears to be reversed. This observation is based on the comment made in the article that transmission electron microscopy (TEM) images of these MTJs show that 0.4 nm Mg / 1.5 nm MgO barriers are slightly thicker than 1.5 nm MgO barriers, which would likely cause the RA product to be higher for this thicker junction. However, the RA as a function of barrier thickness data does not suggest that this is so. Instead, the data is labeled such that the thinnest junctions in the study are Mg/MgO barriers, and these MTJs are presented as having lower RA values for comparable barrier thickness. It is very likely that the data is mislabeled, but if this is the case, then

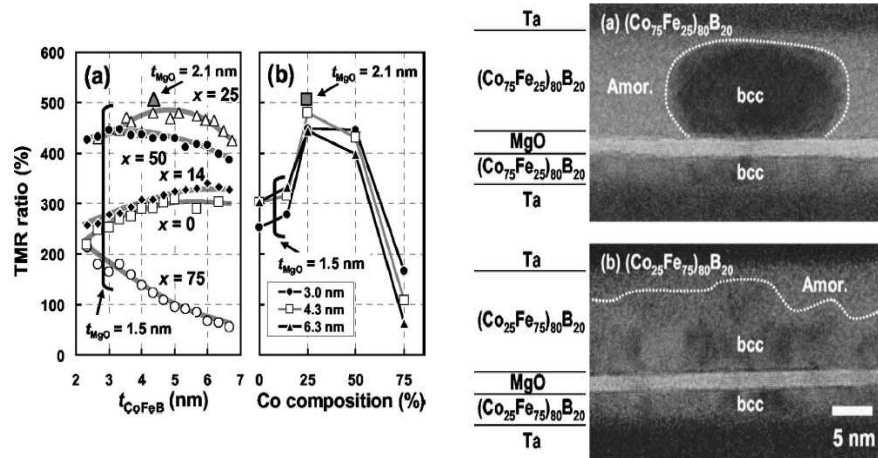
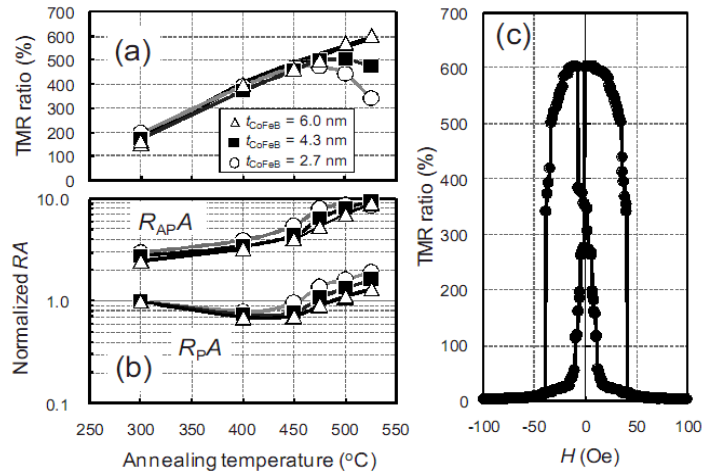


Figure 2.12: Studies of various CoFeB alloy electrodes and their effect on TMR in MgO MTJs (from ref[24] and [25]).

the primary conclusion of this paper, that ultra-thin Mg/MgO barriers generate MTJs with lower RA products, is incorrect. Regardless, the next installment from the Anelva team, the work of Nagamine and co-workers [28], shows that use of a Ta getter in conjunction with direct rf sputtering of an MgO barrier forms superior junctions. While the issue of the performance of Mg/MgO barriers is confusing, the conclusion that Mg/MgO barriers are more crystalline than MgO barriers (as shown by x-ray diffraction and TEM), is correct. In addition, if the data is in fact reversed with regards to Mg/MgO versus MgO barrier performance, then the data from this paper is in complete agreement with the studies presented in chapter 4 of this dissertation.

Other interesting developments that relate to MgO-based MTJ formation are being researched by several groups throughout the world. Isogami and co-workers (Takahashi Group, Tohoku University) have used rapid infrared heating of the bottom electrode - MgO barrier structure before top electrode deposition which currently achieves $\sim 1.6 \Omega(\mu\text{m})^2$ and 210% TMR and shows great promise for future MTJs. [29] Also, the use of highly spin polarized Heusler alloy electrodes have shown great promise in MgO-based MTJs. [30–32] However, the enhancements afforded by these materials are observed at low temperature but not at room temperature and the materials are quite difficult to make in the proper crystal orientation.

Some other exciting theoretical studies in conjunction with experimental investigations have advanced the field. Zhang and co-workers and Mathon and co-workers demonstrated that interfacial FeO in a Fe / MgO / Fe MTJ significantly reduces TMR due to the removal of the symmetry of the available Bloch states at the electrode - barrier interfaces. [33, 34] Meyerheim and co-workers measured

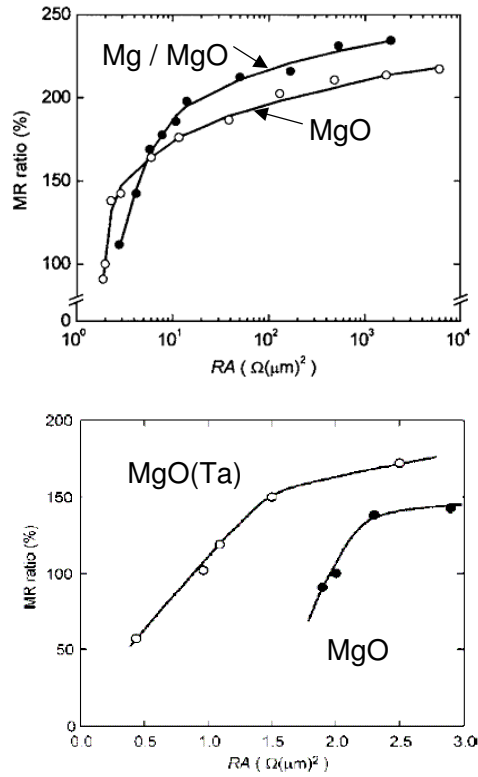


Figure 2.13: Studies of RA product reduction for different MgO barrier deposition techniques. The data in the top panel (from ref[26]) is labeled differently from how the authors of the paper label them, as described in the text. The data in the bottom panel (from ref[27]) compares MgO barriers deposited with an without a Ta getter.

the formation of FeO using x-ray diffraction [35] and then followed these structural studies with theoretical modeling that including FeO on both sides of the MgO should restore the symmetry and enhance TMR. [36] Butler and co-workers extended their theory to include body centered cubic (bcc) Co / MgO / bcc Co MTJs and showed that the TMR in this system should be even higher than that of bcc Fe / MgO / bcc Fe. [37] The natural crystal structure of Co is hcp, but in an experimental tour de force, Yuasa and co-workers strained 4\AA layers of Co into the bcc structure by growing Fe / Co / MgO / Co / Fe MTJs and confirmed the theoretical results. [38] Yuasa and co-workers also showed that in the CoFeB / MgO / CoFeB MTJ structure the MgO barrier imprints its crystal structure onto the electrodes during annealing which explains the high degree of crystallinity observed in these MTJs. [39]

The materials work that has advanced the ability to achieve high TMR in low RA MTJs has made these structures excellent candidates for magnetic random access memory (MRAM), sensors, and logic applications. While there are certainly many new aspects of this system to be explored and possibly optimized, the future looks very bright for the use of MgO-based MTJs in a wide array of electronic device applications.

2.1.1 Hard Disk Drive Read Heads and Magnetic Random Access Memory

As result of the demonstrated ability of spin-polarized currents to efficiently reverse the orientation of a thin film nanomagnet [40, 41], MRAM is now emerging as an universal computer memory solution and is poised to replace both dynamic and

static RAM (see Fig. 2.14 and 2.15). [42] Due to the nearly infinite write-cycling capability and long retention time of roughly 10 years possible with magnetic materials as well as the scalability of thin film devices, spin-torque MRAM may even displace FLASH memory in many demanding non-volatile memory applications. The key challenge, which was discussed earlier in this chapter, is to fully understand and to further improve the efficiency of MTJs in the ultra-thin (~ 1 nm) barrier, low RA product regime that is optimal for MRAM devices written by spin-polarized currents, and also to adapt the MgO barrier technology to be compatible with more magnetically attractive (soft) electrode materials, such as permalloy ($\text{Ni}_{81}\text{Fe}_{19}$, Py), to better enable switching and sensor applications.

The expansion of the computer hard disk drive industry fueled worldwide demand for greater information storage capacity and generated thin-film technologies that are robust and inexpensive. Substantial miniaturization of devices and broadened understanding of nano-scale thin-film materials have allowed the industry to expand significantly over the last ten years. The hard disk drive industry gained new benchmarks in 2007 when Hitachi Global Storage Technologies announced a 4 Terabyte desktop hard drive and NEC and Toshiba announced operational magnetic memory chips that champion the MRAM effort, but clearly identify device density and signal strength as two key challenges. In MRAM, the memory state is stored in a magnetic bit (an MTJ) that can have one of two magnetic configurations. Magnetic memory is advantageous because information is stored in thermodynamically stable magnetic fields unlike charge-based technologies that require significant power to refresh the memory state. Although susceptible to failure during re-writing cycles, charge-based FLASH memory is inexpensive and this has kept MRAM from emerging as a dominant non-volatile memory technology. The research currently conducted addresses advancement in the density, signal

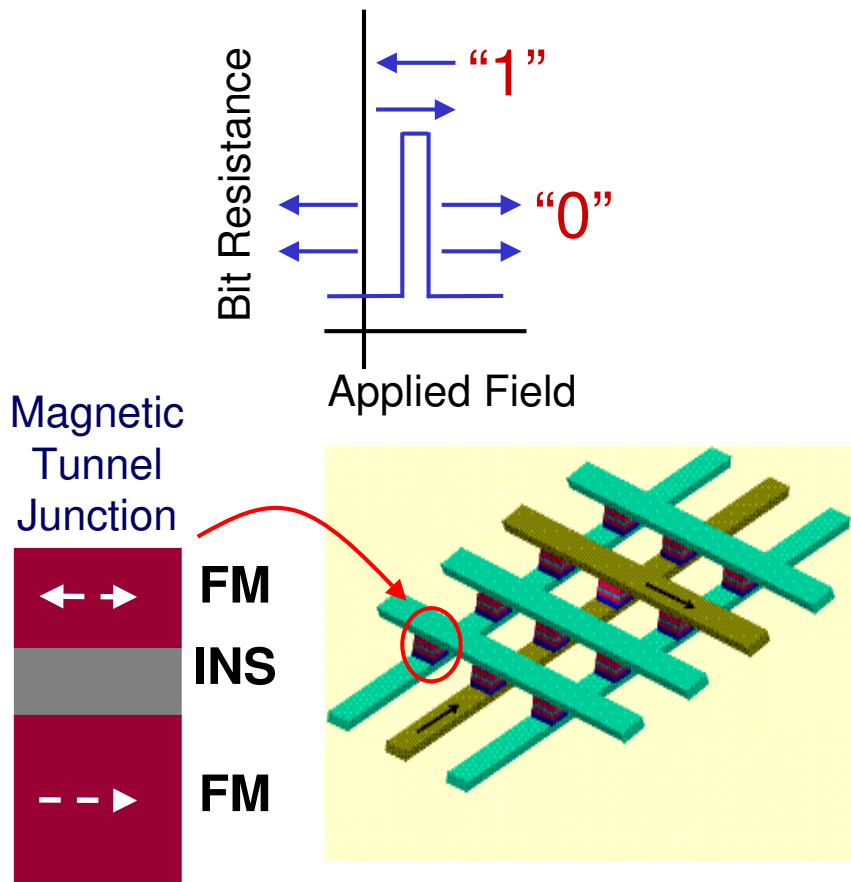
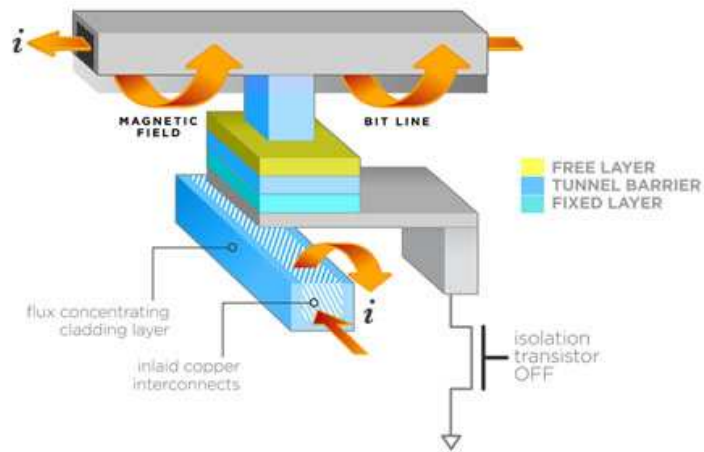


Figure 2.14: Schematic of a MRAM array using MTJs as the memory element (bit).

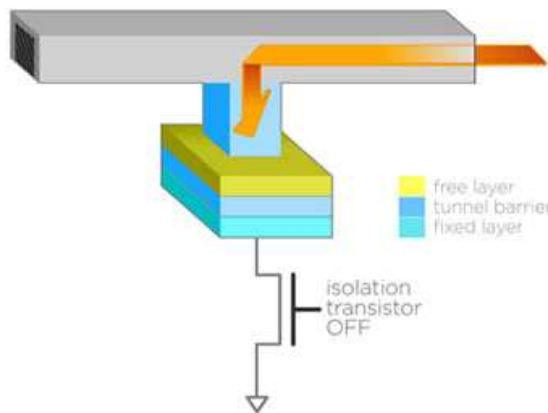
strength, and speed of MRAM, which are the necessary ingredients to surpass SRAM, DRAM, and FLASH technologies.

Promising MRAM architectures involve MTJs that can be written using spin transfer torque switching (STTS) provide possible reduction of bit size and improvements in switching. [43] STTS is a phenomenon in nanoscale magnetic structures where, unlike in GMR devices, no applied magnetic field is necessary to switch the magnetization of the free layer with respect to the reference layer. Instead, large current densities ($\sim 10^6$ A/cm²) of spin-polarized electrons can impart a torque on the free layer and thus switch the orientation of its magnetization. When tunneling spin-polarized electrons are incident upon a nano-ferromagnet with anti-parallel magnetization, the component of the electron spin that is parallel with the magnetization is transmitted and the anti-parallel component of electron spin is reflected. Since angular momentum must be conserved in the process, the transverse component of the electron spin generates a torque on the nanomagnet. For a sufficiently high current, the critical current (I_C), the generated torque is large enough to switch the magnetization of the nanomagnet, allowing writing of a memory state. This dramatically reduces the footprint of an MRAM cell by removing wires that generate the magnetic fields necessary for toggle-based switching. [43] However, to achieve large densities, fast switching speeds, and low power consumption, and compete with existing SRAM, DRAM, and FLASH memories, new breakthroughs in barrier technology and device implementation are necessary.

The major applications for MTJs are magnetic sensors, hard disk drive read heads, and MRAM. If the noise floor of an MgO-based MTJ can be reduced, then cheap thin film sensors with applications such as magnetocardiograms can be achieved that will be of significant benefit to society. Given that the RC time con-



<http://www.everspin.com/technology-toggle-ram.html>



<http://www.everspin.com/technology-spin-mram.html>

Figure 2.15: Comparison of MRAM cell size for toggle and STT MRAM (from ref[44]).

stant is significantly large in an MTJ (larger than ~ 1 ns) it is unlikely that MTJs will continue to be used in hard disk drive read heads. MRAM is the most exciting application for MTJs, especially when STTS is incorporated into the MRAM cell. With this particular application in mind, several materials advances can potentially reduce I_C while possibly maintaining thermal stability. The equation for I_C for a nanomagnet with in-plane magnetization shows that a highly spin polarized material with low damping and small saturation magnetization could be used to reduce I_C .

$$I_C = \frac{1}{\eta} \left(\frac{2e}{\hbar} \right) \frac{\alpha}{|\cos\phi|} (V_m H_K M_S) \left(1 + \frac{2\pi M_S}{H_K} + \frac{H}{H_K} \right) \quad (2.3)$$

In this equation for I_C , η is the spin polarization factor, e is the electron charge, α is the phenomenological (Gilbert) damping coefficient, ϕ is the angle between the spin direction and one of the two coordinate axes perpendicular to the direction of current flow, V_m is the nanomagnet volume, H_K is the uniaxial-anisotropy field, and H is the applied magnetic field (see ref [44] for the details of the calculation).

The trade-off is the thermal stability of the free layer in the MTJ. The thermal transition lifetime τ_L of the nanomagnet also includes M_S in the expression for the thermal energy barrier E_o .

$$\tau_L = \tau_A e^{\frac{E_o}{k_b T}} \quad (2.4)$$

$$E_o = \frac{1}{2} V_m M_S H_K \quad (2.5)$$

New MRAM architectures are currently under development, but these issues

are key to the advancement of MRAM as a universal memory solution. The use of highly spin polarized, low M_S materials may be beneficial for reducing I_C , provided that the thermal stability of the MTJ can be maintained.

2.2 Thin Film Growth

The samples that incorporate MgO or AlN tunnel barrier layers made for the experiments discussed in the following chapters were grown either in the preparation chambers in D7 (Prep 1 and Prep 2), or in the the seven gun AJA sputtering system. The growth and preparation chambers in D7 were already outfitted with thermal and electron beam evaporation capabilities thanks to many previous students. The most recent additions made to the chamber just before I joined the group were managed by Andrew Perrella and Phil Mather who assisted Aycan Yurtsever and Ozhan Ozatay in fabricating the electron beam evaporator for Prep 2. Phil Mather and Andrew Perrella designed and assembled Prep 2 and installed the New BEEM system. Phil Mather installed two 2" sputtering guns, along with a throttle valve and a capacitance manometer so that Prep 2 has sputtering capability. He also installed an atomic Nitrogen source, or Nitrogen cracker, which was used in the growth of some of the AlN films discussed in Chapter 6. With help from Praveen Gowtham, I moved two additional 2" sputtering guns from the old "trashcan" system to the Prep 2 system so that now Prep 2 has 4 sputtering guns and 3 electron beam evaporators. Mark Tseng, Yun Li, and I also moved the atomic Nitrogen source to Prep 1 so that it can be used to nitridize film surfaces grown in Prep 1 without transferring the samples through the load lock and risking oxidation. Previously Phil Mather fabricated and installed a heater into Prep 1 so that samples can be annealed in-situ and transferred to either BEEM system, or

to the XPS system without additional oxidation. The preparation chambers in D7 now have the capability to sputter multilayer film stacks for study in either BEEM system or the XPS with the vacuum transfer operation. Over the years I have used the prep chambers in D7 to make a variety of sample structures. My first project was working with Andrew Perrella to study the scattering BEEM signal from Au/Si Schottky diodes. I also worked with Eileen Tan and Phil Mather in my early days making various structures incorporating AlO_x layers, primarily for study in the XPS system. Andrew Perrella, Phil Mather, Eileen Tan, and I worked together to realize Andrew Perrella's original concept for a vacuum transfer from the BEEM system load lock to the XPS system. Ultimately I did these transfers alone for the majority of my XPS studies.

The AJA sputtering system was originally set up by Frank Albert, Jordan Katine, and Nathan Emley, and during my time in the Buhrman Group it was managed by Nathan Emley, Greg Fuchs, Ilya Kravorotov, and Pat Braganca. The first project I completed during my first summer in the group was to assist Nathan Emley in putting a seventh gun in the AJA system. The system originally had 6 sputtering guns, but the successful growth of the film stack for the initial three-terminal spin-transfer device concept required seven guns. Nathan Emley had the original concept for the addition of the seventh gun and asked me to figure out how to put it in the chamber. I used AutoCAD to make detailed drawings of the chamber as it existed at that time and then designed the shutter mechanism around the six other guns. Rodney Bowman from the LASSP machine shop made the parts for me and drilled holes in a 6" flange to accommodate the sputtering gun that Nathan Emley purchased from Kurt Lesker, Inc. Jeff Koski welded the gun into the flange once the gun height was set and then we installed the gun giving the AJA system the capability to sputter 7 different materials. I also made

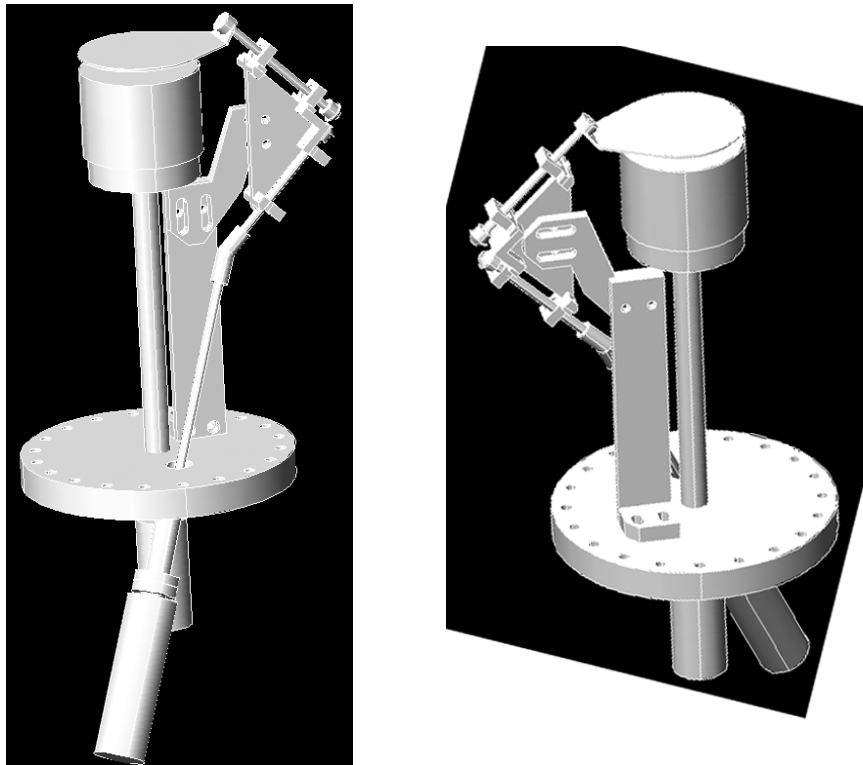


Figure 2.16: AutoCAD renderings of the seventh gun installation for the AJA system.

a chimney for the seventh gun so that the plasma formed over the gun could be better controlled to reduce cross-contamination.

Several years later and after exploring the CoFeB / MgO system in detail with XPS and STS, the next obvious step in the MTJ research was to make working MgO MTJs for transport measurements. I figured this would allow me to better correlate the materials work that Judy Cha and I had done and that it would also expand the types of systems that could be made in-house by the Buhrman and Ralph Groups. To achieve these goals, I have exerted significant effort to develop a process which yields very good MTJ stacks specifically designed for spin transfer junction experiments for the future. In the paragraphs that follow, I describe in full detail and fully disclose all of the important steps that I found necessary to create such structures. There are several ways to form MgO barriers and there will most certainly be improvements and modifications that push the MTJ research effort in new directions. What follows is not presented as a panacea, nor is it presented as any great revolution, merely the result of hard work and my hope is that it provides the group with more flexibility in growing future structures.

2.2.1 Growth Process for MgBO MTJ Thin Film Stacks

Seed Layer and Bottom Electrode Deposition

Two major challenges one faces in forming high quality thin film MTJs are the film smoothness and the abruptness of the film interfaces, particularly the interfaces between the electrodes and the tunnel barrier. The first layers that merit investigation in the growth of a thin film device are the bottom seed layers, or smoothing layers, grown on thermally oxidized Si wafers. These seed layers serve several pur-

poses. First, the seed layers act to promote deposition of smooth electrode layers. Second, these layers are used to engineer the sheet resistance (R_S) of the bottom layers. This is particularly important for current-in-plane tunneling (CIPT) [45, 46] samples where the bottom electrode R_S must be carefully controlled. To search for the optimal seed layer structure, I investigated film structures using AFM measurements of film surface roughness, XRD measurements of film crystallinity, and van der Pauw measurements of R_S . The majority of the XRD studies were performed by Pinshane Huang, while I carried out the AFM and R_S measurements.

I used the AJA sputtering system specifically for making the Mg-B-O-based MTJ structures (discussed in detail in Chapter 4) for CIPT measurements. While the procedures described here were developed for CIPT samples, they are also applicable to the growth of layers for patterning nanopillars or other electronic devices. In CIPT measurements of thin film stacks, the R_S values of the top (R_T) and bottom (R_B) electrodes are related to the tunnel barrier RA product and the minimum probe spacing in the CIPT measurement (λ) through the formula below, calculated by Worledge and Trouilloud. [45]

$$\lambda = \sqrt{\frac{RA}{R_T + R_B}} \quad (2.6)$$

To promote current flow through the film stack, R_T should be at least 0.1 times R_B , however, a reasonable rule of thumb is to grow a film stack such that R_T is twice R_B . [45] Moderately thick rf-sputtered MgO tunnel barriers, on the order of ~ 1.5 nm thick, typically have an RA product on the order of ($\sim 10^2$ - $10^3 \Omega(\mu\text{m})^2$). Using a standard CIPT probe configuration which has a minimum probe spacing of $\lambda \sim 1.5 \mu\text{m}$, R_B should be $\sim 15 \Omega/\square$ and R_T should be $\sim 30 \Omega/\square$ to optimize the CIPT measurement. Thinner MgO tunnel barriers on the order of ~ 1.1 nm

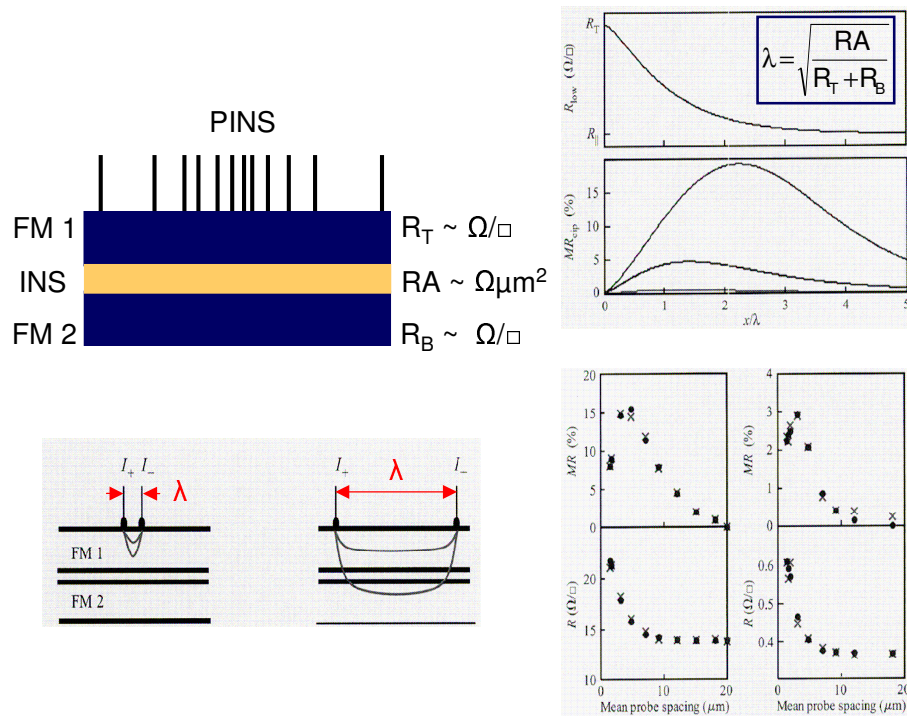


Figure 2.17: Schematic of CIPT measurement (from ref[46] and [47]).

thick, typically have an RA product on the order of ($\sim 10 \Omega(\mu\text{m})^2$). For barriers of this thickness using a standard CIPT probe R_B should be $\sim 1.5 \Omega/\square$ and R_T should be $\sim 3.0 \Omega/\square$, which can be quite difficult to achieve.

The ultimate goal of the experiments described in this section is to form MTJs with properties suitable for STT-MRAM architectures. A typical 1-Transistor 1-MTJ MRAM circuit requires impedance matching of the MTJ to the transistor which usually has a resistance of $\sim 0.5 - 1 \text{ k}\Omega$. Inducing spin transfer torque requires extremely small devices with lateral dimensions on the order of $\sim 100 \text{ nm}$ on a side. For the purposes of estimating the range of tunnel barrier RA products necessary for an STT-MRAM MTJ, assume an elliptical device area with a major axis (a) of length $\sim 150 - 300 \text{ nm}$ and a minor axis (b) of length $\sim 50 - 100 \text{ nm}$. So, the device area range is roughly $\sim 0.06 - 0.02 \mu\text{m}^2$. Multiplying the MTJ device area by the transistor resistance range gives an estimate of the range of required RA products for impedance matching the MTJ for STT-MRAM, namely $RA \sim 3 - 24 \Omega(\mu\text{m})^2$. Sputtered MgO tunnel barriers that exhibit such low RA products are usually on the order of $\sim 1.0\text{-}1.2 \text{ nm}$ thick, making them rather difficult to grow. With such a thin tunnel barrier, the interfacial roughness of the electrodes can lead to pinholes or shorts in the barrier which will diminish the TMR and thus the sensitivity of the MTJ. To measure such an MTJ structure with CIPT using the standard $1.5 \mu\text{m}$ probes, the structure must be engineered such that R_B is $\sim 0.15 \Omega/\square$ and R_T is $\sim 0.3 \Omega/\square$, all the while maintaining a smooth bottom electrode surface.

To facilitate the formation of low R_S bottom electrodes, the use of Ta / CuN multi-layers has proven quite successful on thermally oxidized Si wafers. [5, 21] To promote film smoothness, the Ta layers are best grown using conventional dc

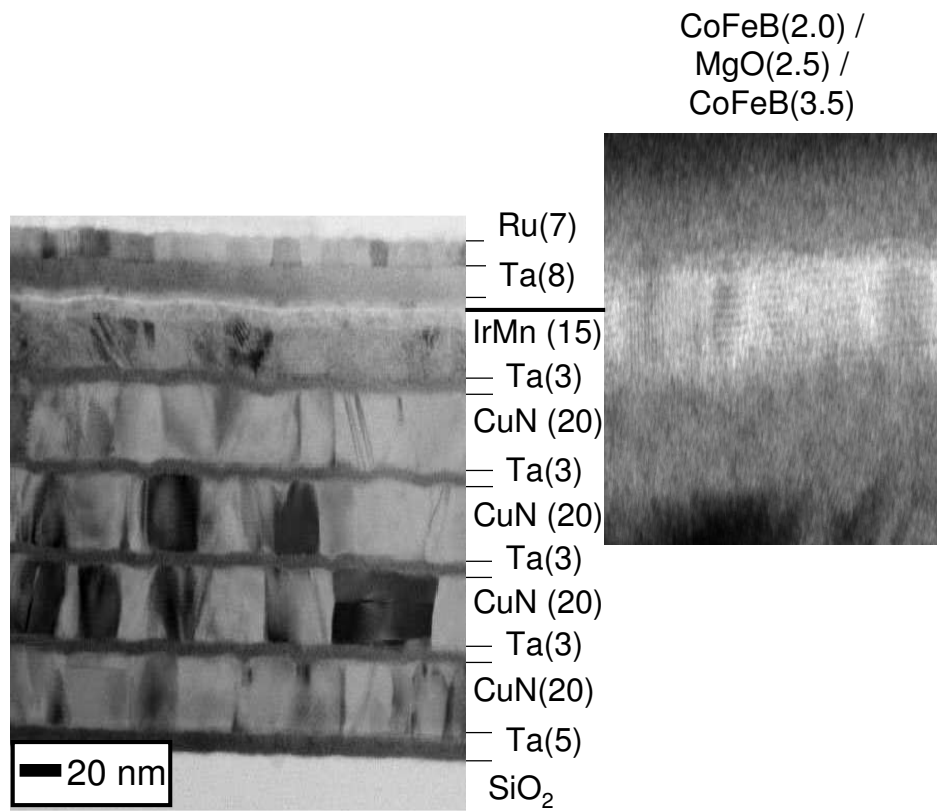


Figure 2.18: TEM images of typical MgO MTJ CIPT structure grown in the AJA system (data courtesy of J. Cha).

sputtering at a high power of 350 W in 2 mTorr of ultra high purity (UHP) Ar at a gas flow rate of 8 standard cubic centimeters per minute (sccm). This tends to form Ta films that are amorphous and reasonably smooth as shown by the TEM image in Fig. 2.18. The CuN films are best grown using reactive dc sputtering. This process has been optimized for CIPT stacks by reactively sputtering in a mixture of UHP Ar and UHP N₂ at a relatively low power of 100 W. This is accomplished by first lighting the Cu sputtering gun at 2 mTorr and 100 W in 8 sccm of Ar and then increasing the Ar flow rate to 32 sccm. Once the plasma has stabilized, which usually takes only a second or two, the N₂ is introduced into the chamber at a flow rate of 1 sccm. CuN films grown by this method have resistivity properties similar to Cu films. This process is adapted from and identical to the process used to form TaN layers with reactive DC sputtering which uses the same gas mixture and sputtering power. As in the case of the CuN films, smooth TaN films can be grown by first lighting the Ta sputtering gun at 2 mTorr and 100 W in 8 sccm of Ar, then increasing the Ar flow rate to 32 sccm, and finally introducing N₂ into the chamber at a flow rate of 1 sccm. While further optimization may certainly prove beneficial, these growth parameters form CuN and TaN films that have roughly 3% N content and are rather smooth.

In attempts to grow smooth, low sheet resistance, anti-ferromagnetically pinned bottom electrodes, I have studied several multi-layer stacks. These stacks have been examined with AFM to investigate the surface smoothness, and with a four-point line probe apparatus fabricated by Ozhan Ozatay which uses the van der Pauw method to determine the sheet resistance of the film multi-layer. The four pins of the van der Pauw probe are equally spaced and a variable current (I) is passed between the outer two pins while the voltage (V) between the inner two pins is measured. Using Ohm's law, the resistance (R) of the film multi-layer

is determined by dividing the voltage by the input current $R = V/I$. The sheet resistance is calculated according to the van der Pauw method by multiplying this measured resistance by a geometric factor.

$$R_S = \frac{\pi}{\ln 2} R = \frac{\pi}{\ln 2} \frac{V}{I} \quad (2.7)$$

One bottom electrode multi-layer stack configuration that has been studied is 5 Ta / 20 CuN / 3 Ta / 15 Ir₂₀Mn₈₀ / 4 Co₆₀Fe₂₀B₂₀ (numbers are film thicknesses in nm). This stack has an R_S of $\sim 1 \Omega/\square$ and has a mean surface roughness of ~ 0.2 nm and an RMS surface roughness of ~ 0.3 nm. Another stack that works equally well, perhaps even better, is 5 Ta / 20 CuN / 5 Ta / 15 Ir₂₀Mn₈₀ / 4 Fe₆₀Co₂₀B₂₀ (numbers are film thicknesses in nm). This stack has an R_S of $\sim 0.9 \Omega/\square$ and has a mean surface roughness of ~ 0.3 nm and an RMS surface roughness of ~ 0.35 nm.

Other layers can be used to form smooth bottom electrodes. Multi-layers of Ta and Ru, specifically 5 Ta / 20 Ru / 3 Ta / 20 Ru / 3 Ta / 20 Ru / 3 Ta / 25 IrMn / 4 CFB has proven to be quite smooth with a mean roughness of $\sim .17$ nm and an RMS roughness of ~ 0.22 nm. Another alternative is to use layers of Ta and TaN. Here, a layer of TaN, which is very smooth, is grown on a seed layer of Ta upon the thermally oxidized Si surface. While both of these layer structures promote the growth of smooth bottom electrode layers, they are each too resistive for CIPT and have thus not been pursued further than as demonstrations of smoothing layers. However, these layers could be quite useful as seed layers for device wafers that do not require low bottom electrode sheet resistances. Although this may be the case, capacitance issues may dominate in such structures if the bottom electrode sheet

resistance is too high. Therefore, it is highly likely that the Ta / CuN multi-layer structure will prove the most useful for future device structure growth.

Another approach to forming low R_S bottom electrodes is to use a thermally oxidized Si wafer that has been coated with a thick layer of Cu and then its surface made flat and smooth with chemical mechanical polishing (CMP). This idea was suggested by Daniel Worledge since the team at IBM Yorktown Heights found it to be a successful way to get low R_S values. The samples I have studied were made by Niloy Mukherjee at Intel and are thanks to a discussion between Bob Buhrman and Brian Doyle of Intel. Niloy grew ~ 100 nm thick Cu films on twelve inch diameter thermally oxidized Si wafers and then he CMP processed the wafers such that they had a surface roughness of less than 0.2 nm as measured by him with AFM. Using these substrates, I have found that almost any combination of film layers results in a film stack which has an extremely small R_S value of $\sim 0.05 \Omega/\square$, which is sufficiently low for any low RA barrier CIPT measurement. However, the surface copper oxide is difficult to remove and thus poor film adhesion issues arise making film surfaces rough and nonuniform. In addition, the Cu may diffuse during annealing, therefore for the purposes of these experiments I have used the Ta/CuN multilayer stack for the bottom electrode seed layer.

The MgO (MgBO) Tunnel Barrier

The most crucial step in the growth of MgO based MTJs is obviously the deposition of the MgO barrier itself. Different research groups have developed diverse approaches to this deposition. In my opinion, the most successful technique is that of Daniele Mauri, who developed a three-step process where first a layer of Mg is deposited by dc sputtering, then a layer of MgO is deposited with ion beam depo-

sition or reactive dc sputtering of Mg in an Ar/O₂ atmosphere, then the Mg/MgO bilayer is oxidized. The details of this process, at least to the degree that IBM (now the intellectual property of Hitachi Global Storage) was willing to disclose them, can be found in the patent of the film deposition process. [22] This MgO deposition process is what was used by Parkin and co-workers in ref [17]. Renu Dave at Everspin also worked out a successful deposition process involving Mg/MgO bilayer deposition. [47] With this process, Mg/MgO bilayers can be oxidized by a number of techniques, or films can be grown directly on the bottom electrode with rf sputtering. Researchers in Japan, most notably the team of Shinji Yuasa, have used electron beam deposition of MgO in conjunction with molecular beam epitaxy (MBE) deposition to form their MTJs. The research team at Canon Anelva in Japan has also worked out very successful deposition techniques, ultimately advocating the direct deposition of MgO by rf sputtering on the bottom electrode. However, before depositing the MgO, the Anelva team first deposits Ta as a getter. Their publications do not make clear exactly how they do this, but based on conversations that I've had with Anelva team members, my opinion is that they light the Ta gun, but leave its shutter closed. Then Ta is deposited on the shutter interior and the gettering action of the Ta acts like a sublimation pump and absorbs some of the oxygen which is evolved during the MgO deposition. Multiple groups throughout the world have adopted this approach and confirm its utility. The net result is that the deposition technique for the MgO barrier depends on the desired application of the MTJ.

The first topic is the MgO target itself. Cost is an important consideration for an academic group, so I chose to use sintered MgO targets. In sputtering it is important to keep the target reasonably cool during deposition. Water cooling lines run through the AJA guns and a copper mesh sheet is placed between the target

and the copper cathode block for each gun. In an effort to keep the MgO target cool, I have used a 0.125" thick MgO target with a 0.125" thick copper backing plate. The two materials are bonded together with indium paste and help keep the target cool. The total target thickness is 0.25" which fills up the entire AJA gun gap. Such targets can be easily purchased from Williams Advanced Materials. At the present time, the targets cost around \$450 and require about 4 weeks of lead time for delivery. To prevent contamination from the stainless steel parts of the gun, I made a new clamping ring, identical to the stainless steel factory AJA part, out of Al. All of the MgO films discussed in this dissertation, except the e-beam films, were made with such a clamping ring in place. I made two copies, one for the AJA and another for the sputtering gun in the prep 2 system in D7, both are stamped "AL" so that they will not be confused for stainless.

The target to sample distance in the AJA system is about 7 inches, and the MgO deposition (at least the way I've done it for the CIPT samples) is performed at high sputtering powers to make MgBO. The majority of the films discussed herein were grown at an rf sputtering power of 300 W (Power density ~ 14.9 W/cm²) at 2 mTorr pressure of UHP Ar. Once the bottom electrode layer deposition is complete, turn off the bottom electrode sputtering gun, and raise the chamber pressure to ~ 10 mTorr. Once this pressure is reached, light the MgO gun, typically gun #2 in the AJA system, at an rf power of 20 W. This will begin the electrode oxidation process, but if you move fast, the oxidation will be minimized. As I will discuss later, the electrode oxidation and subsequent boron oxide diffusion into the MgO barrier after annealing is actually beneficial to forming good MTJs. It turns out that the CoFeB / MgO / CoFeB MTJ structure is quite forgiving. Once the gun is lit in an rf plasma, reduce the chamber pressure to 5 mTorr, then to 4 mTorr, then 3, then 2 mTorr. Next, raise the rf power to 300 W with a 3

second ramp up time. At the moment that the gun power reaches ~ 300 W and after you have confirmed that the reflected power is 0 W, open the sputtering gun shutter and begin the film deposition. Using this procedure, the deposition rate for MgO is roughly $\sim 0.01 \pm 0.001$ nm per second. I have experimented with using both Mg and Ta getters during the MTJ deposition. Both appear to be helpful in controlling the plasma oxidation of the early stages of the MgO sputtering process. In using the gettering procedure I have typically used dc sputtering of either Mg or Ta at a power of ~ 50 W. As described above, the shutter for the getter gun is not opened during the MTJ deposition, so the gun merely acts to help control the electrode oxidation. The MgO gun should be turned off as soon as possible after the necessary time is reached to deposit the desired barrier thickness. The typical approach I have used is to light the getter gun just before lighting the bottom electrode gun. Then, I deposit the bottom electrode and leave the getter gun on while lighting, adjusting, and depositing the MgO barrier. I also leave the getter gun on while depositing the top electrode. In my film stack I always use Ta as the capping layer above the top electrode, so when using the Ta gettering procedure it is necessary only to ramp the Ta gun from 50 to 350 W before depositing the capping layer. Although this procedure works great, the next step is to experiment with things like lighting the gun at 2 mTorr and using low rf power for MgO growth to see how these conditions effect the barrier formation.

Alloy Electrode Layers

The electrode layers are best deposited at low power. This is a little surprising since typically higher power means faster deposition rates which leads to smoother films. However, I've found that lower powers for these glassy magnets actually form smoother films than higher powers. Lower powers also have the benefit of

causing less stress to the targets because they do not get nearly as hot at low power. This means the targets are less likely to crack and force a vent. The alloy targets are pretty tricky to make, but Sophisticated Alloys in PA is a fantastic vendor. They have made most of the targets I've used and typically can deliver the desired composition within a few weeks from the time the order is placed.

Capping Layers

The final step to making a CIPT sample stack is to cap the MTJ layers with 8 nm Ta and then 7 nm Ru. With the Ta gettering process, the Ta gun is already on when depositing the top electrode, so all one needs to do is to turn off the top electrode gun and then raise the Ta gun power to 350 W and deposit the Ta cap. For CIPT a Ru top layer is necessary since RuO_x is conducting and therefore the contact resistance between the CIPT probes and the sample top electrode will be minimized.

2.3 Summary

This chapter introduced some of the important work in MTJ technology and also described the sputtering process for the MgBO MTJs that I developed in the AJA sputtering system. The film growth process is reliable, but has many steps. However, I have repeated results several times and can confirm that if one follows these steps with care, MTJs with similar TMR and RA values can be formed.

REFERENCES

- [1] M. Julliere, Tunneling Between Ferromagnetic-Films, *Phys. Lett. A* **54**, 225 (1975).
- [2] S. Maekawa, and U. Gafvert, Electron-Tunneling Between Ferromagnetic-Films, *IEEE Trans. Magn.* **18**, 707 (1982).
- [3] G. A. Prinz, Magnetoelectronics, *Science* **282**, 1660 (1998).
- [4] I. Zutic, J. Fabian, and S. Das Sarma, Spintronics: Fundamentals and applications, *Rev. Mod. Phys.* **76**, 323 (2004).
- [5] W. J. Gallagher and S. S. P. Parkin, Development of the magnetic tunnel junction MRAM at IBM: From first junctions to a 16-Mb MRAM demonstrator chip, *IBM J. Res. Dev.* **50**, 5 (2006).
- [6] J. Z. Sun and D. C. Ralph, Magnetoresistance and spin-transfer torque in magnetic tunnel junctions, *J. Magn. Magn. Mater.* **320**, 1227 (2008).
- [7] S. Yuasa and D. D. Djayaprawira, Giant tunnel magnetoresistance in magnetic tunnel junctions with a crystalline MgO(001) barrier, *J. Phys. D* **40**, R337 (2007).
- [8] P. M. Tedrow and R. Meservey, Spin-Dependent Tunneling into Ferromagnetic Nickel, *Phys. Rev. Lett.* **26**, 192 (1971).
- [9] P. M. Tedrow, and R. Meservey, Spin Polarization of Electrons Tunneling from Films of Fe, Co, Ni, and Gd, *Phys. Rev. B* **7**, 318 (1973).
- [10] P. Grunberg, R. Schreiber, Y. Pang, M. B. Brodsky, and H. Sowers, Layered Magnetic-Structures - Evidence for Antiferromagnetic Coupling of Fe Layers Across Cr Interlayers, *Phys. Rev. Lett.* **57**, 2442 (1986).
- [11] G. Binasch, P. Grunberg, F. Saurenbach, and W. Zinn, Enhanced Magnetoresistance in Layered Magnetic-Structures with Antiferromagnetic Interlayer Exchange, *Phys. Rev. B* **39**, 4828 (1989).
- [12] M. N. Baibich, J. M. Broto, A. Fert, F. N. Vandau, F. Petroff, P. Etienne, G. Creuzet, A. Friederich, and J. Chazelas, Giant Magnetoresistance of (001)Fe/(001)Cr Magnetic Superlattices, *Phys. Rev. Lett.* **61**, 2472 (1988).

- [13] T. Valet and A. Fert, Theory of the Perpendicular Magnetoresistance in Magnetic Multilayers, *Phys. Rev. B* **48**, 7099 (1993).
- [14] J. S. Moodera, L. R. Kinder, T. M. Wong, and R. Meservey, Large Magnetoresistance at Room-Temperature in Ferromagnetic Thin-Film Tunnel-Junctions, *Phys. Rev. Lett.* **74**, 3273 (1995).
- [15] T. Miyazaki and N. Tezuka, Giant Magnetic Tunneling Effect in Fe / Al₂O₃ / Fe Junction, *J. Magn. Magn. Mater.* **139**, L231 (1995).
- [16] D. X. Wang, C. Nordman, J. M. Daughton, Z. H. Qian, and J. Fink, 70% TMR at room temperature for SDT sandwich junctions with CoFeB as free and reference layers, *IEEE Trans. Magn.* **40**, 2269 (2004).
- [17] S. S. P. Parkin, C. Kaiser, A. Panchula, P. M. Rice, B. Hughes, M. Samant, and S.-H. Yang, Giant tunnelling magnetoresistance at room temperature with MgO (100) tunnel barriers, *Nature Materials* **3**, 862–867 (2004).
- [18] S. Yuasa, T. Nagahama, A. Fukushima, Y. Suzuki, K. Ando, Giant room-temperature magnetoresistance in single-crystal Fe/MgO/Fe magnetic tunnel junctions, *Nature Materials* **3**, 868–871 (2004).
- [19] W. H. Butler, X. -G. Zhang, T. C. Schulthess, and J. M. MacLaren, Spin-dependent tunneling conductance of Fe—MgO—Fe sandwiches., *Phys. Rev. B* **63**, 054416 (2001).
- [20] J. Mathon, and A. Umerski, Theory of tunneling magnetoresistance of an epitaxial Fe/MgO/Fe(001) junction, *Phys. Rev. B* **63**, 220403(R) (2001).
- [21] S. Yuasa, A. Fukushima, T. Nagahama, K. Ando, and Y. Suzuki, High Tunnel Magnetoresistance at Room Temperature in Fully Epitaxial Fe/MgO/Fe Tunnel Junctions due to Coherent Spin-Polarized Tunneling, *Jpn. J. Appl. Phys.* **43**, L588 (2004).
- [22] T. Linn and D. Mauri, Method of forming a barrier layer of a tunneling magnetoresistive sensor, United States Patent 6841395, International Business Machines Corporation, Armonk, NY, US (2005).
- [23] D. D. Djayaprawira, K. Tsunekawa, M. Nagai, H. Maehara, S. Yamagata, N. Watanabe, S. Yuasa, Y. Suzuki, and K. Ando, 230% room-temperature magnetoresistance in CoFeB/MgO/CoFeB magnetic tunnel junctions, *Appl. Phys. Lett.* **86**, 092502 (2005).

- [24] S. Ikeda, J. Hayakawa, Y. M. Lee, R. Sasaki, T. Meguro, F. Matsukura, and H. Ohno, Dependence of tunnel magnetoresistance in MgO based magnetic tunnel junctions on Ar pressure during MgO sputtering, *Japn. J. Appl. Phys. Part 2* **44**, L1442 (2005).
- [25] Y. M. Lee, J. Hayakawa, S. Ikeda, F. Matsukura, and H. Ohno, Giant tunnel magnetoresistance and high annealing stability in CoFeB/MgO/CoFeB magnetic tunnel junctions with synthetic pinned layer., *Appl. Phys. Lett.* **90**, 212507 (2007).
- [26] S. Ikeda, J. Hayakawa, Y. Ashizawa, Y. M. Lee, K. Miura, H. Hasegawa, M. Tsunoda, F. Matsukura, and H. Ohno, Tunnel magnetoresistance of 604% at 300 K by suppression of Ta diffusion in CoFeB/MgO/CoFeB pseudo-spin-valves annealed at high temperature, *Appl. Phys. Lett.* **93**, 082508 (2008).
- [27] K. Tsunekawa, D. D. Djayaprawira, M. Nagai, H. Maehara, S. Yamagata, N. Watanabe, S. Yuasa, Y. Suzuki, and K. Ando, Giant tunneling magnetoresistance effect in low-resistance CoFeB/MgO(001)/CoFeB magnetic tunnel junctions for read-head applications, *Appl. Phys. Lett.* **87**, 072503 (2005).
- [28] Y. Nagamine, H. Maehara, K. Tsunekawa, D. Djayaprawira, N. Watanabe, S. Yuasa, and K. Ando, Ultralow resistance-area product of $0.4 \Omega(\mu\text{m})^2$ and high magnetoresistance above 50% in CoFeB/MgO/CoFeB magnetic tunnel junctions, *Appl. Phys. Lett.* **89**, 162507 (2006).
- [29] S. Isogami, M. Tsunoda, K. Komagaki, M. Sato, K. Sunaga, Y. Uehara, and M. Takahashi, New fabrication process for ultra-thin crystalline mgo barrier and resultant giant tmr with low ra in cofeb/mgo/cofeb mtjs, Presentation AD-08, MMM conference (2008).
- [30] U. Geiersbach, A. Bergmann, and K. Westerholt, Structural, magnetic and magnetotransport properties of thin films of the Heusler alloys Cu_2MnAl , Co_2MnSi , Co_2MnGe and Co_2MnSn , *J. Magn. Magn. Mater.* **240**, 546 (2002).
- [31] T. Marukame, T. Kasahara, K. Matsuda, T. Uemura, and M. Yamamoto, Fabrication of fully epitaxial magnetic tunnel junctions using full-Heusler alloy $\text{Co}_2\text{Cr}_{0.6}\text{Fe}_{0.4}\text{Al}$ thin film and MgO tunnel barrier, *Japn. J. Appl. Phys. Part 2* **44**, L521 (2005).
- [32] T. Ishikawa, T. Marukame, H. Kijima, K. -I. Matsuda, T. Uemura, M. Arita, and M. Yamamoto, Spin-dependent tunneling characteristics of fully epitaxial magnetic tunneling junctions with a full-Heusler alloy Co_2MnSi thin film and a MgO tunnel barrier, *Appl. Phys. Lett.* **89** (2006).

- [33] X. G. Zhang, W. H. Butler, and A. Bandyopadhyay, Effects of the iron-oxide layer in Fe-FeO-MgO-Fe tunneling junctions., *Phys. Rev. B* **68**, 092402 (2003).
- [34] J. Mathon and A. Umerski , Theory of tunneling magnetoresistance in a disordered Fe/MgO/Fe(001) junction, *Phys. Rev. B* **74**, 140404 (2006).
- [35] H. L. Meyerheim, R. Popescu, N. Jedrecy, M. Vedpathak, M. Sauvage-Simkin, R. Pinchoux, B. Heinrich, and J. Kirschner, Surface x-ray diffraction analysis of the MgO/Fe(001) interface: Evidence for an FeO layer, *Phys. Rev. B* **65**, 144433 (2002).
- [36] C. Tusche, H. L. Meyerheim, N. Jedrecy, G. Renaud, A. Ernst, J. Henk, P. Bruno, and J. Kirschner, Oxygen-induced symmetrization and structural coherency in Fe/MgO/Fe(001) magnetic tunnel junctions, *Phys. Rev. Lett.* **95**, 176101 (2005).
- [37] X. G. Zhang and W. H. Butler, Large magnetoresistance in bcc Co/MgO/Co and FeCo/MgO/FeCo tunnel junctions, *Phys. Rev. B* **70**, 172407 (2004).
- [38] S. Yuasa, A. Fukushima, H. Kubota, Y. Suzuki, and K. Ando, Giant tunneling magnetoresistance up to 410% at room temperature in fully epitaxial Co/MgO/Co magnetic tunnel junctions with bcc Co(001) electrodes, *Appl. Phys. Lett.* **89**, 042505 (2006).
- [39] S. Yuasa, Y. Suzuki, T. Katayama, and K. Ando, Characterization of growth and crystallization processes in CoFeB/MgO/CoFeB magnetic tunnel junction structure by reflective high-energy electron diffraction, *Appl. Phys. Lett.* **87**, 242503 (2005).
- [40] J. A. Katine, F. J. Albert, R. A. Buhrman, E. B. Myers, and D. C. Ralph, Current-driven magnetization reversal and spin-wave excitations in Co/Cu/Co pillars, *Phys. Rev. Lett.* **84**, 3149 (2000).
- [41] E. B. Myers, D. C. Ralph, J. A. Katine, R. N. Louie, and R. A. Buhrman, Current-induced switching of domains in magnetic multilayer devices, *Science* **285**, 867 (1999).
- [42] www.physorg.com/news113591322.html (2008).
- [43] <http://www.everspin.com/technology-toggle-ram.html>,
<http://www.everspin.com/technology-spin-mram.html> (2008).

- [44] J. Z. Sun, Spin-current interaction with a monodomain magnetic body: A model study, *Phys. Rev. B* **62**, 570 (2000).
- [45] D. C. Worledge and P. L. Trouilloud, Magnetoresistance measurement of unpatterned magnetic tunnel junction wafers by current-in-plane tunneling., *Appl. Phys. Lett.* **83**, 84 (2003).
- [46] D. W. Abraham, P. L. Trouilloud, and D. C. Worledge, Rapid-turnaround characterization methods for MRAM development, *IBM J. Research. Dev.* **50**, 55 (2006).
- [47] R. W Dave, G. Steiner, J. M. Slaughter, J. J. Sun, B. Graigo, S. Pietambaram, K. Smith, G. Grynkewich, M. DeHerrera, J. Akerman, and S. Tehrani, MgO-based tunnel junction material for high-speed toggle magnetic random access memory, *IEEE Trans. Magn.* **42**, 1935 (2006).

CHAPTER 3
X-RAY PHOTOELECTRON SPECTROSCOPY STUDIES OF
CoFeB / MgO BILAYERS

3.1 Introduction

The growth of ultra-thin MgO tunnel barrier layers presents interesting challenges with regards to controlling electrode oxidation and forming ideal electrode-barrier interfaces. Several deposition techniques have been successfully employed to grow MgO tunnel barriers in MTJs which achieve high TMR. [1–7] However, it is particularly important in sputtered MTJs that the structures are annealed after growth in order to crystallize the electrodes and thus activate the junctions. [1–7] In this chapter, I present X-ray Photoelectron Spectroscopy (XPS) studies which illuminate the electrode oxidation process and the subsequent chemical changes in the tunnel barriers and near the electrode-barrier interface that occur due to annealing. [8] The most widely used electrode materials in published works on MgO-based MTJs are ferromagnetic CoFeB alloys. These alloys are amorphous as-grown but crystallize during annealing. [9] However, in order for the electrodes to crystallize, the glass-forming B must leave the electrode. This raises the question as to the whereabouts of the B after annealing. The XPS data presented here show that in CoFeB thin films, the B within the electrode is reactive with O. If the electrode B is in close proximity to O, such as O chemisorbed on the electrode surface, or if the electrode B is oxidized during the barrier layer growth, then the B can diffuse out of the electrode towards the surface of the thin film structure.

The XPS data that I present in this chapter show that the deposition of MgO on a CoFeB alloy electrode forms B, Fe, and Co oxides to varying degrees depend-

ing upon the MgO deposition technique. This study suggests that both plasma oxidation and thermal oxidation of a sufficiently thick Mg layer grown on a CoFeB electrode do not appear to substantially oxidize the electrode and that subsequent annealing of these bilayers forms chemically good MgO barriers. However, if the Mg layer is not thick enough, then B within the electrode diffuses out of the electrode and reacts with surface O to form B oxide and the surface material formed is a mixed Mg-B oxide. This study also shows that MgO barriers formed with electron beam (eb) evaporation only slightly oxidize CoFeB electrodes while more substantial electrode oxidation occurs during the growth of radio frequency (rf) sputtered MgO layers. The data presented in this chapter clearly show that rf sputtering of thicker MgO layers and layers grown at higher sputtering pressures form greater amounts of B, Fe, and Co oxides. This suggests that the rf sputtering process acts to plasma oxidize the electrode with a thicker MgO layer or higher chamber pressure during sputtering equating to a larger effective O dose. The most interesting finding of this work is that vacuum annealing reduces the Fe and Co oxides formed in the rf sputtering process, but that the B oxide remains in the MgO barrier creating a mixed MgBO tunnel barrier.

The XPS data presented here taken from rf sputtered samples clearly show that after annealing a chemical shift occurs in the spectra from the Mg, B, and O species, indicating the local chemistry of the MgBO tunnel barrier has changed. The data in this chapter also confirm that insertion of an Mg layer between the CoFeB electrode and the MgO barrier is a successful way to reduce the initial electrode oxidation. Previous research by scientists at the Canon Anelva corporation suggests that Mg/MgO bilayer barriers have better TMR and RA attributes than rf sputtered MgO barriers. [5] However, the results in this chapter show that such Mg/MgO bilayer barriers still allow B oxide incorporation in the MgO barrier dur-

ing annealing if the Mg layer is thinner than 1.4 nm, although the post-annealed B oxide incorporation occurs in these structures to a lesser degree than in the case of fully rf sputtered MgO barriers. Researchers at Freescale Semiconductor (now Everspin) previously demonstrated optimized performance for their MTJs with barrier layers made with a "natural oxidation" process of 1.4-1.6 nm thick Mg layers. [6] These two studies [5, 6] suggest that good MgO barriers can be formed by controlling electrode oxidation. The results of the XPS study described in this chapter in conjunction with the studies presented in chapter 4 provide clear evidence that the formation of a MgBO barrier material has beneficial properties in working MTJs. The primary focus of the XPS data presented in this chapter is to provide deeper insight regarding the chemical changes that take place in a variety of CoFeB / MgO bilayer systems and to begin to unravel some of the materials physics inherent in MgO-based MTJs using B-alloyed ferromagnetic electrodes.

3.2 Sample Preparation

I grew the thin films in this study on thermally oxidized Si(100) substrates in a vacuum system with a base pressure of $\sim 2 \times 10^{-9}$ Torr. The majority of these studies incorporate a 20 nm base electrode, deposited from a $\text{Co}_{60}\text{Fe}_{20}\text{B}_{20}$ (CFB), or $\text{Fe}_{60}\text{Co}_{20}\text{B}_{20}$, (FCB) alloy target, which I made using dc magnetron sputtering in 1 mTorr of ultra-high purity (UHP) Ar. The thermal oxidation experiments use a thinner 6 nm base electrode. Section 4 of this chapter discusses the direct oxidation of the CFB and FCB electrode materials. For these samples, I first sputtered the electrode layer and then transferred the sample into the system load lock chamber where I exposed it to UHP O_2 for various times. Section 5 of the chapter discuss the results of plasma and thermal oxidation of a thin Mg layer grown on CFB.

For the plasma oxidation studies, I sputtered the bilayer sample and then exposed to an O₂ plasma. I formed this by first introducing a 67%Ar 23%O₂ gas mixture into the growth chamber at a pressure of 1 mTorr. [6] Then I struck an rf plasma on an MgO target at a power of 100 W with the gun shutter closed and rotated the sample to face the sputtering gun which exposed the sample surface to the O₂ plasma for a short period of time. I conducted the thermal oxidation experiments in the same manner as described above for the electrode oxidation experiments.

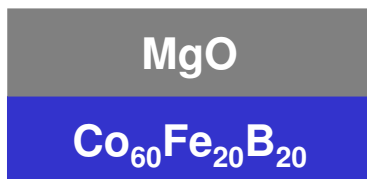
The last sections of this chapter discuss experiments where I deposited eb evaporated (section 6) or rf sputtered (section 7) MgO layers on either CFB or FCB electrodes. I grew the eb evaporated layers using a stoichiometric MgO source and carried out the deposition at a chamber pressure of less than $\sim 1 \times 10^{-8}$ Torr. I made the rf sputtered layers from a sintered MgO target using a sputtering power of 100 W (power density ~ 4.9 W/cm²) in an Ar pressure of either 1 or 10 mTorr. In addition to these studies, I investigated the formation of an Mg/MgO bilayer barrier in section 8. For these samples I first deposited a thin Mg layer (0.5 or 1.0 nm) on a CFB electrode and then rf sputtered an MgO layer on the Mg layer. Figure 3.1 provides a list of all the experiments discussed in this chapter. I made identical pairs of each sample structure and annealed one of each pair in vacuum ($P_{Anneal} \sim 1 \times 10^{-9}$ Torr) at 300, 350, or 375 °C for one hour or for one and a half hours. Once prepared, I vacuum-transferred the samples were with a portable turbopump station ($P_{PumpingStation} \sim 5 \times 10^{-9}$ Torr) to a Surface Science Laboratories SSX-100 x-ray photoelectron spectrometer for investigation.



Thermal Oxidation



Thermal Oxidation



Plasma Oxidation of Mg
Thermal Oxidation of Mg
e-beam Evaporation of MgO
RF Sputtering of MgO
Mg/MgO[rf] Bi-layer



e-beam Evaporation of MgO
RF Sputtering of MgO

Figure 3.1: Description of the thin film structures investigated using XPS that are discussed in this chapter.

3.3 Spectra Peak Fitting

As with any XPS study, it is paramount that a consistent peak fitting rubric is used to analyze each of the data sets in a particular experimental investigation. If such care is not taken, misinterpretation of the data can occur, leading to incorrect conclusions regarding the changes in the chemical environment of the samples studied. For this study, I calibrated the XPS detector to the Au $4f_{7/2}$ line at 84 eV and each of the acquired data sets to the strong intensity metallic Co $2p_{3/2}$ and Fe $2p_{3/2}$ photoemission lines at 778.3 and 707.0 eV respectively. [10] Along with a low resolution survey scan over the energy range of 0-1000 eV, I acquired five high resolution regions from each of the samples in this experiment. The B 1s (~ 180 -210 eV) spectral region, the Co 3p, Fe 3p, and Mg 2p (~ 35 -70 eV) spectral region, the O 1s (~ 525 -545 eV) spectral region, the Fe 2p (~ 700 -735 eV) spectral region, and the Co 2p (~ 770 -810 eV) spectral region, together provide an in-depth picture of the chemical environment of the samples. Comparison of identical samples before and after annealing, and comparison of samples prepared by different methods unveils data trends that provide clues to the chemical nature of the barrier and electrode materials and to the oxidation processes occurring in these structures.

Figure 3.2 shows the peak fitting scheme I used for each of the samples in this study. Using this type of consistent fitting approach, one can easily identify peaks attributable to metal oxides and distinguish changes in the relative intensity of metal and metal oxide peaks. The B 1s spectrum exhibits two peaks, which are typical of most CoFeB / MgO structures. The peak at ~ 188 eV is representative of B in the CoFeB alloy while the peak at ~ 192 eV is due to the oxidized B species (see Fig. 3.3 for reference B oxide spectra). [10–12] The Mg 2p, Fe 3p, and Co 3p

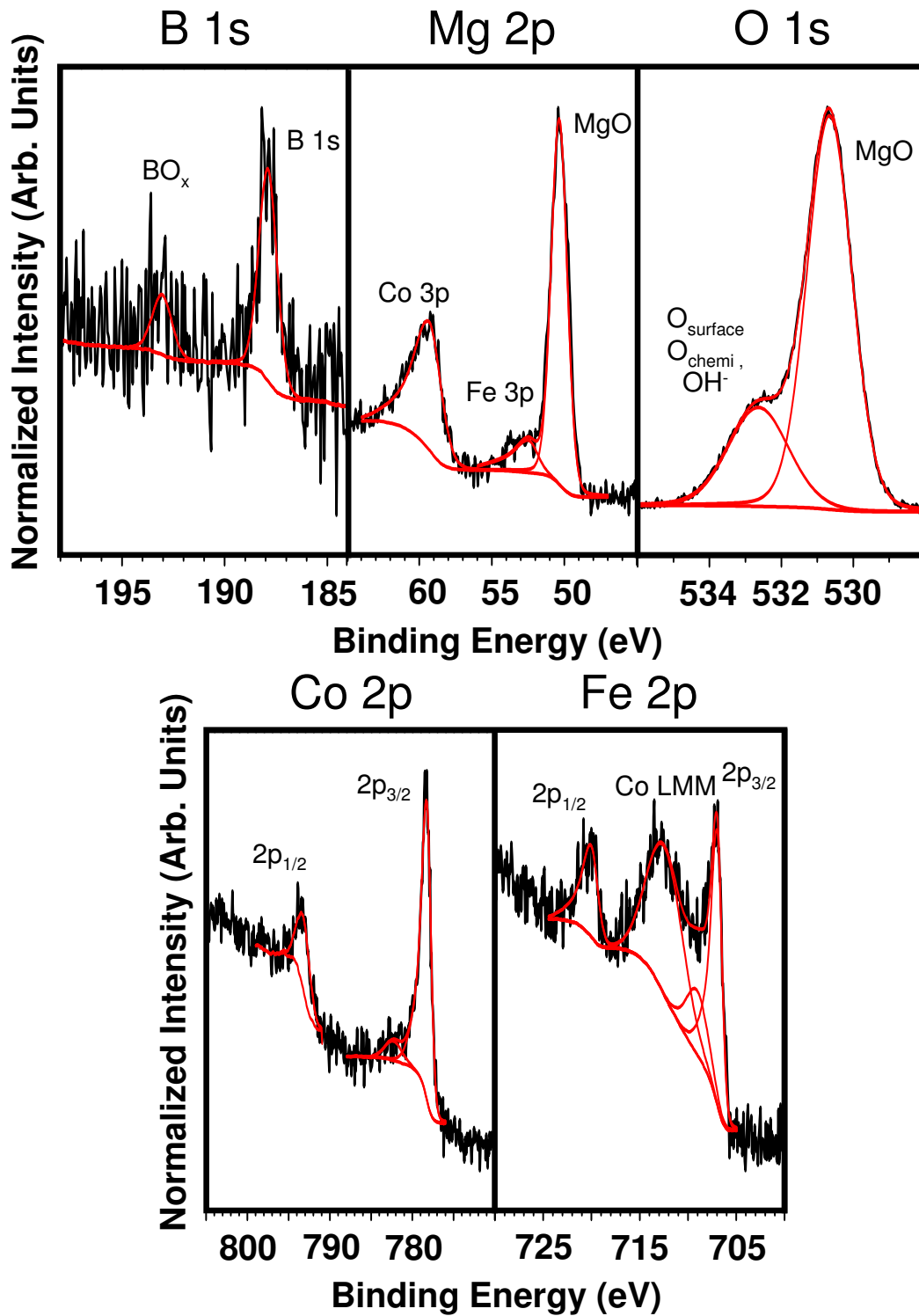


Figure 3.2: XPS peak fitting scheme for the B 1s, (Mg 2p, Co 3p, and Fe 3p), O 1s, Fe 2p, and Co 2p spectral regions for data taken from a 20 nm $\text{Co}_{60}\text{Fe}_{20}\text{B}_{20}$ /2 nm eb evaporated MgO sample.

spectral region for this sample has three peaks, which is typical of an electrode that is not heavily oxidized. The peak at ~ 50.0 eV is attributable to the Mg atoms in the MgO layer (see Fig. 3.4 for reference Mg oxide spectra) [10, 13–15] and the peaks at ~ 52.7 eV and ~ 59.4 eV are respectively attributable to the metallic Fe and Co within the alloy electrode. [10] This spectral region also allows investigation of the presence of Fe (~ 55 - 56 eV) and Co (~ 61 eV) oxides formed in the sample structure [10], which can be confirmed with greater resolution through study of the Fe 2p and Co 2p spectral regions.

The Co 2p and Fe 2p regions are typical of CFB-based sample structures. The Co 2p region shows two peaks attributable to metallic species, one at ~ 778.3 eV and one at ~ 793.0 eV which are due to the Co $2p_{3/2}$ and Co $2p_{1/2}$ orbitals respectively. CoFeB thin film samples that are more heavily oxidized (see Fig. 3.7 and Fig. 3.8) exhibit more peaks and give a clear indication of the presence of Co oxides (see Fig. 3.5 for Co oxide reference spectra). [10, 16] The Fe 2p region shows three peaks. The peaks at ~ 707.0 eV and ~ 720.0 eV are due to the metallic Fe $2p_{3/2}$ and Fe $2p_{1/2}$ orbitals. [10] As with the Co 2p spectral region, CoFeB samples that are more heavily oxidized (see Fig. 3.7 and Fig. 3.8) exhibit a more complicated peak structure making Fe oxide identification a reliable process (see Fig. 3.6 for reference Fe oxide spectra). [10, 17] The broad peak at ~ 713 eV is the Co $L_3M_{45}M_{45}$ Auger transition. [10] This peak has nothing to do with oxidation and clouds investigation of the Fe $2p_{3/2}$ region. A similar Auger peak, the Fe $L_3M_{45}M_{45}$ transition (see Fig. 3.8) [10], is also apparent in samples utilizing FCB alloy electrodes, but it appears in the Co $2p_{3/2}$ region. This observation shows that study of these alloy materials will always rely upon close examination of the higher Binding Energy (BE) region of the Co 2p and Fe 2p spectral regions, and that the higher concentration transition metal atomic species in the alloy will

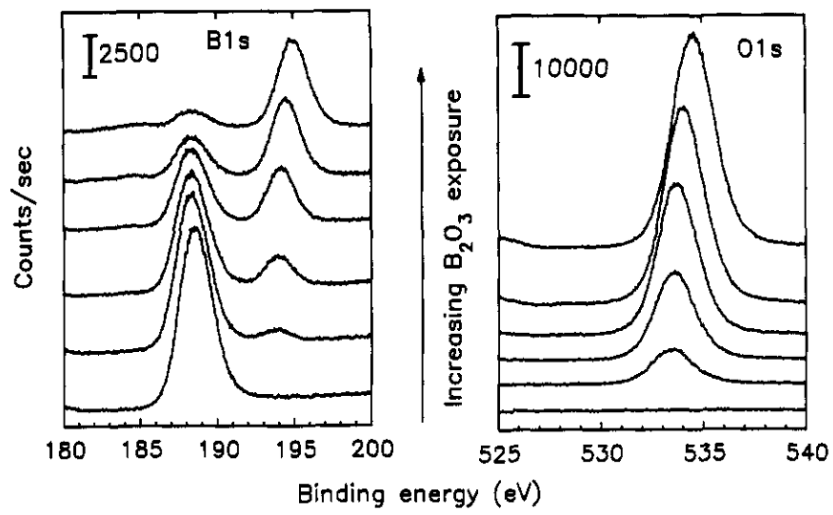


Figure 3.3: B 1s and O 1s spectra from B₂O₃ thin films grown on Ta (from ref. [11]).

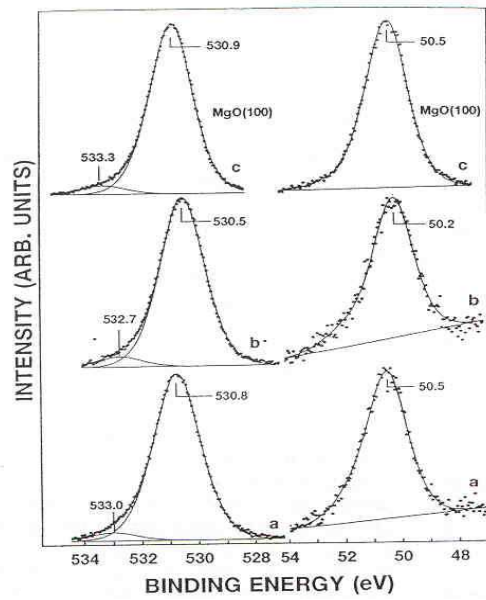


Figure 3.4: Mg 2p and O 1s spectra from thermally oxidized Mg thin films grown on Mo (from ref. [14]).

contribute an Auger peak to the 2p spectrum of the lower concentration transition metal atomic species of the alloy. Despite the complications due to the presence of these Auger peaks, electrode oxidation is clearly distinguishable in the Co 2p_{1/2}, Fe 2p_{1/2}, Co 3p, Fe 3p, and B 1s spectral regions.

The O 1s spectral region is the most difficult to interpret. The sample shown in Fig. 3.2 is representative of a well-formed MgO layer. The peak at ~ 530 eV is indicative of O atoms within the MgO layer and the peak at ~ 533 eV, in this case, is likely due to surface O or hydroxide species that are chemisorbed to the MgO surface. [13, 15, 18] As will be shown in later sections of this chapter, the O 1s region becomes much more complicated when a mixed Mg-B-O surface is formed. B oxide typically yields an O 1s peak in the ~ 532 - 533 eV range (see Fig. 3.3) which overlaps with the surface O species. In contrast, Mg, Fe, and Co oxides all yield O 1s peaks in the lower BE range of ~ 529 - 531 eV (see Figs. 3.4-3.6). [14-17] Despite the complexities of the spectra from these sample structures, trends in chemical shifts and changes in relative peak intensities provide a reasonably consistent approach, along with close examination of the metallic spectral regions, for correct identification of oxide species.

3.4 Oxidation of CoFeB Thin Films

The growth of an oxide on a metal surface allows for the possibility of oxidation of the underlying metal film layer. Due to the complex nature of the photoemission spectra, study of the direct oxidation of the CoFeB alloy electrode surface helps to clarify the oxidation processes that are present in CoFeB / MgO bilayer samples. In this section I present the results from oxidation and annealing studies of CFB

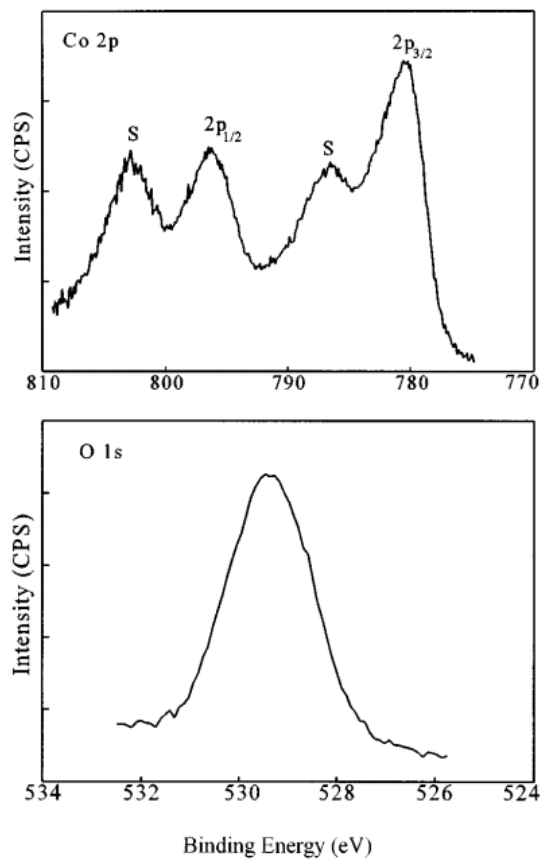


Figure 3.5: Co 2p and O 1s spectra from Co_3O_4 thin films grown on CoO (from ref. [16]).

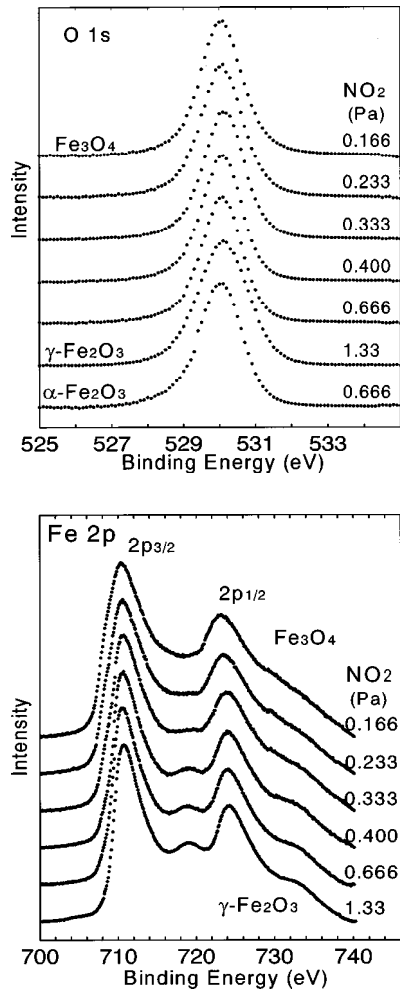


Figure 3.6: Fe 2p and O 1s spectra from various Fe oxide films grown on MgO or Al₂O₃ (from ref. [17]).

and FCB thin films. Fig. 3.7 shows the B 1s, Fe and Co 3p, O 1s, Fe 2p, and Co 2p spectral regions taken from CFB samples that were exposed to light ($\sim 10^{-4}$ Torr-second) or significant (~ 15 Torr-second) oxidation doses. A light oxidation dose forms only a slight amount of Fe and B oxide, but the Co remains un-oxidized. This is a result of the greater electron affinities (E_A) of Fe ($E_{A,Fe} \sim 0.15$ eV) and B ($E_{A,B} \sim 0.28$ eV) relative to Co ($E_{A,Co} \sim 0.66$ eV) [19], which suggest that Fe is the most likely species to oxidize, then B, and then Co. Therefore, moving samples around in vacuum is sufficient exposure for Fe and B oxide formation, but not for Co oxide formation. However, a higher O₂ dose (~ 15 Torr-second) oxidizes all three electrode species such that a mixed surface oxide forms. I base this determination on observation of the additional oxide peaks that appear in the Fe 2p, Co 2p, Fe 3p, and Co 3p spectral regions. The transition metal oxides are most easily identified in the 2p regions due to the larger relative peak intensities and increased complexity of the spectral peak structure. The equal concentration of Fe and B appears to promote the oxidation of both species over Co, although the higher 15 Torr-second dose significantly oxidizes the Co electrode content.

In addition to the CFB oxidation study, I also studied oxidation and post-oxidation annealing of FCB. Fig 3.8 shows the data from these FCB samples, which are similar to the data from CFB samples with a few significant differences. The Fe 3p and Co 3p region shows that the relative intensity of the Fe 3p and Co 3p peaks is the inverse of the relative intensity of the peaks from a CFB sample. This is because of the difference in atomic concentration between the alloys. Also, the Fe LMM Auger transition peak is prominent in the Co 2p spectral region as previously discussed. The data suggest that a light oxidation forms only a slight amount of Fe oxide. I draw this conclusion both from the absence of a significant B oxide peak in the B 1s spectrum and also from the O 1s spectrum, which is

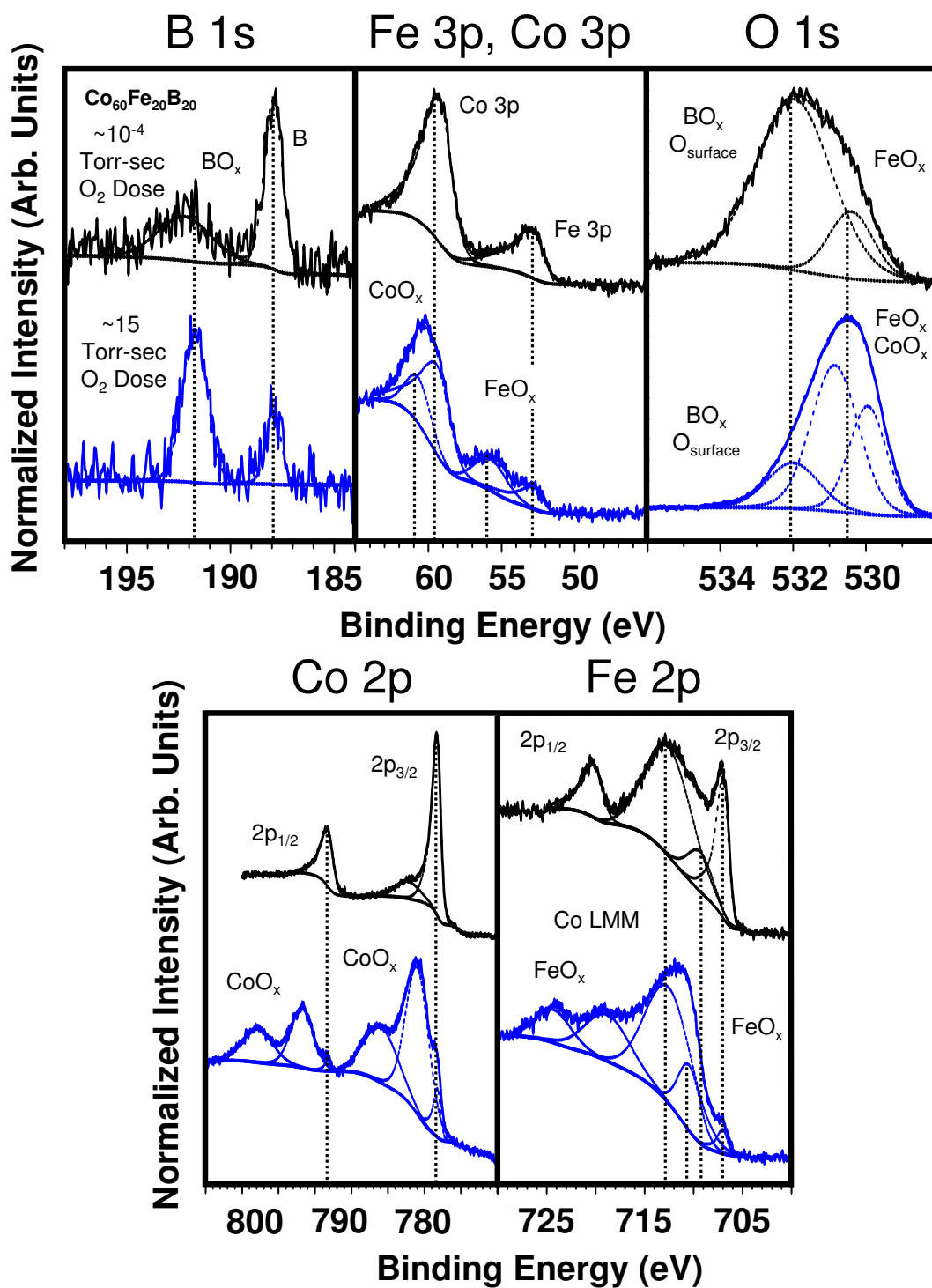


Figure 3.7: XPS data from lightly ($\sim 10^{-4}$ Torr-second O_2 dose) and significantly (~ 15 Torr-second O_2 dose) oxidized 20 nm $\text{Co}_{60}\text{Fe}_{20}\text{B}_{20}$ films.

centered around ~ 530.5 eV and is thus indicative of Fe or Co oxide. [16, 17] After annealing there are striking changes in the B 1s and O 1s spectra. A substantial B oxide peak evolves and the O 1s peak has shifted to a higher BE of nearly ~ 533 eV. There is no presence of either Fe or Co oxide peaks in the various Co and Fe spectral regions. These features together are indicative of a mixture of B oxide and surface O species. [11, 12] These findings suggest that the B in the electrode diffuses out of the electrode during annealing and reacts with the surface O and Fe oxide, reducing the Fe oxide and forming B oxide. A heavier oxidation dose dramatically increases the intensity of the Fe and Co oxide peaks, although the B oxide peak shows surprisingly low intensity. This behavior can be attributed to the greater reactivity of Fe with O in comparison to B and Co. Also, careful inspection of the admittedly noisy B 1s spectrum shows no clear metallic B signature. So, it is likely the heavier oxidation dose oxidizes all three electrode species, as in the CFB case. Annealing this sample has a similar effect to what is shown in the lighter oxidation dose sample. Annealing reduces the Fe and Co oxides while the B oxide peak increases dramatically in relative intensity, demonstrating again both the diffusive and reactive nature of B from within the alloy electrode.

These studies of CFB and FCB alloy thin films suggest that all three electrode species can be oxidized if the oxidation dose is large enough. The studies also show that annealing an oxidized alloy thin film changes the nature of the surface oxide by increasing the B oxide content and reducing the Fe and Co oxides. This is most likely due to the partial crystallization of the alloy material during the annealing process. The alloy cannot fully crystallize if any glass-forming B remains within the electrode. Therefore, during the anneal some B diffuses out of the electrode and reacts with the surface O or reduces the transition metal oxides at the film surface. In sections 7 and 8 of this chapter, and in chapter 4, I show show that

the diffusive and reactive nature of B has significant consequences in MTJs with rf sputtered MgO barriers in conjunction with B-based alloy electrodes.

3.5 Plasma and Thermal Oxidation of CoFeB / Mg Bilayers

In an effort to understand the impact of the diffusion and reaction of B both during growth and during annealing, I investigated thermal and plasma oxidation of an Mg layer. In Fig. 3.9 the relevant spectral regions from 1.4 nm thick Mg films grown on CFB and plasma oxidized for either 10 or 30 seconds are displayed for structures before and after annealing. Previous research shows that a 1.4 nm thick Mg film which is plasma oxidized forms a good barrier material. [6] The data presented in this section show that a 1.4 nm thick Mg film exposed to plasma oxidation is fully oxidized while the underlying CFB electrode remains un-oxidized. After annealing, the electrode still remains un-oxidized and there is no increased B oxide peak intensity. Annealing these films to 375°C does slightly modify the MgO barrier material. After annealing, both the Mg 2p and O 1s MgO peaks exhibit a chemical shift to lower BE and the surface O peak decreases in intensity. This behavior is indicative of surface O being driven into the MgO material and the subsequent formation of a more chemically stable MgO layer. [13–15, 18] These data suggest that a sufficiently thick (1.4 nm) Mg layer is an effective way to protect the underlying electrode from oxidation.

A more extensive study of the thermal oxidation of an Mg layer grown on CFB confirms that the minimum Mg film thickness required to prevent the oxidation of the CFB electrode is 1.4 nm. Fig. 3.10 shows data from two sets of experiments.

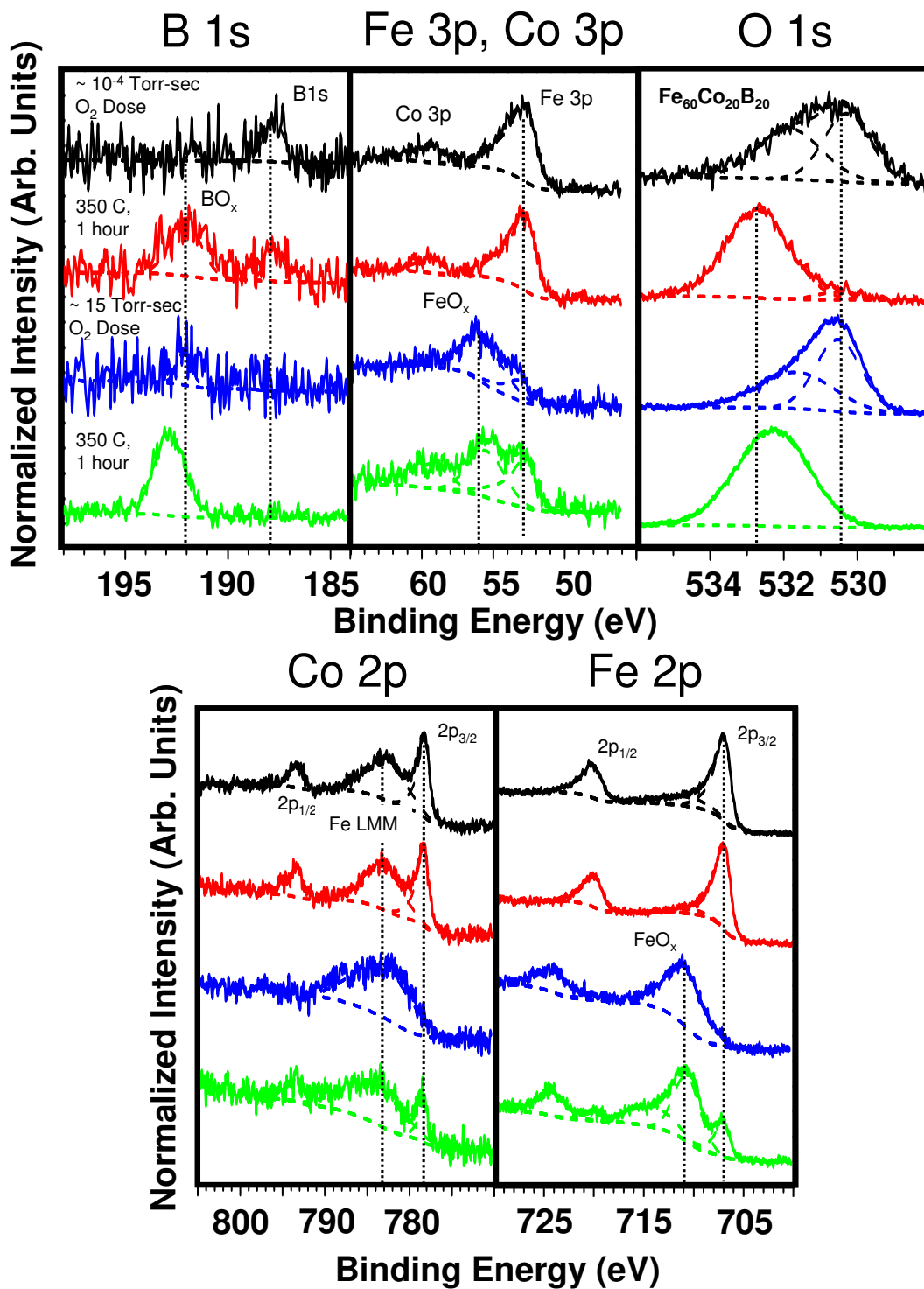


Figure 3.8: XPS data from lightly ($\sim 10^{-4}$ Torr-second O_2 dose) and significantly (~ 15 Torr-second O_2 dose) oxidized 20 nm $\text{Fe}_{60}\text{Co}_{20}\text{B}_{20}$ films before and after annealing.

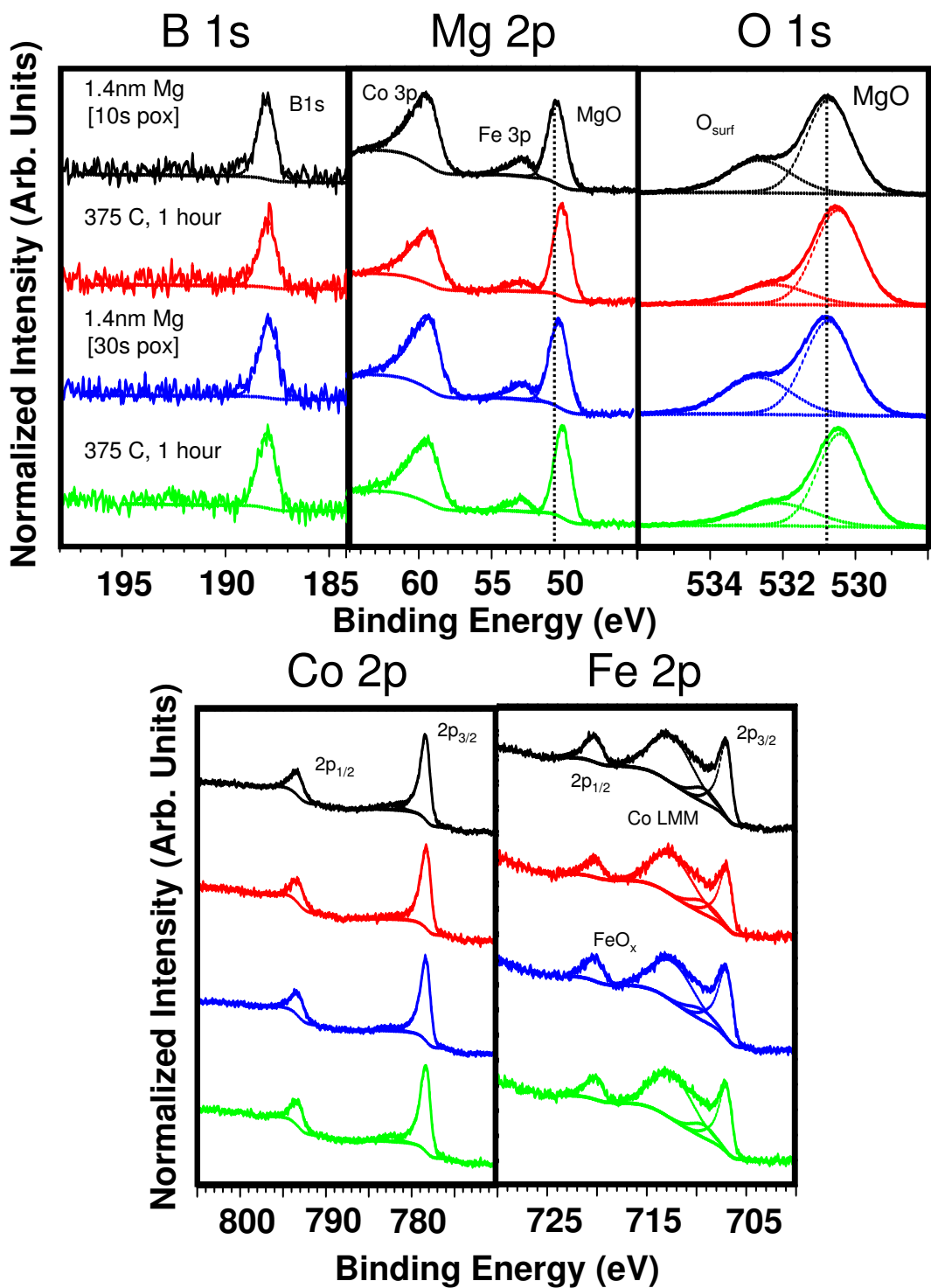


Figure 3.9: XPS data from plasma oxidized 1.4 nm thick Mg thin films deposited on 20 nm thick CFB base electrodes before and after annealing.

In these experiments, I first deposited varying thicknesses of Mg on CFB and then exposed them to different O₂ doses. I also annealed the samples to 300°C for 90 minutes after O₂ exposure to study the diffusion and oxidation of B during the anneal. The data reveal that while 1.0 nm of Mg is sufficient to fully protect the CFB electrode during the initial oxidation, annealing diffuses B out of the electrode for all three oxidation doses that were studied. More importantly, the data shows that the B in the electrode is most likely to oxidize only after annealing in this process. Both 1.0 nm and 1.2 nm (not shown) thermally oxidized Mg layers show an increase in B oxide signal intensity after annealing. This suggests that the annealing process is the key reason for the additional B oxide content in the surface oxide and that diffusion of B during the anneal is the most likely explanation for the B oxide signal intensity increase. The Mg 2p and O 1s MgO peaks show increased signal intensity and a chemical shift to lower BE after annealing while the surface O peak shows a decrease in signal intensity after annealing. As in the plasma oxidized case, this suggests that the surface O is driven into the MgO layer, presumably filling O vacancies in the MgO, forming a more stoichiometric material. An additionally interesting feature of the data is the decrease of the Mg 2p MgO peak intensity after annealing in the un-oxidized case. This is probably due to the diffusion of electrode B during annealing towards the film surface where it is subsequently oxidized. The surface oxide becomes a mixture of Mg and B oxides, with the B oxide above the MgO in the film stack.

A thicker 1.4 nm Mg layer, as in the plasma oxidized case, is sufficient to both protect the CFB electrode from oxidation and also to prevent the significant increase in B content in the surface oxide after annealing. In this case, no B oxide signal intensity is apparent in samples measured before or after annealing. As in the plasma oxidized experiments, the Mg 2p and O 1s MgO peaks shift to

lower BE after annealing and the surface O 1s peak decreases in intensity after annealing. These features again suggest the formation of a more chemically stable MgO layer. As in the 1.0 nm thick Mg sample, the un-oxidized 1.4 nm Mg layer is different from the two oxidized samples. The Mg 2p spectral region for the un-oxidized version of this sample shows two Mg peaks, which are attributable to the oxidized and un-oxidized Mg species. [10, 13–15] After annealing, only one peak is present which shows that annealing has oxidized all of the MgO by reacting the un-oxidized Mg with surface O. As in the plasma oxidation experiments, these thermal oxidation experiments demonstrate that an Mg layer 1.4 nm thick is necessary to fully protect the CFB electrode from oxidation and to prevent incorporation of B into the surface oxide during annealing.

3.6 Electron Beam Evaporated MgO Layers on CoFeB electrodes

Electron beam evaporation of an MgO tunnel barrier is an effective way to form high quality MTJs both in terms of coherent crystallinity and in terms of high junction TMR. [3, 20] Typically this deposition technique is used in conjunction with Molecular Beam Epitaxy (MBE) electrode film growth, but for the purposes of exploring electrode oxidation, and also to serve as a comparison for MgO barriers grown with other deposition methods, this section discusses experiments where I eb evaporated MgO barriers on both CFB and FCB electrodes. Fig. 3.11 displays the spectra from 1.0 and 2.0 nm thick eb evaporated MgO layers grown on CFB layers. Inspection of the Co 2p, Fe 2p, and Mg 2p spectral regions shows that there is no indication of Co or Fe oxide in these samples. The B 1s region does show a

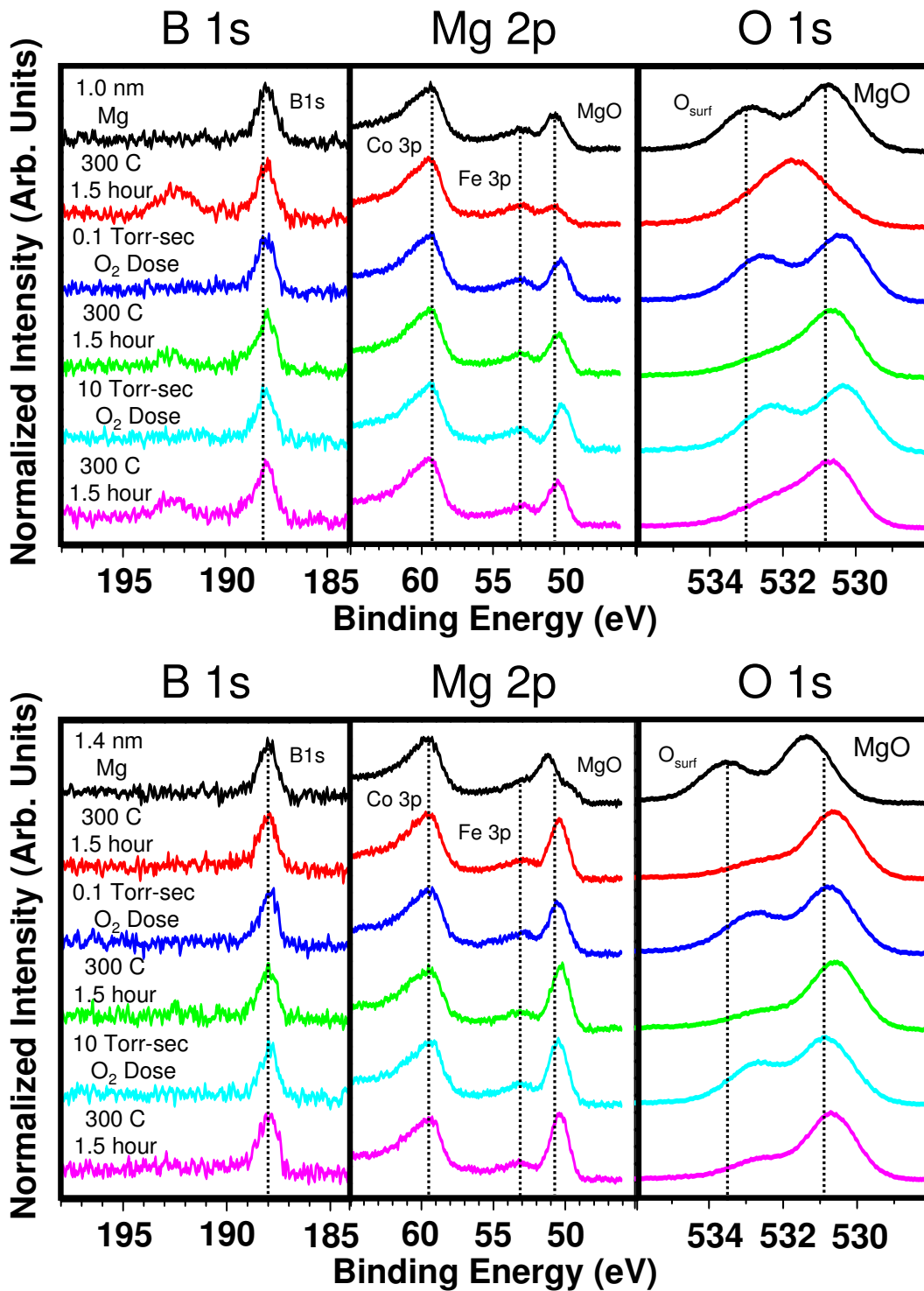


Figure 3.10: XPS data from thermally oxidized 1.0 and 1.4 nm thick Mg thin films deposited on 6 nm thick CFB base electrodes before and after annealing.

small intensity B oxide peak which I attribute to the slight oxidation of B at the electrode surface due to O ions liberated during evaporation. In-situ measurements with a Residual Gas Analyzer taken by Phil Mather [21] show that O is evolved during the evaporation process. The O 1s spectra display two distinct peaks, one at ~ 530 eV attributable to O in the MgO layer, the other at ~ 533 eV, attributable to chemisorbed O and possibly hydroxide species on the MgO surface. [13, 15] Both the O 1s and the Mg 2p peaks due to the MgO layer shift slightly to higher BE as the film thickness increases from 1 to 2 nm, which is attributable to the image charge effect. [22] Compositional analysis using the lower BE O 1s and Mg peaks finds these eb evaporated MgO layers are approximately stoichiometric. Other than a slight increase in the B oxide peak intensity, there appears to be no significant change in the chemistry of these samples after annealing.

I repeated this series of experiments on FCB electrodes and the results are quite similar to the study discussed in the previous paragraph. Fig. 3.12 shows the spectra from 1.0 and 2.0 nm thick eb evaporated MgO layers grown on FCB electrodes. The Fe 2p and Co 2p spectral regions do not show any indication of oxide formation before or after annealing, but the B 1s region has the signature of a broad B oxide peak which does increase slightly in signal intensity after annealing, as in the CFB-based study. The O 1s region shows the highest B oxide intensities for the 1.0 nm thick MgO layer, particularly after annealing, which again suggests that the B diffuses out of the electrode during annealing. The decreased relative intensity of the B oxide peak for the thicker MgO film is likely due to increased scattering from the thicker MgO material on top of the electrode. These observations advocate the possibility that the B oxide formed in these samples is at or near the FCB / MgO interface. Unlike the samples grown on CFB, there is no image charge shifting of the Mg 2p and O 1s MgO peaks as a function of film thickness.

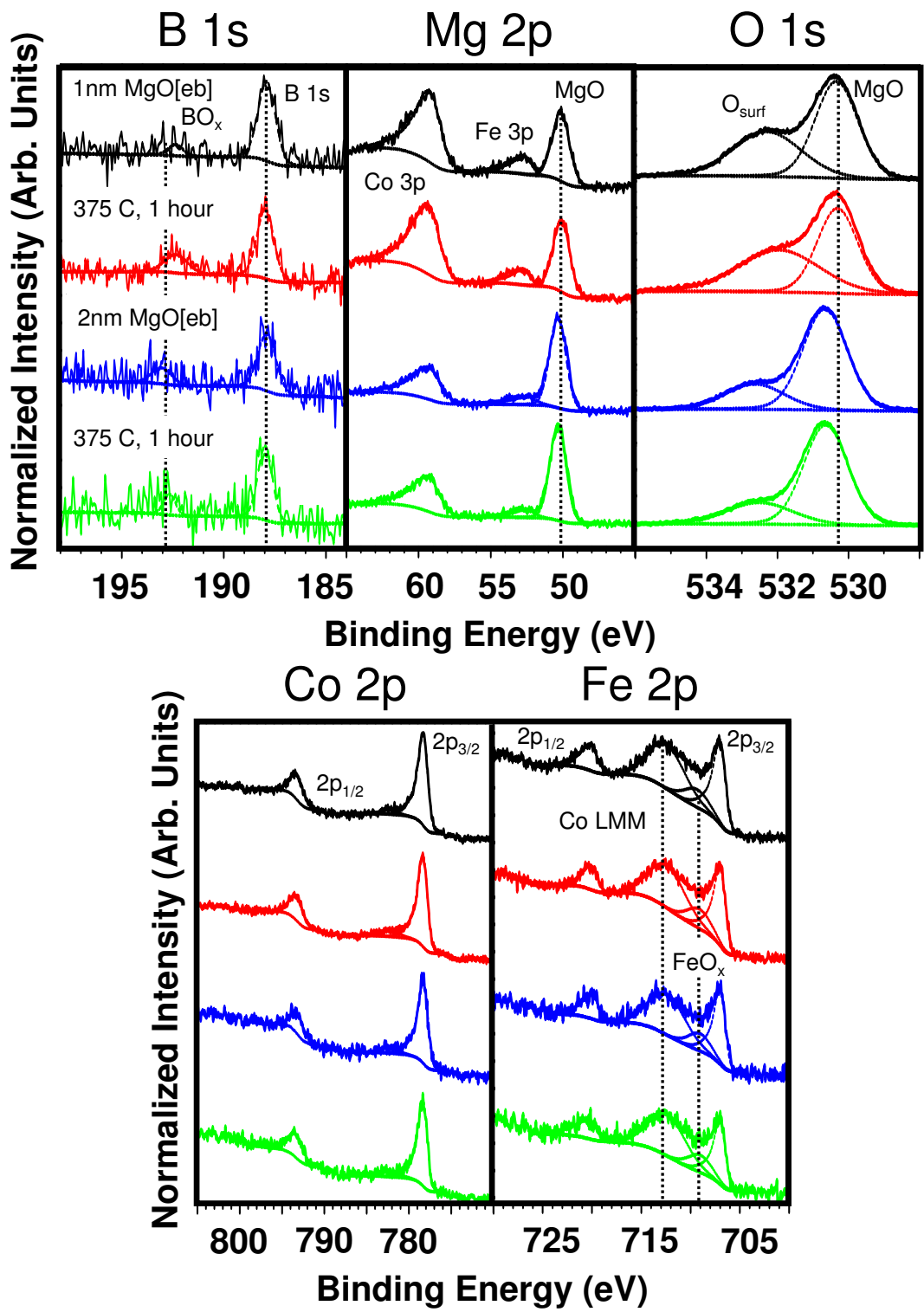


Figure 3.11: XPS data from 1.0 and 2.0 nm thick electron beam evaporated Mg layers grown on CFB electrodes before and after annealing

This, along with the comparatively larger B oxide content, is most probably due to a more efficient reaction between electrode B and O evolved in the evaporation process for the FCB electrode alloy. This structure forms more B oxide at the FCB / MgO interface which appears to compensate the image charge effect by pinning the FCB E_F within the MgO bandgap such that the MgO conduction band is closer to the FCB E_F . This suggests that the formation of interfacial B oxide can effect electrode E_F pinning which ultimately determines the tunnel barrier energy barrier height.

3.7 Radio Frequency Sputtered MgO Layers on CoFeB electrodes

The most successful deposition technique for forming high TMR low resistance area (RA) product MTJs is rf sputtering of an MgO target. [1, 2, 4, 5, 7] This method is technologically viable since it is compatible with existing circuit processing protocols and can generate uniform, large area thin film stacks. Previous studies show that one major reason why this deposition method is so successful is that rf sputtering of MgO barrier layers in conjunction with B-alloyed ferromagnetic electrodes forms MTJ structures that crystallize from the barrier material into the electrode. Specifically, the MgO tunnel barrier imprints its crystal structure onto the initially amorphous electrodes as the electrodes crystallize during the annealing process. [9] However, in order to crystallize, the B must leave the electrode, which begs the question addressed in detail in chapter 4: where does the B go during the annealing process? The studies discussed in this section clearly show that rf sputtering of MgO significantly oxidizes the B-alloyed electrodes and the

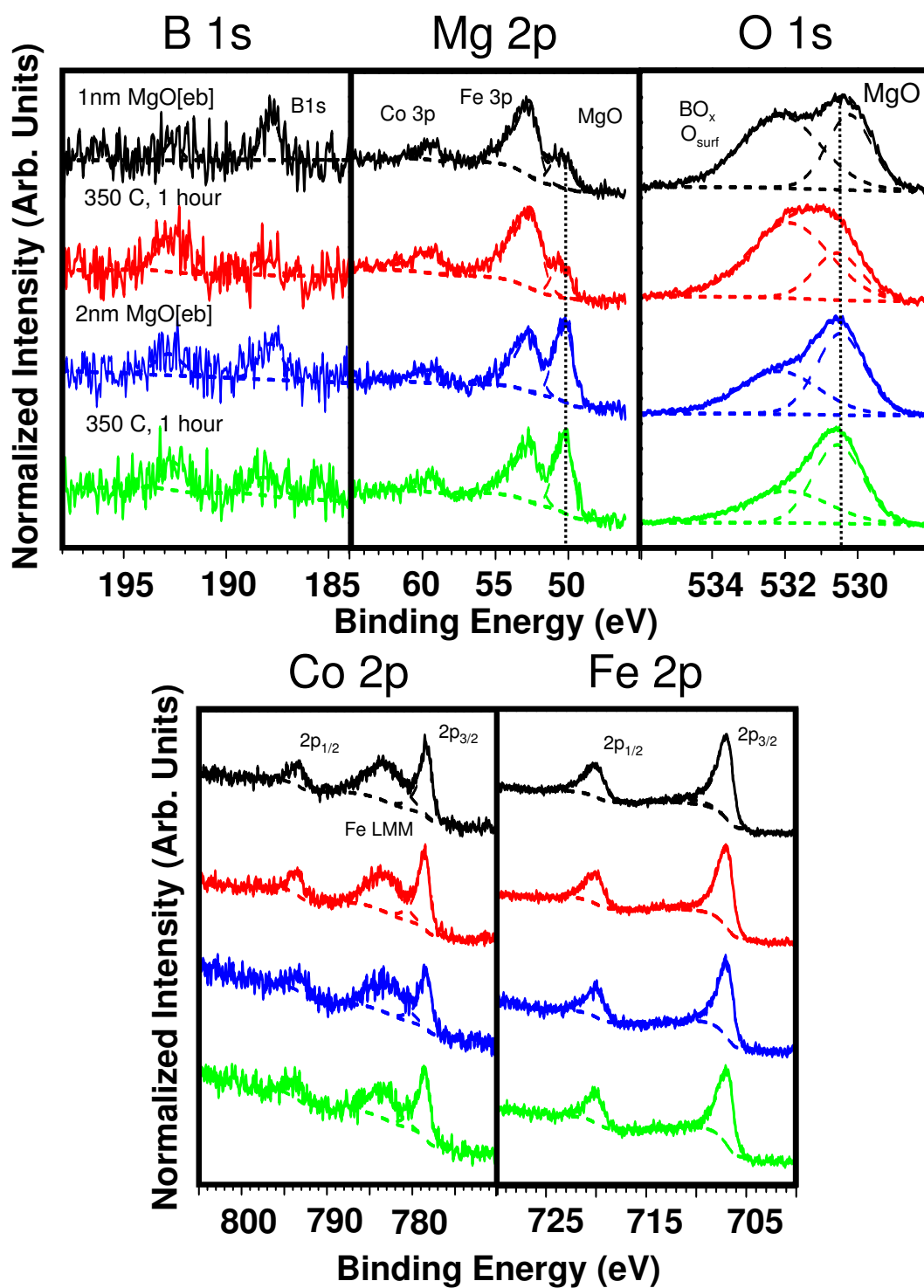


Figure 3.12: XPS data from 1.0 and 2.0 nm thick electron beam evaporated MgO layers grown on FCB electrodes before and after annealing.

chemical nature of the tunnel barrier material is substantially modified during the annealing process. This observation has major consequences for optimization of future MgO-based MTJ circuits and raises the question as to whether a significant B oxide component mixed into the MgO tunnel barrier is detrimental or beneficial to the MTJ performance.

In Fig. 3.13 I show data from two rf sputtered CFB / MgO bilayers before and after annealing. The B oxide peak at ~ 192 eV is quite large compared to eb evaporated MgO samples and the relative intensity of the B oxide peak is greater for a 2 nm thick MgO layer where Fe and Co oxides are also clearly present. This establishes that B oxide is formed throughout the rf process by O^{2-} ions released during the sputtering of the MgO target. The observation that the initial formation of B oxide is favored in electrode oxidation is consistent with the previously discussed XPS measurements of CoFeB electrodes exposed to different O_2 doses. The O 1s spectrum from the 1 nm thick MgO sample also has a broad dominant peak at ~ 531 eV and a much smaller peak at ~ 530 eV, with the latter attributable to MgO and Fe oxide. Based on the previous peak identifications and the clear presence of significant B oxide content, the higher BE O 1s peak is attributable to B oxide, surface O, and possibly some mixed Mg-B oxide. The O 1s spectrum for the 2 nm thick MgO layer can also be fit with two broad peaks, but both peaks are shifted to higher BE relative to the 1 nm thick MgO layer data. The lower BE O 1s peak has gained intensity and is likely the convolution of MgO with Fe and Co oxide signals.

The effects of annealing are considerably different for rf sputtered MgO barriers in comparison to the MgO barriers formed by other methods that I discussed previously. The rf sputtering process forms substantial B oxide and annealing

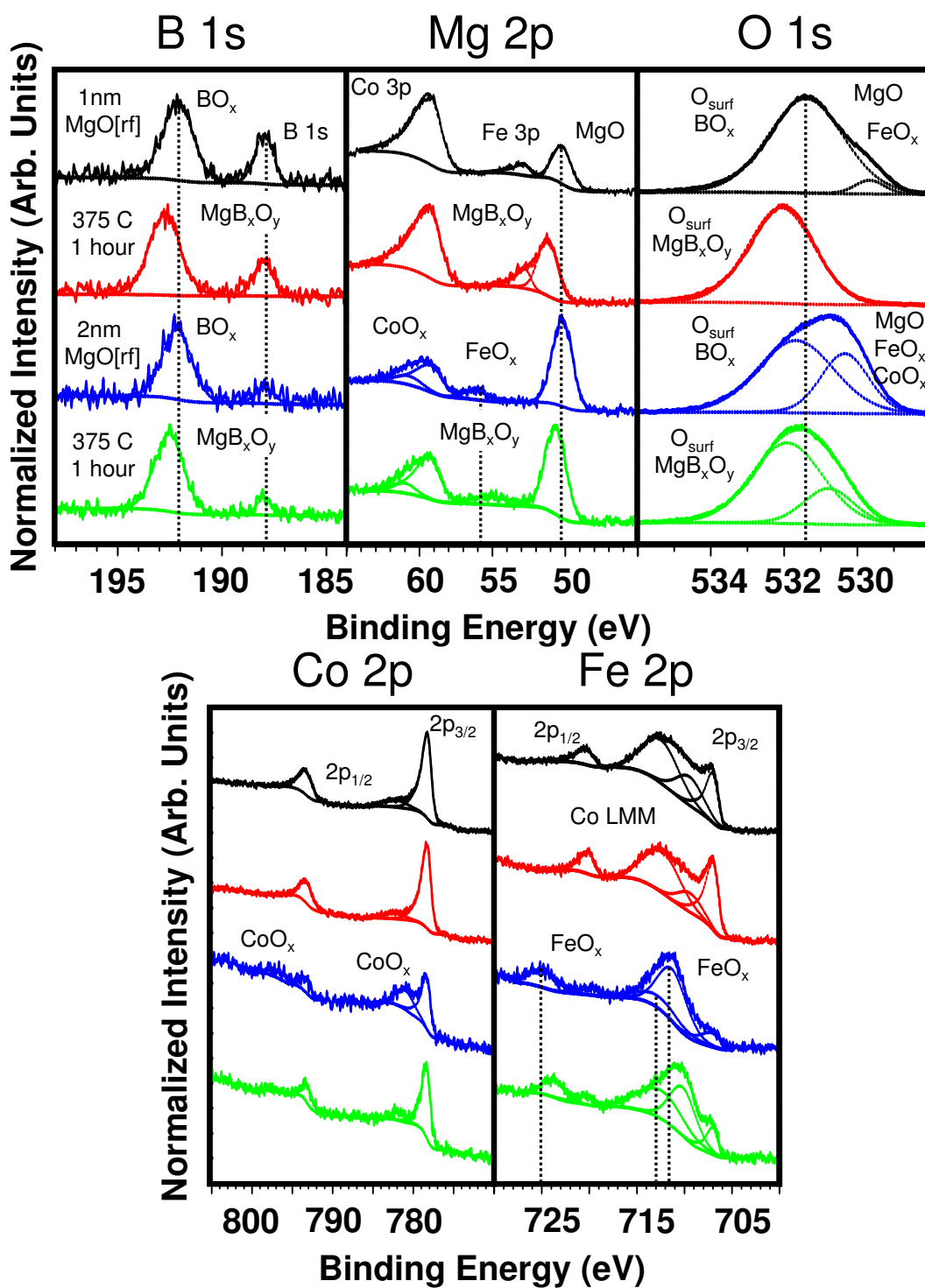


Figure 3.13: XPS data from 1.0 and 2.0 nm thick rf sputtered MgO layers (1 mTorr) grown on CFB electrodes before and after annealing.

further increases the intensity of the B oxide signal in these films. The B:Mg cation ratio in the oxide changes from ~ 0.6 before annealing to ~ 0.8 after annealing for a 1 nm MgO layer and from ~ 0.3 before annealing to ~ 0.5 after annealing for a 2 nm MgO layer. This provides further indication that a substantial amount of B diffuses into the MgO barrier during annealing. Previous XPS depth profiling studies (shown in Fig. 3.16) yielded a similar conclusion for annealed CoFeB/MgO-based structures. [23] The rf sputtered MgO data from the study in this chapter also shows that annealing significantly reduces the Co and Fe oxide peaks and shifts these transition metal oxide peaks to lower BE. These modifications indicate a reduction in the oxidation state of the Co and Fe cations and suggest that B from the electrode is responsible for the reduction of the Co and Fe oxides. The most important feature of the data from these rf sputtered MgO barrier layers is that annealing shifts the oxidic Mg and B peaks to higher BE by roughly 1 eV for the 1 nm thick MgO layer. A shift of almost 1 eV is also apparent in the O 1s spectrum and the broad peak structure has become more uniform after annealing. This same peak shifting behavior is present in the 2 nm thick MgO layer samples, but to a lesser degree. This collective shifting of the Mg, B, and O peaks in samples with significant B oxide content suggests that after annealing the oxide is an intermixed MgBO material. In this case the upward shifts of the Mg, B, and O peaks can be explained by the Mg^{2+} cations being in a lower average state of O coordination than in pure MgO and the oxidic B in a more ordered or a higher oxidation (B^{3+} as opposed to B^{2+}) state after annealing. The presence of B oxide mixed within the rf sputtered MgO barrier has also been observed in full MTJ stacks using electron energy-loss spectroscopy. [24]

I repeated this experiment for a higher rf sputtering pressure of 10 mTorr. The results of this study (Fig. 3.14) are similar to the 1 mTorr study but show some

significant qualitative differences. The relative intensities of the B, Fe, and Co oxide peaks are larger for the two sample thicknesses than for the 1 mTorr case. Given that deposition rate calibrations are estimated from very thick samples (greater than 50 nm thick) it is reasonable to conjecture that the higher pressure deposition actually forms a thicker oxide in the ultra-thin limit. This is due both to a more efficient MgO deposition process and also to enhanced plasma oxidation. Also, the O 1s spectra appear to have greater MgO content as evidenced by the central location of the peak structure occurring at low BE relative to the 1 mTorr case. Despite these differences, the shifts in BE of the Mg, B, and O peaks are still quite pronounced after annealing for both the 1 and 2 nm thick samples.

I also studied rf sputtering of MgO at 1 mTorr on a FCB electrode, as shown in Fig. 3.15. The data from these films are very similar to the data from the 1 mTorr CFB study with the major differences in the Mg 2p, Fe 3p, and Co 3p region being due to the differences in alloy composition. There does appear to be more B oxide formed in these samples than in the CFB case, as in the FCB eb evaporated MgO study, which could be due to a difference in vacuum deposition conditions between the studies. The relative intensity of the Fe and Co oxide peaks, both before and after annealing, is very similar to both the 1 and 10 mTorr CFB study and the peak shifting of the Mg, B, and O species is apparent in these films. These findings suggest that while there may be some small variation in the initial amount of B, Fe, and Co oxides that form during the MgO rf sputtering deposition, B from the electrode will always act to reduce the Fe and Co oxides and will mix with the MgO layer to form a Mg-B-O barrier material.

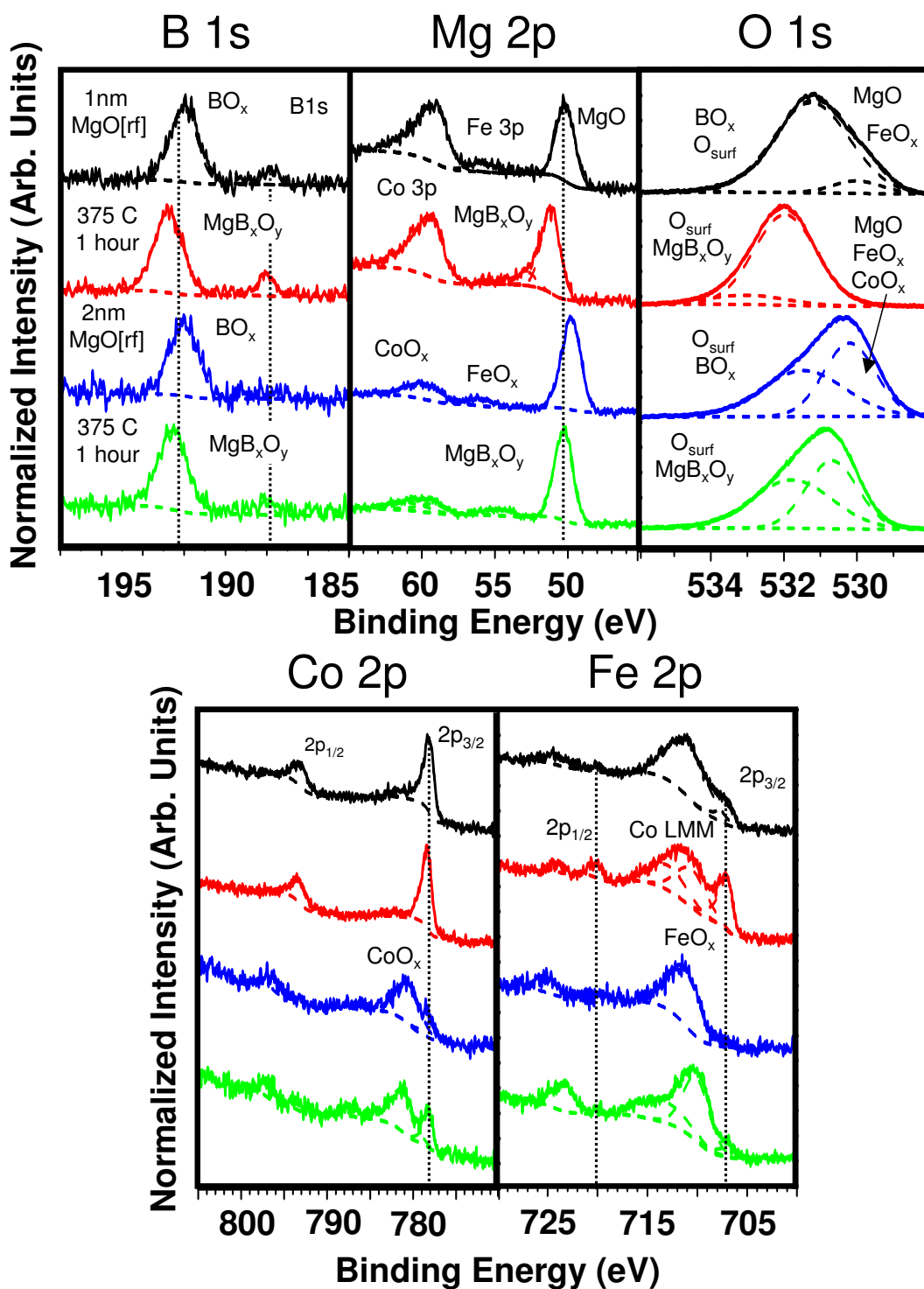


Figure 3.14: XPS data from 1.0 and 2.0 nm thick rf sputtered MgO layers (10 mTorr) grown on CFB electrodes before and after annealing.

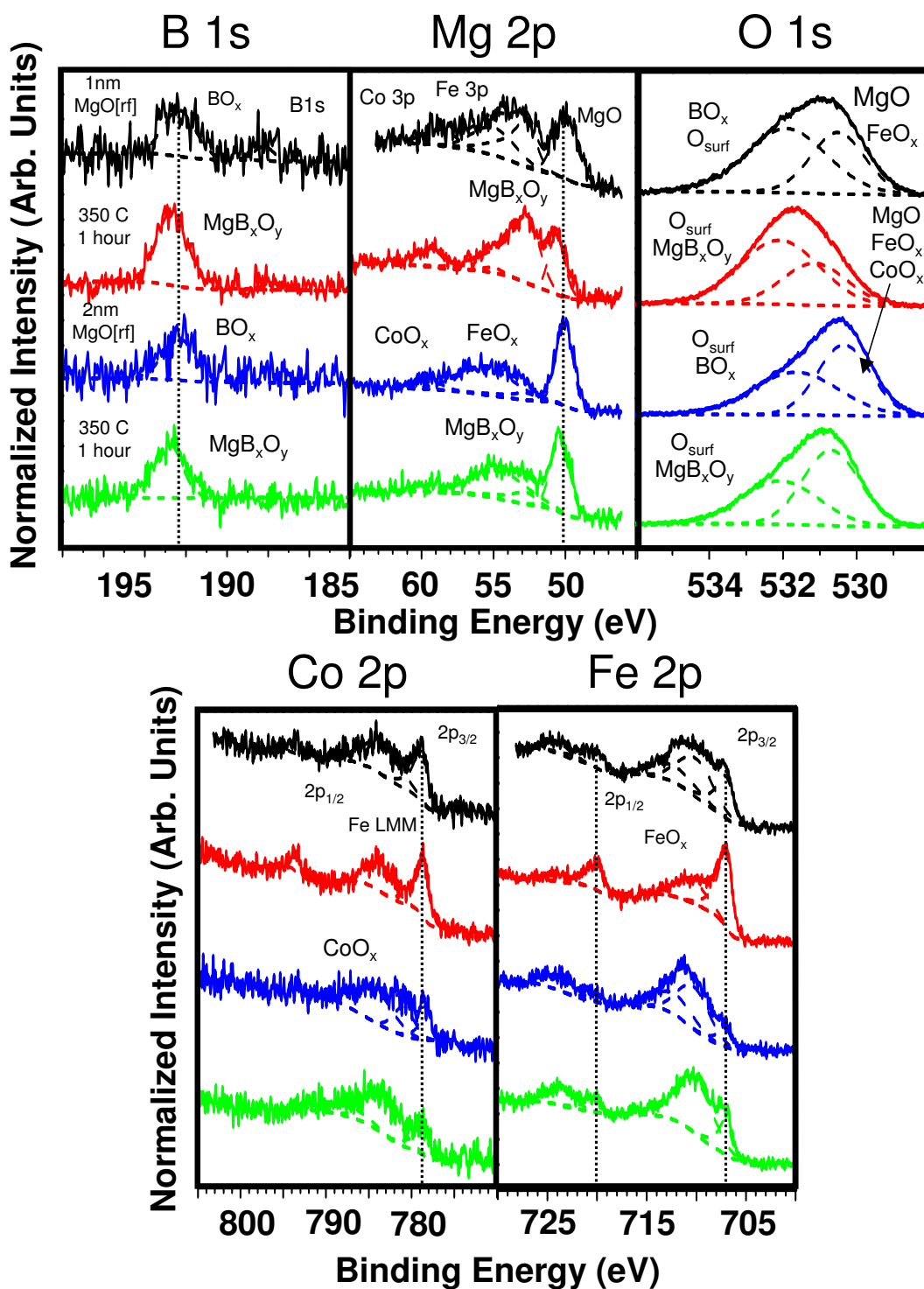


Figure 3.15: XPS data from 1.0 and 2.0 nm thick rf sputtered MgO layers (1 mTorr) grown on FCB electrodes before and after annealing.

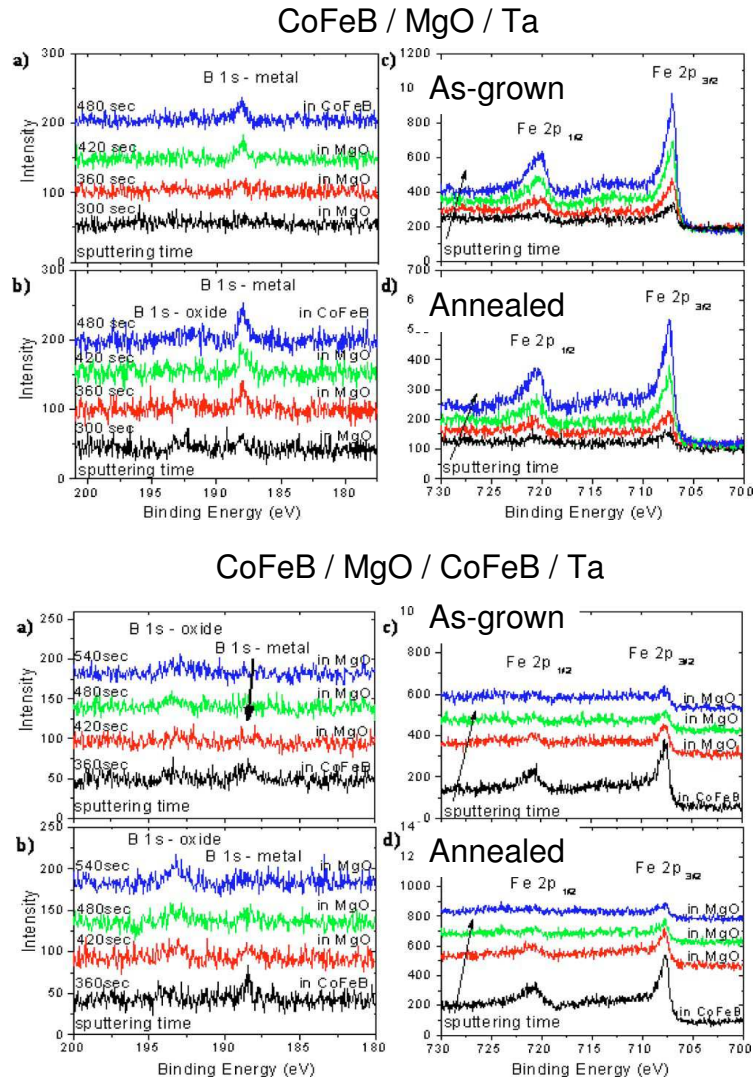


Figure 3.16: XPS depth profiling data from CoFeB/MgO/Ta and CoFeB/MgO/CoFeB/Ta structures before and after annealing (from ref [23]).

3.8 Sputtered Mg / MgO Bilayers on CoFeB electrodes

Deposition of a Mg seed layer between the electrode and the tunnel barrier is a successful way to increase the crystallinity of the MgO material both before and after annealing. [5] The studies that I discuss in this section probe the chemical changes that take place in such Mg/MgO bilayers in comparison to fully rf sputtered MgO barrier layers. Fig. 3.17 and Fig. 3.18 show XPS spectra from CFB/Mg/MgO trilayer samples. There is clear indication of B oxide formation in the data from the thin 0.5 nm Mg seed layer samples shown in Fig. 3.17, but there does not appear to be any Fe or Co oxide formation in these samples. After annealing, both the 0.5 nm Mg / 0.5 nm MgO and 0.5 nm Mg / 1.0 nm MgO structures exhibit the peak shifting behavior previously discussed for rf sputtered MgO barrier layers. These findings confirm that a very thin (0.5 nm) Mg layer, while sufficient to increase the crystallinity of the MgO barrier, is not sufficiently thick to prevent B oxide incorporation into the MgO layer. However, this process may also depend upon the amount of O present in the deposition chamber and the chamber pressure during the MgO deposition.

In contrast, the data shown in Fig. 3.18 indicate that a 1.0 nm thick Mg layer is thick enough to prevent the initial formation of B oxide during deposition of a thin (0.5 nm) MgO layer. From these studies I conclude that the underlying Mg layer, if sufficiently thick, serves effectively as a sink or getter for the O^{2-} ions that evolve during the rf sputter process. The Mg layer prevents electrode oxidation until it is fully oxidized, either by deposition of a thicker MgO layer or by reaction of the Mg with surface O during annealing. These findings give strong indications that after the Mg layer is fully oxidized, formation of B oxide at the CoFeB/MgO interface begins.

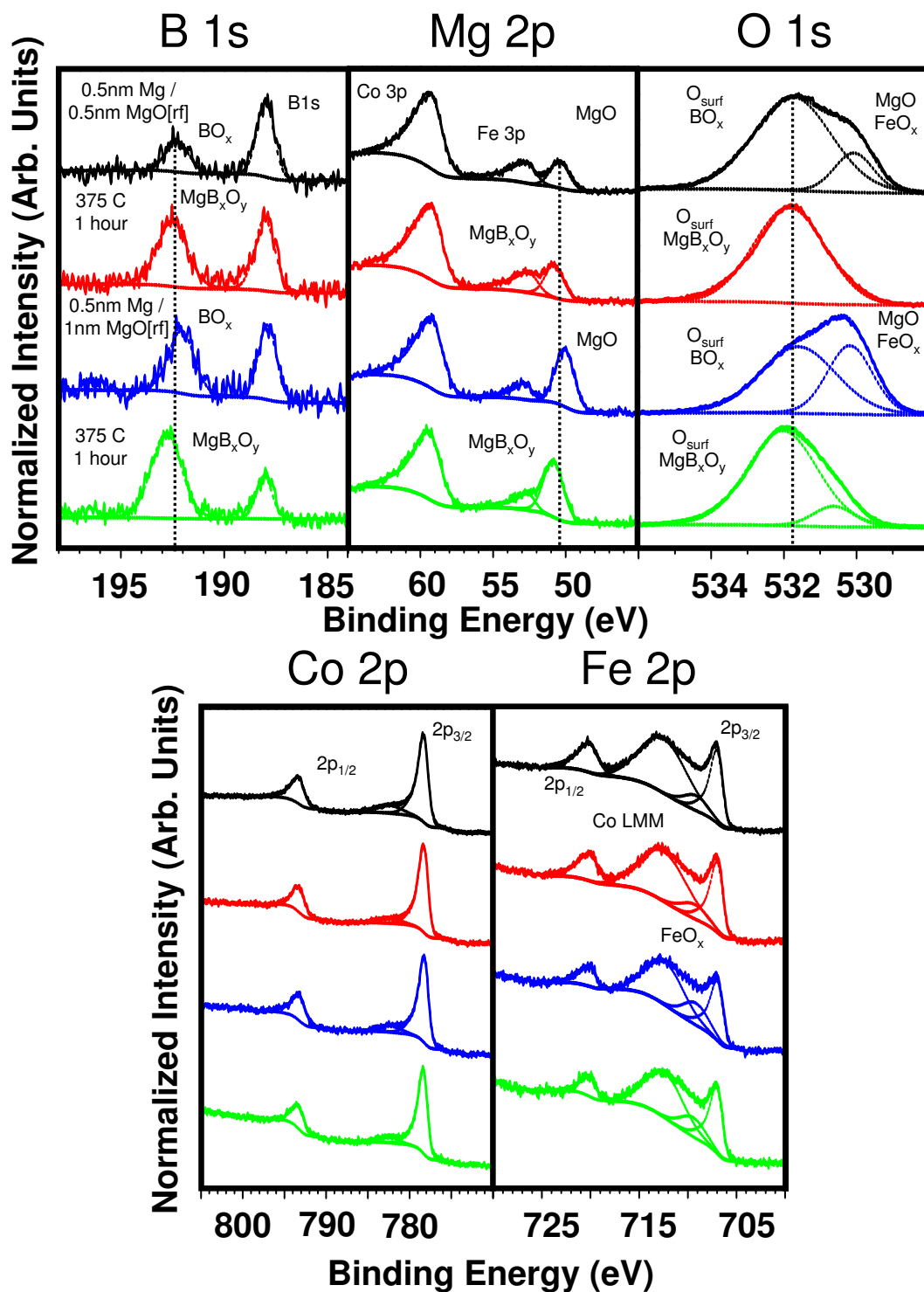


Figure 3.17: XPS data from sputtered Mg / MgO bilayers grown on CFB electrodes before and after annealing.

The O 1s spectra from these Mg/MgO bilayer barrier samples provide useful insights for understanding the rf sputtered MgO O 1s spectra. The O 1s spectrum from the 1 nm Mg/ 0.5 nm MgO sample is similar to spectra from eb evaporated MgO samples, and compositional analysis indicates that the 1 nm Mg/ 0.5 nm MgO process results in the formation of an MgO layer that is approximately stoichiometric. In comparison, while the 0.5 nm Mg/1nm MgO sample also shows an O 1s peak at ~ 530 eV, the higher BE O 1s peak is larger and centered at ~ 532 eV while the B 1s spectrum indicates a substantial oxidic B component. Based on this, I attribute the large, broad O 1s peak centered at ~ 532 eV to a mixture of surface O and B oxide.

In contrast, the spectra for the 1 nm Mg/ 0.5 nm MgO sample show that when there is little B oxide initially present, annealing measurably increases the oxidic B signal, but does not have the effect of making B a substantial component (greater than 5%) of the oxide. After annealing the B:Mg cation ratio in the oxide becomes ~ 0.1 for the 1 nm Mg/ 0.5 nm MgO sample and changes from ~ 0.25 to ~ 0.6 for the 0.5 nm Mg/ 1 nm MgO sample. Thus, if the initial B oxide content is low, after annealing there is no detectable shift of the Mg 2p peak and the oxide has the character of MgO that is slightly doped with B oxide. Alternatively, if the initial oxidic B content is higher, a major shift of the Mg, B, and O peaks to higher BE occurs upon annealing suggesting the formation of an atomically mixed MgBO barrier material with a substantial ($\sim 10\%$) B component.

3.8.1 Use of a Ta getter During rf Sputtering

The research team at Canon Anelva in Japan recently showed that using a Ta getter during the deposition of the MgO barrier by rf sputtering forms MTJs that are

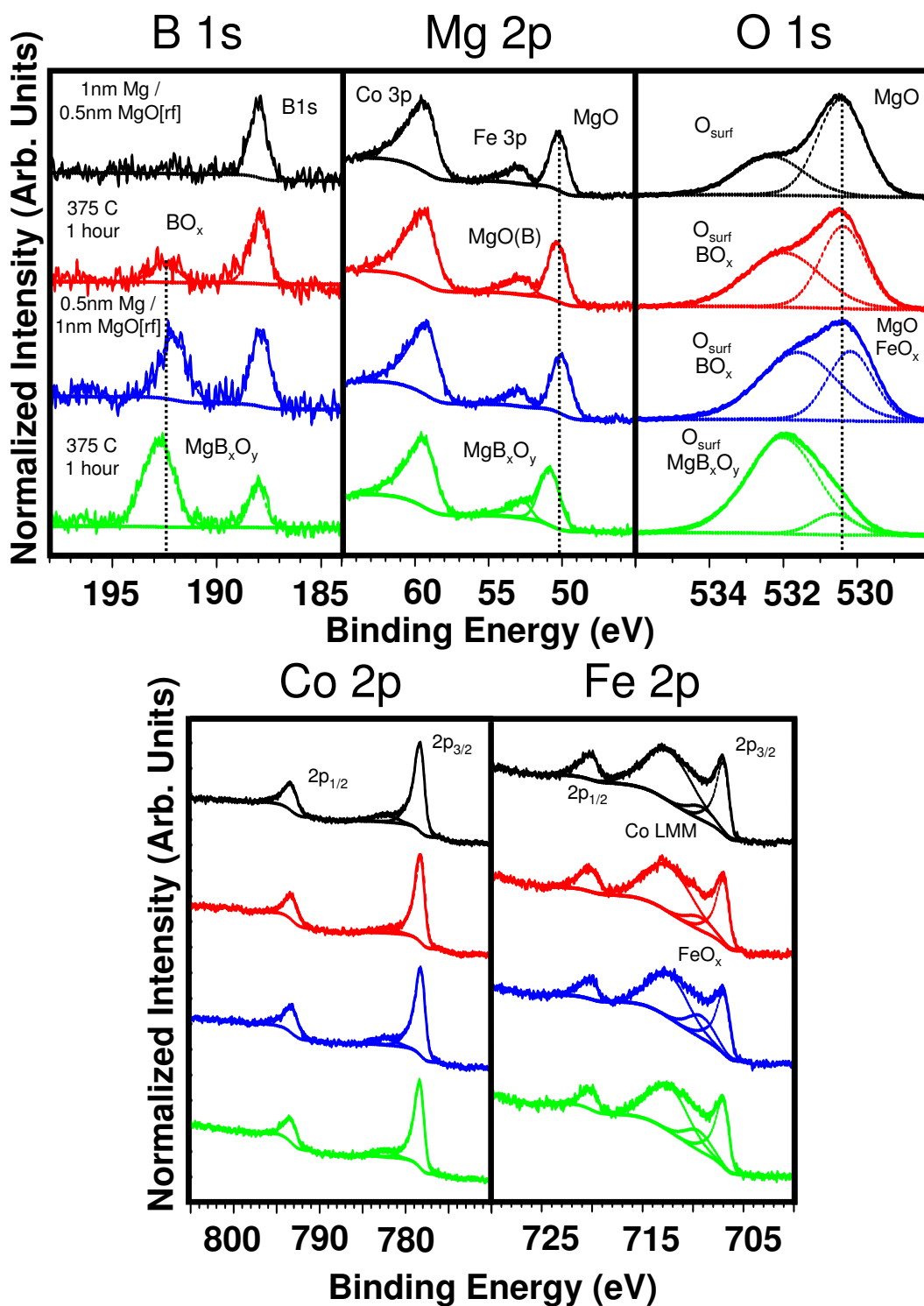


Figure 3.18: XPS data from sputtered Mg / MgO bilayers grown on CFB electrodes before and after annealing.

capable of achieving ultra-low RA products ($\sim 0.5 \Omega(\mu\text{m})^2$) with reasonably high TMR values of $\sim 50\%$ after annealing. [25] This process will be described in more detail in the next chapter. However, within the context of XPS studies, it is worth mentioning here that while this process certainly decreases the electrode oxidation during the initial stages of MgO barrier layer growth, it does not completely prevent electrode oxidation in such samples. In fact, data from an XPS study (Fig. 3.19) of structures formed using the process outlined in ref [25] appears to be quite consistent with the findings discussed in this chapter. [26] Specifically, the O 1s spectra are very likely representative of the presence of B oxide in the tunnel barrier. Without the Ta getter the high BE O 1s peak intensity is much larger, but in both cases there is a high BE O 1s component which is likely due to B oxide. In the next chapter I will discuss in more detail the beneficial effects the B oxide has on the chemical, electronic, structural, and electron transport properties of sputtered MTJs.

3.9 Summary

Using XPS I observe the formation of B oxide, and in some cases Fe and Co oxide, at the interface of rf sputtered CoFeB/MgO bilayers. I attribute this result to the evolution of a substantial quantity of O^{2-} ions during the initial stages of the deposition of rf sputtered MgO layers. I find that vacuum annealing promotes reduction of the Fe and Co oxides and forms a mixed Mg-B oxide tunnel barrier layer as evidenced by the substantial chemical shift of the Mg, B, and O peaks. Both eb deposition of MgO and insertion of a thin Mg layer between the CoFeB electrode and the MgO layer substantially reduce or eliminate the amount of B, Fe, and Co oxides initially formed. However, I find that some B is still incorporated

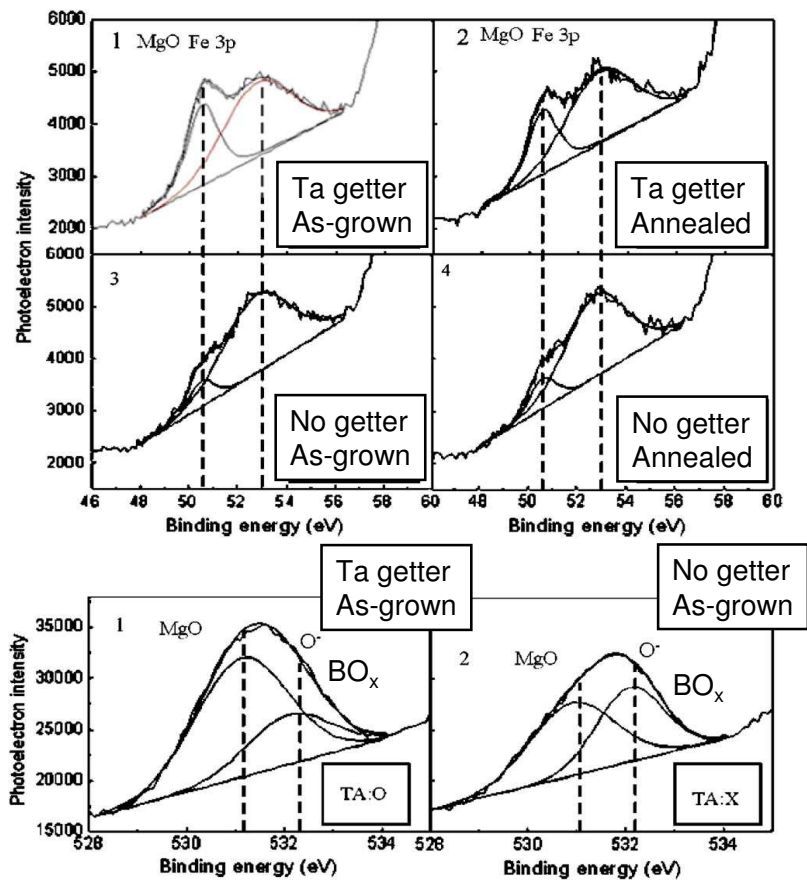


Figure 3.19: Comparison of XPS data from sputtered MgO barrier layers grown with or without the use of a Ta getter (adapted from ref[26]). The Ta getter process reduces but does not eliminate the formation of MgBO, as shown by the intensities of the peak at ~ 532 eV.

into the MgO tunnel barrier after annealing unless an Mg layer 1.4 nm thick or thicker is deposited on the CoFeB electrode before the MgO is formed.

Using compositional analysis of as-grown CoFeB/MgO samples, which for the sake of simplicity assumes a uniform distribution of B oxide, I yield an estimate of less than 2% B oxide content in eb evaporated MgO layers but significantly more B oxide content (greater than 5%) in rf sputtered MgO layers. The B:Mg ratio decreases with increased film thickness which indicates that the B oxide is formed more readily during the initial stages of the MgO deposition process. However, the B oxide signal intensity increases with increased MgO thickness for rf sputtered samples indicating that some electrode oxidation takes place throughout the rf sputtering deposition process. In Mg/MgO bilayers there is no clear signal of B oxide in the 1 nm Mg/ 0.5 nm MgO sample while the B:Mg cation ratio in the 0.5 nm Mg/ 1 nm MgO sample is ~ 0.25 , similar to the ratio for the 2 nm rf sputtered MgO layer sample structure.

The lack of substantial Fe and Co oxide formation in the un-oxidized CFB and FCB samples demonstrates that significant electrode oxidation does not take place during the dc sputtering process or upon limited exposure to typical vacuum system pressures. Instead, it is the exposure of the electrode to O, either through direct oxidation (O_2) or during the deposition of MgO (O^{2-}), that causes the electrode species to oxidize. Therefore, the increased crystallinity observed in MTJs with MgO barriers that is achieved by inclusion of an Mg layer or through use of gettering materials during the MgO deposition, is due to the capture of O^{2-} liberated from the MgO target in the early stages of sputtering. From the XPS studies discussed in this chapter I conclude that a reaction between the O evolved in the MgO formation process and B from the electrode, especially in rf sputtered

MgO barriers, appears to be an inherent part of the growth and processing of MgO-based MTJs. The investigation now turns to the benefits of MgBO tunnel barriers which I address in the next chapter.

REFERENCES

- [1] T. Linn and D. Mauri, Method of forming a barrier layer of a tunneling magnetoresistive sensor, United States Patent 6841395, International Business Machines Corporation, Armonk, NY, US (2005).
- [2] S. S. P. Parkin, C. Kaiser, A. Panchula, P. M. Rice, B. Hughes, M. Samant, and S.-H. Yang, Giant tunnelling magnetoresistance at room temperature with MgO (100)tunnel barriers, *Nature Materials* **3**, 862–867 (2004).
- [3] S. Yuasa, T. Nagahama, A. Fukushima, Y. Suzuki, K. Ando, Giant room-temperature magnetoresistance in single-crystal Fe/MgO/Fe magnetic tunnel junctions, *Nature Materials* **3**, 868–871 (2004).
- [4] D. D. Djayaprawira, K. Tsunekawa, M. Nagai, H. Maehara, S. Yamagata, N. Watanabe, S. Yuasa, Y. Suzuki, and K. Ando, 230% room-temperature magnetoresistance in CoFeB/MgO/CoFeB magnetic tunnel junctions, *Appl. Phys. Lett.* **86**, 092502 (2005).
- [5] K. Tsunekawa, D. D. Djayaprawira, M. Nagai, H. Maehara, S. Yamagata, N. Watanabe, S. Yuasa, Y. Suzuki, and K. Ando, Giant tunneling magnetoresistance effect in low-resistance CoFeB/MgO(001)/CoFeB magnetic tunnel junctions for read-head applications, *Appl. Phys. Lett.* **87**, 072503 (2005).
- [6] R. W Dave, G. Steiner, J. M. Slaughter, J. J. Sun, B. Graigo, S. Pietambaram, K. Smith, G. Grynkewich, M. DeHerrera, J. Akerman, and S. Tehrani, MgO-based tunnel junction material for high-speed toggle magnetic random access memory, *IEEE Trans. Magn.* **42**, 1935 (2006).
- [7] S. Ikeda, J. Hayakawa, Y. Ashizawa, Y. M. Lee, K. Miura, H. Hasegawa, M. Tsunoda, F. Matsukura, and H. Ohno, Tunnel magnetoresistance of 604% at 300 K by suppression of Ta diffusion in CoFeB/MgO/CoFeB pseudo-spin-valves annealed at high temperature, *Appl. Phys. Lett.* **93**, 082508 (2008).
- [8] J. C. Read, P. G. Mather, and R. A. Buhrman, X-ray photoemission study of CoFeB/MgO thin film bilayers, *Appl. Phys. Lett.* **90**, 132503 (2007).
- [9] S. Yuasa, Y. Suzuki, T. Katayama, and K. Ando, Characterization of growth and crystallization processes in CoFeB/MgO/CoFeB magnetic tunnel junction structure by reflective high-energy electron diffraction, *Appl. Phys. Lett.* **87**, 242503 (2005).

- [10] J. F. Moulder, W. F. Stickle, P. E. Sobol, and K. D. Bomben, *Handbook of X-Ray Photoelectron Spectroscopy*, ULVAC-PHI, Inc. and Physical Electronics USA, Inc., Chigasaki, Japan (1995).
- [11] Y. Wang and M. Trenary, Surface chemistry of boron oxidation. 2. The reactions of boron oxides B_2O_2 and B_2O_3 with boron films grown on tantalum(110), *Chem. Mater.* **5**, 199 (1993).
- [12] W. E. Moddeman, A. R. Burke, W. C. Bowling, and D. S. Foose, Surface oxides of boron and $B_{12}O_2$ as determined by XPS, *Surf. Interface Anal.* **14**, 224 (1989).
- [13] J. C. Fuggle, XPS, UPS and XAES Studies of oxygen adsorption on polycrystalline Mg at 100K and 300K, *Surf. Sci.* **69**, 581 (1977).
- [14] J. S. Corneille, J.-W. He, and D. W. Goodman, XPS characterization of ultrathin MgO films on a Mo(100) surface, *Surf. Sci.* **306**, 269 (1994).
- [15] D. Peterka, C. Tegenkamp, K.-M. Schroder, W. Ernst, and H. Pfnur, Oxygen surplus and oxygen vacancies on the surface of epitaxial MgO layers grown on Ag(100), *Surf. Sci.* **431**, 146 (1999).
- [16] G. A. Carson, M. H. Nassir, and M. A. Langell, Epitaxial growth of Co_3O_4 on CoO(100), *J. Vac. Sci. Technol. A* **14**, 1637 (1996).
- [17] T. Fujii, F. M. F. de Groot, G. A. Sawatzky, F. C. Voogt, T. Hibma, and K. Okada, In situ XPS analysis of various iron oxide films grown by NO_2 -assisted molecular-beam epitaxy, *Phys. Rev. B* **59**, 3195 (1999).
- [18] E. Tan, P. G. Mather, A. C. Perrella, J. C. Read, and R. A. Buhrman, *Phys. Rev. B.* **71**, 161401 (2005).
- [19] D. R. Lide, ed., "*Electron Affinities*" in *CRC Handbook of Chemistry and Physics, 88th Edition*, CRC Press/Taylor and Francis, Boca Raton, FL. (Internet Version 2008).
- [20] S. Yuasa, A. Fukushima, H. Kubota, Y. Suzuki, and K. Ando, Giant tunneling magnetoresistance up to 410% at room temperature in fully epitaxial Co/MgO/Co magnetic tunnel junctions with bcc Co(001) electrodes, *Appl. Phys. Lett.* **89**, 042505 (2006).

- [21] P. G. Mather, *Electronic Structure of Oxide Tunnel Barriers and Gallium Arsenide-Ferromagnet Interfaces*, Ph.D. thesis, Cornell University (2006).
- [22] R. Browning, M. Sobolewski, and C. R. Helms, Effect of electrostatic screening on energy positions of electron spectra near SiO₂/Si interfaces, *Phys. Rev. B* **38**, 13407 (1988).
- [23] J. Bae, W. Lim, H. Kim, T. Lee, K. Kim, and T. Kim, Compositional change of MgO barrier and interface in CoFeB/MgO/CoFeB tunnel junction after annealing, *J. Appl. Phys.* **99**, 08T316 (2006).
- [24] J. J. Cha, J. C. Read, R. A. Buhrman, D. A. Muller, Spatially resolved electron energy-loss spectroscopy of electron-beam grown and sputtered CoFeB/MgO/CoFeB magnetic tunnel junctions, *Appl. Phys. Lett.* **91**, 062516 (2007).
- [25] Y. Nagamine, H. Maehara, K. Tsunekawa, D. Djayaprawira, N. Watanabe, S. Yuasa, and K. Ando, Ultralow resistance-area product of $0.4 \Omega(\mu\text{m})^2$ and high magnetoresistance above 50% in CoFeB/MgO/CoFeB magnetic tunnel junctions, *Appl. Phys. Lett.* **89**, 162507 (2006).
- [26] Y. S. Choi, Y. Nagamine, K. Tsunekawa, H. Maehara, D. D. Djayaprawira, S. Yuasa, and K. Ando, Effect of Ta getter on the quality of MgO tunnel barrier in the polycrystalline CoFeB/MgO/CoFeB magnetic tunnel junction, *Appl. Phys. Lett.* **90**, 012505 (2007).

CHAPTER 4

CHEMICAL, ELECTRONIC, STRUCTURAL, AND MAGNETIC INVESTIGATION OF MgBO BASED MTJS

4.1 Motivation

Nanoscale MTJs are the key device element in next generation MRAM and in the read heads of contemporary ultra-dense data storage architectures. The deposition procedures optimized for these applications may also be applied to future, large area, low noise thin film sensors. Although read head sensors currently exist which exploit the MTJ as a sensor element, if low noise MTJs are formed with the same deposition techniques, then cheap thin film sensors could potentially replace several much more expensive technologies, particularly in the bio-medical field. In the present day, MRAM shows a great deal of promise for the development of universal memory. The ability to control both spin-polarized tunneling through an atomic-scale tunnel barrier and magnetic field toggle switching of the ferromagnetic electrodes in the MTJ have already led to the production of commercial MRAM. [1] MRAM combines the nonvolatile nature of FLASH with the high speeds of dynamic RAM, and could potentially replace both as a universal memory solution. Although toggle-based MRAM has demonstrated remarkable performance to date, the use of spin torque (ST) to switch the resistance state of the MTJ provides the possibility of substantially reducing the area and power consumption necessary for an MRAM bit. This can dramatically increase the memory density, however there are several challenges that must be addressed to achieve this goal. One important challenge is the reduction of the tunneling current density necessary to rapidly switch the relative orientation of the MTJ electrodes. Another substantial

challenge is the reduction of the time required to make such a switch. Improvement of the tunnel barrier material may provide a solution to the first challenge. If the tunnel barrier acts as an efficient spin-filter and has enhanced physical, chemical, and thermal stability, then less current density may be required to switch between MTJ resistance states. Both the first and second challenges are addressed through careful engineering of the free electrode with a material that has a low saturation magnetization (M_S). [2] The critical current for switching (I_C) is proportional to $(M_S)^2$, while the thermal stability of the free layer is proportional to (M_S) . [3] However, it is crucial to achieve a balance where devices exhibit room temperature thermal stability but achieve low critical current values. I discuss these topics in greater detail in Chapter 2 along with a discussion of the relevant research performed to date. With these issues in mind, exploration of barrier and free electrode engineering are of significant importance for the potential enhancement of ST switching in MTJs for future ST-MRAM bits.

4.2 Introduction

The development of MTJs with MgO barriers that exhibit large TMR [4–6] through the engineering of optimal electrode materials [7–9] and barrier deposition techniques [10–14] shows promising results applicable to MRAM and to magnetic sensing in advanced data storage, biomedical, and security applications. Ideal crystal structures and interfaces are central to the theoretical model for high TMR in epitaxial Fe/MgO/Fe MTJs. [15–18] These models predict enhanced spin polarization and TMR of properly oriented crystalline electrodes through a spin-filtering tunneling effect. Spin-filtering improves TMR through dissimilar decay rates for electrode majority and minority spin states within the MgO barrier.

The influence of crystal structure on spin-filtering is clearly supported by experimental results from sputtered CoFeB/MgO/CoFeB MTJs, where the low TMR of as-deposited structures with amorphous electrodes increases substantially upon annealing. [4, 5, 7, 8, 10–14] During annealing, the (001) normal MgO barrier influences the crystallization of the adjacent electrodes [19], forming body centered cubic (bcc) electrodes which have the requisite spin-split electrode wave-function symmetries to generate high TMR. This crystallization need not be extensive, as a recent theoretical study finds that one crystalline Fe monolayer is sufficient to yield high TMR. [20] Therefore, diffusion of Fe to the barrier interfaces, or segregation of Fe at the barrier interfaces during each the growth or annealing stages of MTJ formation could have a significant impact on device TMR.

There are key materials issues regarding the formation of ultra-thin, low resistance area (RA) product tunnel barriers which still need to be addressed to better meet the requirements of high-impact technological applications such as ST-MRAM and ultra-high-density data storage [21] including developing a junction technology that is tolerant to invariable atomic defects in a wafer-scale process. Epitaxial Fe/MgO/Fe junctions with tunnel barriers formed by electron beam deposition (EBD), have ideal crystal orientation, albeit with misfit dislocations in the MgO. [6, 9] Such MTJs exhibit large TMR that decreases with decreasing barrier thickness, in agreement with theoretical predictions. Larger TMR can be obtained with B-alloyed Co-Fe electrodes and MgO barrier layers produced by radio frequency (rf) sputtering deposition. [10] This plasma process forms O ions that invariably oxidize the base alloy electrode surface during the initial stages of the barrier deposition [22–25], even if a getter is employed [14]. Though plasma oxidation predominantly forms B oxide, some Fe and Co oxide also form at the bottom MgO interface unless a sufficiently thick Mg buffer layer is deposited before

the MgO to fully scavenge the free oxygen ions that would otherwise reach the ferromagnetic electrode. [24, 26] Such Mg/MgO bilayer barriers do not yield the best results in the ultra-thin regime. [11, 12, 14] The subsequent deposition of the top electrode layer forms additional interfacial oxides through its reaction with surface oxygen on the MgO barrier. [24, 26] The as-grown sputtered barrier is a composite of MgO and B oxide. Annealed sputtered junctions typically show a very high TMR that does not significantly decrease with thickness until the ultra-thin limit, where the TMR drops off rapidly due to the detrimental effects of pinholes and barrier defect states. Annealing modifies the chemical and electronic structure of the tunnel barrier, resulting in the formation of a MgBO barrier material which produces large TMR, low RA MTJs.

4.3 Experimental Techniques

To understand the beneficial effect of B oxide incorporation in low RA, high TMR MgBO MTJs and to thus advance and expand its exploitation in critical technological applications, my collaborators and I investigated the correlated characterization of MgBO MTJs with current-in-plane tunneling (CIPT) [27], analytical scanning transmission electron microscopy (STEM) utilizing electron energy-loss spectroscopy (EELS), scanning tunneling spectroscopy (STS), and magnetometry measurements. In the sections that follow, I present the results of CIPT, STEM/EELS, and magnetometry studies of different MTJ structures, each with anti-ferromagnetically pinned base electrodes and tunnel barriers grown using rf sputtering of an MgO target. I compare the use of $\text{Co}_{60}\text{Fe}_{20}\text{B}_{20}$ (CFB) or $\text{Fe}_{60}\text{Co}_{20}\text{B}_{20}$ (FCB) alloys for both electrodes with structures utilizing electrodes composed of permalloy, $\text{Ni}_{81}\text{Fe}_{19}$ (Py), alloyed with boron. For these junctions I

used $\text{Ni}_{77}\text{Fe}_{18}\text{B}_5$ (Py_{95}B_5) and $\text{Ni}_{65}\text{Fe}_{15}\text{B}_{20}$ ($\text{Py}_{80}\text{B}_{20}$) alloys as the free electrodes. I also present the results of STS studies of the electronic structure of MgBO barrier layers, EBD MgO barriers, and sputtered Mg/MgO bilayer barriers. Comparison of the TMR and RA of Mg/MgO and MgBO barrier junctions of comparable thickness suggests that the mixing of B oxide into the MgO barrier is positively correlated with achieving higher TMR and lower RA values. I attribute this result to the improved electronic structure, and possibly to enhanced spin-filtering properties, of ultra-thin MgBO in comparison with MgO.

I grew the thin film stacks for the CIPT, EELS, and magnetometry studies in the AJA vacuum system which has a nominal base pressure of 3×10^{-9} Torr and contains seven magnetron sputtering sources. To achieve a low bottom electrode sheet resistance, necessary for CIPT study of low RA barriers, I used a Ta/CuN multi-layer below the MTJ film stack. This low resistance under-layer stack, 5 nm Ta / [20 nm CuN / 3 nm Ta]_{x4}, served to also form a smooth surface to help seed growth of the MTJ layers. I discuss the development of these seed layers and their surface morphology characteristics in more detail in Chapter 2. On the seed layer I grew a 15 nm IrMn anti-ferromagnetic pinning layer, then the MTJ, then a capping layer 8 nm Ta / 7 nm Ru to facilitate the CIPT measurement. The MTJ structure was 4 nm base electrode / MgBO / 2 nm top electrode. I grew the MgBO layer with radio frequency sputtering at high power (300 W, 2" target; Power density $\sim 14.8 \text{ W/cm}^2$) in Ar while a getter material (Mg or Ta) was also being deposited within the deposition chamber. The CuN layer was grown using reactive dc sputtering of Cu in an Ar / N (32:1) mixture. Otherwise, the film layers were grown with conventional dc sputtering in Ar on 3" diameter thermally oxidized Si wafers. The thickness of the MgBO layers studied varied from 1.1 to 2.1 nm, with the lower thickness limit set by the ability to obtain reliable CIPT

data for the sample.

I cut the centers of the wafers into small $\sim 1 \text{ cm}^2$ chips, yielding several samples with a particular barrier thickness and electrode alloy combination. I then annealed the chips in modest vacuum of $\sim 3 \times 10^{-6}$ Torr to 250, 300, or 350°C, for up to 2 hours in the CCMR vacuum annealing furnace. Each chip was then studied with CIPT using a CAPRES tool by Audie Castillo, P. J. Chen, or me. The CIPT measurement yields TMR, RA, and the sheet resistance values for both the top and the bottom electrodes. I used the sheet resistance values as a check of the accuracy of the CIPT fit to assure its validity. Both the top and bottom electrode sheet resistance fit values were similar to those I measured with the van der Pauw technique using electrode test layers measured in a dipper made by Ozhan Ozatay. Magnetometry measurements were made with a Shb instruments MESA series B-H looper by Audie Castillo, P. J. Chen, or me. Judy Cha prepared chips from these same wafers for STEM/EELS, TEM, and CBED study using mechanical polishing and ion milling to create thin wedge-shaped samples of structures identical to those studied with CIPT. Judy Cha took all of the STEM/EELS, TEM, and CBED data discussed in this chapter. For spectral imaging, she used a 100 kV NION Ultra-STEM with a $\sim 0.1 \text{ nm}$, 100 pA aberration-corrected probe and 10 milli-second per pixel acquisition time to acquire a 64 x 64 pixel spectral map, where each pixel contains a spectrum that includes B, O, Mn, Fe, and Co edges. [28] For the remainder of the STEM/EELS studies, she used a 200 kV FEI Tecnai F20-ST STEM fitted with a monochromator and a Gatan imaging filter 865-ER. She focused the electron beam to form a 0.2 nm diameter probe with a convergence semi-angle of $\sim 9.6 \text{ mrad}$ and to reduce the electron dose per unit area for minimum radiation damage, she took EELS spectra in a line parallel to the electrode-barrier interface. She set the spectrometer dispersion to 0.3 eV/channel

or 0.5 eV/channel to capture the wide energy range needed to record all edges simultaneously, resulting in an energy resolution of 1 eV. For CBED measurements, she changed the convergence angle to 2 mrad to produce smaller diffracting disks which overlap less with neighboring disks for clearer diffraction patterns. At a convergence angle of 2 mrad the resolution of the probe degrades to roughly 1 nm.

The samples I studied with scanning tunneling microscopy were grown in the prep 2 sputtering growth chamber which has a base pressure of $\sim 2 \times 10^{-9}$ Torr. I used GaAs (100) chips that were first etched in ammonium hydroxide and then flash annealed in-situ [29] before CFB base electrodes were grown on them using dc sputtering. I grew the barrier layers directly on the CFB base electrodes using electron beam evaporation (as discussed in Chapter 3), lower rf sputtering power (100 W, 2" target; Power density ~ 4.9 W/cm²) to grow MgBO barriers (this is the same procedure used for the samples discussed in Chapter 3), or dc sputtering of Mg seed layers before rf sputtering MgO. Mg/MgO bilayer barriers, rf sputtered MgBO layers, and EBD MgO layers grown on the CFB electrodes were studied. I studied these samples before and after vacuum annealing in prep 2 in the connected STM chamber (Old BEEM) in ultra-high vacuum ($\sim 5 \times 10^{-10}$) Torr. I took current-voltage spectra at multiple spots on the sample surface approximated the density of states by taking dI/dV of the average from these spectra.

4.4 Electron Energy-Loss Spectroscopy Data from a Single Interface Sample

Clear evidence that a MgBO barrier material forms in an rf sputtered MgO layer grown on a B-alloyed ferromagnetic electrode is shown in Fig. 4.1, which displays

EELS spectroscopic images taken by Judy Cha from an annealed IrMn / CFB / MgO(10 nm) / Ta structure. The B spectral map and the RGB map both show that the first few nanometers of the barrier layer contain substantial B oxide content. Examples of the raw EELS spectra used to compose the 2D spectral map are shown in Fig. 4.2. The inset shows the 64 by 64 pixel spectrum image where each pixel contains an EEL spectrum. Two spectra from the spectrum image shown in Fig. 4.1 are plotted as examples. The spectrum taken near the CoFeB / barrier interface in Fig. 4.2 shows a clear B oxide signature, indicative of MgBO. In contrast, the O K-edge of the spectrum acquired deep in the MgO layer shows three clear peaks which is attributable to more bulk-like MgO. The shaded areas indicate the energy windows over which the EELS edges are integrated to obtain the relative concentration of each element, normalized to the maximum O intensity. The relative concentration of a particular element, for example B, to O is obtained by scaling the integrated intensity of B by $\sigma(O)/\sigma(B)$, where $\sigma(X)$ is the cross-section of X using the Hartree-Slater model. [30] The images in Fig. 4.1 are the concentration maps of Co, B, Mn, and Fe relative to O obtained using this procedure. These EELS data show that only at a thickness greater than ~ 2 nm does the stoichiometry and coordination of the oxide approach that of bulk MgO (Fig. 4.2). The Fe, Co, and Mn spectral maps in Fig. 4.1 demonstrate that the transitional MgBO layer also contains Fe, Co and Mn ions to varying degrees that surprisingly do not destroy TMR behavior of MgBO MTJs, as I will show in the following sections of this chapter.

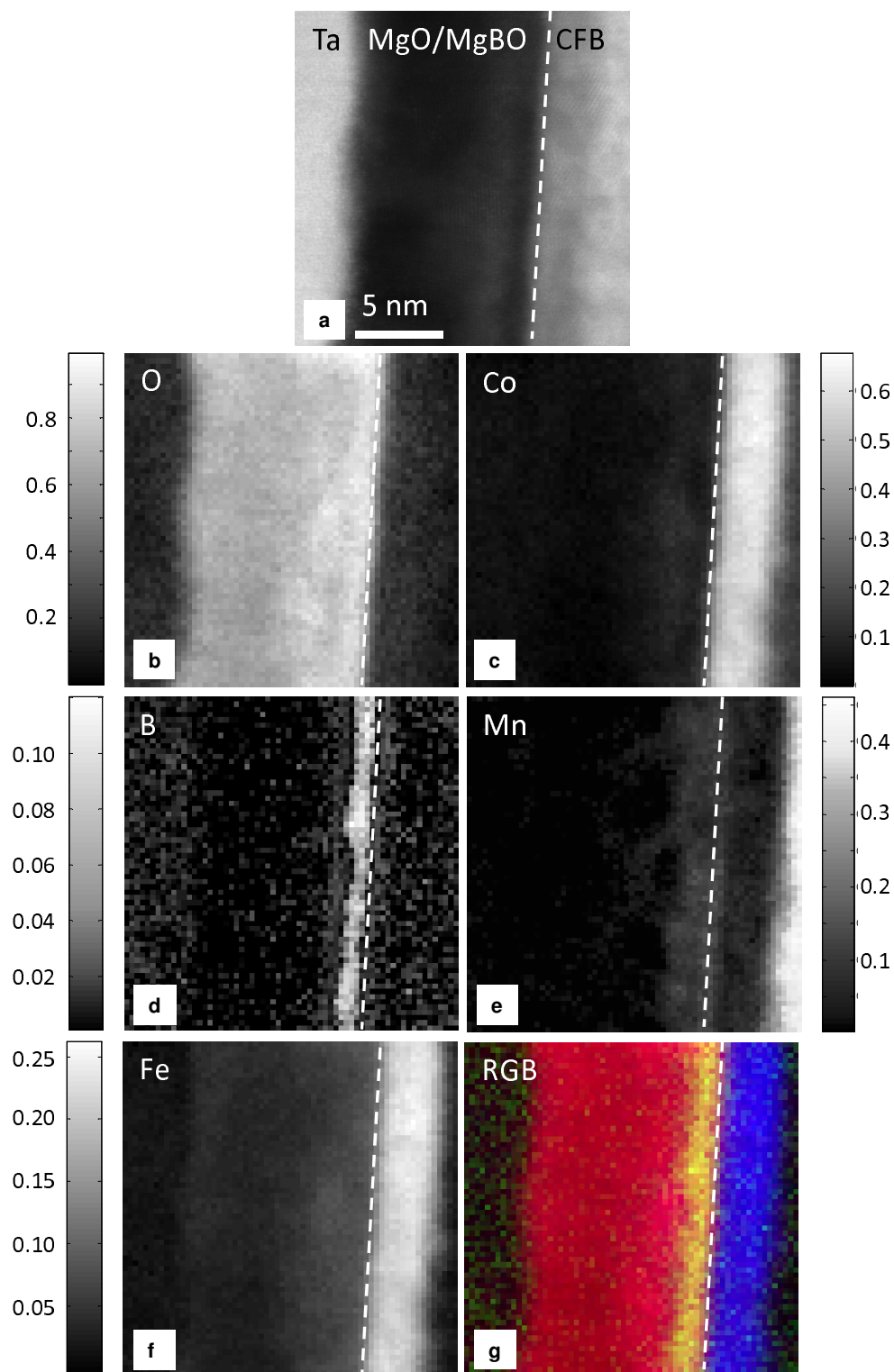


Figure 4.1: Spectroscopic images from an annealed IrMn / CFB / MgO(10 nm) / Ta structure (Figure courtesy of J. Cha).

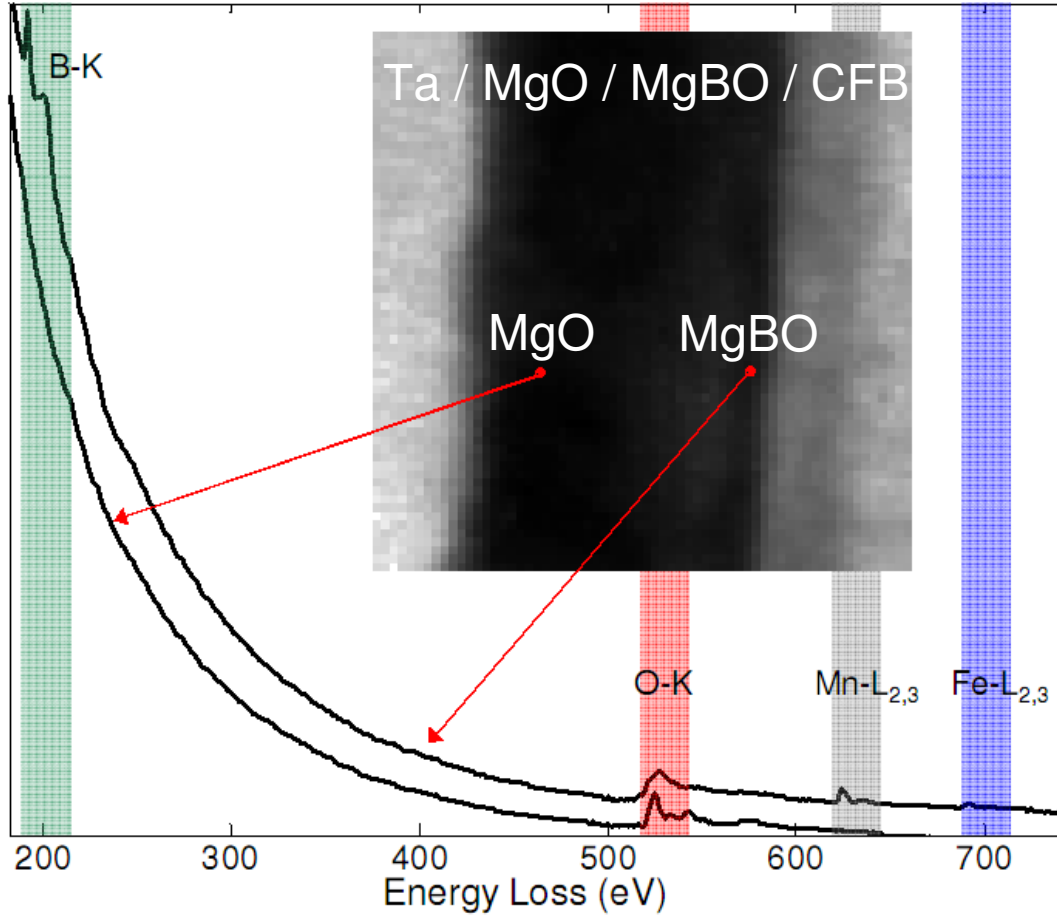


Figure 4.2: Individual EELS data from the MgBO and MgO regions of the annealed IrMn / CFB / MgO(10 nm) / Ta structure (Figure courtesy of J. Cha).

4.5 Electron Energy-Loss Spectroscopy Data from MgBO

MTJs

EELS data from completed MTJs confirm that for thin tunnel barriers formed by rf sputtering, electrode oxides are present at the two barrier interfaces, and the signature of B oxide is present within the barrier in both the as-deposited case and after annealing (Fig. 4.3). Upon annealing, some of the un-oxidized B in the electrode adjacent to the interface reduces the transition metal oxides at the

interface as a thermodynamic consequence of the structure. The relative heats of formation per oxygen atom for the primary oxides of interest are: $\Delta H_f^\circ_{B_2O_3/O} \sim -425$ kJ/mol $< \Delta H_f^\circ_{Fe_2O_3/O} \sim -275$ kJ/mol $< \Delta H_f^\circ_{FeO/O} \sim -272$ kJ/mol $< \Delta H_f^\circ_{Co_3O_4/O} \sim -223$ kJ/mol at 300K. [31] This does not dramatically change the B oxide component in the barrier and does not fully reduce all of the interfacial transition metal oxides. Also, during the annealing process the un-oxidized B within the electrode diffuses into the adjacent non-ferromagnetic film layers as the initially amorphous material crystallizes, as shown in Fig.4.4. Meanwhile, remaining un-reduced Fe, Co, and Mn cations can mix into the MgBO layer, presumably driven by strain and defects in the deposited MgBO layer.

Fig. 4.3 exhibits EELS data from the central region of the ~ 1.1 nm MgBO barrier in a CFB/MgBO/Py₉₅B₅ and a FCB/MgBO/Py₈₀B₂₀ junction, before and after annealing at 350 °C. The data are plotted together with data taken from a single crystal MgO sample for comparison. The Mg and O K-edge data indicate that the Mg and O coordination are not the same as in bulk MgO [26, 32], and there is little change in the spectra upon annealing, although the Mg spectrum does sharpen slightly for the FCB-Py₈₀B₂₀ sample. The Mg and O K edges from the CFB-Py₉₅B₅ sample are not as well formed. This is attributable to increased interfacial electrode oxide formation during growth and insufficient B content in the top electrode to reduce these oxides during the anneal. [24] For both sample structures the B K edge spectra show a sharp π^* peak near ~ 195 eV, indicative of B trigonally coordinated with O [33], which indicates the presence of BO₃ radicals that have mixed into the MgO during the growth process. After annealing, the intensity of the π^* peak is roughly the same (within the accuracy of the measurement) as in the as-deposited case for both sample structures. Comparison of the intensities of the B K-edge data with the O K-edge data taken from the central

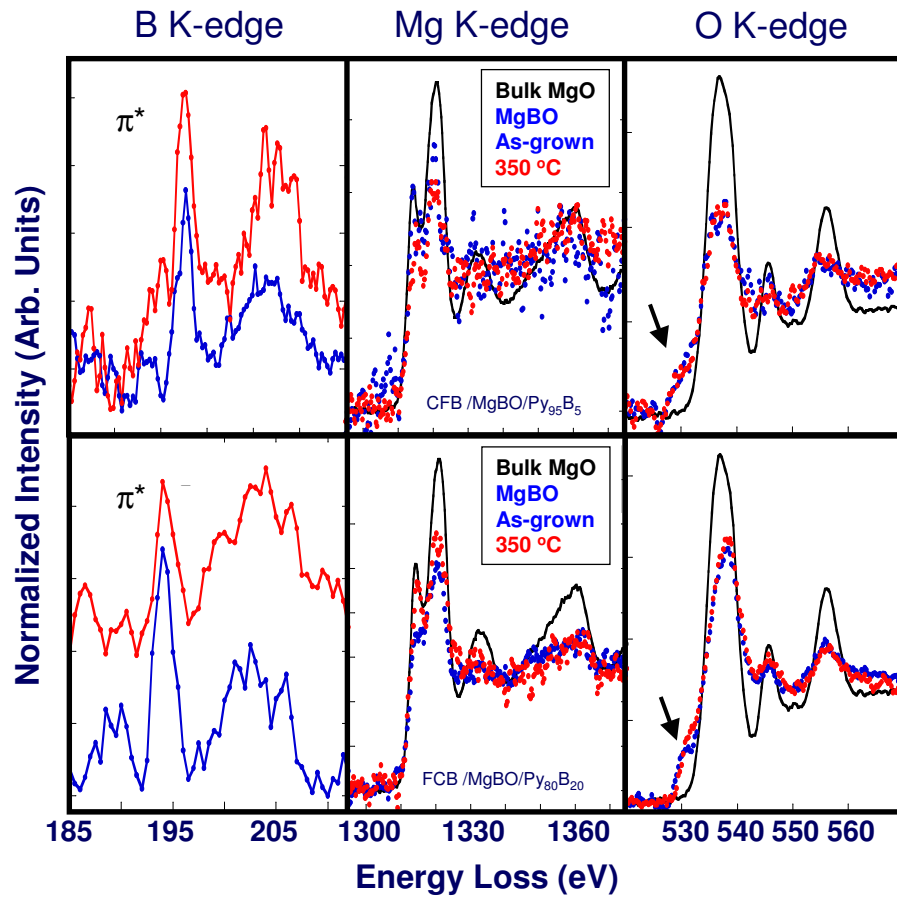


Figure 4.3: EELS data from as-grown and annealed CFB / 1.1nm MgBO / Py₉₅B₅ and CFB / 1.1nm MgBO / Py₈₀B₂₀ MTJ samples (data courtesy of J. Cha).

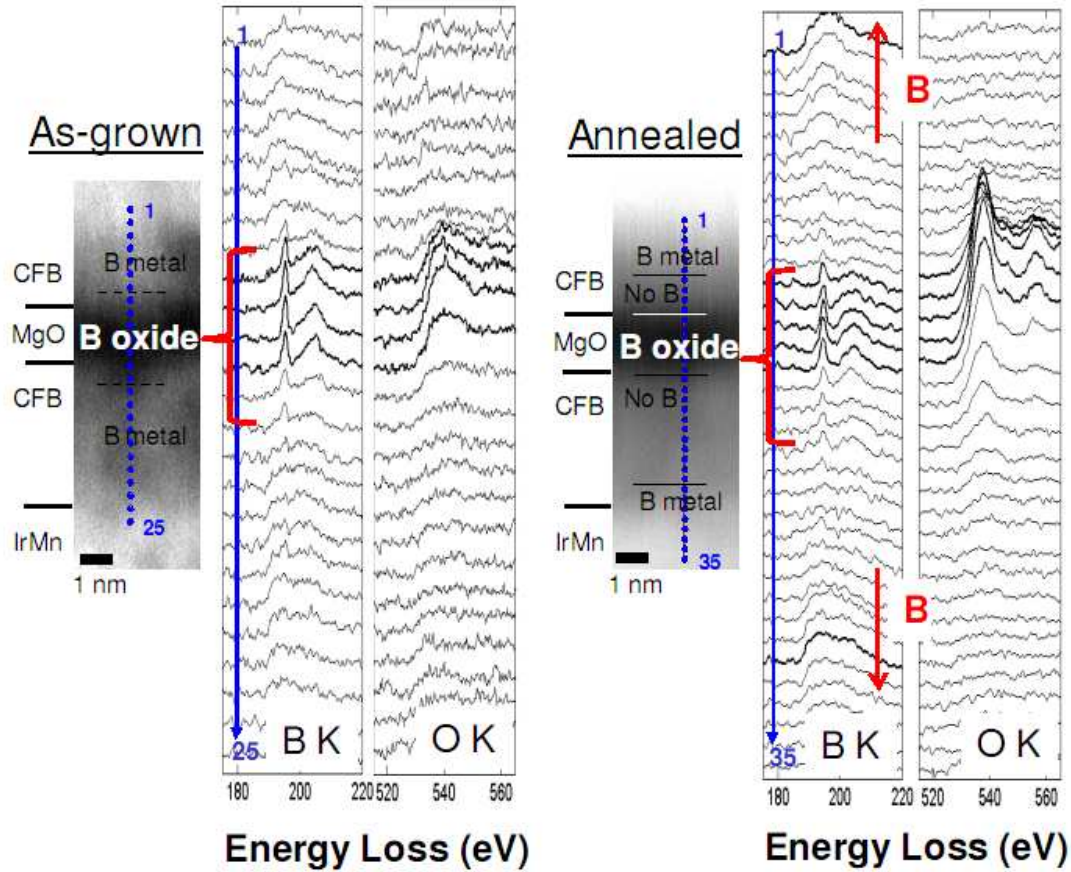


Figure 4.4: Multiple EELS data taken sequentially from one electrode to the other for as-grown and annealed versions of a CFB / 1.6nm MgBO / CFB MTJ (data courtesy of J. Cha).

region of the MgBO barrier gives an estimated relative concentration of B to O in the oxide of $\sim 0.08 \pm 0.02$ before and after annealing. The estimated relative concentration of Mg to O in the oxide is $\sim 0.67 \pm 0.1$. This yields an estimated barrier stoichiometry of $\text{Mg}_{0.38}\text{B}_{0.05}\text{O}_{0.57}$. [30] It is known that a mixture of MgO and B_2O_3 can react to form several Mg-B-O compounds which have trigonal coordination of oxygen to B [34], consistent with the EELS spectra. Finally, an interesting feature of the O spectrum is the presence of a pre-peak of low energy states below the expected O K-edge peak, as indicated by the arrows in Fig. 4.3. We attribute these pre-edge states before and after annealing to oxide disorder and

to BO_3 , FeO_x , CoO_x and MnO_x incorporation in the tunnel barrier.

The clear presence of B within the oxide tunnel barrier has interesting consequences with regards to annealing. Fig. 4.4 shows STEM annular dark field (ADF) images as well as B and O EELS K-edges from an as-grown and an annealed version of a CFB / 1.6 nm MgBO / CFB junction that shows 229% TMR with an RA product of $534 \Omega(\mu\text{m})^2$. Blue dots on the STEM-ADF images indicate the probe spots from which EEL spectra were acquired. The numbers 1-25 or 1-35 are the sequential EEL point spectra taken from the two samples. EELS data from the as-grown sample show that B oxide forms during growth, and that the O within this region of the barrier is significantly disordered as indicated by the O-K edge which has only one broad peak. For the annealed sample, the O K-edge data indicates the O in the barrier becomes better coordinated, as indicated by the presence of three peaks in the O K-edge, and the B oxide remains within the barrier. The boron in the alloy that is not oxidized in the film growth diffuses out of the electrodes into the adjacent non-ferromagnetic material as indicated by the B-depleted regions in the electrodes. It should be noted that the O K-edge line spectra shown in Fig 4.3 do not show a significant change in the O-O coordination upon annealing, unlike the samples measured here. We attribute this difference to the poly-crystallinity of the MgBO layer. Thus, in spot-mode, where the electron probe is focused to below one nm in diameter, scatter is present in the O K-edge. To avoid the issue of such scatter due to both the small probe diameter and the poly-crystalline nature of the MgBO barrier, the EEL spectra are mostly acquired in line mode where the probe rasters in a perpendicular fashion through the film layers as a line that is $\sim 4\text{-}5$ nm long parallel to the film layers during data acquisition, yielding a spatially averaged measurement.

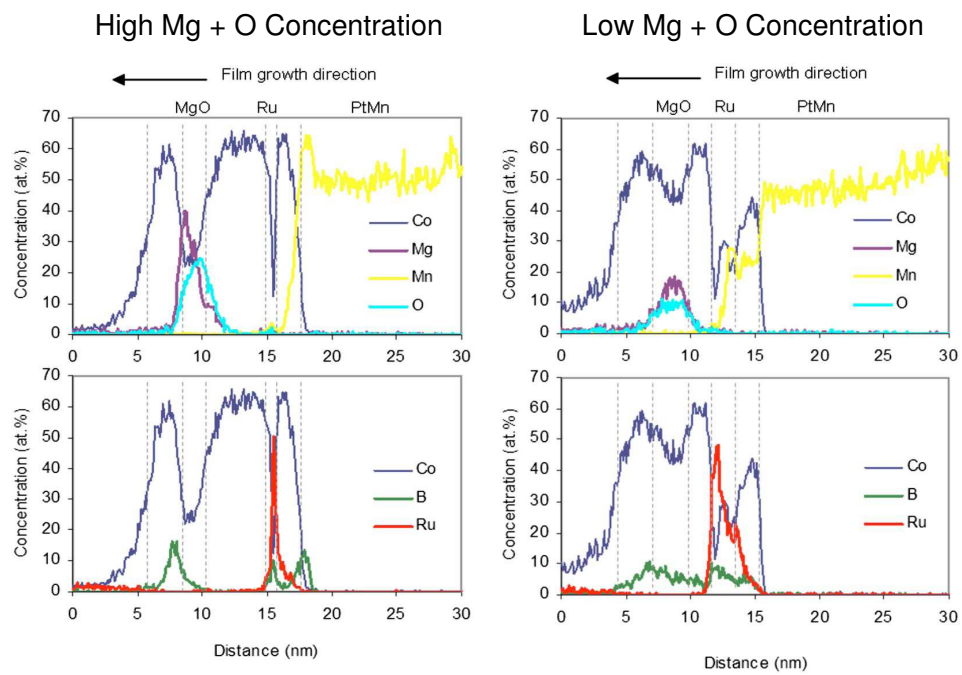


Figure 4.5: 3DAP studies of MgO MTJ structures showing B diffusion and segregation (from ref [25]).

Recently 3 dimensional atom probe (3DAP) studies of samples grown by the Hitachi Global Storage group suggest that B from the CoFeB alloy electrodes segregates at the MgO tunnel barrier interfaces. [25] 3DAP data from this study are shown in Fig. 4.5. The 3DAP data were taken from regions within the tunnel barrier that show high concentrations of Mg ($\sim 40\%$) and O ($\sim 24\%$) within the barrier and low concentrations of Mg ($\sim 18\%$) and O ($\sim 10\%$) within the barrier. Although the high concentration region data show some apparent segregation of B at the electrode - barrier interface, the low concentration data show B content approaching 10 % in the tunnel barrier, in agreement with our EELS studies. In addition, 3DAP has an experimental issue with regards to uniformity since the sample is made into a needle that is effectively evaporated. The evaporated material is measured with a mass spectrometer while the evaporation rate is measured. Assuming a uniform evaporation rate, the sample is reconstructed layer-by-layer to yield atomic resolution. However, with an insulating oxide, this is problematic since the material most likely does not evaporate uniformly. This may be what is apparent in the spatial maps presented by Pinitsoontorn and co-workers [25], which show a highly non-uniform distribution of Mg and O in the tunnel barrier of the MTJ structures they studied.

4.6 Scanning Tunneling Spectroscopy Data

The beneficial effect of the mixing of BO_3 into the MgO tunnel barrier has been observed with comparative in-situ ultra-high-vacuum STS measurements of the electronic structure of thin MgO layers grown on CFB electrodes by three different techniques. In Fig. 4. I present STS results obtained from a 2 nm EBD MgO layer, a 0.5 nm Mg/ 1.0 nm MgO bilayer, and a 2 nm MgBO layer, taken before

and after in-situ annealing. Each trace represents averaged STS data taken at multiple spots on the sample. In the EBD MgO case, wherein oxidation of the base electrode does not occur, the STS data indicates a band gap of ~ 3 eV with no band offset, but significant band-tailing to nearly the Fermi level (0 V), and there is only a small change, primarily in the band offset, upon annealing. Similar results were previously reported by Phil Mather using STS measurements of EBD MgO and dc-reactively sputtered Mg/MgO bilayers deposited on (001) Fe (Fig. 4.7). [29] As in the cited work, the small band gap and low energy band-tail states of EBD MgO on CFB can be attributed to lattice distortion and atomic defects in the crystalline MgO arising from strain at the oxide-electrode interface. This is supported by STS measurements of 3 nm EBD MgO layers that are sufficiently thick to relax the interfacial strain and show the full ~ 7.8 eV bulk MgO band gap (Fig. 4.7). [29]

When Mg/MgO bilayers are formed on CFB electrodes there is significantly less electrode oxidation than for rf sputtered MgO layers. [24] As-formed, the bilayer sample exhibits a relatively large bandgap, ~ 4 eV, as measured by STS, with markedly fewer band-tail states than EBD MgO. This can be attributed to the formation of nearly stoichiometric MgO through oxidation of the Mg layer during deposition. After annealing, the bandgap decreases only slightly, but the STS measurement indicates the development of band tail states that extend to close to the Fermi level. This suggests that there is insufficient BO_3 available to fully relax the strain between the now crystalline electrode and the barrier layer, which exhibits electronic band structure similar to that of an EBD MgO layer.

The STS data of the as-grown MgBO barrier material shows a relatively wide band gap (~ 4 eV), with a significant band offset. The higher band gap and

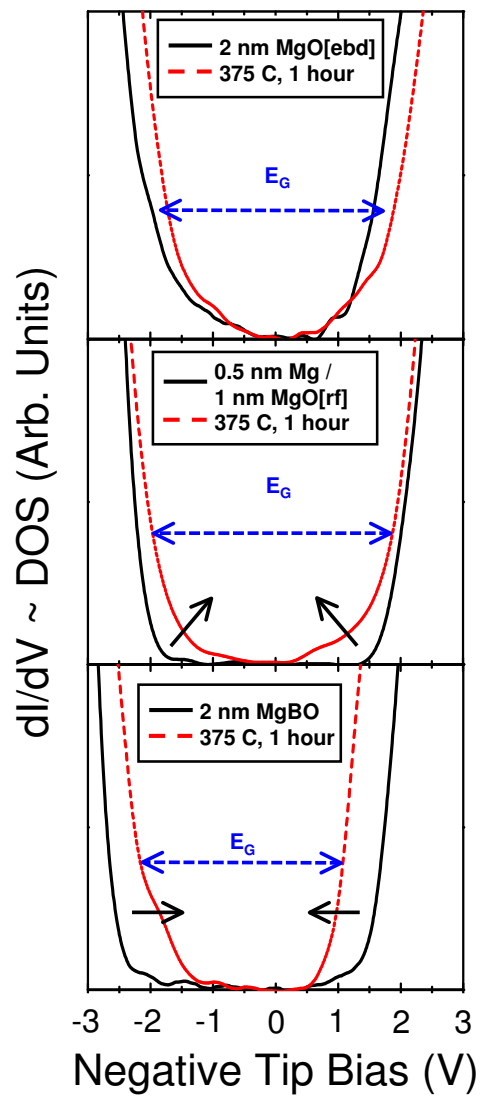


Figure 4.6: STS data taken from ebd grown MgO, sputtered bilayer Mg/MgO, and rf sputtered MgBO materials on CFB electrodes.

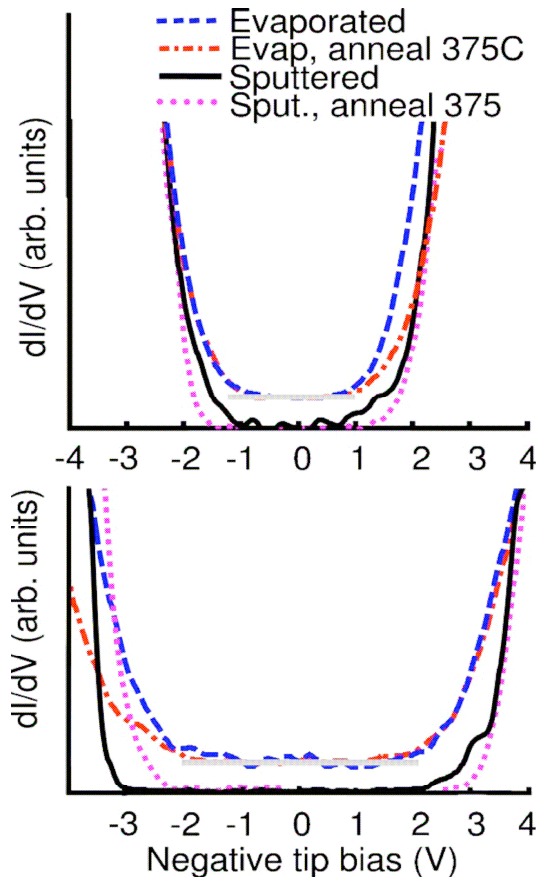


Figure 4.7: STS data taken from ebd grown MgO and sputtered bilayer Mg/MgO barriers on Fe electrodes (from ref[34]).

reduced band tailing in comparison to EBD MgO can be attributed to the strain reducing effect of the B oxide and the different electronic structure of MgBO versus MgO. The band offset is due to the change in barrier electronic band structure and electrode Fermi level pinning that arises from the formation of the MgBO adjacent to the electrode due to the high level of B oxide incorporation in the rf sputtering process. After annealing and the subsequent atomic rearrangement of the Mg, B, and O barrier species [24], the band gap shrinks substantially to ~ 2.5 eV, smaller than EBD MgO or Mg/MgO barriers, reflective of the change in the barrier physical and electronic structure. This result is consistent with calculations from Derek Stewart at CNF who's work currently suggests the barrier material is likely to be kotoite ($\text{Mg}_3\text{B}_2\text{O}_6$). [34, 35] The low but well defined band gap and the absence of a significant density of band tail states indicates that in the MgBO case there is a nearly optimal concentration of BO_3 in the barrier layer after annealing. While STS measurements of vacuum exposed MgBO layers do not necessarily precisely reveal the electronic structure of the tunnel barrier in a completed junction, the results certainly point to the reason why MgBO barriers are better than MgO barriers in the ultra-thin regime.

4.7 Comparison of MgBO and Mg/MgO MTJs

The CIPT data shown in the upper panel of Fig. 4.8 confirms that the formation of B oxide during the MTJ growth process positively influences the barrier spin-filtering properties. Although the as-grown TMR for these junctions is relatively low, as expected from the literature, there is a clear trend of increasing TMR with decreasing barrier thickness, in direct opposition to what is predicted by theoretical models of MgO MTJs. [15–17] This result can be attributed to advantageous spin-

filtering of the disordered, composite MgBO, which becomes more dominant as the overall barrier thickness decreases. However, it may also be that the thinner barriers have less detrimental interfacial oxide which degrades TMR.

Theoretical studies previously concluded that defect states at the electrode-tunnel barrier interface of ultra-thin MgO barriers decrease TMR through resonant tunneling of minority spin electrons through these interface states. This effect should increase with decreasing barrier thickness [36–38], assuming a constant density of such interfacial states. The formation of MgBO barriers may be suppressing the formation of such minority electron channels, as well as enhancing the magnetic coherency of the electrode surface [39], through suppression of the oxidation of the ferromagnetic elements when sufficient B is included in the electrode composition. However, the unpredicted barrier thickness dependence of TMR in as-grown MgBO-MTJs suggests that the role of the B oxide may be greater than simply suppressing defect formation and lowering the barrier height. In particular, induced ferromagnetism in the barrier oxide [40, 41], could be enhancing the spin-filtering of the ferromagnet-tunnel barrier interfaces.

The CIPT data in Fig. 4.8 show that MgBO barrier layers (formed by rf sputtering at a power density of $\sim 14.9 \text{ W/cm}^2$ while using a Mg getter) have quite different spin-filtering properties and variation of TMR with barrier thickness than Mg/MgO bilayer barriers. These data indicate that barriers formed by the Mg/MgO bilayer sputtering process, which reduces or eliminates the B oxide content in the barrier [24], yield substantially lower TMR and higher RA values than MgBO barriers of equivalent thickness. This result is consistent with earlier studies that sputtered MgO (chemically probably closer to MgBO) barriers work better than Mg/MgO (chemically probably closer to MgO) barriers (upper panel

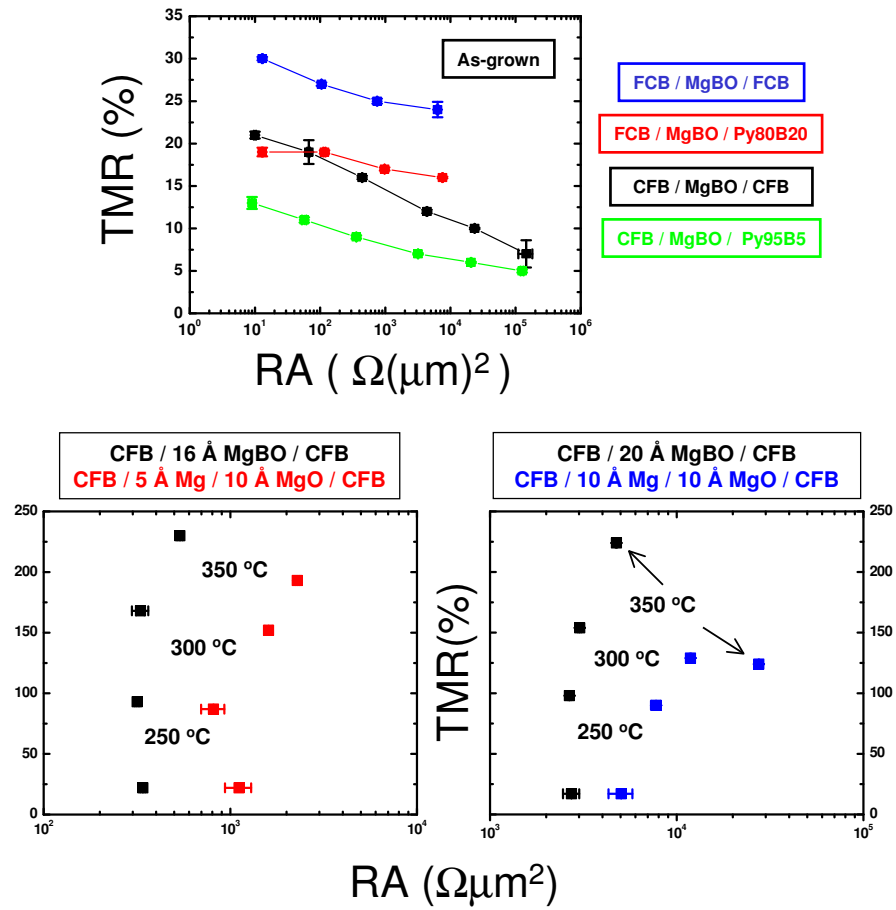


Figure 4.8: Comparative CIPT data from as-grown MgBO MTJs with different electrode combinations and from MTJs with MgBO and Mg/MgO tunnel barriers of similar thickness.

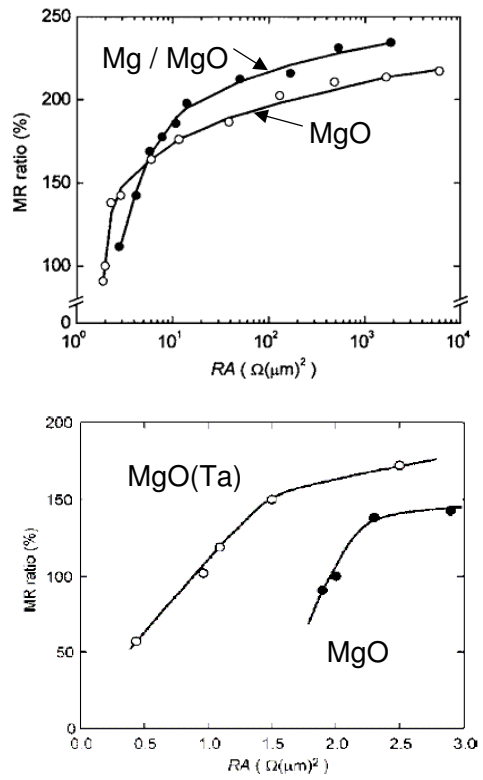


Figure 4.9: Transport data from ref [11] (upper panel) and ref [12] (lower panel) comparing various barrier deposition methods.

Fig. 4.9). [11] The Anelva team later found that use of Ta as a getter before barrier deposition provided the best results in terms of low RA and high TMR (lower panel Fig. 4.9). [12] However, this barrier material is also likely to be at least partially composed of MgBO as discussed in the previous chapter. [14] Other film studies show that lower TMR results after annealing from the use of a thicker Mg seed layer (see Fig. 4.10). These studies also show the presence of B oxide at the electrode-barrier interface or in the barrier itself. [23] The measurement of comparative TMR and RA for equivalent thickness MgBO and Mg/MgO barriers suggests that obtaining significant B oxide content in the tunnel barrier by rf sputtering of the MgO layer onto a B alloyed electrode is beneficial to spin-dependent tunneling through ultra-thin barriers.

STEM images, taken by Judy Cha, of two of the samples from which the data in Fig. 4.8 was taken are shown in Fig. 4.11 and Fig. 4.12. The images in Fig. 4.11 show that the MgBO growth process does not form crystalline barriers in either the as-grown or the annealed state. In fact, while annealing does appear to improve the electrode crystallinity of this CFB / 1.6nm MgBO / CFB structure, both top and bottom electrodes are polycrystalline or nanocrystalline at best showing regions of crystallized electrode material and regions of amorphous electrode material. In addition, there are some regions that show coherent crystallization from the bottom electrode through the barrier and into the top electrode. However, these regions are few and the image data suggest the tunneling transport in such a structure is not uniformly planar.

The image data in Fig. 4.12 of a CFB / 1 nm Mg / 1 nm MgO / CFB structure shows a substantial improvement in barrier crystallinity in the as-grown state in comparison with the MgBO barrier material shown in Fig. 4.11. Here the as-grown

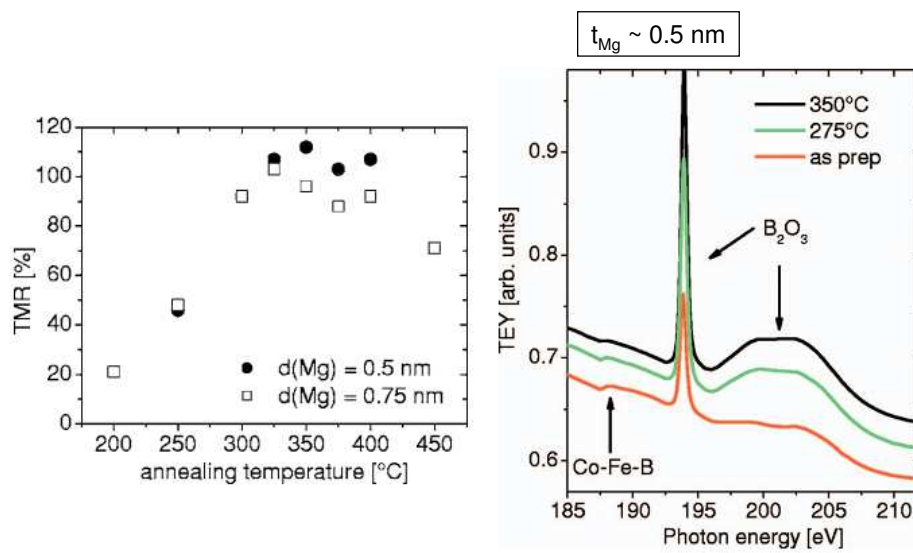
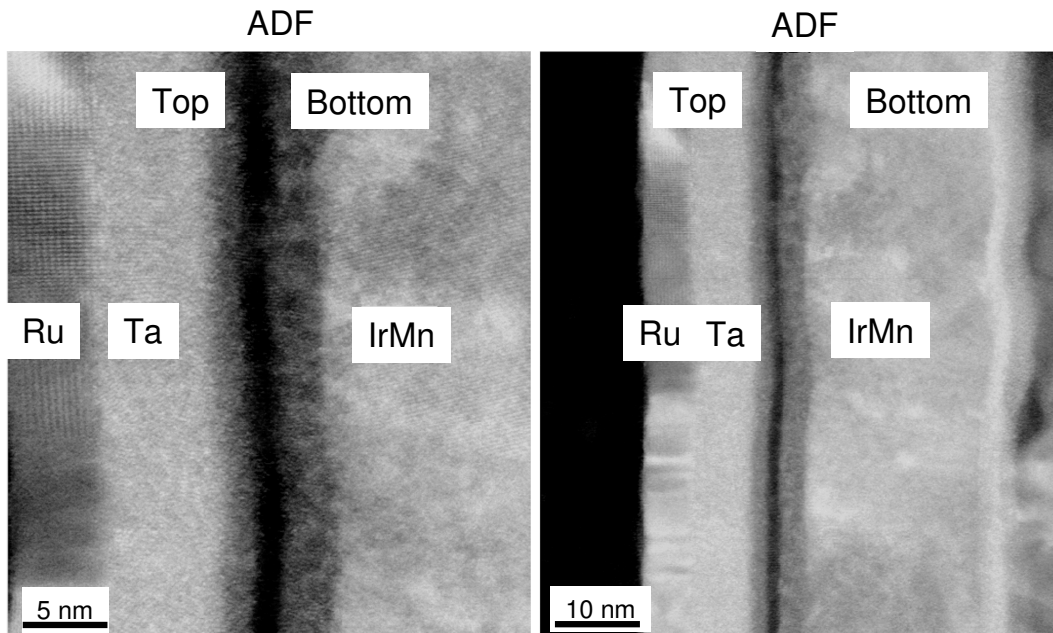


Figure 4.10: Transport data showing TMR response to annealing for different thickness Mg seed layers and X-ray absorption data from ref [23].

1.6nm MgBO As-grown: $RA \sim 340 \Omega\mu m^2$, $TMR \sim 22\%$



Annealed 350°C, 90 min: $RA \sim 534 \Omega\mu m^2$, $TMR \sim 229\%$

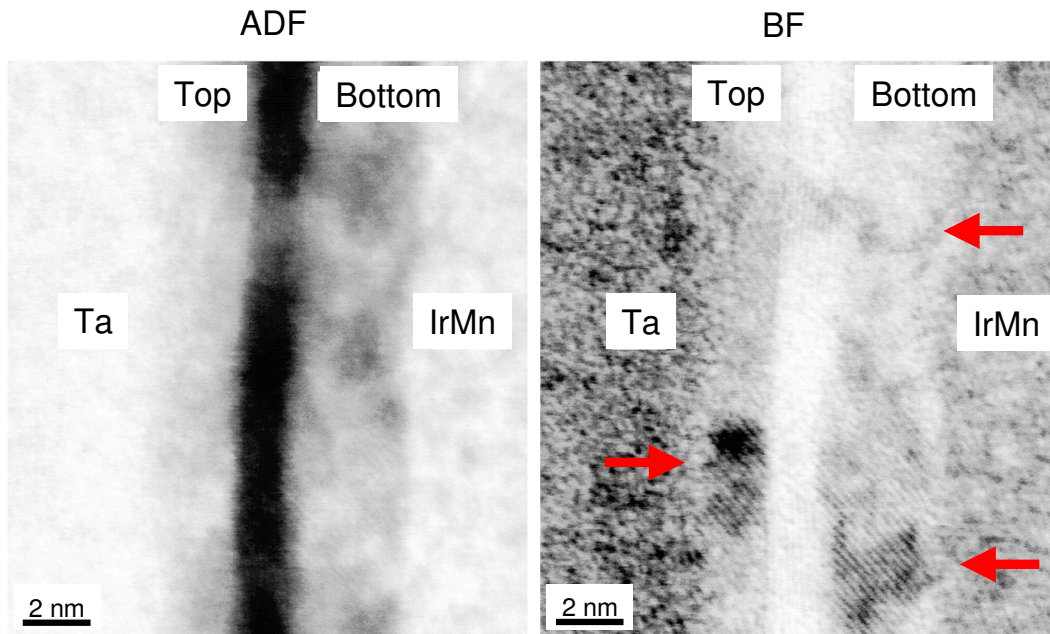


Figure 4.11: STEM images of a CFB/1.6nm MgBO/CFB MTJ structure before and after annealing (data courtesy of J. Cha).

barrier looks highly crystalline in some regions which confirms previous reports in the literature that use of such a Mg seed layer enhances MgO barrier crystal structure. [11] However, after annealing the degree of electrode crystallization is about the same or perhaps even less than in the case of the MgBO barrier sample. While the Mg/MgO barrier is more crystalline in the as-grown state, after annealing it does not appear more crystalline. Also, the top electrode - barrier interface appears more likely to crystallize coherently which raises the question as to whether some interfacial oxide formation during growth is in fact beneficial to the MTJ crystallization during annealing.

4.8 CIPT Studies

In addition to the initial CIPT studies discussed above, I investigated combinations of electrode alloys to see which materials combinations worked best with the MgBO barrier material. A comparison of the CIPT results from CFB/MgBO/CFB, FCB/MgBO/FCB, CFB/MgBO/Py₉₅B₅, and FCB/MgBO/Py₈₀B₂₀ MTJs is shown in Fig. 4.13. The as-grown data from this figure is shown in the upper panel in Fig. 4.8. After annealing, the TMR of the junctions increases dramatically as expected. The symmetric CFB and FCB junctions show the highest TMR in the 160-190% range after a 350°C anneal, and there is slight variation of TMR with thickness over the 1.1 to 1.7 nm range. Both of these structures achieve a TMR of $\sim 160\%$ with an RA product of $\sim 20 \Omega(\mu\text{m})^2$ for ~ 1.1 nm thick MgBO barriers.

The results for the CFB / MgBO / Py₉₅B₅ and FCB / MgBO / Py₈₀B₂₀ structures shown in Fig. 4.13 suggest that the B content in the free electrode alloys

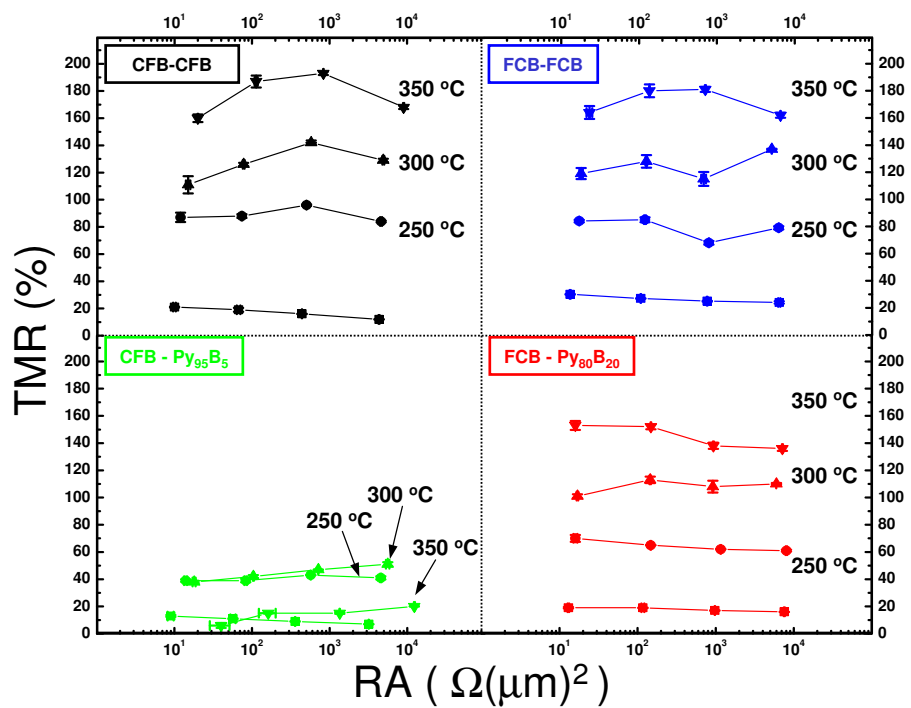


Figure 4.13: CIPT data from MgBO-MTJs with various electrode combinations and barrier thicknesses.

plays a significant role in the junction performance. The TMR of the Py_{95}B_5 free electrode junctions more than doubles to $\sim 40\%$ with moderate annealing (250 and 300°C), but drops back to $\sim 10\%$ after annealing at 350°C . The junctions with a $\text{Py}_{80}\text{B}_{20}$ free electrode show a steadily increasing TMR with annealing temperature reaching a maximum value of $\sim 155\%$ after annealing to 350°C . Both electrode combinations achieve relatively low RA values of $\sim 15 \Omega(\mu\text{m})^2$ in junctions incorporating a ~ 1.1 nm thick MgBO barrier layer after annealing to 350°C . While the lower B content PyB alloy electrode does not achieve very high TMR it may still be a useful material for switching and sensing structures. The higher B content PyB alloy electrode achieves device performance that nearly matches that of the CFB and FCB electrodes suggesting that this may be an ideal electrode material for MgBO MTJs.

A summary of the majority of the CIPT data taken to date is displayed in Fig. 4.14. To date the thinnest MgBO barriers formed are about 1.1 nm thick and can achieve relatively low RA with high TMR. While MgBO barriers using a Mg getter instead of a Ta getter clearly show higher TMR, it is not yet known whether or not the behavior will persist into the ultra-thin barrier regime. In addition, while the base electrode layers for each structure have been optimized in terms of smoothness (see Chapter 2), for CIPT measurements a low bottom electrode sheet resistance is required. It may be possible to form smoother electrode layers on different seed layer structures, like a Ta / Ru multi-layer, in MTJ structures that will be lithographically patterned. Also, the film grain structure may play a significant role in forming thinner MgBO barriers and may thus have a significant impact on device performance. These topics are certainly the focus of one thrust of the work that continues on these systems. The B-based alloys also show some interesting behavior in terms of orange peel coupling which is discussed below.

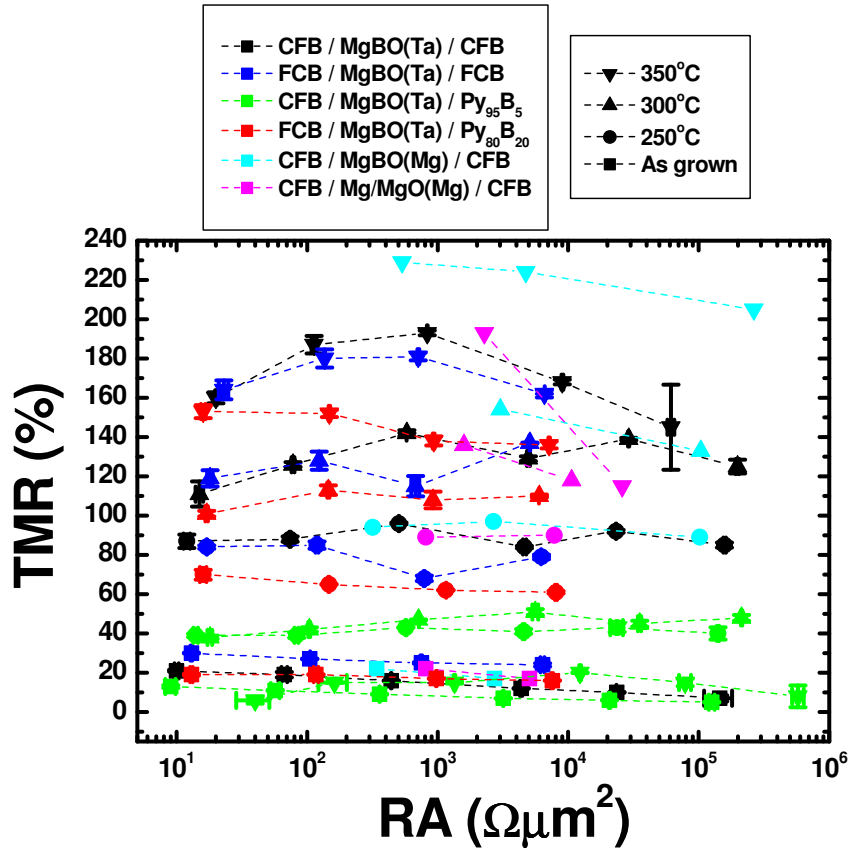


Figure 4.14: Summary of CIPT data from MgBO-MTJs with various electrode combinations, barrier thicknesses, and getter processes used during deposition.

With this enhancement and the possibility of forming even thinner barrier layers, lower RA product MTJs may be possible in structures with comparable or higher TMR values. However, the MTJs formed to date have RA values that are sufficient for STT switching and dynamics studies and the noise characteristics of these junctions are of great interest for possible sensor structures.

4.8.1 Discussion of RA vs. t Plots

The WKB approximation is sometimes used to estimate the electronic barrier height (energy difference between the junction Fermi level and the barrier conduction band minimum) of the tunnel barrier in MgO MTJs. [6] While this procedure provides an estimate of the energy barrier, it does not provide evidence of direct tunneling. In fact, several transport mechanisms will yield an exponential increase of barrier resistance with increasing barrier thickness and only detailed studies of the junction behavior as a function of bias voltage and temperature can give some clues about the nature of the electron transport in the MTJ, although such measurements do not give a unique interpretation. [42] However, comparison with previous work and with STS measurements warrants a quick diversion into the WKB approximation. Starting with the tunneling probability where k is the wave vector of a tunneling electron, \hbar is Planck's constant over 2π , m^* is the effective electron mass, E is the tunnel barrier energy gap, and the 1-D integral is taken over the barrier thickness.

$$T \sim \text{Exp} \left(-2 \int |k(x)| dx \right) \quad (4.1)$$

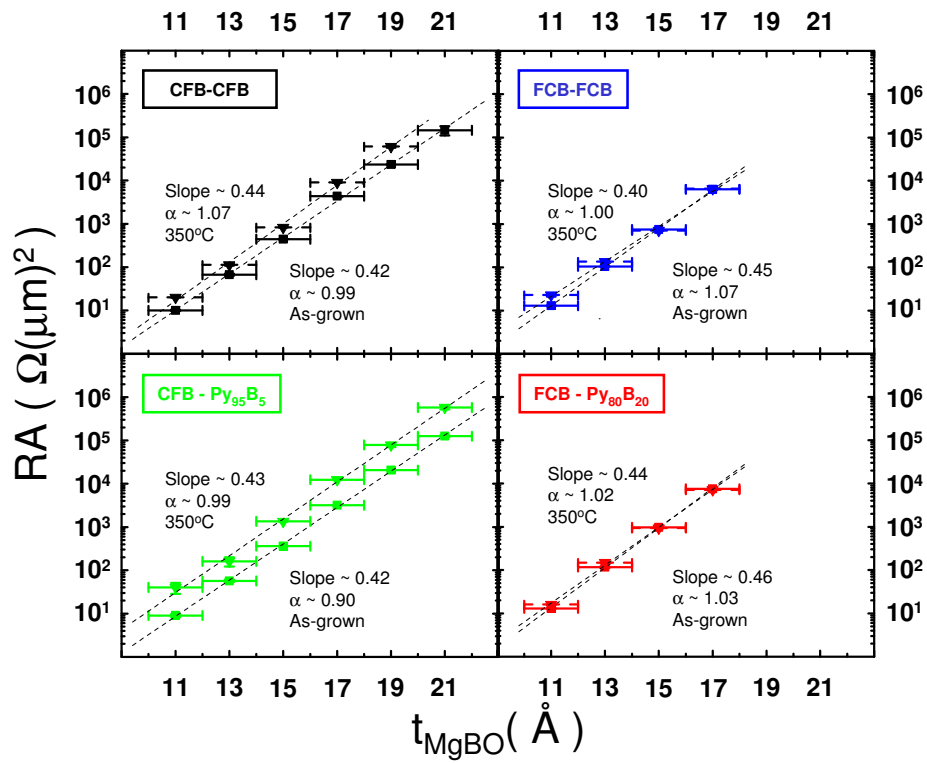


Figure 4.15: Semi-log plots of the data from Fig. 4.13 showing RA product as a function of tunnel barrier thickness.

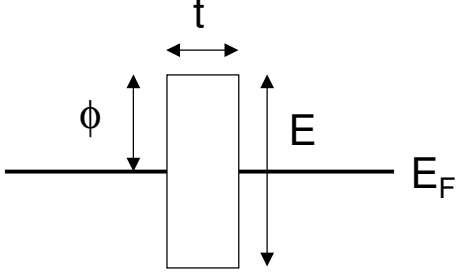


Figure 4.16: Schematic of an ideal tunnel barrier.

$$k(x) = \frac{\sqrt{2m^*E}}{\hbar} \quad (4.2)$$

This gives an estimate of the tunneling probability.

$$T \sim \text{Exp} \left(-2 \int \frac{\sqrt{2m^*E}}{\hbar} dx \right) = \text{Exp} \left(-\frac{\sqrt{8m^*E}}{\hbar} t \right) \quad (4.3)$$

This estimates the junction resistance (as tunneling probability goes down, junction resistance goes up, so the exponential is positive here).

$$R \sim \text{Exp} \left(\frac{\sqrt{8m^*E}}{\hbar} t \right) \quad (4.4)$$

Then estimate the junction RA product as a function of barrier thickness where the energy barrier height (ϕ) is estimated to be half of the energy gap (E).

$$RA(t) \sim \text{Exp} \left(\frac{\sqrt{16m^*\phi}}{\hbar} t \right) \quad (4.5)$$

If the data is plotted as $\log_{10}RA$ versus t (as in Fig. 4.15), then the slope of the data will yield some information about the barrier height in this approximation.

$$\text{Log}_{10}(RA(t)) = \frac{\ln(RA(t))}{\ln(10)} = \frac{1}{\ln(10)} \frac{\sqrt{16m^*\phi}}{\hbar} t \quad (4.6)$$

So the slope of a linear fit of such a plot has units of $\frac{1}{A}$.

$$\text{slope} = \frac{1}{\ln(10)} \frac{\sqrt{16m^*\phi}}{\hbar} \quad (4.7)$$

This can be used to estimate the barrier height in eV, assuming a free electron mass.

$$\phi = \frac{(\hbar \ln(10) \text{slope})^2}{16m^*} = 0.48(\ln(10) \text{slope})^2 = 2.52(\text{slope})^2 \quad (4.8)$$

An alternative approach is to simply fit the data to a simple exponential as in equation 4.5 with two fitting parameters, the amplitude (A) and the decay rate (α).

$$RA(t) = A \text{Exp}(\alpha t) \quad (4.9)$$

This fitting scheme also yields an estimate for the barrier height.

$$\phi = \frac{(\hbar \alpha)^2}{16m^*} = 0.48(\alpha)^2 \quad (4.10)$$

Using these two fitting schemes I can fit the data in Fig. 4.14 and estimate the barrier height of the MgBO material in the various MTJ structures. For the symmetric CFB structures, the barrier height is ~ 0.4 eV in the as-grown condition and ~ 0.5 eV after annealing to 350°C. For the symmetric FCB structures, the

barrier height is ~ 0.5 eV in the as-grown condition and ~ 0.4 eV after annealing to 350°C . The CFB/MgBO/Py₉₅B₅ structure has a barrier height of ~ 0.4 eV before and ~ 0.5 eV after annealing. Finally, the FCB/MgBO/Py₈₀B₂₀ structure has a constant barrier height of ~ 0.5 eV before and after annealing. While these estimates are certainly not the most accurate way to determine the barrier height, these values are all in rough agreement with what is observed with STS ($\phi \sim 0.5$ eV). Future transport studies will surely help clarify this issue with time.

4.9 TEM images of Ni-Fe-B Free Electrode Layers

The materials and transport studies discussed in the previous sections of this chapter show that higher B content in the PyB alloy electrodes is beneficial towards achieving high TMR in low RA MgBO MTJs. To investigate the influence of the increased B content on the crystal structure, Judy Cha has taken TEM images of the CFB / 1.1 nm MgBO / Py₉₅B₅ and FCB / 1.1 nm MgBO / Py₈₀B₂₀ structures before and after annealing. The TMR and RA values of these junctions is shown in Fig. 4.13. The CFB / 1.1 nm MgBO / Py₉₅B₅ MTJ has a TMR of $\sim 13\%$ before annealing which decreases to $\sim 6\%$ after annealing to 350°C , meanwhile the RA product changes from $\sim 9 \Omega(\mu\text{m})^2$ before annealing to $\sim 40 \Omega(\mu\text{m})^2$ after annealing. However, the FCB / 1.1 nm MgBO / Py₈₀B₂₀ MTJ has a TMR of $\sim 19\%$ before annealing which increases to $\sim 153\%$ after annealing to 350°C and the RA product changes only slightly from $\sim 13 \Omega(\mu\text{m})^2$ before annealing to $\sim 16 \Omega(\mu\text{m})^2$ after annealing.

The cross-sectional TEM imaging and nanometer spot size convergent beam electron diffraction (CBED) study shown in Fig. 4.17 clarify the structural reasons

for the successful use of $\text{Py}_{80}\text{B}_{20}$ as the free electrode in MgBO junctions and for the less successful results achieved with Py_{95}B_5 . The images of the two types of junctions show that the MgBO barriers are polycrystalline in both cases, but the electrodes exhibit quite different crystal structure. The Py_{95}B_5 electrode has some texturing in the as-grown case, but after annealing to 350°C becomes less textured as is clearly indicated by the CBED image. In contrast, the as-deposited $\text{Py}_{80}\text{B}_{20}$ electrode is amorphous, as expected for such a high concentration of the glass-forming B component [43], but after annealing to 350°C , the TEM and CBED measurements reveal that it has a highly textured (001) cubic crystal structure, which is optimal according to the theoretical coherent spin-dependent tunneling model. [15, 16]

The unsuccessful results for junctions using the Py_{95}B_5 free electrode arise from its low B content. This results in a polycrystalline electrode in the as-deposited case, due to the insufficient amount of the glass forming component, which remains polycrystalline after annealing. The low B content allows more oxidation of the ferromagnetic components of the PyB surface during growth due to reaction with surface oxygen on the MgO barrier. This also decreases BO_3 formation, so these junctions do not gain the beneficial tunnel barrier strain reduction upon annealing. In contrast, the use of a more B-rich, and initially amorphous $\text{Py}_{80}\text{B}_{20}$ top electrode is successful in forming a (001) textured cubic Py film upon annealing. This material provides sufficient B to both protect the Py components from oxidation and to mix in a significant amount of BO_3 into the top portion of the MgBO barrier during film growth promoting formation of low RA, high TMR MTJs.

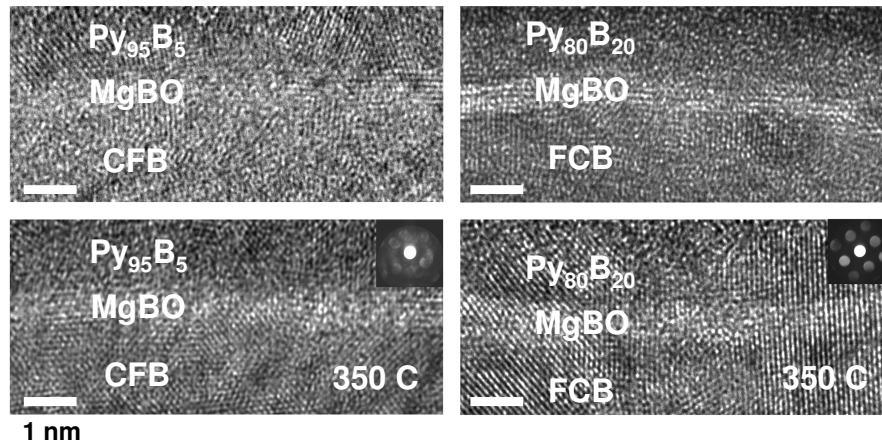


Figure 4.17: TEM images and CBED patterns (insets) of as-grown (AG) and annealed (A) MgBO MTJs using different PyB free electrode layers. (Figure courtesy of J. Cha).

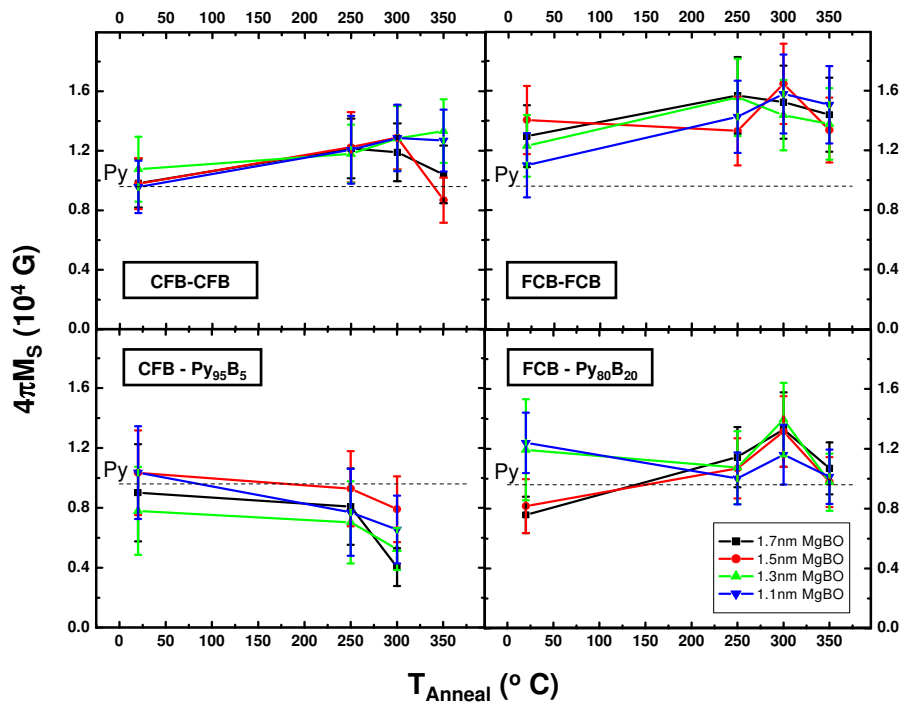


Figure 4.18: Measurements of free layer M_S values for MTJs with various electrode combinations as a function of annealing temperature.

4.10 M_S and H_C measurements

The previous sections of this chapter investigated the electronic, chemical, and structural properties of MgBO MTJs. Studies of the magnetic performance of the free layers also provide extremely useful information for device characterization and for optimization of future structures. The measurements of M_S as a function of anneal temperature yield some very interesting results. However, in order to fully appreciate the data a calibration of the measured values is required. The B-H loop used measures magnetic flux (Φ) which for the samples in this study has units of nWb. Bill Egelhoff measured a 10 nm thick Py film with a surface area of $\sim 1 \text{ cm}^2$, similar to the samples in this study, with both the loop and with a vibrating sample magnetometer (VSM) which measures magnetic flux density (B) which has units of G. The figure of merit I use here is the saturation magnetization, $4\pi M_S$, which has units of G. To get this, I use the fundamental relation $B = 4\pi M + H$. For these thin film samples, $4\pi M_S$ is on the order of 10^4 G while the applied field (H) is only swept from about -100 Oe to about 100 Oe. Therefore, $H \ll M$ and $B \approx 4\pi M$. To get from Φ_S to M_S I calibrate with the properties of the Py calibration sample. So for the measured samples, I use the following equation to convert the loop measurement of Φ_S into M_S .

$$4\pi M_{S,sample} = \Phi_{S,sample}(nWb) \left(\frac{B_{S,Py}(G)}{\Phi_{S,Py}(nWb)} \right) \left(\frac{V_{Py}(cm^3)}{V_{sample}(cm^3)} \right) \quad (4.11)$$

In the preceding equation, V_{Py} is the volume of the calibration Py film, and V_{sample} is the volume of the sample being measured. I measured the surface area of each sample, but the free electrode film thickness is an estimate based on TEM measurements from Judy Cha. Using elementary error propagation [44] it is easy to get

an estimate of the uncertainty of the measurement for M_S , which is shown in equations below. The largest contribution to the uncertainty in B is from the looper measurement itself, so the relative uncertainty is $(\frac{\sigma_B}{B}) \sim 3\text{-}5\%$. The uncertainty in the film volume contributes much more to the uncertainty in the measurement of M_S . For the film volume, the relative uncertainty is $(\frac{\sigma_V}{V}) \sim 16\%$, which is due primarily to uncertainty in the free layer thickness.

$$M = \frac{B}{V} \quad (4.12)$$

$$\sigma M^2 = \left(\frac{\partial M}{\partial B} \sigma_B \right)^2 + \left(\frac{\partial M}{\partial V} \sigma_V \right)^2 \quad (4.13)$$

$$\left(\frac{\sigma M}{M} \right)^2 = \left(\frac{\sigma_B}{B} \right)^2 + \left(\frac{\sigma_V}{V} \right)^2 \quad (4.14)$$

$$\sigma M = M \sqrt{\left(\frac{\sigma_B}{B} \right)^2 + \left(\frac{\sigma_V}{V} \right)^2} \quad (4.15)$$

The $4\pi M_S$ data from all the free electrode alloys is shown in Fig. 4.18. As expected from the literature [43], the saturation magnetization of CFB and FCB increases as B diffuses out of the electrodes during annealing. The measurements show that for moderate annealing (250°C), both PyB free electrodes have a $4\pi M_S$ comparable to that of Py ($4\pi M_S \sim 9600\text{ G}$), the dashed line in Fig. 4.18. However, the magnetization of the $\text{Py}_{80}\text{B}_{20}$ layer is, to within measurement accuracy, the same as that of Py and it does not change significantly with annealing. In this material, the increased B content prevents the formation transition metal oxides which are likely to be magnetically dead or antiferromagnetic. The magnetization

data suggest that after annealing, the B has diffused out of the electrode leaving a polycrystalline electrode with a magnetization similar to that of Py. In contrast, the magnetization of the Py_{95}B_5 electrode goes down as the annealing temperature increases, until after a 350°C anneal there is no magnetic response from the electrode. This is probably due to electrode oxidation, driven by the anneal, which forms an ever thicker magnetically dead layer.

The measurements of free layer H_C shown in Fig. 4.19 also provide interesting insights regarding the use of the various alloy free layers. The CFB free electrode samples show a moderate H_C of ~ 9 Oe for as-grown samples, which increases slightly after moderate annealing, but on average remains roughly constant for the entire annealing range. However, the H_C of FCB samples significantly decreases from ~ 12 to ~ 8 Oe after moderate annealing and then increases slightly at higher temperatures. The H_C behavior of the PyB electrodes is similar and appears to be somewhat dependent upon coupling to the base electrode. The Py_{95}B_5 electrode displays a roughly constant H_C of ~ 3 Oe for a moderate anneal, which increases slightly and then disappears after high temperature annealing. The H_C of the $\text{Py}_{80}\text{B}_{20}$ electrode, similar to the FCB electrode, decreases from ~ 9 Oe to ~ 6 Oe after moderate annealing and then increases slightly after high temperature treatment. For both PyB alloys, the lowest H_C values are observed for thin (~ 1.1 nm) MgBO barriers, suggesting the electrode coupling is beneficial in terms of magnetic softness in this barrier thickness range.

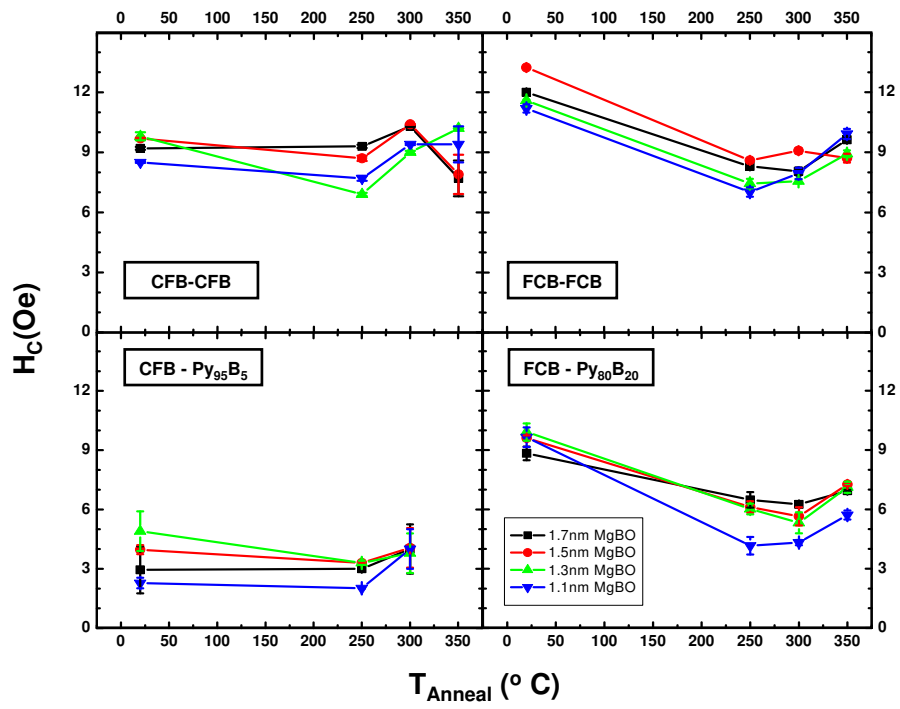


Figure 4.19: Measurements of free layer H_C values for MTJs with various electrode combinations as a function of annealing temperature.

4.11 Free Layer Coupling

Coupling between the free and fixed electrode layers shifts the center of the free layer magnetization loop from the origin by the amount of the coupling field strength. Neel or orange peel coupling, which occurs due to film roughness at the electrode - tunnel barrier interfaces in MTJs, can greatly influence the magnetic behavior of the free layer. This property tends to ferromagnetically couple the free layer to the fixed layer. This behavior is controlled by several physical properties of the MTJ, as shown in the cartoon in Fig. 4.20 (ref [45], where t_S is the free layer thickness, t_H is the fixed layer thickness, d is the tunnel barrier thickness, and both h and λ describe the interfacial roughness. These properties are related by the equation for the dipolar coupling field (equation 4.14), or exchange field (H_d), between the free and fixed layers, due to Kools and co-workers. [45, 46]

$$H_d = \frac{\pi^2 h^2 M_H}{\sqrt{2} \lambda t_S} e^{\left(\frac{-2\sqrt{2}\pi d}{\lambda}\right)} \left(1 - e^{\left(\frac{-2\sqrt{2}\pi t_S}{\lambda}\right)}\right) \left(1 - e^{\left(\frac{-2\sqrt{2}\pi t_H}{\lambda}\right)}\right) \quad (4.16)$$

M_H is the magnetization of the fixed layer and this equation is highly useful with regards to understanding the coupling that occurs for different barrier thicknesses and the changes that occur after annealing since each of the quantities in the equation is measurable.

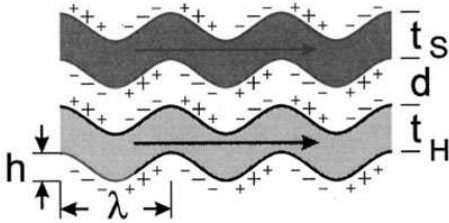


Figure 4.20: Schematic of orange peel coupling in an MTJ (from ref[44]).

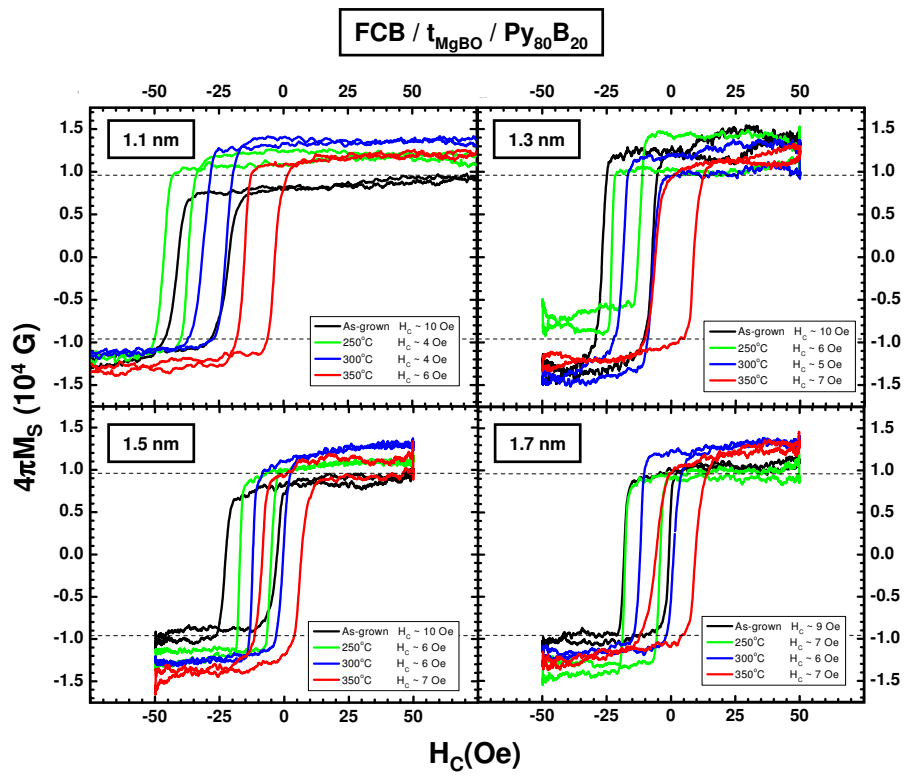


Figure 4.21: Magnetization loops of $\text{Py}_{80}\text{B}_{20}$ free layers as a function of MgBO barrier thickness and annealing temperature.

The magnetization loops in Fig. 4.21 show how the coupling changes for MgBO MTJs with $\text{Py}_{80}\text{B}_{20}$ free layers and FCB fixed layers. As the barrier gets thinner, the coupling is stronger, but for barriers thicker than 1.1 nm the coupling can be almost completely eliminated after annealing to 350°C . Such behavior was observed by Dave and co-workers, who measured an exchange field on the order of 2-5 Oe after annealing to 350°C in MgO MTJs with NiFe free layers that exhibited $\sim 90\%$ TMR with an RA product of $\sim 1\text{-}5 \text{ k}\Omega(\mu\text{m})^2$. [13] The MgBO MTJs with $\text{Py}_{80}\text{B}_{20}$ free layers and barriers thicker than 1.1 nm in my study achieve nearly the same coupling behavior ($\sim 1\text{-}3$ Oe after annealing to 350°C) with significant improvements in TMR and RA. Although the coupling field is dramatically reduced by annealing, some of the coupling strength (~ 10 Oe) in the MTJ with the thinnest (1.1 nm) MgBO barrier is still present even after annealing to 350°C .

Figure 4.22 compares the coupling in various MTJ structures as a function of MgBO barrier thickness (1.1-1.7 nm) and annealing temperature. The trend of the data is similar for all the systems, but samples with FCB base electrodes show a greater decrease in coupling as they are annealed. While interfacial roughness certainly plays a role in the coupling, electrode oxidation and subsequent oxide reduction during annealing could contribute to the reduced coupling after annealing. However, the templating effect of the MgBO barrier upon the B-rich alloys during annealing may significantly decrease the effective interfacial roughness. We can use equation 4.14 to provide an estimate of the scale of the effect which will help determine what the dominant mechanism is for the reduced coupling. From the previous section, the saturation magnetization of the FCB material is roughly $\sim 1.42 \times 10^4$ G, and the fixed layer and free layer thicknesses are 4.0 and 2.5 nm respectively. For a barrier thickness of 1.1 nm using the measured values of H_d , λ , the wavelength of the interfacial roughness, needs to be on the order of 8 nm

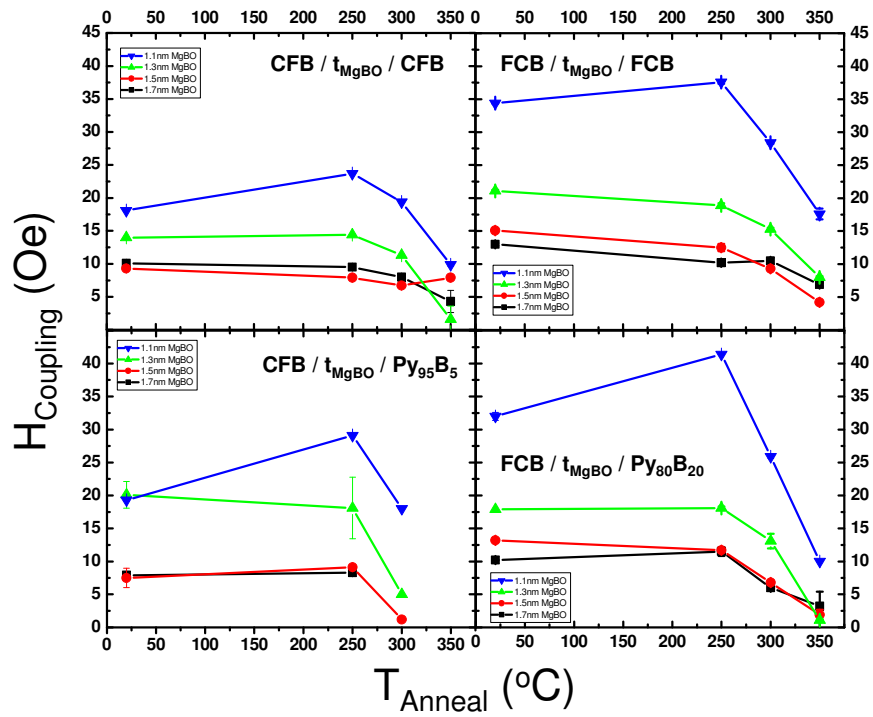


Figure 4.22: Free layer coupling field measurements of MTJs as a function of MgBO barrier thickness (1.1-1.7 nm) and annealing temperature.

to yield changes in h , the amplitude of the interfacial roughness, that are reasonable. For $\lambda \sim 8$ nm, the changes in h for each annealing step are 2-6 Å, which is a significant fraction of the barrier thickness. This suggests that oxide reduction may be playing a more significant role in changing the electrode coupling in these MgBO MTJs.

Upon 350 °C annealing, the coupling decreases in all samples, with the most pronounced decrease apparent in FCB/MgBO/Py₈₀B₂₀ MTJs. After annealing, these MTJs with barrier thicknesses ~ 1.1 nm, exhibit a coupling field of ~ 2.5 Oe which is indicative of very magnetically smooth junctions. However, the coupling is higher (~ 10 Oe) for MTJs with 1.1 nm barriers, which is likely due to the onset of significant ferromagnetic interlayer exchange coupling. [47]

4.12 Summary and Conclusions

In summary, rf sputtering of MgO in conjunction with B alloyed ferromagnetic electrodes results in the formation of MgBO tunnel barriers that create barriers that have good spin-filtering capabilities in the ultra-thin barrier limit. Upon annealing, trigonal BO₃ is still evident within the MgBO layer and the resultant tunnel barrier has an electronic band gap that is smaller than that of an MgO layer of the same thickness, but with fewer low energy defect states that can provide minority spin tunneling channels. The result is quite high TMR in annealed MgBO MTJs, which is nearly thickness independent in the ultra-thin regime until pinholes begin to shunt the tunnel barrier. By employing Py₈₀B₂₀ free layers, I have been able to produce MTJs that also show little dependence of TMR upon RA. The Py₈₀B₂₀ electrodes are amorphous as deposited, but allow the MgBO

barrier to template a cubic crystal structure during annealing. These high B content PyB alloys also show good magnetic behavior, with M_S values similar to that of Py, small H_C values, and significant reduction of magnetic coupling with annealing. These results demonstrate that magnetically soft Py electrodes can be successfully incorporated in high performance MTJs for both MRAM and field sensing applications.

REFERENCES

- [1] www.everspin.com.
- [2] P. M. Braganca, I. N. Krivorotov, O. Ozatay, A. G. F. Garcia, N. C. Emley, J. C. Sankey, D. C. Ralph, and R. A. Buhrman, Reducing the critical current for short-pulse spin-transfer switching of nanomagnets., *Appl. Phys. Lett.* **87**, 112507 (2005).
- [3] J. Z. Sun, Spin-current interaction with a monodomain magnetic body: A model study, *Phys. Rev. B* **62**, 570–578 (2000).
- [4] T. Linn and D. Mauri, Method of forming a barrier layer of a tunneling magnetoresistive sensor, United States Patent 6841395, International Business Machines Corporation, Armonk, NY, US (2005).
- [5] S. S. P. Parkin, C. Kaiser, A. Panchula, P. M. Rice, B. Hughes, M. Samant, and S.-H. Yang, Giant tunnelling magnetoresistance at room temperature with MgO (100)tunnel barriers, *Nature Materials* **3**, 862–867 (2004).
- [6] S. Yuasa, T. Nagahama, A. Fukushima, Y. Suzuki, K. Ando, Giant room-temperature magnetoresistance in single-crystal Fe/MgO/Fe magnetic tunnel junctions, *Nature Materials* **3**, 868–871 (2004).
- [7] S. Ikeda, J. Hayakawa, Y. Ashizawa, Y. M. Lee, K. Miura, H. Hasegawa, M. Tsunoda, F. Matsukura, and H. Ohno, Tunnel magnetoresistance of 604% at 300 K by suppression of Ta diffusion in CoFeB/MgO/CoFeB pseudo-spin-valves annealed at high temperature, *Appl. Phys. Lett.* **93**, 082508 (2008).
- [8] Y. M. Lee, J. Hayakawa, S. Ikeda, F. Matsukura, and H. Ohno, Giant tunnel magnetoresistance and high annealing stability in CoFeB/MgO/CoFeB magnetic tunnel junctions with synthetic pinned layer., *Appl. Phys. Lett.* **90**, 212507 (2007).
- [9] S. Yuasa, A. Fukushima, H. Kubota, Y. Suzuki, and K. Ando, Giant tunneling magnetoresistance up to 410% at room temperature in fully epitaxial Co/MgO/Co magnetic tunnel junctions with bcc Co(001) electrodes, *Appl. Phys. Lett.* **89**, 042505 (2006).
- [10] D. D. Djayaprawira, K. Tsunekawa, M. Nagai, H. Maehara, S. Yamagata, N. Watanabe, S. Yuasa, Y. Suzuki, and K. Ando, 230% room-temperature

- magnetoresistance in CoFeB/MgO/CoFeB magnetic tunnel junctions, *Appl. Phys. Lett.* **86**, 092502 (2005).
- [11] K. Tsunekawa, D. D. Djayaprawira, M. Nagai, H. Maehara, S. Yamagata, N. Watanabe, S. Yuasa, Y. Suzuki, and K. Ando, Giant tunneling magnetoresistance effect in low-resistance CoFeB/MgO(001)/CoFeB magnetic tunnel junctions for read-head applications, *Appl. Phys. Lett.* **87**, 072503 (2005).
- [12] Y. Nagamine, H. Maehara, K. Tsunekawa, D. Djayaprawira, N. Watanabe, S. Yuasa, and K. Ando, Ultralow resistance-area product of $0.4 \Omega(\mu\text{m})^2$ and high magnetoresistance above 50% in CoFeB/MgO/CoFeB magnetic tunnel junctions, *Appl. Phys. Lett.* **89**, 162507 (2006).
- [13] R. W Dave, G. Steiner, J. M. Slaughter, J. J. Sun, B. Graigo, S. Pietambaram, K. Smith, G. Grynkewich, M. DeHerrera, J. Akerman, and S. Tehrani, MgO-based tunnel junction material for high-speed toggle magnetic random access memory, *IEEE Trans. Magn.* **42**, 1935 (2006).
- [14] Y. S. Choi, Y. Nagamine, K. Tsunekawa, H. Maehara, D. D. Djayaprawira, S. Yuasa, and K. Ando, Effect of Ta getter on the quality of MgO tunnel barrier in the polycrystalline CoFeB/MgO/CoFeB magnetic tunnel junction, *Appl. Phys. Lett.* **90**, 012505 (2007).
- [15] W. H. Butler, X. -G. Zhang, T. C. Schulthess, and J. M. MacLaren, Spin-dependent tunneling conductance of Fe—MgO—Fe sandwiches., *Phys. Rev. B* **63**, 054416 (2001).
- [16] J. Mathon, and A. Umerski, Theory of tunneling magnetoresistance of an epitaxial Fe/MgO/Fe(001) junction., *Phys. Rev. B* **63**, 220403(R) (2001).
- [17] X. G. Zhang, W. H. Butler, and A. Bandyopadhyay, Effects of the iron-oxide layer in Fe-FeO-MgO-Fe tunneling junctions., *Phys. Rev. B* **68**, 092402 (2003).
- [18] X. G. Zhang and W. H. Butler, Large magnetoresistance in bcc Co/MgO/Co and FeCo/MgO/FeCo tunnel junctions., *Phys. Rev. B* **70**, 172407 (2004).
- [19] S. Yuasa, Y. Suzuki, T. Katayama, and K. Ando, Characterization of growth and crystallization processes in CoFeB/MgO/CoFeB magnetic tunnel junction structure by reflective high-energy electron diffraction, *Appl. Phys. Lett.* **87**, 242503 (2005).

- [20] C. Heiliger, M. Gradhand, P. Zahn, and I. Mertig, Tunneling Magnetoresistance on the Subnanometer Scale., *Phys. Rev. Lett.* **99**, 066804 (2007).
- [21] J. Z. Sun and D. C. Ralph, Magnetoresistance and spin-transfer torque in magnetic tunnel junctions., *J. Magn. Magn. Mater.* **320**, 1227–1237 (2008).
- [22] J. Bae, W. Lim, H. Kim, T. Lee, K. Kim, and T. Kim, Compositional change of MgO barrier and interface in CoFeB/MgO/CoFeB tunnel junction after annealing, *J. Appl. Phys.* **99**, 08T316 (2006).
- [23] J. Schmalhorst, A. Thomas, G. Reiss, X. Kou, and E. Arenholz, Influence of chemical and magnetic interface properties of Co-Fe-B/MgO/Co-Fe-B tunnel junctions on the annealing temperature dependence of the magnetoresistance., *J. Appl. Phys.* **102**, 053907 (2007).
- [24] J. C. Read, P. G. Mather, and R. A. Buhrman, X-ray photoemission study of CoFeB/MgO thin film bilayers, *Appl. Phys. Lett.* **90**, 132503 (2007).
- [25] S. Pinitsoontorn, A. Cerezo, A. K. Petford-Long, D. Mauri, L. Folks, and M. J. Carey, Three-dimensional atom probe investigation of boron distribution in CoFeB/MgO/CoFeB magnetic tunnel junctions, *Appl. Phys. Lett.* **93** (2008).
- [26] J. J. Cha, J. C. Read, R. A. Buhrman, D. A. Muller, Spatially resolved electron energy-loss spectroscopy of electron-beam grown and sputtered CoFeB/MgO/CoFeB magnetic tunnel junctions, *Appl. Phys. Lett.* **91**, 062516 (2007).
- [27] D. C. Worledge and P. L. Trouilloud, Magnetoresistance measurement of unpatterned magnetic tunnel junction wafers by current-in-plane tunneling., *Appl. Phys. Lett.* **83**, 84 (2003).
- [28] D. A. Muller, L. Fitting Kourkoutis, M. Murfitt, J. H. Song, H. Y. Hwang, J. Silcox, N. Dellby, and O. L. Krivanek, Atomic-Scale Chemical Imaging of Composition and Bonding by Aberration-Corrected Microscopy., *Science* **319**, 1073–1076 (2008).
- [29] P. G. Mather, J. C. Read, and R. A. Buhrman, Disorder, defects, and band gaps in ultrathin (001) MgO tunnel barriers., *Phys. Rev. B.* **73**, 205412 (2006).
- [30] J. J. Cha, Ph.D. thesis, Cornell University (2009).

- [31] D. R. Lide, ed., "Standard Thermodynamic Properties of Chemical Substances" in *CRC Handbook of Chemistry and Physics, 88th Edition*, CRC Press/Taylor and Francis, Boca Raton, FL. (Internet Version 2008).
- [32] Th. Lindner, H. Sauer, W. Engel, and K. Kambe, Near-edge structure in electron-energy-loss spectra of MgO., *Phys. Rev. B.* **33**, 22 (1986).
- [33] H. Sauer, R. Brydson, P. N. Rowley, W. Engel, and J. M. Thomas, Determination of coordinations and coordination-specific site occupancies by electron-energy-loss spectroscopy: an investigation of B-oxygen compounds., *Ultramicroscopy* **49**, 198–209 (1993).
- [34] T. Mutluer and M. Timucin, Phase Equilibria in the system MgO-B₂O₃., *J. Am. Ceram. Soc.* **58**, 196–197 (1975).
- [35] D. A. Stewart, unpublished.
- [36] K. D. Belashchenko, J. P. Velev, and E. Y. Tsymbal, Effect of interface states on spin-dependent tunneling in Fe/MgO/Fe tunnel junctions., *Phys. Rev. B.* **72**, 140404(R) (2005).
- [37] J. P. Velev, M. Ye Zhuravlev, K. D. Belashchenko, S. S. Jaswal, E. Y. Tsymbal, T. Katayama, and S. Yuasa, Defect-mediated properties of Magnetic Tunnel Junctions., *IEEE Trans. Mag.* **43**, 2770–2775 (2007).
- [38] E. Y. Tsymbal, K. D. Belashchenko, J. P. Velev, S. S. Jaswal, M. van Schilfgaarde, I. I. Oleynik, and D. A. Stewart, Interface effects in spin-dependent tunneling., *Prog. Mat. Sci.* **52**, 401–420 (2008).
- [39] E. Negusse, A. Lussier, J. Dvorak, Y. Idzerda, S. R. Shinde, Y. Nagamine, S. Furukawa, K. Tsunekawa, and D. D. Djayaprawira, Magnetic characterization of CoFeB/MgO and CoFe/MgO interfaces., *Appl. Phys. Lett.* **90**, 092502 (2007).
- [40] I. S. Elfimov, S. Yunoki, and G. A. Sawatsky, Possible Path to a New Class of Ferromagnetic and Half-Metallic Ferromagnetic Materials., *Phys. Rev. Lett.* **89**, 216403 (2002).
- [41] J. Osorio-Guillen, S. Lany, S. V. Barabash, and A. Zunger, Magnetism without Magnetic Ions: Percolation, Exchange, and Formation Energies of Magnetism-Promoting Intrinsic Defects in CaO., *Phys. Rev. Lett.* **96**, 107203 (2006).

- [42] C. W. Miller, Z.-P. Li, I. K. Schuller, R. W. Dave, J. M. Slaughter, and J. Akerman, Origin of the breakdown of Wentzel-Kramers-Brillouin-based tunneling models, *Phys. Rev. B* **74**, 212404 (2006).
- [43] C. D. Graham, Jr. and T. Egami, Magnetic Properties of Amorphous Alloys., *Ann. Rev. Mater. Sci.* **8**, 423–457 (1978).
- [44] P. R. Bevington and D. K. Robinson, *Data Reduction and Error Analysis for the Physical Sciences, 2nd edition*, McGraw-Hill, Boston, MA (1992).
- [45] S. Tegen, I. Monch, J. Schumann, H. Vinzelberg, and C. M. Schneider, Effect of Neel coupling on magnetic tunnel junctions, *J. Appl. Phys.* **89**, 8169 (2001).
- [46] J. C. S. Kools, W. Kula, D. Mauri, and T. Linn, Effect of finite magnetic film thickness on Neel coupling in spin valves, *J. Appl. Phys.* **85**, 4466 (1999).
- [47] T. Katayama, S. Yuasa, J. Velev, M. Y. Zhuravlev, S. S. Jaswal, and E. Y. Tsymbal, Interlayer exchange coupling in Fe/MgO/Fe magnetic tunnel junctions, *Appl. Phys. Lett.* **89**, 112503 (2006).

X-RAY PHOTOELECTRON SPECTROSCOPY STUDIES OF THE OXIDATION OF MgB₂ THIN FILMS

5.1 Introduction

The relatively large coherence length ($\sim 5\text{nm}$) in comparison to cuprate superconductors, quasi three-dimensional character, and high superconducting transition temperature ($T_C \sim 39\text{ K}$) of MgB₂ make it an attractive material for superconducting electronics, potentially allowing circuit operation at $\sim 20\text{ K}$. [1–11] Recent advances in producing high quality, low resistivity thin films with well-connected MgB₂ grains are quite encouraging, as is the ability to produce good quality barrier layers on such films for tunnel junction studies. [12–24] These achievements motivate the effort to further optimize and tailor the growth of robust tunnel barriers that can be formed on thin MgB₂ films suitable for the fabrication of high performance MgB₂-based Josephson junctions (JJs). However, there is variation in the quality of JJs with tunnel barriers produced using different methods which suggests that the MgB₂ surface is sensitive to the atmosphere and temperature at which the tunnel barrier is formed. Both MgB₂-tunnel barrier interfaces are of great importance to maintain the high T_C of the electrodes and not reduce the critical current density (J_C) of the JJ. To date, MgB₂-based JJs have not exhibited the high J_C performance and low junction specific resistance required for most technologically important applications. This points to better understanding of the chemistry and electronic structure of the surface oxides of high quality MgB₂ films as a possible pathway for the optimization of high quality tunnel barriers to further the development of MgB₂-based superconductor electronics.

In this chapter, I present results from an XPS study of high quality MgB_2 thin films and the surface oxides that form on these films under various processing conditions. The XPS spectra reveal that the composition of the MgB_2 surface oxide and sub-surface (~ 5 nm) components can vary substantially depending upon the details of in-situ, post-growth oxidation processes. Such techniques have been recently utilized to form successful insulator layers in Pb / Mg-B-O / MgB_2 tunnel junction studies. [21–24] The native MgB_2 oxide is a mixed Mg-B oxide, but in-situ exposure to O_2 or N_2 can form a more MgO-like surface oxide. The oxidation process, as shown in the cartoon in Fig. 5.1, depletes the film surface of Mg, forming MgO_x , and promotes development of elemental B, and B sub-oxide near the film surface. The degree of formation of the elemental B, and B sub-oxide species appears to be dependent upon the method of delivery of O to the film surface as well as the sample temperature during oxidation. The presence of semi-metallic elemental B and semi-conducting B sub-oxide could indicate other possible current paths can exist in such oxide tunnel barriers that are likely to be a source of electronic noise as well as potentially detrimental to the superconducting electronic device behavior.

Results of ion milling and water etching experiments further illuminate details of the MgB_2 XPS spectra and help inform the investigation of the surface chemistry and thin film oxidation process. During ion milling, even in ultra-high vacuum, the surface of the MgB_2 thin film is modified, forming an MgO-like surface layer and components of elemental B, B oxide, and B sub-oxide. During water exposure, the MgB_2 surface is both oxidized and etched leaving the surface of the remaining film rich in elemental B and B sub-oxide. This study contributes more insight into improving the understanding of various changes in chemistry that can occur in high quality MgB_2 film surfaces under different processing conditions and provides

potentially useful guidance towards the formation of optimal tunnel barrier layers for MgB₂-based thin film electronics.

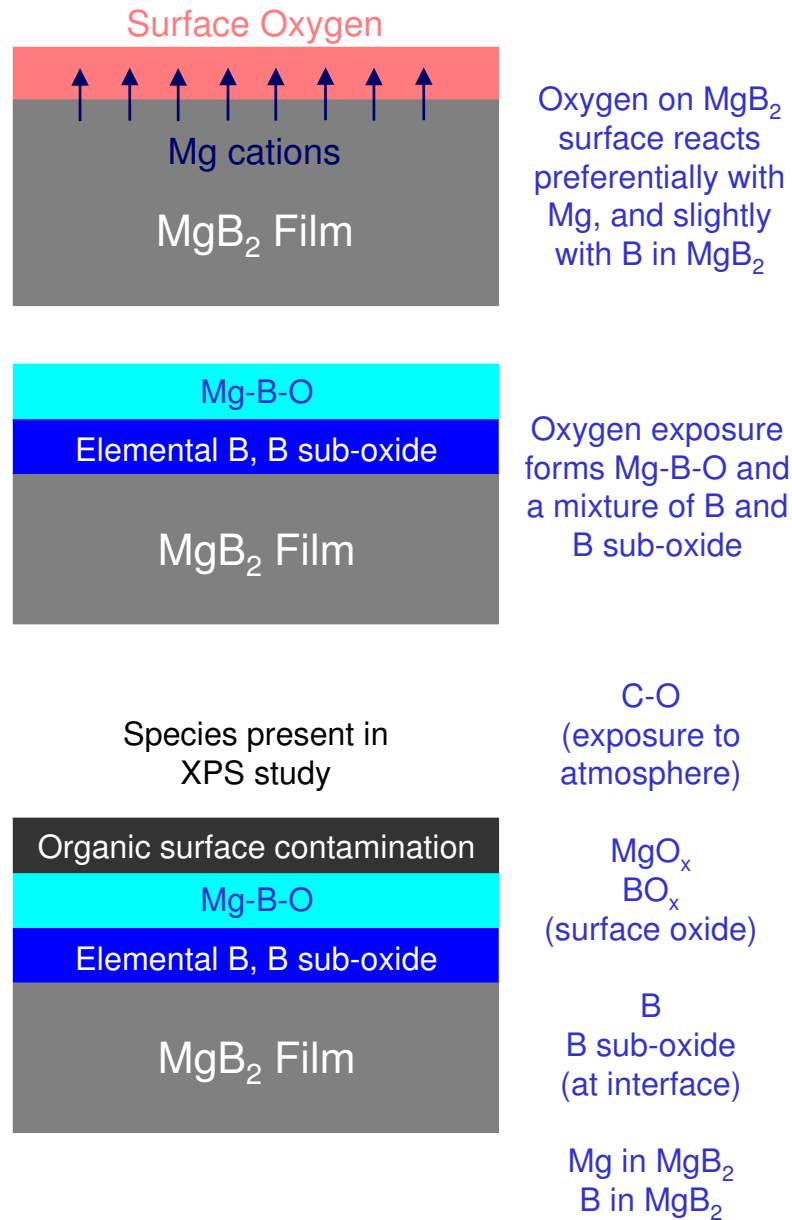


Figure 5.1: Proposed process of oxidation of the MgB₂ thin film surface.

5.2 Experimental Details

I calibrated the spectrometer used to acquire the data that are presented in this chapter to the Au $4f_{7/2}$ line at 83.96 eV and I carefully studied initial samples to measure the location of the Mg 2p and B 1s peaks attributable to MgB₂ to a resolution of approximately 0.5 eV. I assigned peak locations after careful spectrometer calibration to Au and Cu, and through comparison of the primary C 1s signal with the background adventitious carbon signature in this XPS system, which is found at ~ 235.9 eV on several sample surfaces (MgO, AlO_x, Fe, etc.). The initial investigation of un-treated MgB₂ films provides the correct locations of the XPS peaks attributable to the Mg and B atoms in the MgB₂ film. In later samples where the surface oxide is sufficiently thick to block the signal of the underlying film, the strongest C 1s signal provides an additional calibration to the Au calibration, although such calibration must be applied with great care since adventitious surface C is not metallic and is thus susceptible to chemical shifts. The adventitious C 1s signal at ~ 235.9 eV appears on all the samples studied in this chapter and is primarily due to a surface layer (~ 1 -2 nm) of organic C from atmospheric exposure before study in the XPS system. However, measurable changes in the MgB₂ film and its surface oxide are reliably and repeatedly observed beneath this organic layer. All samples were exposed to atmosphere between removal from the deposition system and insertion into the XPS system. While in transit, the samples were vacuum-packed in containers with desiccant, and between measurements the samples were stored in a vacuum desiccator. The samples used in water etching experiments were measured then removed from the XPS system, exposed to water and then atmosphere before re-introduced into the XPS system. In order to compare the relative surface and sub-surface film compositions, all samples presented in this chapter were measured at different take-off angles of $\sim 20^\circ$ or $\sim 90^\circ$ to

probe the surface and sub-surface chemistry respectively.

I examined two types of MgB_2 thin films, grown by other researchers, in this study. Yi Cui of Penn. State used the hybrid physical-chemical vapor deposition (HPCVD) technique [13] to grow MgB_2 on 6H-SiC substrates and Brian Moeckly used his reactive evaporation (RE) technique [18] to grow MgB_2 on R- Al_2O_3 substrates. Standard HPCVD thin film samples were cooled to near room temperature (RT) in a background pressure of $\sim 1 \times 10^{-6}$ Torr after growth in H_2 carrier gas before removal from the vacuum chamber. In one alternative case, the film was held at the 700 °C growth temperature for roughly 15 minutes after the B_2H_6 source gas was turned off, and the film surface was exposed to Mg vapor before the sample was cooled to RT and then removed from the growth chamber. Another alternative was to cool the film after growth to ~ 200 or 400 °C for a period of time up to half an hour in an ultra-high-purity (UHP) N_2 atmosphere before lowering the sample temperature to RT and then removing it from the growth chamber. Standard RE samples were typically deposited in a background pressure of $\sim 1 \times 10^{-7}$ Torr and then cooled in a background pressure of $\sim 5 \times 10^{-8}$ Torr to near RT before removal from the growth chamber. RE samples of different thicknesses were exposed to UHP O_2 for several minutes at ~ 240 or 400 °C before exposure to atmosphere. The high quality of the air-exposed HPCVD and RE films, along with the thin native oxide and surface carbon layers that form on these films, make systematic study of the film surfaces possible. For both growth processes, sample temperature plays a substantial role in the surface oxidation rate.

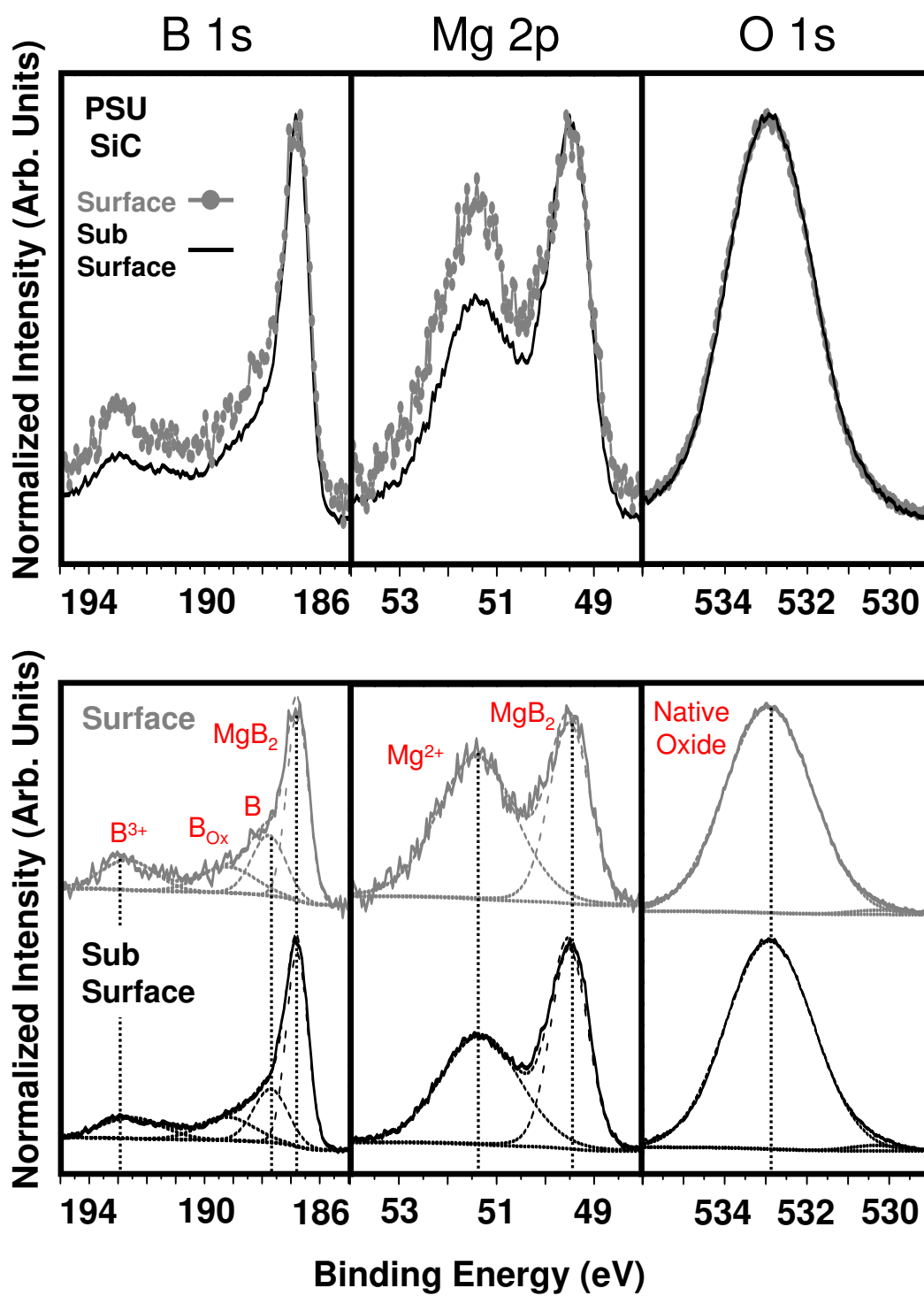


Figure 5.2: Normalized angle-dependent XPS data from a control HPCVD MgB₂ thin film sample.

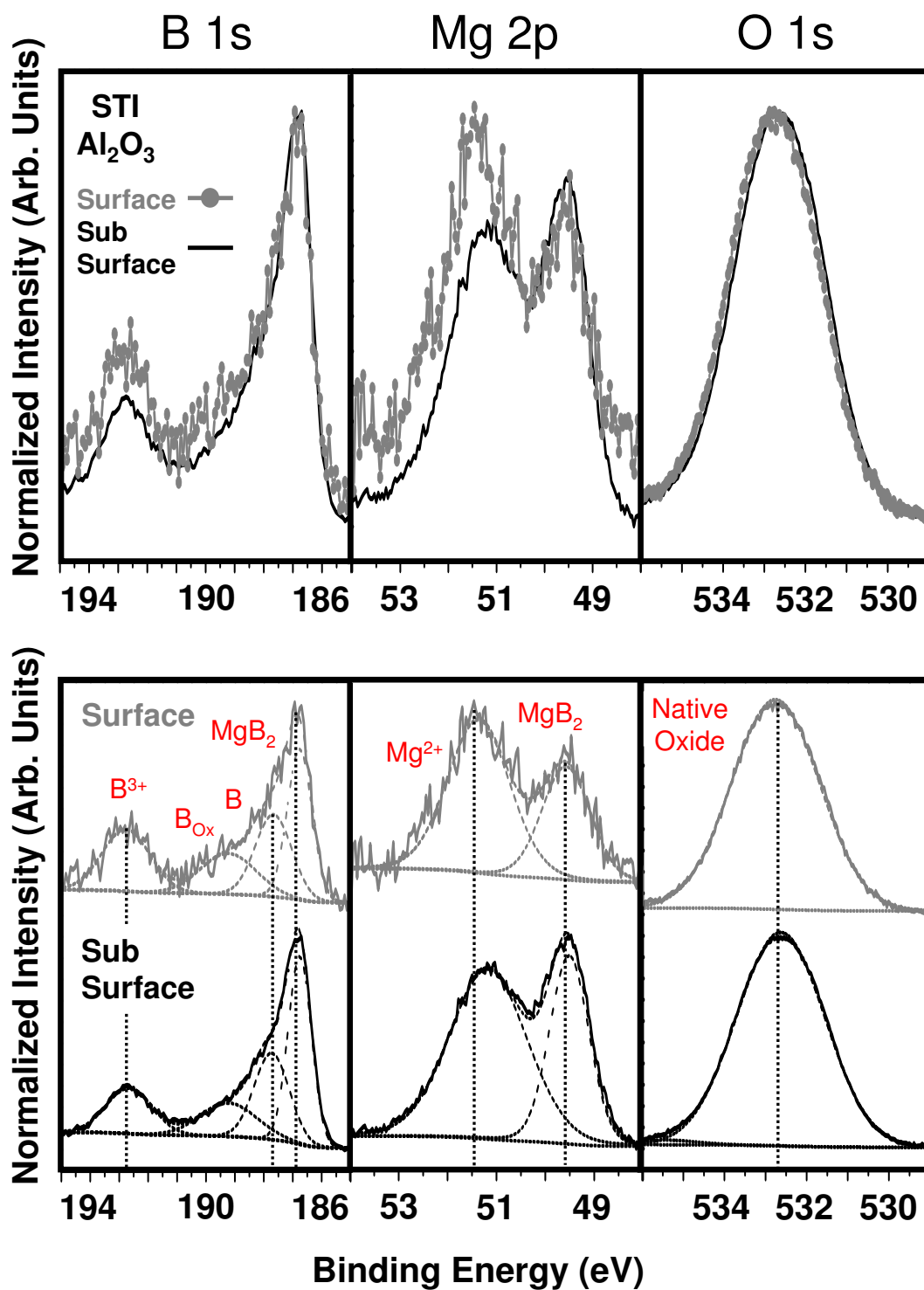


Figure 5.3: Normalized angle-dependent XPS data from a control RE MgB₂ thin film sample.

5.3 Spectral Peak Identification in Control Samples

Similar Mg 2p, B 1s, and O 1s XPS regions are evident throughout this study for both HPCVD and RE film growth processes. Spectra from standard HPCVD and RE MgB₂ films are shown in Fig. 5.2 and Fig. 5.3 respectively. In addition, spectra from RE films grown on a variety of substrate materials is shown in Fig. 5.4. The upper panels of Fig. 5.2 and Fig. 5.3 show angle dependent measurements, acquired at the different take-off angles described above, which provide a comparison of surface and sub-surface spectra to aid identification of surface oxide species. The lower panels show the detailed peak fits of the same data used to analyze the sample chemistry. Two metallic peaks, one each in the Mg 2p (at ~ 49.5 eV) and B 1s (at ~ 186.7 eV) spectral regions, are clearly distinguishable by their small line widths and the spectra in these regions are normalized to the intensity of these metallic peaks.

Although there is some disagreement in the literature regarding the proper assignment of the various peaks in the MgB₂ spectrum, [25, 26] the high quality of the thin film samples and careful spectrometer calibration yield data that clearly show these are the metallic peaks due to the Mg and B species within the MgB₂ film. This is in agreement with the original assignment of Vasquez and co-workers (see Fig. 5.5) [25] who attribute the shift to lower BE of the MgB₂ B 1s peak location from its position in elemental B samples to the charge transfer that occurs from Mg to B in the MgB₂ crystal structure (see Fig. 5.6). There is not a corresponding shift to higher BE for the Mg signal from MgB₂ in comparison to that from metallic Mg. This is because of a strong initial state effect due to the large value of the Madelung energy relative to the Mg ionization energy. [27] The writing of Garg and co-workers [26] suggests that the MgB₂ peaks exist at loca-

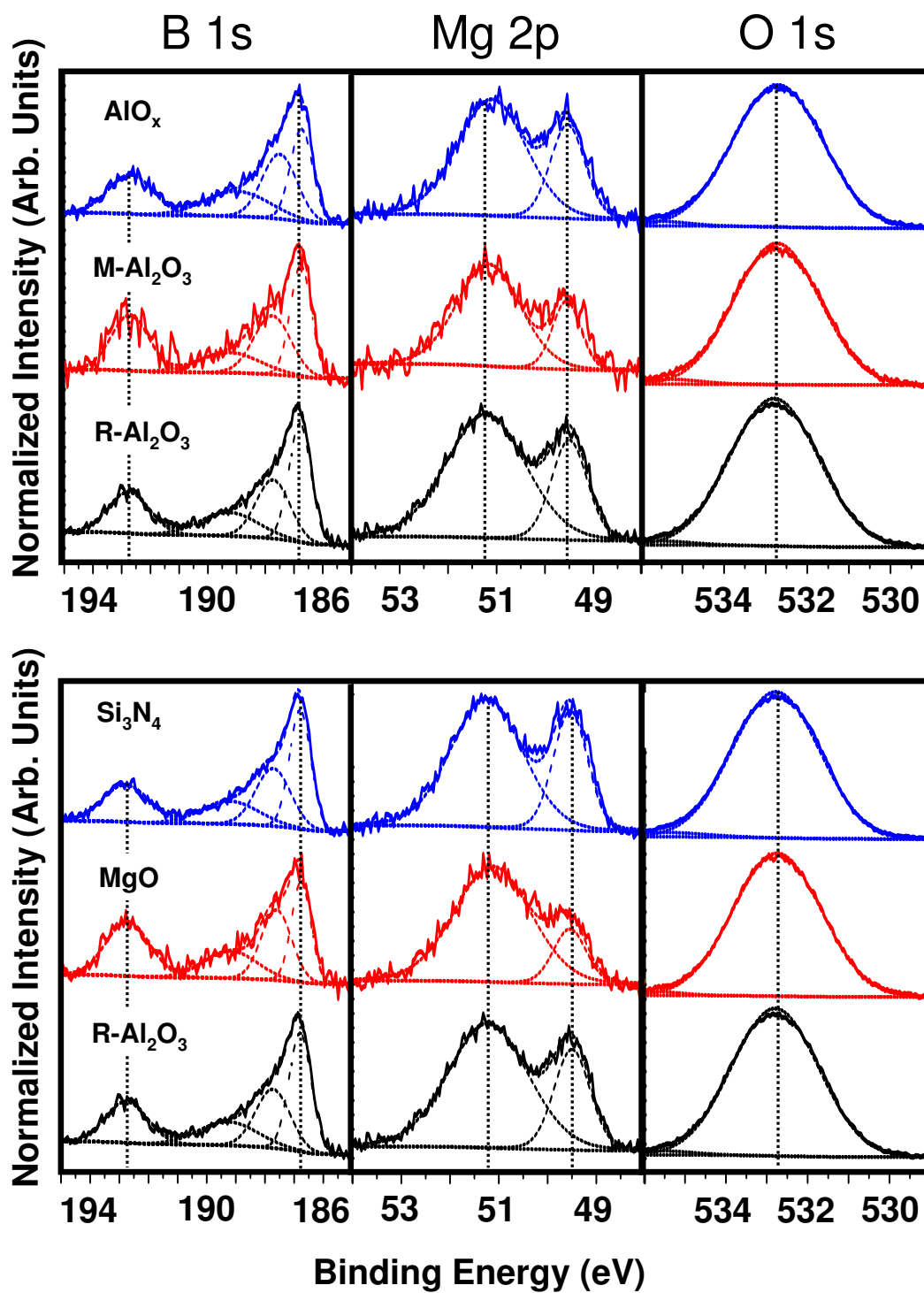


Figure 5.4: XPS data from RE deposited MgB_2 thin films grown on a variety of substrates.

tions different than those measured by Vasquez and co-workers. However, careful inspection of the data presented in this publication (see Fig. 5.7) clearly show that the data is actually in agreement with the data of Vasquez. The confusion lies in a misinterpretation of the data after Ar ion milling. The authors suggest that ion milling cleaned the sample surface, but in fact, ion milling oxidized the MgB₂ surface. The data in Fig. 5.7, shows the evolution of the MgB₂ film and oxide peaks, revealing that the lowest BE Mg 2p (labeled "unreacted Mg") and B 1s (labeled "unreacted B") peaks increase in relative intensity after in-situ scraping, suggesting these are the MgB₂ peaks, consistent with the interpretation of Vasquez. It is only after ion milling that these film peaks disappear, creating the confusion, and prompting the authors to incorrectly label the peaks at ~ 51.5 eV and ~ 188 eV as being due to MgB₂. These peaks are in fact attributable to the Mg surface oxide (~ 51.5 eV) and to the elemental B and B suboxide (~ 188 eV) that form during the ion milling process, which will be discussed in more detail later in this chapter. In conjunction with these two earlier reports, the data from the control samples of the study discussed in this chapter (Fig 5.2 and Fig. 5.3) additionally suggest that the lowest Mg 2p and B 1s peaks at ~ 49.5 eV and ~ 186.7 eV are due to the MgB₂ film.

The native surface oxide that forms on both HPCVD and RE grown MgB₂ thin films that are first exposed to atmosphere at relatively low temperatures (< 200 °C) is not that thin (~ 3 -4 nm) and is composed of both Mg and B oxides, as shown in Fig. 5.2 and Fig. 5.3. The highest BE peak in the Mg 2p (B 1s) spectral region, centered at ~ 51.5 eV (~ 193 eV), is an Mg²⁺ (B³⁺) signal that arises from an atomically mixed Mg-B surface oxide, which is also reflected in the broad O 1s peak centered at ~ 533 eV. Due to atmospheric exposure, these surface oxide peaks are likely reflective of a mixture of several surface oxides. The likely

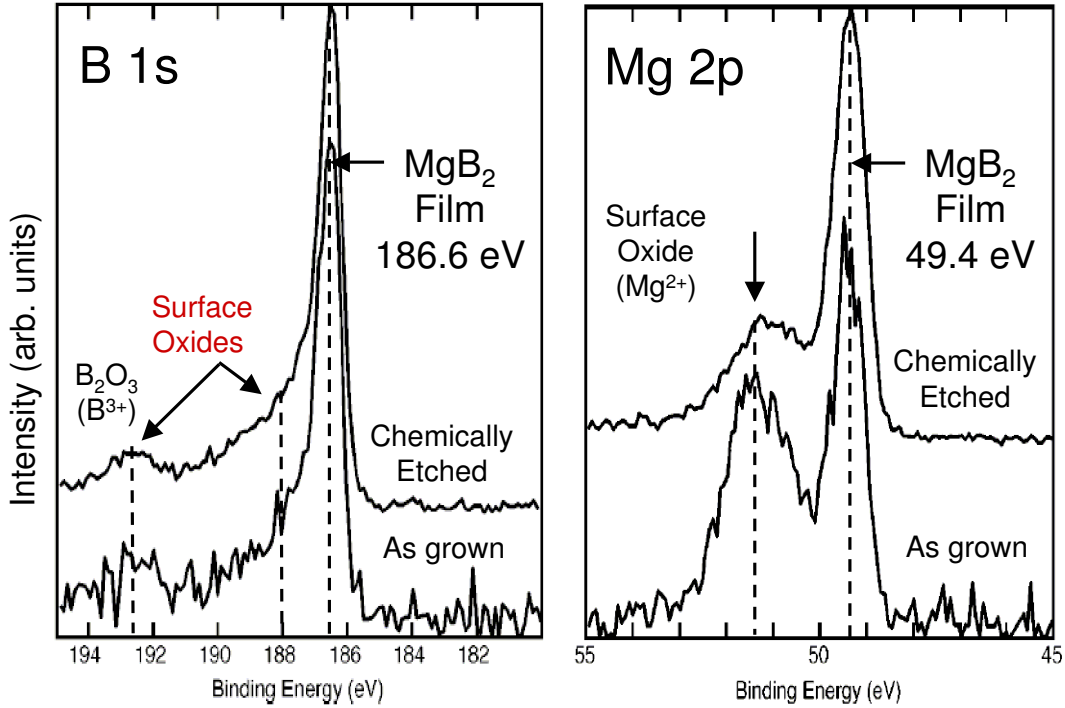


Figure 5.5: XPS data from a PLD-deposited MgB_2 thin film sample, from ref[25].

Mg oxide species are MgO ($\text{Mg}^{2+} \sim 50\text{-}51$ eV, $\text{O}^{2-} \sim 530\text{-}531$ eV), MgO_2 ($\text{Mg}^{2+} \sim 51\text{-}52$ eV, $\text{O}^{1-} \sim 532\text{-}533$ eV), $\text{Mg}(\text{OH})_2$ ($\text{Mg}^{2+} \sim 51\text{-}52$ eV, $(\text{OH})^{1-} \sim 532\text{-}533$ eV), and MgCO_3 ($\text{Mg}^{2+} \sim 52\text{-}53$ eV, $\text{O}^{1-} \sim 532\text{-}533$ eV). [28–31] The likely B oxide species are B_2O_3 ($\text{B}^{3+} \sim 192\text{-}193$ eV, $\text{O}^{2-} \sim 532\text{-}533$ eV), and $\text{B}(\text{OH})_3$ ($\text{B}^{3+} \sim 192\text{-}193$ eV, $(\text{OH})^{1-} \sim 532\text{-}533$ eV). [32–34] Data from more heavily oxidized samples, which will be discussed in more detail in the next sections, show that the formation of an MgO-like surface oxide generates a strong signal in the O 1s spectral region that is easily identified even with the additional O 1s signal from the native surface oxide.

The two remaining peaks in the B 1s spectral region are due to the formation of elemental B and B sub-oxide. Both Moddeman and co-workers [32] (see Fig. 5.8) and Ong and co-workers [34] studied B sub-oxide (B_6O) material and both suggest

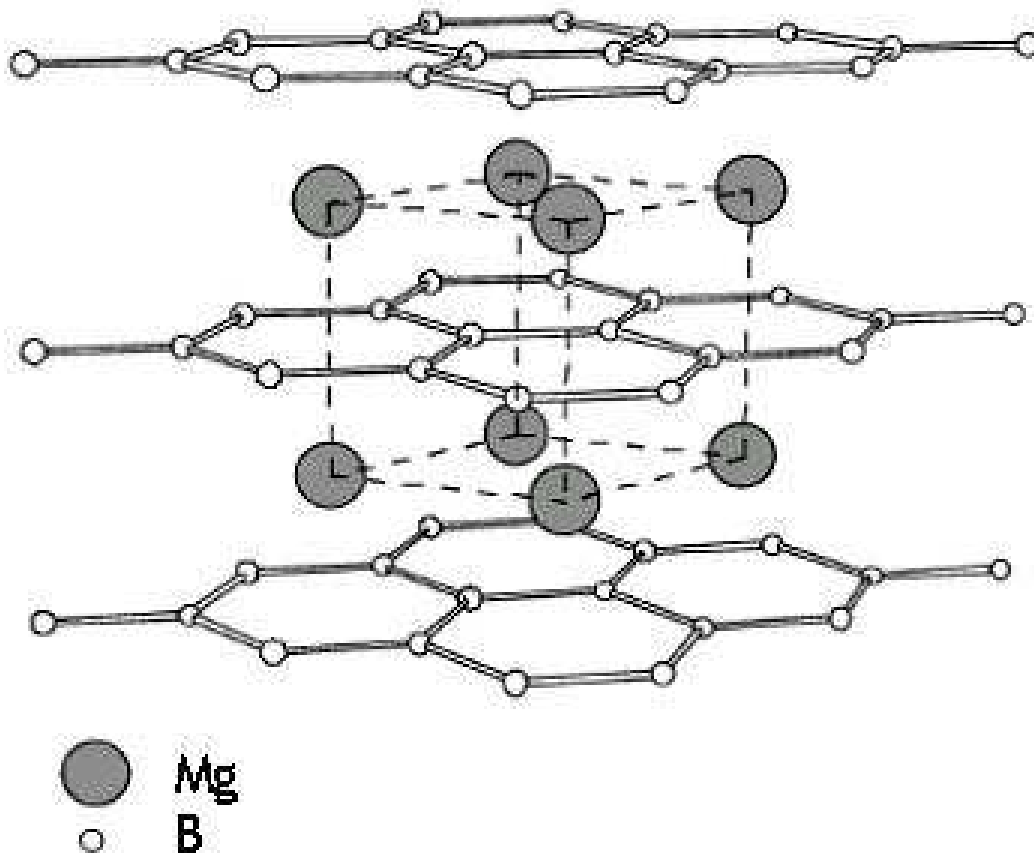


Figure 5.6: The MgB₂ crystal structure.

the lower BE peak (here at ~ 188 eV) is due to elemental B in cluster form while the higher BE peak (here at ~ 189 eV) is due to B, in a low oxidation state (B sub-oxide) bonded with O. The greater intensity of this peak in the surface scans shown in Fig. 5.2 and Fig. 5.3 suggests the sub-oxide is on top of the MgB₂ film, or at least at the MgB₂ / surface oxide interface. The behavior of these elemental B and B sub-oxide peaks in relation to the Mg²⁺ and B³⁺ oxide peaks is discussed in the next section in spectra from MgB₂ samples were intentionally oxidized to form tunnel barrier materials. The presence of these peaks indicate the oxidation techniques used form both semi-metallic (elemental B) and semi-conducting (B sub-oxide) species that are either at the MgB₂ / surface oxide interface or mixed into the surface oxide. These B-based materials are likely detrimental to tunneling

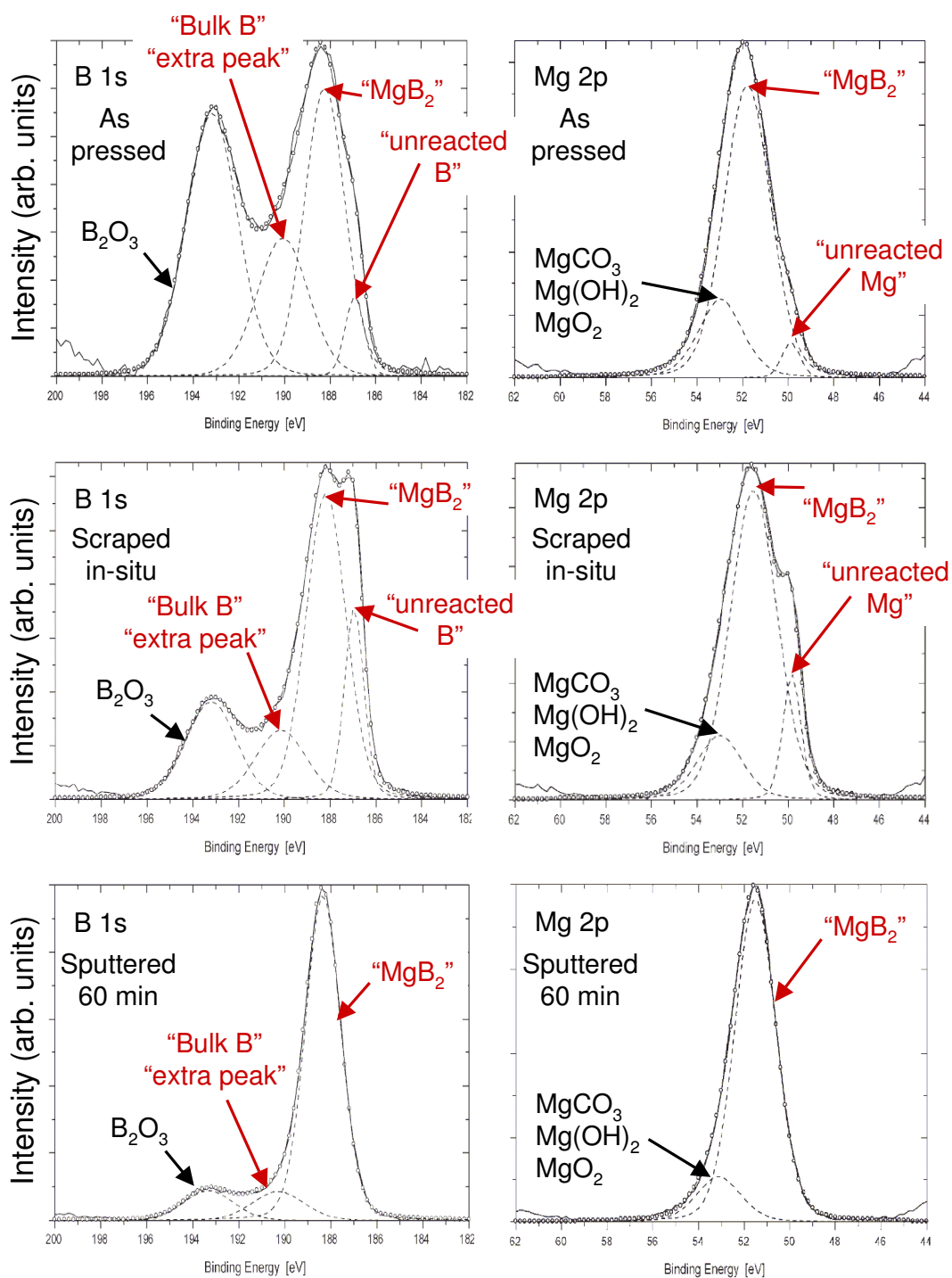


Figure 5.7: XPS data from a pressed MgB_2 pellet that has been scraped and ion milled in-situ, from ref[26]. The labels in red are due to the authors.

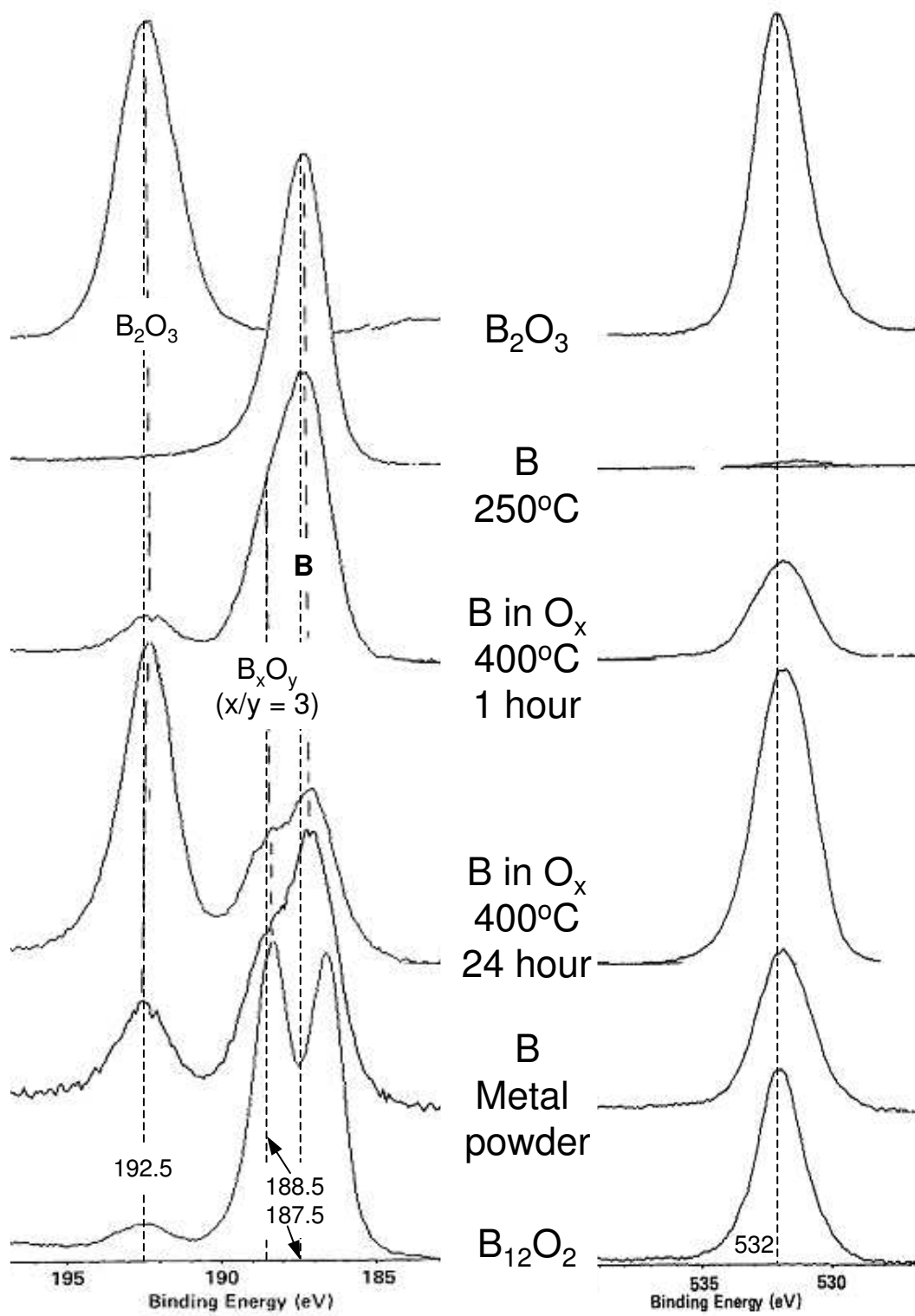


Figure 5.8: XPS data from various B and B oxide samples, from ref[32].

transport in JJ structures as they represent other possible conduction channels within the barrier. In this sense, the formation of these B species during thin film oxidation could be responsible for the low J_C and T_C values measured in such samples. However, point contact spectroscopy measurements on similar RE films [35], and HPCVD junction spectroscopy measurements of MgB_2 / native oxide / Pb junctions [22, 23] show that the mixed oxide surface of these air exposed films creates good quality tunnel barriers for measurements of the MgB_2 energy gaps (Fig. 5.9).

Using standard XPS techniques [36], the film surface and subsurface stoichiometry for each sample is estimated as shown in equation 5.1. The relative stoichiometry of the film sub-surface is estimated using the lowest BE Mg 2p peak (~ 49.5 eV), and the lowest BE B 1s peak (~ 186.7 eV) using a consistent peak fitting scheme. $C_{Mg,sample}$ and $C_{B,sample}$ are respectively the concentrations of Mg and B in the film. $I_{Mg2p,sample}$ and $I_{B1s,sample}$ are the relative intensities (area under the peak) of the Mg 2p and B 1s photoelectrons from the film, and ASF_{Mg2p} (0.3335) and ASF_{B1s} (0.486) are the atomic sensitivity factors for Mg 2p and B 1s photoelectrons as measured with this spectrometer. [37] This estimate for stoichiometry is best considered relative and not exact atomic concentration, as the uncertainty in the stoichiometry is roughly 10-15 %. Using this scheme, the estimated relative stoichiometry of both the HPCVD and RE control samples is $\text{MgB}_{1.3}$. A similar scheme with Mg, B, C, and O is used to determine the relative stoichiometry of the surface oxide on each sample.

$$\frac{C_{Mg,sample}}{C_{B,sample}} = \left(\frac{I_{Mg2p,sample}}{I_{B1s,sample}} \right) \left(\frac{ASF_{B1s}}{ASF_{Mg2p}} \right) \quad (5.1)$$

While this equation yields a relative stoichiometry of each film, in order to

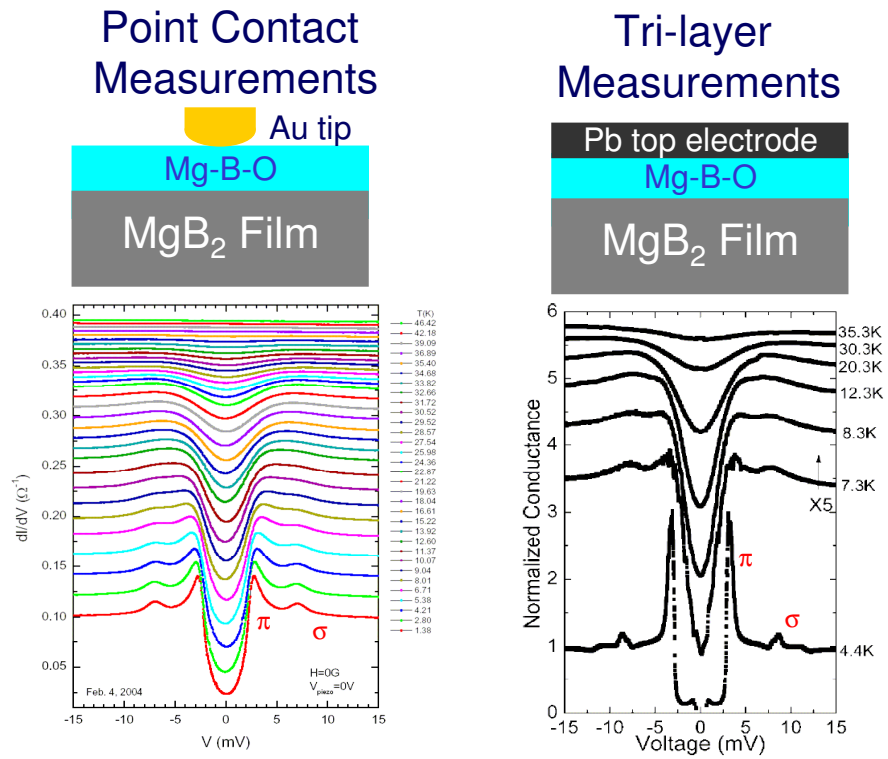


Figure 5.9: Conductance data from point contact and heterostructure measurements incorporating MgB₂ thin films with native surface oxide barriers, from ref [35] and ref [22].

accurately assign a stoichiometry to each sample film these values should be calibrated to a standard. The procedure for this is outlined in equations 5.2 - 5.4. Here C_{Mg,MgB_2} and C_{B,MgB_2} are respectively the concentrations of Mg and B in the MgB_2 standard and I_{Mg2p,MgB_2} and I_{B1s,MgB_2} are the relative intensities of the Mg 2p and B 1s photoelectrons from the MgB_2 film. Then, we can use the ASF values for the standard (ASF_{Mg2p,MgB_2} and ASF_{B1s,MgB_2}) as a calibration factor and ultimately estimate a stoichiometry that is calibrated to the standard film as shown in equation 5.4.

$$\frac{C_{Mg,MgB_2}}{C_{B,MgB_2}} = \frac{1}{2} = \left(\frac{I_{Mg2p,MgB_2}}{I_{B1s,MgB_2}} \right) \left(\frac{ASF_{B1s,MgB_2}}{ASF_{Mg2p,MgB_2}} \right) \quad (5.2)$$

$$\left(\frac{ASF_{B1s,MgB_2}}{ASF_{Mg2p,MgB_2}} \right) = \frac{1}{2} \left(\frac{I_{Mg2p,MgB_2}}{I_{B1s,MgB_2}} \right) \quad (5.3)$$

$$\frac{C_{Mg,sample}}{C_{B,sample}} = \frac{1}{2} \left(\frac{I_{B1s,MgB_2}}{I_{Mg2p,MgB_2}} \right) \left(\frac{I_{Mg2p,sample}}{I_{B1s,sample}} \right) \quad (5.4)$$

Using XPS thickness estimation techniques, a relative thickness of the surface oxide layer for each exposure experiment is acquired, as shown in equations 5.5 and 5.6. The approach is that of Hill and co-workers, [38] where for a take-off angle of 90° , thickness estimates for the surface oxide are easily calculated using the peak intensity ratios for metallic and oxidic components of a single atomic species. Since clearly there are Mg and B oxides present in these samples, the model used for estimating oxide thicknesses in these experiments involves two simple bilayer structures, MgB_2 / MgO and MgB_2 / B_2O_3 . Although it is expected that the actual surface oxide is a mixture of Mg, B, and C oxides, this model provides a relative estimate for the total surface oxide thickness by adding the individual Mg

and B oxide estimates.

$$t_{MgO} = \lambda_{Mg2p,MgO} \left(\ln \left\{ 1 + \frac{I_{Mg2p,MgO}}{I_{Mg2p,MgB_2}} \right\} \right) \quad (5.5)$$

$$t_{B_2O_3} = \lambda_{B1s,B_2O_3} \left(\ln \left\{ 1 + \frac{I_{B1s,B_2O_3}}{I_{B1s,MgB_2}} \right\} \right) \quad (5.6)$$

$$t_{oxide} = t_{MgO} + t_{B_2O_3} \quad (5.7)$$

The inelastic mean free path for Mg 2p photoelectrons when scattering through MgO is $\lambda_{Mg2p,MgO}$ (~ 2.9 nm), and the inelastic mean free path for B 1s photoelectrons when scattering through B_2O_3 is λ_{B1s,B_2O_3} (~ 3.3 nm). I estimated both of these values using the work of Tanuma and co-workers. [39] Similar to the notation above, $I_{Mg2p,MgO}$ is the relative intensity of Mg 2p photoelectrons from the MgO surface oxide and I_{B1s,B_2O_3} is the relative intensity of B1s photoelectrons from the B_2O_3 surface oxide. Using this simple model, the control RE and HPCVD MgB_2 films have surface oxide layers of ~ 3.1 and ~ 4.3 nm of respective relative thickness. I show all the estimates for film and surface oxide stoichiometry along with surface oxide thickness for HPCVD and RE films in Tables 5.1 and 5.2 at the end of this chapter.

As discussed previously, there are at least three B species in different oxidation states, one Mg oxide species, and probable surface hydrocarbons. Given all of this surface oxidation and likely contamination due to atmospheric exposure, the lower bound for the uncertainty of this thickness estimate is ~ 10 -15%. The XPS data show that the surface is clearly a mixture of oxides, however, using this technique

relative thickness estimates are acquired for surface oxides formed using different oxidation techniques. This is discussed in detail in the next section. While this model does not capture the mixed oxide nature of the surface oxide, the thickness approximation does yield helpful information, particularly when correlated with transport measurements of similar structures, regarding which processes are best suited for junction formation.

5.4 Annealed and Oxidized HPCVD MgB₂ Films

Both HPCVD and RE growth processes form high T_C thin films which are compatible with all-MgB₂ JJ formation provided a thin, insulating tunnel barrier layer can be formed on the MgB₂ surface. This insulating layer must also be robust enough to withstand the growth temperature of the top electrode deposition without weakening its physical and electronic structure. In an effort to identify an ideal barrier layer formation procedure with oxidation of HPCVD growth MgB₂, we studied two techniques, attempting to form a thin layer of MgO on the MgB₂ film surface. Using HPCVD processes, one post-growth oxidation approach is to hold the film at 700°C for 15 minutes after turning off the B₂H₆ source gas, which exposes the surface to both Mg vapor and the H₂ carrier gas. While the high volatility of elemental Mg suggests that such a treatment might have no effect, the XPS spectra shown in Fig. 5.10 indicate that this process successfully forms an MgO-like surface material. The reaction between the Mg vapor, the carrier gas, and the ambient atmosphere within the vacuum system does form MgO as well as suppress the formation of B sub-oxide and elemental B. While the treatment may effect the surface, the film has an estimated relative stoichiometry of MgB_{1.4}, nearly the same value as the control HPCVD sample.

The surface oxide formed in this process is relatively thick (~ 3.4 nm relative thickness), but the process does not appear very efficient or reproducible based on previous transport measurements. [22] This may be due to clustering of Mg on the MgB₂ surface, or to accumulation of the MgO material at grain boundaries. [22] However, this process does form a more pure MgO component in the surface layer, which is seen most clearly in the O 1s spectrum (Fig. 5.10) where a secondary peak is now found centered at ~ 531 eV, fairly close to the expected 530-530.5 eV peak position for MgO, and far below the main O 1s peak at 533 eV that arises from the Mg-B surface oxide. The Mg 2p and B 1s scans show the typical signatures of the native Mg-B oxide, but there is less signal intensity from the elemental B and B sub-oxide region in comparison to the oxide of the control film. The Mg²⁺ peak is also found at slightly lower BE than for the control sample native oxide, which is attributable to lower B oxide concentration in the surface oxide due to the Mg vapor exposure. These observations point to clear suppression of B introduction into the tunnel barrier layer during growth. This arguably confirms that the principal effect of post-growth, high-temperature annealing of an HPCVD film in Mg vapor is to add a small amount of Mg to the surface, which is subsequently oxidized by the ambient atmosphere in the HPCVD system. However, due to the poor wetting of Mg on the MgB₂ surface, this process likely forms a discontinuous MgO layer. [22] Although these barriers are not ideal, they do point to an interesting aspect of the surface oxidation. Specifically, that adding surplus Mg to the surface suppresses B incorporation in the surface oxide.

The other post-deposition treatment of HPCVD films that we investigated is the exposure of the film to UHP N₂ at a sample temperature of either 200 C or 400°C for a period of time before final cooling to RT and exposure to atmosphere. Due to residual O in the growth chamber and the absence of H₂ during this process,

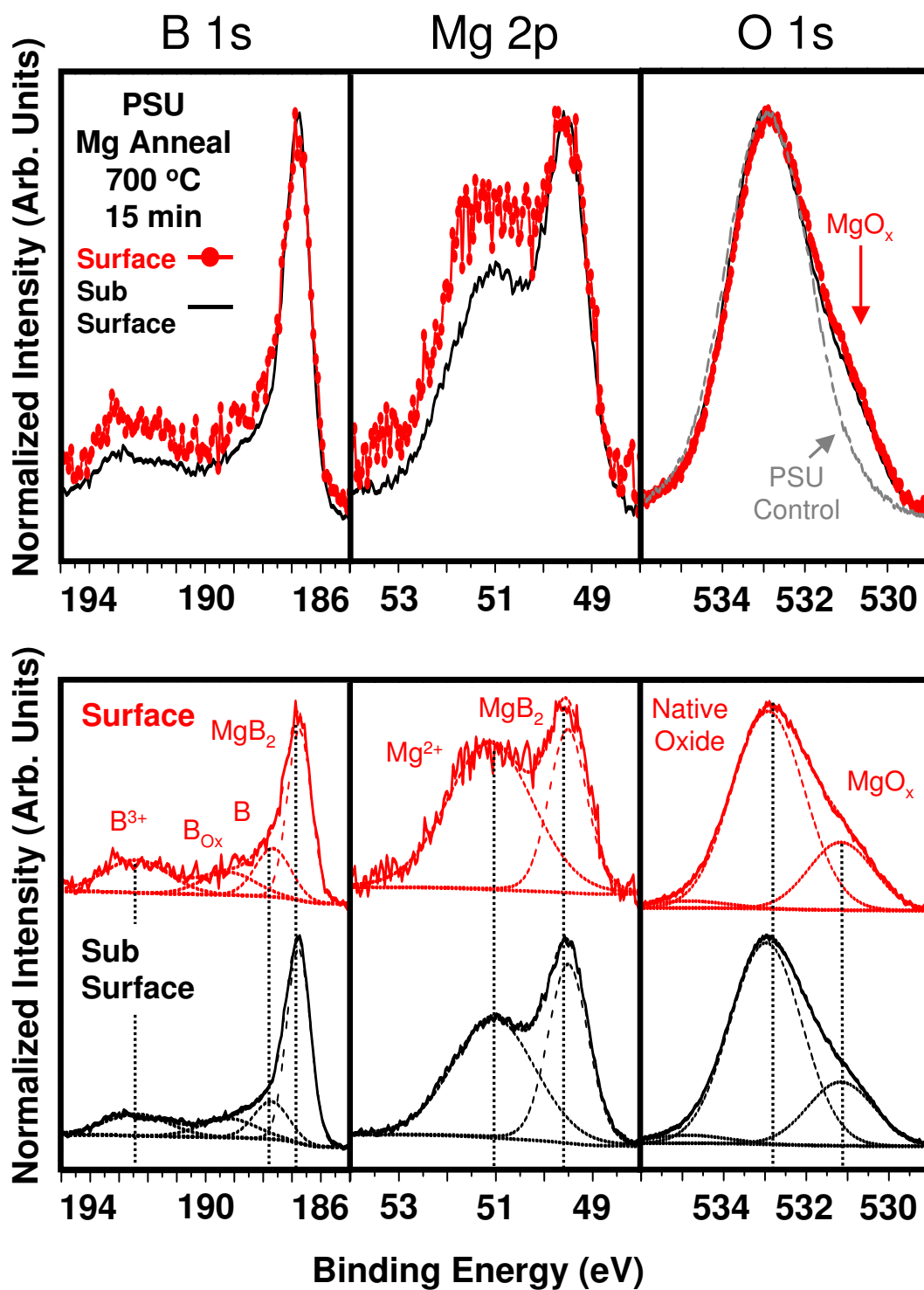


Figure 5.10: XPS data from an HPCVD MgB_2 thin film treated with post-growth annealing in Mg vapor.

the result is a high temperature oxidation of the MgB_2 surface. The data shown in Fig. 5.11 are from a sample that was exposed to such oxidation at 400°C for 90 seconds. The enhanced Mg^{2+} and B^{3+} oxide peak intensities reveal that the surface has a thicker mixed Mg-B oxide coating (~ 4.2 nm relative thickness) than does a standard HPCVD sample. The low BE peak in the O 1s spectrum at ~ 531 eV, indicates the additional presence of a separate MgO-like oxide component, as in the Mg-vapor annealed film. In addition to the increased oxide thickness, there are two other notable aspects to the XPS data. First, the two different angle-dependent O 1s spectra suggest that there is a slightly larger portion of the MgO-like component deeper in the oxide than at its surface. Second, the B 1s peak centered at ~ 188 eV, that is attributable to B sub-oxide, is much larger, particularly in the more surface sensitive spectrum. These results indicate that a 90 second, 400°C exposure to UHP nitrogen increases the thickness of the mixed surface oxide, and in addition forms an oxide component that is close to pure MgO through Mg diffusion out of the surface of the MgB_2 material, leaving layers or clusters of elemental B and B sub-oxide behind at the MgB_2 -surface oxide interface. Given the layered nature of MgB_2 , the most likely process for this out-diffusion of Mg ions is along the a-b plane to grain boundaries where the Mg can react with O ions to form the MgO component. This is consistent with the MgO component being slightly deeper in the film than the mixed Mg-B surface oxide. Although the surface oxide is dramatically changed in this process, the estimated relative film stoichiometry is $\text{MgB}_{1.4}$, the same value as for the Mg annealed HPCVD sample.

This understanding of the high temperature MgB_2 oxidation process is further confirmed by holding an HPCVD film at temperature in a UHP N_2 ambient atmosphere for a considerably longer time of thirty minutes. The XPS spectra for two such films, shown in Fig. 5.12, reveal Mg 2p and O 1s peaks characteristic

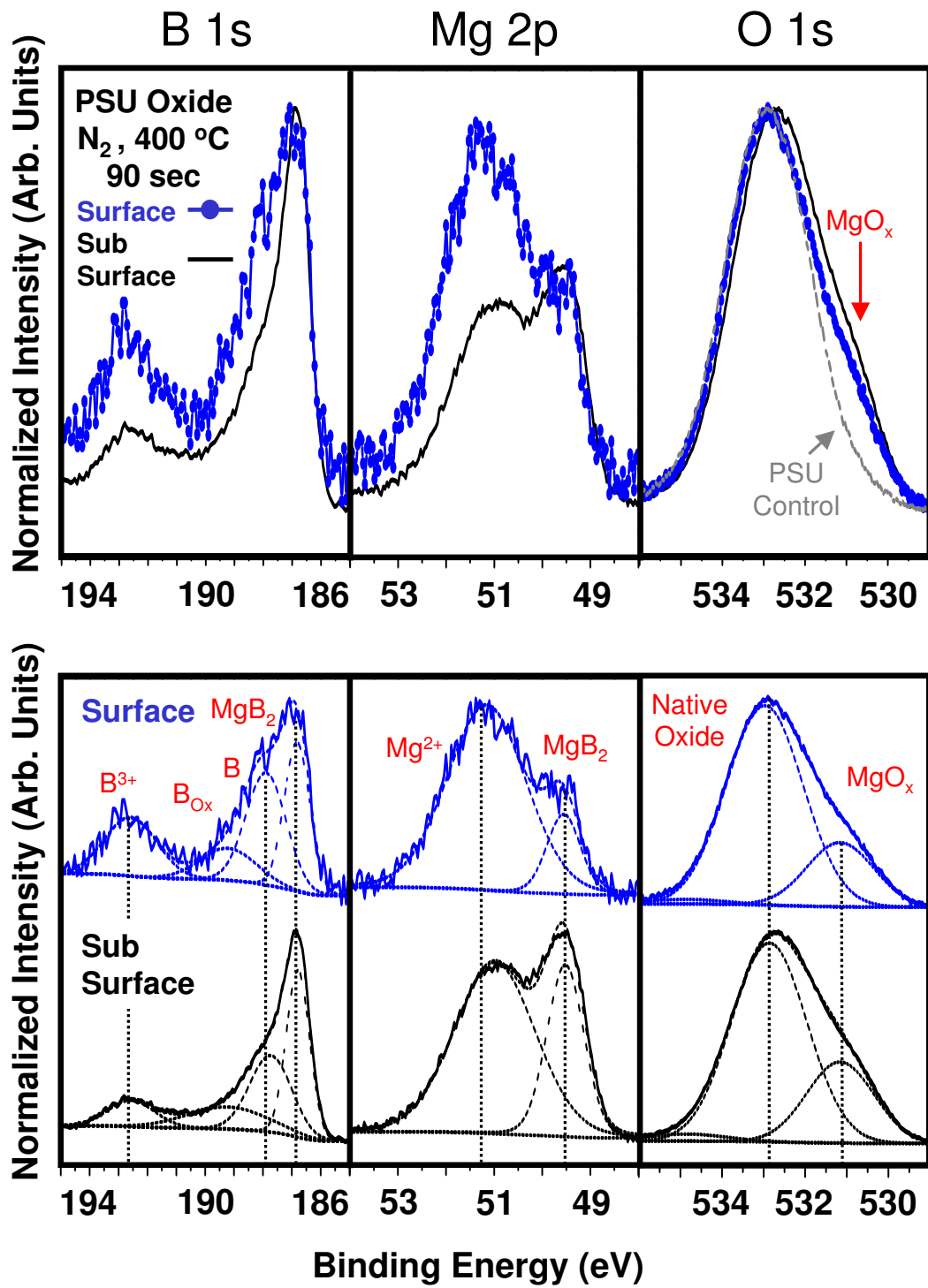


Figure 5.11: XPS data from an HPCVD MgB₂ thin film exposed to UHP N₂ after growth for 90 seconds at a sample temperature of 400°C.

of thermally oxidized MgO, including a surface layer with a O 1s peak at ~ 533 eV that is due to either MgO₂ or Mg(OH)₂. This MgO thermal oxide layer is sufficiently thick, > 5 nm, after 400°C exposure, that there is no detectable signal from the underlying film, thus a stoichiometry estimate is not possible. Alternatively, if a HPCVD film is held at 200°C for 30 minutes in a nominal UHP N₂ atmosphere, the XPS spectra of the resultant thermal oxide is quite similar to that of a standard HPCVD film. In this case, the surface oxide formed is ~ 3.1 nm of relative thickness and the estimated film stoichiometry is MgB_{1.3}, both of which are similar to the control sample. This demonstrates that the out-diffusion rate of Mg at 200°C and below is insufficient to form a significant MgO layer on top of the thin native mixed Mg-B oxide layer that forms initially upon exposure of the MgB₂ surface to O₂. The higher process temperature of 400°C is sufficient to form thick oxide barriers that appear MgO-like and although XPS cannot see beneath the thick oxide layer formed in this case, the MgB₂ / MgO interface may contain some elemental B and B sub-oxide which are possibly detrimental to supercurrent transport.

5.5 Oxidized RE MgB₂ Films of Different Thicknesses

In RE growth, an atomic layer of B is evaporated onto a hot substrate which is then rotated into a pocket heater where the B reacts with Mg vapor and the substrate is then rotated back out into the B deposition chamber to repeat the process. Due to the strong gettering ability and the low vapor pressure of Mg, the effect of the background reactive gases within the Mg oven is negligible. However, the background gases in the B deposition chamber, $P_{base} \sim 10^{-7}$ Torr, can react with the MgB₂ surface when the substrate is located there. The longer deposition

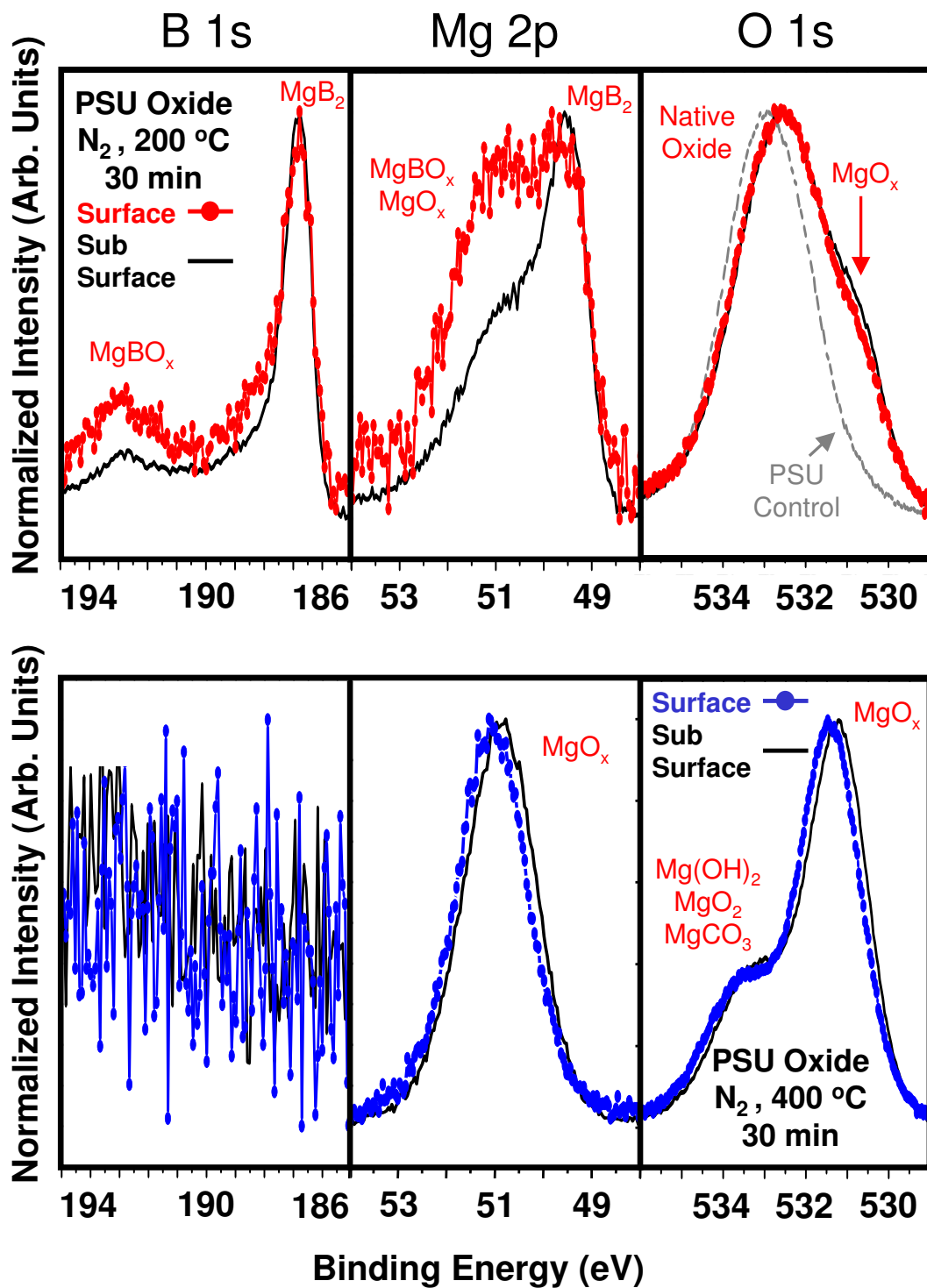


Figure 5.12: Comparison of XPS data from MgB₂ thin films exposed to UHP N₂ for 30 minutes at a sample temperature of 200°C (upper panel) or 400°C (lower panel).

time necessary for growing a 500 nm film versus the time required to grow a 150 nm film clearly impacts the surface oxide formation. The data from control RE films of 150 nm and 500 nm thicknesses, shown in Fig. 5.13 and 5.14, suggest that the film thickness does impact the surface oxidation. In these control films, the spectra from the thinner 150 nm film shows the clear signature of an MgO-like species in the O 1s spectral region, while the thicker 500 nm film does not. The Mg^{2+} and B^{3+} peaks are significantly less intense for the thinner sample than for the thicker 500 nm sample. This behavior is present in all of the samples studied in this section. The thinner version of each oxygen exposure experiment shows a clear MgO-like peak, but less intense peaks for the Mg and B oxides, than its thicker counterpart. The data from the control samples (Fig. 5.13 and Fig. 5.14) suggests that the thicker 500 nm film oxidizes more upon atmospheric exposure. This accounts for the increased Mg and B oxide peak intensities, and also explains the lack of an MgO-like peak in the O 1s spectrum for the 500 nm thick sample.

Comparison of the surface and sub-surface spectra for both control RE film thicknesses (Fig. 5.13 and Fig. 5.14) indicates that the elemental B and B sub-oxide inclusions extend as deep into the material as is probed by the photo-emitted electrons. While other, bulk sensitive, analytical methods are needed to confirm this, this data suggests that it is small regions of elemental B and B sub-oxide caused by repeated exposure of the surface of the growing film to background O that accounts for the higher than ideal low-temperature residual resistivity of RE MgB_2 films that has generally been observed, as well as the comparatively high magnetic pinning strength of such films. [18]

The estimated relative stoichiometry for the 150 nm control film is $\text{MgB}_{0.9}$ while the estimated relative stoichiometry for the 500 nm film is $\text{MgB}_{1.1}$, which

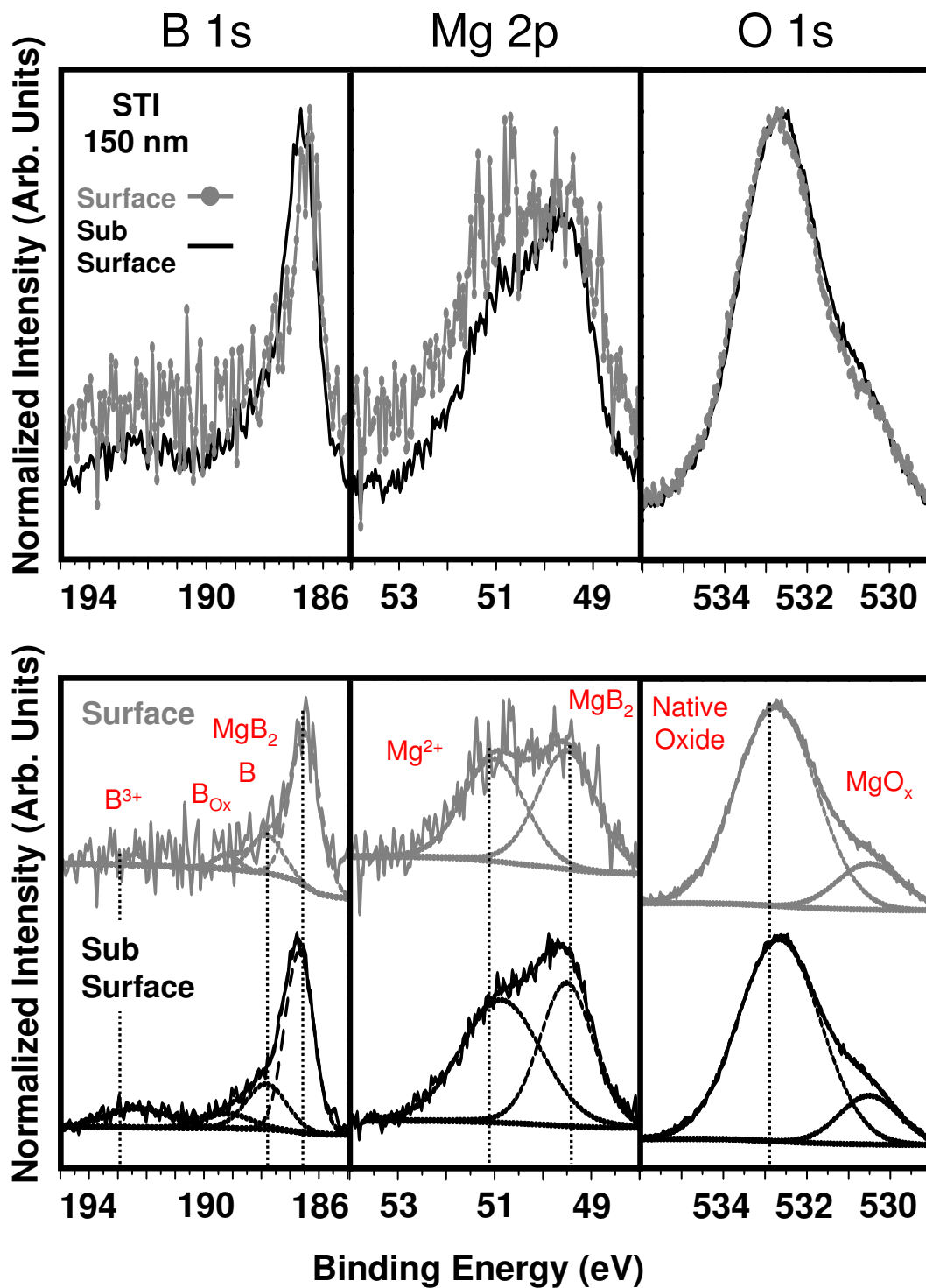


Figure 5.13: XPS data from a 150 nm thick RE MgB₂ thin film.

does suggest that more B is reacted into a thicker RE film. The surface oxide formed is ~ 3.1 nm of relative thickness for the 150 nm film and ~ 3.6 nm of relative thickness for the 500 nm film. The samples also show an increased O content measured in the surface oxide which supports the claim that some O is reacted into the growing film, likely during the B deposition process. Therefore, in a thicker film, the surface Mg-B oxide peak at ~ 533 eV has significantly greater intensity relative to the MgO peak at ~ 530.5 eV and thus the native oxide peak washes out the signal from the MgO peak.

The RE film growth process has the capability to grow smooth films of uniform thickness on a variety of substrate materials over large areas. The combination of this growth technique with the ability to form robust tunnel barriers that can withstand the deposition temperature required to grow a top MgB₂ electrode makes the growth and subsequent fabrication of all-MgB₂ JJs on large area substrates a very real possibility. To study the effect of oxidation upon RE grown films, and to study the plausibility of this technique for tunnel barrier formation, RE films were exposed to UHP O at sample temperatures of 240 or 400°C. The spectra from 150 nm and 500 nm RE films that were post-growth oxidized at 240°C are shown in Fig. 3.15 and Fig. 3.16 respectively. As in the control sample case, spectra from the thin 150 nm film show two distinct O 1s peaks, one clearly attributable to MgO, and the other due to the native surface oxide. The Mg²⁺ peak is shifted to lower BE which suggests greater Mg content in the surface oxide, and remarkably the B 1s spectra show no significant B oxide. However, there is a slight amount of elemental B and B sub-oxide present. The data from this sample suggests that a thin MgO-like material is successfully formed on the 150 nm MgB₂ film in this process. The relative stoichiometry of this sample is MgB_{0.8} and the relative surface oxide thickness is ~ 2.9 nm. These findings support the claim that Mg

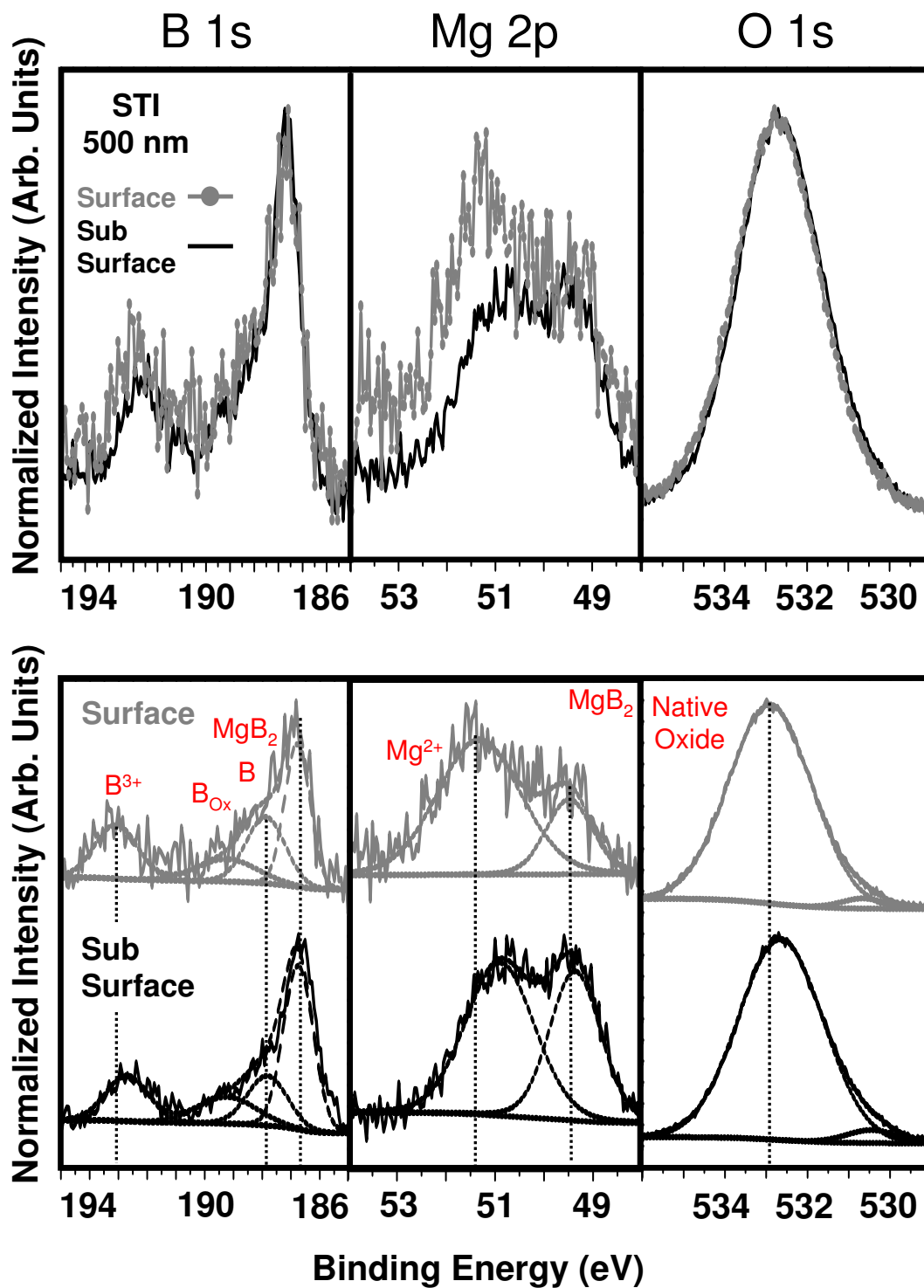


Figure 5.14: XPS data from a 500 nm thick RE MgB₂ thin film.

is pulled out of the surface and oxidized when the film is exposed to O_2 . Here, although the pocket heater is not pressurized with Mg during the oxidation, the sample rotation and its passage through the pocket heater during oxidation clearly supply some Mg to the sample surface during the oxidation process. As previously noted, Mg-rich MgB_2 surfaces form better barriers in MgB_2 / native oxide / Pb junctions. [24]

In comparison, the 500 nm film spectra show a shift to higher BE of the Mg^{2+} peak, increased B oxide, elemental B, and B sub-oxide peak intensities, and a singular O 1s peak (Fig. 5.16). These data are again indicative, as in the control sample case, of the formation of a surface oxide that has the character of the MgB_2 native oxide. The thicker film appears less likely to form an MgO-like surface oxide, but the overall thickness of the surface oxide formed on this film is greater than the surface oxide formed on the 150 nm thick film. The greater likelihood of the formation of a surface oxide that is more similar to native MgB_2 oxide than to MgO on thicker films suggests that such films are more stable in terms of the Mg to B bonding. The relative stoichiometry of this sample is $MgB_{1.4}$, which supports the claim that a greater amount of B is reacted into a thicker RE film. The relative surface oxide thickness is ~ 4.1 nm. Although the surface oxide that forms is composed of both Mg and B oxides, such barrier materials were successfully used in several junction measurements, as discussed previously. This may point to such mixed oxide materials as easier to form and potentially more reliable in JJ structures.

It is well known that the oxygen solubility in MgB_2 increases with temperature. [40] This is demonstrated in the results of RE film oxidation experiments carried out at a sample temperature of $400^\circ C$, which are shown in Fig. 5.17 and Fig.

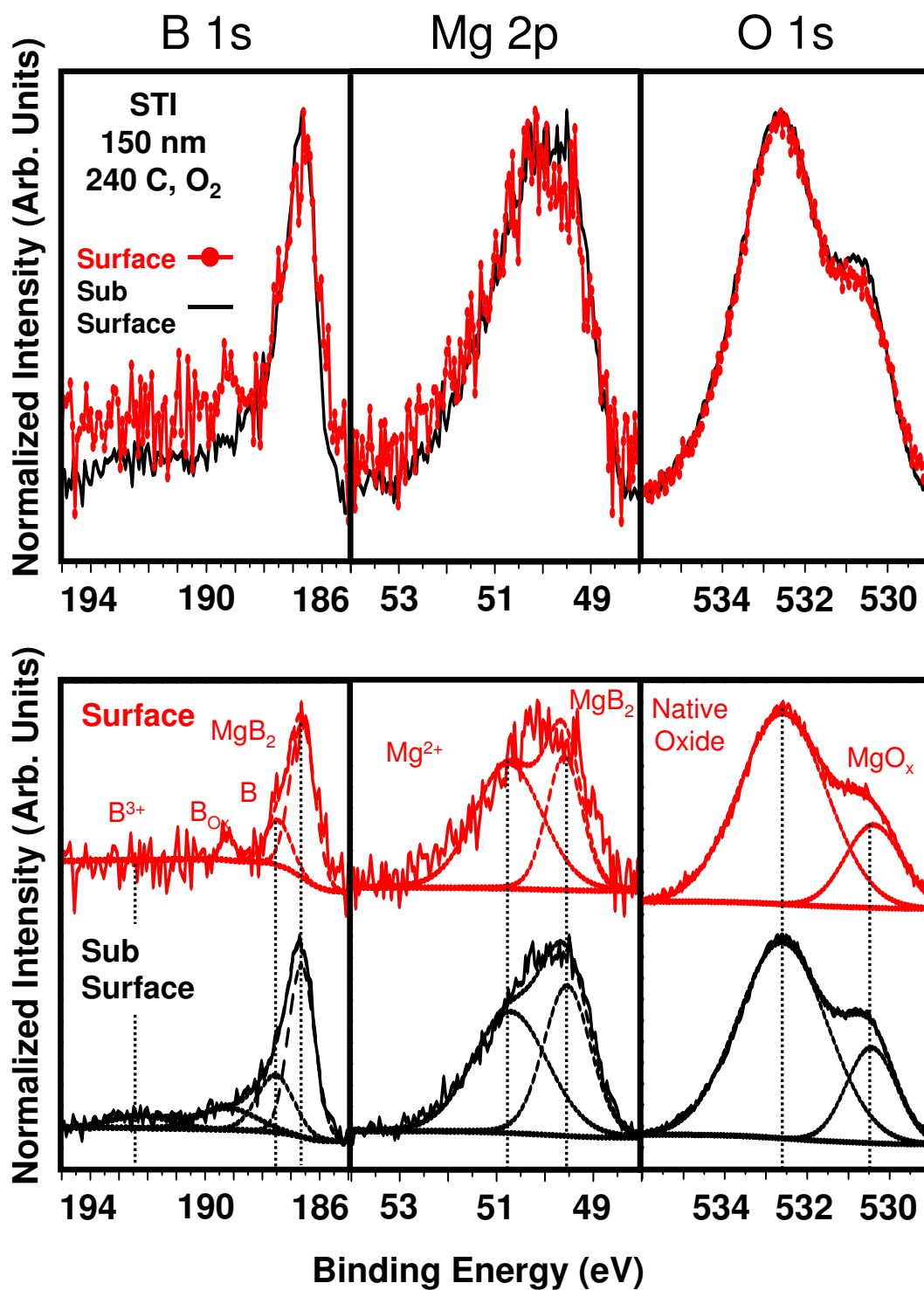


Figure 5.15: XPS data from a 150 nm thick RE MgB₂ thin film exposed to O₂ at a sample temperature of 240°C.

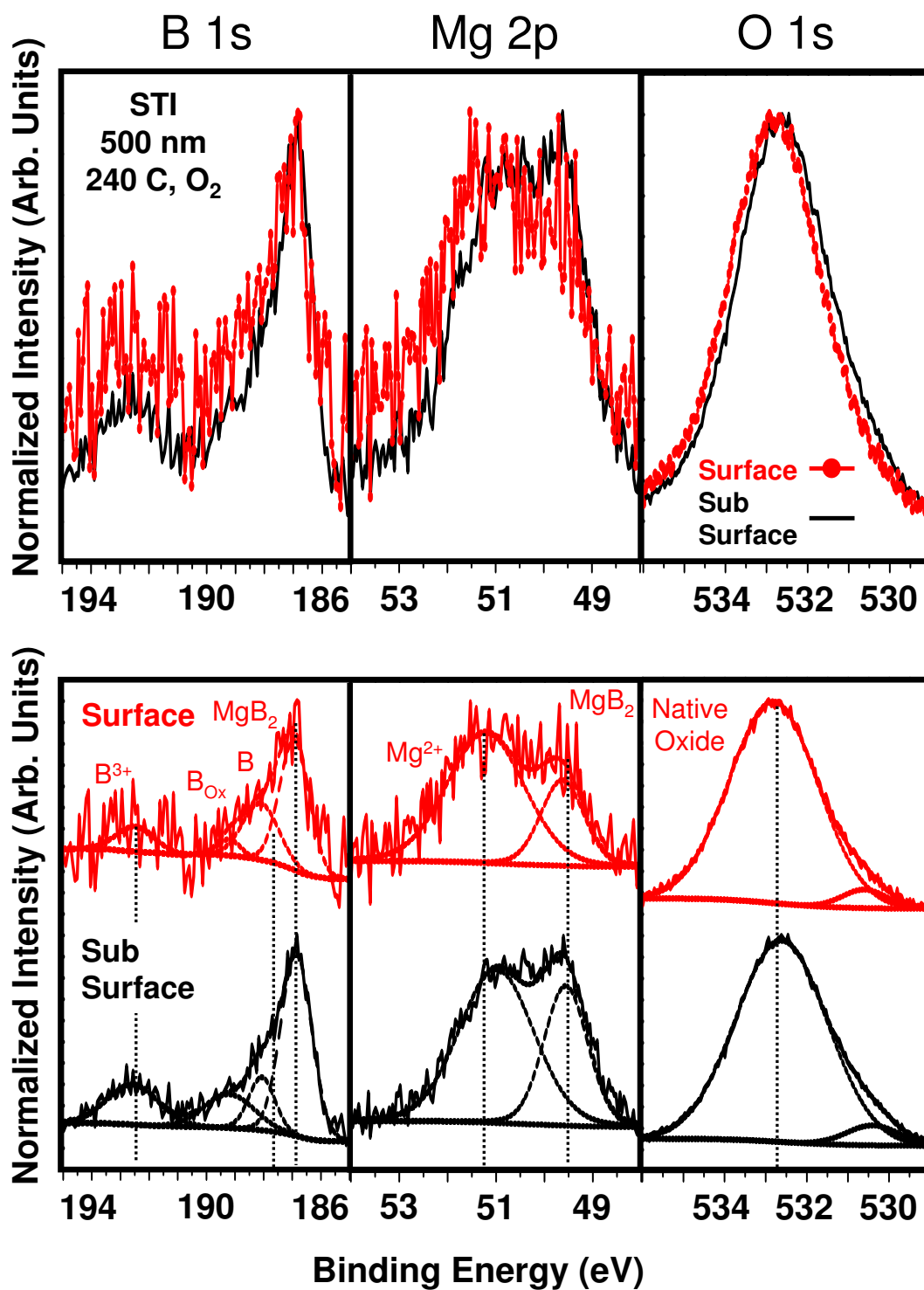


Figure 5.16: XPS data from a 500 nm thick RE MgB₂ thin film exposed to O₂ at a sample temperature of 240°C.

5.18. As in the two previously discussed experiments, the thinner 150 nm film O 1s spectra show the clear presence of an MgO-like species. In addition, and as in the other experiments, the 150 nm 400°C sample (Fig. 5.17) shows little B oxide formation and an Mg oxide peak which is shifted to lower BE. Close inspection of the O 1s spectra show that the subsurface spectrum has a higher MgO-like peak intensity. This provides some clarity regarding the MgO formation. It appears that the MgO species forms deeper in the film and that the native surface oxide then forms on top. The relative stoichiometry of the film is $\text{MgB}_{0.8}$ and the surface oxide is estimated at > 6.3 nm in relative thickness. It is probable that these measurements are not indicative of a simple, layered oxide system, but that there are non-uniformities in the MgB_2 / MgO / native oxide structure that forms.

The companion 500 nm thick, 400°C sample (Fig. 5.18) shows no signatures of the underlying MgB_2 film, so no stoichiometry estimate is possible, as in the case of the HPCVD sample oxidized at 400°C. No estimate of surface oxide thickness can be given either, except to comment that since the film photoemission peaks cannot be observed, the surface oxide must be greater than 6-7 nm thick. The Mg 2p spectra are indicative of an MgO-like species and the O 1s spectra suggest MgO_2 , $\text{Mg}(\text{OH})_2$, MgCO_3 , the native MgB_2 oxide, or some combination of all of these species. The clearly noisy B 1s spectra is due to the low intensity of this spectral region relative to the Mg 2p and O 1s spectral regions. These observations indicate that the 400°C oxidation process forms a thick, MgO-like barrier material that could work well in JJ structures if the thickness of the oxide formed is successfully controlled. To grow an all- MgB_2 JJ structure fully in-situ relies upon the ability to heat up the bottom electrode / barrier oxide bilayer without promoting detrimental inter-diffusion or destroying the insulating nature of the barrier oxide. Thus, before the RE MgB_2 400°C oxidation process is cleared as the best candidate for forming

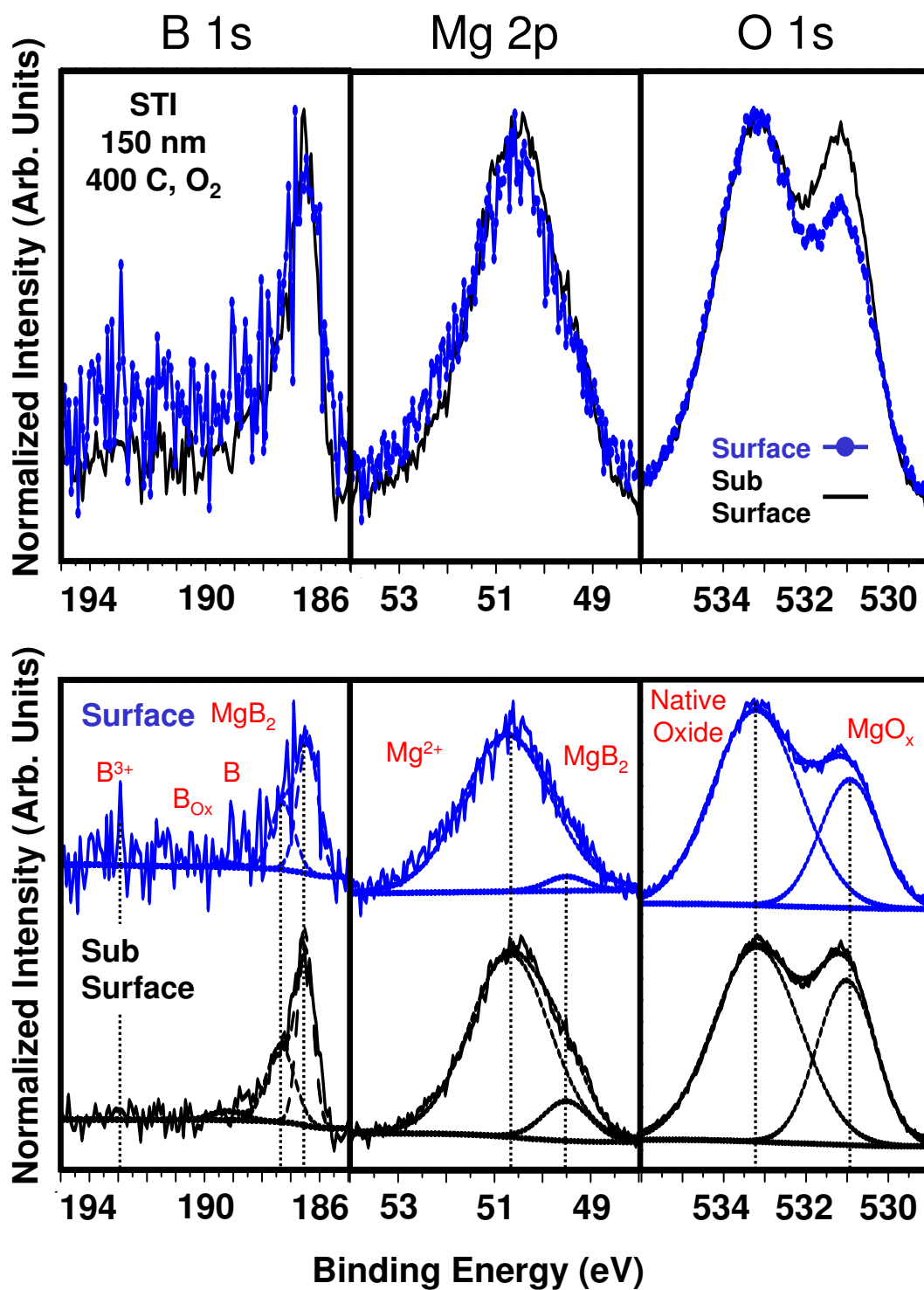


Figure 5.17: XPS data from a 150 nm thick RE MgB₂ thin film exposed to O₂ at a sample temperature of 400°C.

all-MgB₂ JJs, the robustness of the barrier material formed should be studied in detail.

An interesting footnote on this XPS experiment is shown in Fig. 3.19. These AFM scans of the surfaces of the 400°C oxidized MgB₂ films show that the oxidized surface of the thicker MgB₂ film is nominally smoother than the oxidized surface of the thinner MgB₂ film. Also, the grain structure of the thinner film sample shows a greater density of surface protrusions, which may be indicative of Mg diffusion or MgO nucleation. This could suggest that while the thinner film shows more MgO-like surface oxide character, this surface oxide is not of uniform thickness and thus would create pinholes if used in a JJ structure. In addition, the smoothness of the thicker film surface oxide may be beneficial for top electrode growth, especially since the RE process has shown the remarkable ability to form films with nearly identical physical properties on a wide variety of substrate materials. With these observations and comments in mind, RE growth should prove a very viable means to form all-MgB₂ JJ structures for future superconducting electronic devices.

5.6 Effects of Ion Milling on the MgB₂ Thin Film Surface

In preparing samples for UHV XPS studies, it is routine to bombard the surface with an ion beam to remove adventitious surface carbon and native oxides. Previous experiments [26, 41–43] used ion milling in an attempt to clean the surface MgB₂ material. The B 1s spectral region from each of these experiments is shown in Fig. 5.20 where the primary B 1s peak occurs at ~ 188 eV and caused each of these research groups to list this as the BE location for B atoms in MgB₂. While adventitious surface carbon is certainly removed in such a process, the very

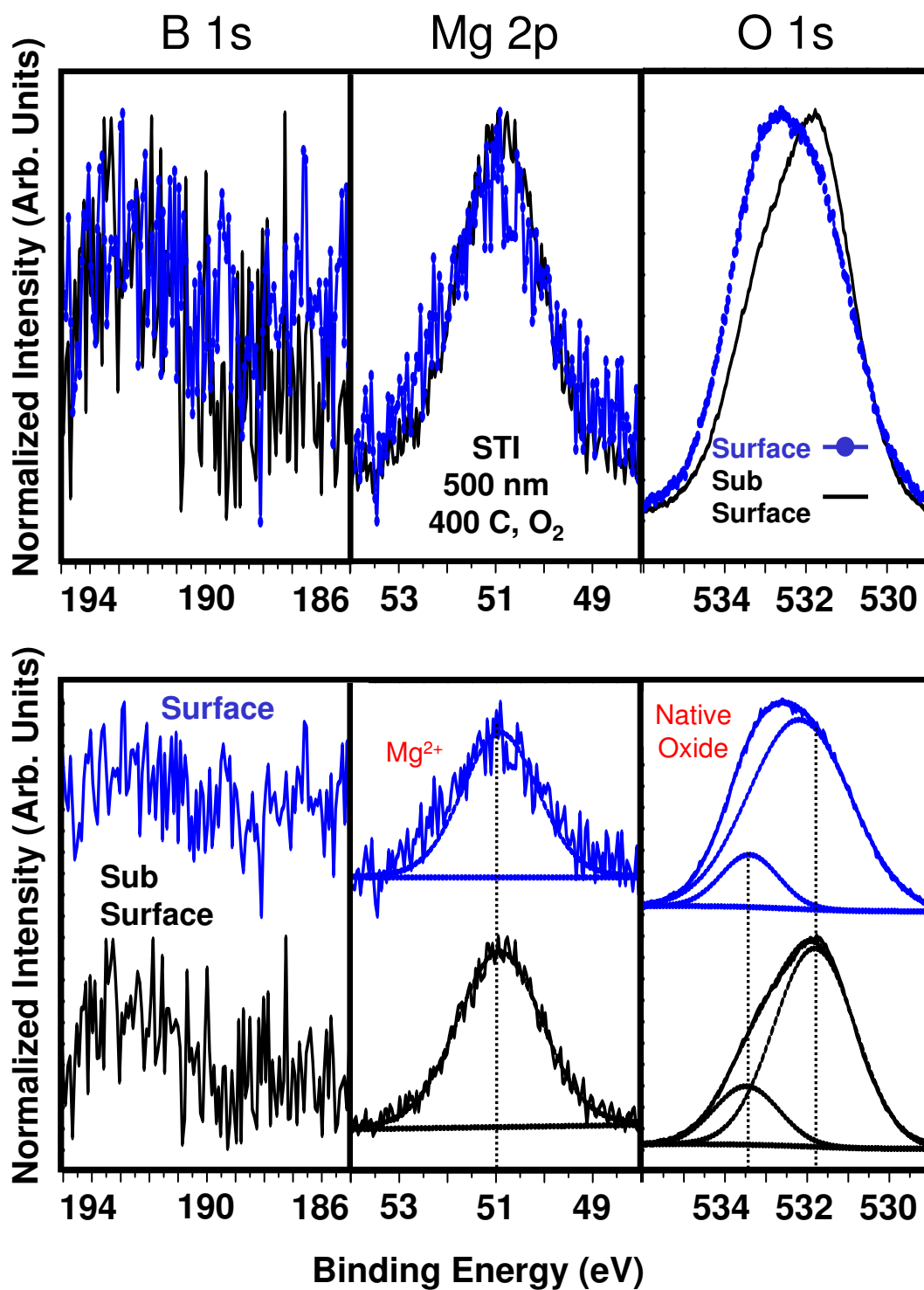


Figure 5.18: XPS data from a 500 nm thick RE MgB₂ thin film exposed to O₂ at a sample temperature of 400°C.

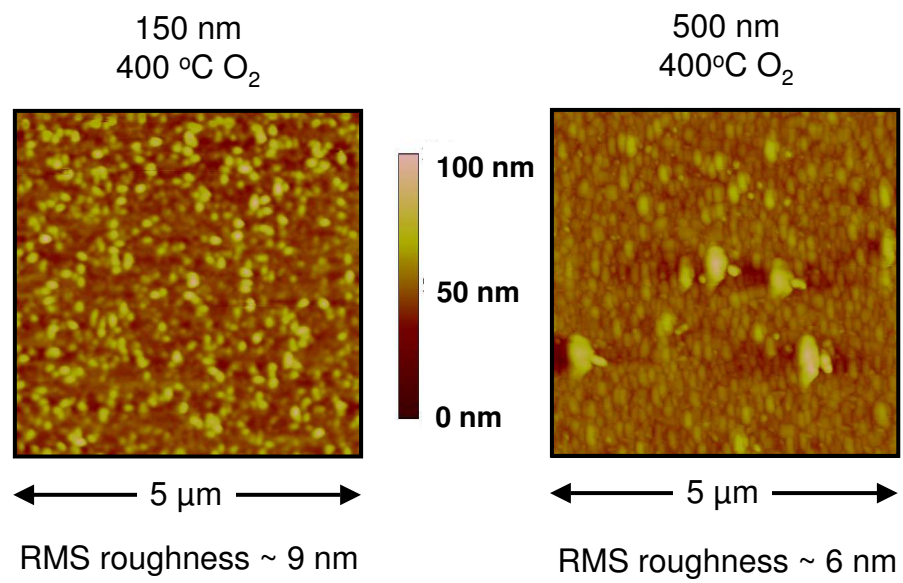


Figure 5.19: AFM scans from the surfaces of 150 nm and 500 nm thick RE MgB₂ thin films exposed to O₂ at a sample temperature of 400°C.

high reactivity of Mg, particularly when exposed to energetic O ions, and the low ion-milling rate of B, can change the chemical composition of a MgB₂ surface in unanticipated ways. This is the case even if UHP Ar process gas is used in the ion milling since only a very small residual oxygen component in the process gas and in the background ambient will result in oxygen ion formation that can alter the surface of an MgB₂ film faster than the ion milling removes the altered material.

The data shown in Fig. 5.21 illustrates the effect of Ar ion milling of the surface of a RE grown MgB₂ film deposited on R-Al₂O₃. In comparison to the initial data (also shown in Fig. 5.3), data taken from the sample after storage in a desiccator for roughly one year shows that the surface oxide has changed very little in such low vacuum conditions. The year-old sample was then subjected to ion milling in UHP Ar for 70 minutes at an energy of ~ 3 keV in a chamber pressure of $\sim 1 \times 10^{-8}$ Torr. This process had a major impact on the film surface chemistry. The Mg 2p spectrum shows that a thick layer of oxidized Mg formed on the sample surface, as indicated by the strong Mg²⁺ peak at ~ 51 eV. There is only a small signal from the underlying MgB₂ film found in the Mg 2p and B 1s spectra at ~ 49.5 eV and ~ 186.7 eV respectively. There is also a clear shift in the primary B 1s peak location to ~ 188 eV, which is the signature of elemental B and B sub-oxide, and is what appears in Fig 5.20 [26, 41–43]. The O 1s peak has also shifted to lower BE, which is an additional signature of a Mg-rich surface oxide. Longer exposure to ion milling leaves the surface largely unchanged from this result, with the exception that the intensity of the adventitious C signature (not shown) is greatly decreased. This experiment clarifies that the peaks attributable to the Mg and B atoms in the MgB₂ film are found at BEs of ~ 49.5 and ~ 186.7 eV, respectively. This result also shows the sensitivity of the MgB₂ surface to oxidation, even in UHV, and shows that typical device patterning techniques could significantly alter the

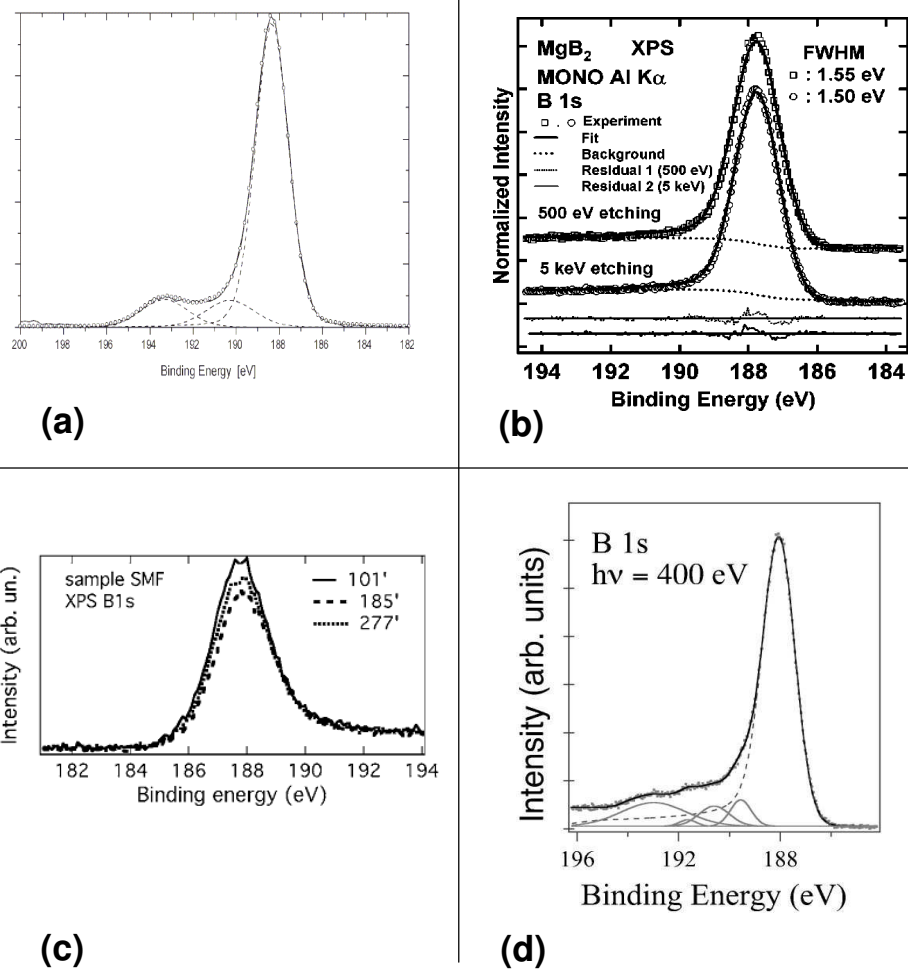


Figure 5.20: B 1s spectra from four experimental investigations, (a) ref [26], (b) ref [41], and (c) ref [42], (d) ref [43], all of which modify the MgB₂ surface with Ar ion milling.

MgB₂ electrode material if care is not taken during the device fabrication.

5.7 Effects of Etching the MgB₂ Thin Film Surface with Water

In the course of standard photolithography processes, samples are sometimes exposed to water. To study the effect of water exposure upon the oxidation of MgB₂, samples were submerged in distilled water for up to 2 hours and then studied with XPS. The XPS data suggest that the typical reaction is to both oxidize and etch the Mg-based oxides while forming elemental B and B sub-oxide. Upon re-exposure to atmosphere, some surface oxidation takes place forming small amounts of MgO, B₂O₃, and their hydroxide counterparts. Fig. 5.22 shows the effect of water etching on HPCVD and RE films of different thicknesses. In this section of the chapter I plot the XPS data (Fig. 5.22 and 5.33) such that the spectral regions all have the same scale and the signal intensities from each measurement are relative and not normalized. The data shows that both films have the same reaction. The B sub-oxide peaks show strong intensity increases while the MgO peak initially decreases and then increases in intensity. The data shows that although the thinner HPCVD film is completely etched away before the thicker RE film, the behavior of both films is essentially the same. The experiment suggests that surface Mg readily reacts with the oxygen in the water, but the B oxidizes much more slowly, if at all. The result of exposing a native MgB₂ oxide surface to water is to form a B rich surface material. After two hours of etching in water, the elemental B and B sub-oxide peaks dominate the B 1s spectrum and the MgB₂ film peaks in both the B 1s and Mg 2p spectra decrease, consistent with increased formation of elemental

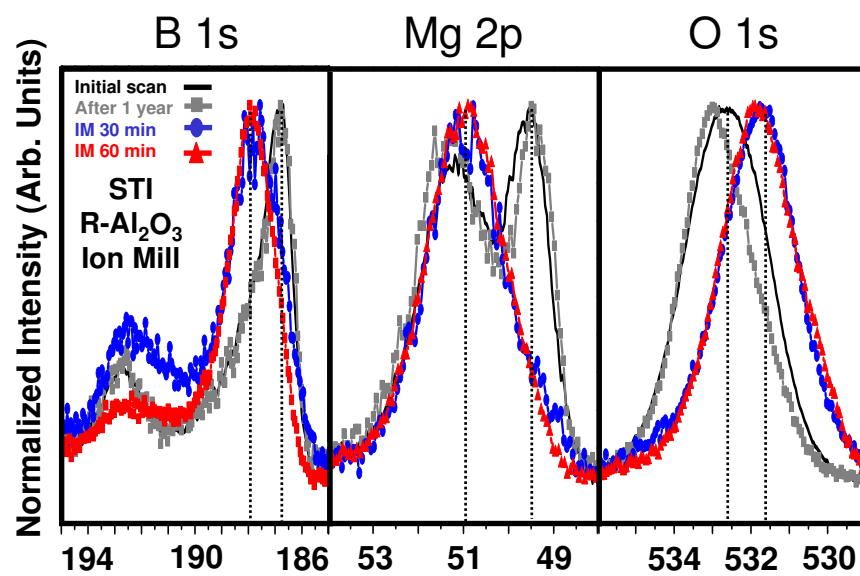


Figure 5.21: XPS data from an RE film, after a year of storage in a dessicator, and after Ar ion milling.

B and B sub-oxide and removal of Mg from the MgB_2 through reaction with OH^- and dissolution into the water. While the signal strengths of the various spectral peaks attributable to the mixed Mg-B oxide drop dramatically as the B sub-oxide content increases, the O 1s peak shows only a small upward shift in BE indicating that the surface oxide remains a mixture of Mg, B and O, albeit with a significant increase in the relative B concentration. This result is in agreement with data from a transport study of water etched HPCVD films which shows a substantial increase in film resistivity after water etching. [44] The C content in the surface oxide increases in relative intensity after initial water exposure and then decreases in relative intensity after prolonged water etching. The XPS measurement of increased B surface content in conjunction with the increased film resistivity suggests that the film surface is predominantly composed of highly resistive B after water etching.

The results of XPS studies of water etching experiments on oxidized HPCVD films is shown in Fig. 5.23. Here the effect of the water etching is largely the same as in the case of the control samples. Study of a sample that was oxidized at 200°C , which has a thin surface oxide layer, shows that the surface MgO component is initially etched away while Mg from the film is oxidized and subsequently etched. After one hour of etching, the film surface shows a significant amount of both MgO and B near the film surface. After two hours of etching, the film surface is largely unchanged which suggests that an MgO surface oxide is relatively effective in protecting the underlying MgB_2 film from water exposure. This claim is confirmed with the study of an HPCVD film that was oxidized at 400°C which initially has a thick MgO surface oxide. Even after two hours of water etching, the film surface still has the signature of MgO with only a small B signal present in the XPS scans. This suggests that a thick MgO layer will etch more slowly and effectively

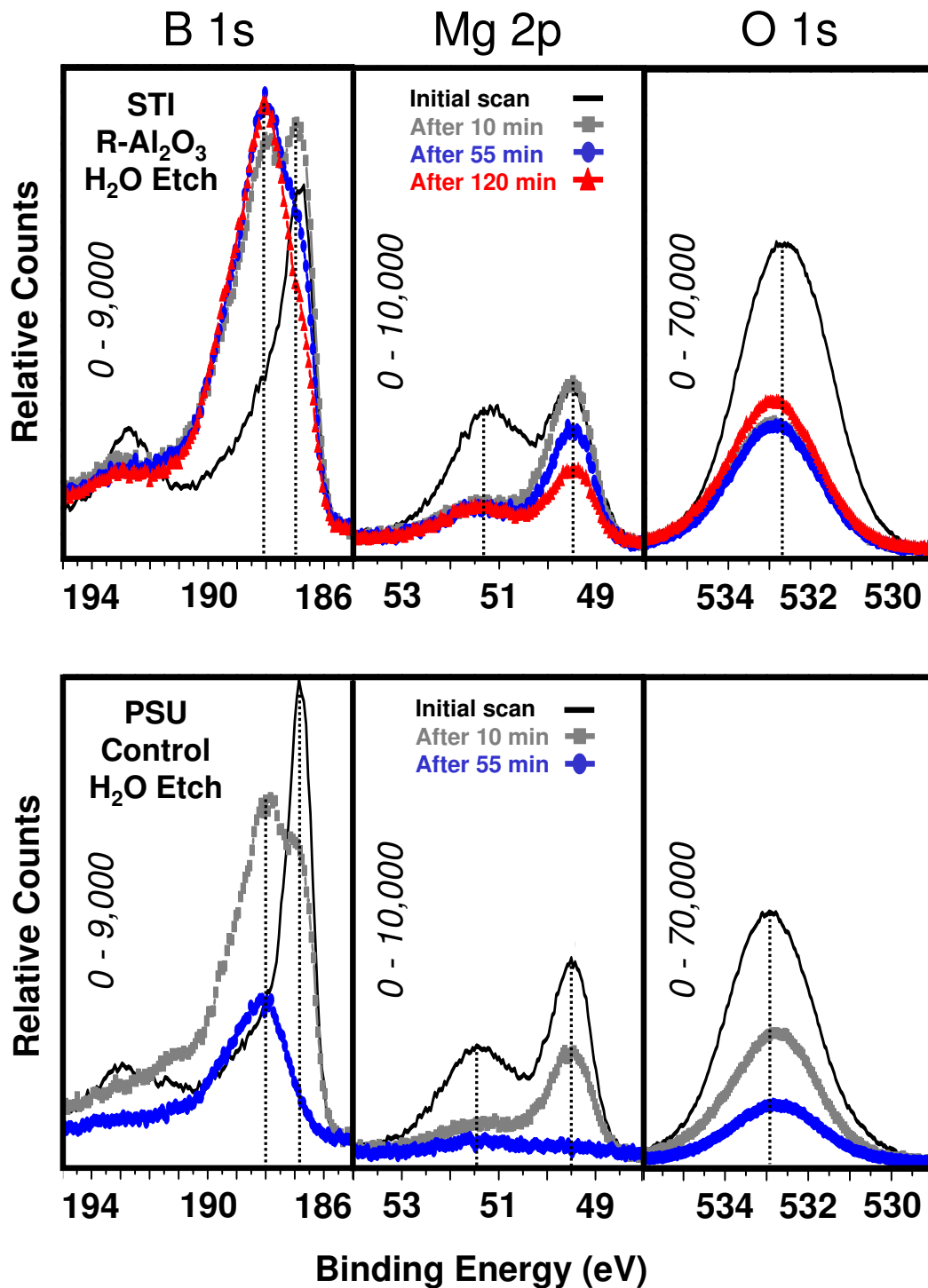


Figure 5.22: XPS data from control RE and HPCVD films etched in water.

protect the underlying MgB₂ film from oxidation and etching due to exposure to water. Hence, the formation of a MgB₂ / MgO bilayer could be a good passivation strategy for film protection in standard photolithography procedures.

5.8 Discussion and Conclusions

The formation of stable, high-quality JJ tunnel barriers on MgB₂ thin film surfaces is the major remaining requirement for the realization of MgB₂-based superconductor electronics. To be useful for most technologically important applications, such a tunnel barrier will have to ultimately be electrically thin, exhibiting a high J_C on the order of 10^4 A/cm², with a low junction specific resistance on the order of $30 \Omega(\mu\text{m})^2$. For typical tunnel barrier heights this will require a barrier thickness in the 1 to 1.5 nm range. Depositing such a thin layer uniformly on a polycrystalline surface, even a highly textured one, is a major if not insurmountable challenge. Hence, forming a thin tunnel barrier by a surface reaction, either through thermal oxidation or plasma nitridation, is the approach that has seen the greatest success in conventional superconducting electronics. Lightly oxidizing the surface of a MgB₂ film in a manner that forms a thin mixed Mg-B oxide is arguably an approach that could prove effective. To date, the best, low specific resistance tunnel contacts reported on MgB₂ films were made on HPCVD or RE films that were lightly oxidized to form a moderately thin ~ 3 -4 nm mixed MgB surface oxide. The possible, thicker oxidation of grain boundary regions by the high temperature oxidation process suggested by this work could also be a beneficial aspect of this approach as it could close off potential shorts. Of course it is essential that any surface oxide survive the deposition of a top electrode. The work presented in this chapter suggests that high temperature oxidation of an MgB₂ film forms a chem-

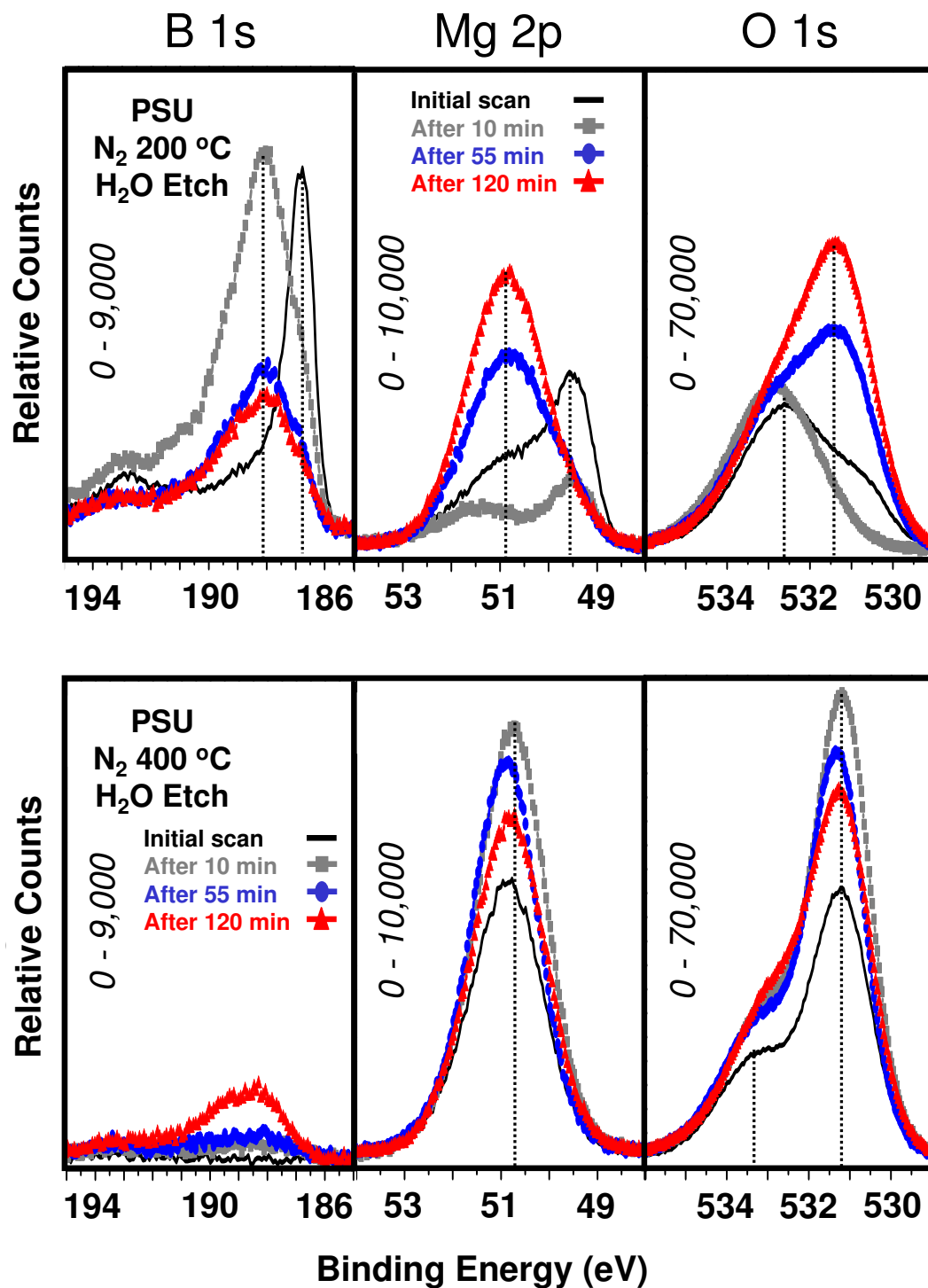


Figure 5.23: XPS data from oxidized HPCVD films etched in water.

ically stable MgO-like barrier material upon which a top MgB₂ electrode could likely be successfully grown. The remaining step to achieve this goal is to optimize the barrier formation process in terms of thickness and to confirm that the bottom electrode-barrier bilayer can withstand the temperature necessary to deposit the top electrode without substantial inter-diffusion or barrier degradation.

In summary, the highly reactive nature of Mg dominates the oxidation of MgB₂ thin film surfaces. The XPS data from MgB₂ films and surface oxides presented in this chapter show that Mg and B are both present in the native surface oxide. Exposure to UHP N₂ or O₂ promotes formation of MgO on the MgB₂ film surface. The surface becomes completely composed of MgO if the oxidation process is carried out at elevated temperature (400°C) for extended time. However, if the oxidation occurs at lower temperature(200°C), then the surface oxide formed is a mixed MgBO material. The layer-by-layer nature of the RE growth process generates an MgB₂ film with greater oxide content throughout, which dominates the composition of thicker films relative to thinner films. Etching experiments show that oxygen delivered using different mechanisms (exposure to atmosphere, N₂ or O₂ exposure at elevated temperatures, ion milling, and water exposure) alters the MgB₂ film surface in similar ways to different extents. O incorporation into the MgB₂ film and formation of elemental B and B suboxide during the film oxidation could influence tunneling transport and degrade device performance. Further correlation of the properties of these material phases and electronic transport studies may yield additional insights into optimal barrier formation techniques for JJ device development.

Table 5.1: Estimated HPCVD MgB₂ film stoichiometries

Sample	Take off angle(°)	Film	Oxide	Film (calibrated)	t _{MgO} (nm)	t _{B₂O₃} (nm)	t _{oxide} (nm)
control	90	MgB _{1.3}	MgB _{1.2} C _{1.3} O _{2.4}	MgB ₂	2.2	0.9	3.1
	20	MgB _{1.2}	MgB _{1.0} C _{1.7} O _{2.8}				
Mg anneal	90	MgB _{1.4}	MgB _{0.9} C _{1.5} O _{2.3}	MgB _{2.1}	2.5	0.9	3.4
	20	MgB _{1.4}	MgB _{0.8} C _{1.4} O _{2.4}				
400°C, N ₂ , 90 sec	90	MgB _{1.4}	MgB _{1.0} C _{0.7} O _{2.1}	MgB ₂	3.3	0.9	4.2
	20	MgB _{1.5}	MgB _{0.7} C _{1.0} O _{2.4}				
200°C, N ₂ , 30 min	90	MgB _{1.3}	MgB _{1.0} C _{1.0} O _{1.8}	MgB ₂	2.4	0.7	3.1
	20	MgB _{1.2}	MgB _{1.0} C _{1.7} O _{2.4}				
400°C, N ₂ , 30 min	90		MgC _{0.3} O _{1.1}				
	20		MgC _{0.4} O _{1.2}				

Table 5.2: Estimated RE MgB₂ film stoichiometries

Sample	Take off angle(°)	Film	Oxide	Film (calibrated)	t_{MgO} (nm)	$t_{B_2O_3}$ (nm)	t_{oxide} (nm)
control	90	MgB _{1.3}	MgB _{1.2} C _{0.8} O _{2.5}	MgB ₂	3.0	1.3	4.3
	20	MgB _{1.1}	MgB _{1.4} C _{1.6} O _{3.4}				
150 nm control	90	MgB _{0.9}	MgB _{0.5} C _{0.4} O _{2.6}	MgB _{1.4}	2.4	0.7	3.1
	20	MgB _{0.7}	MgB _{0.3} C _{1.5} O _{4.1}				
500 nm control	90	MgB _{1.1}	MgB _{0.9} C _{1.0} O _{3.4}	MgB _{1.7}	2.5	1.1	3.6
	20	MgB _{1.4}	MgB _{0.7} C _{0.9} O _{3.0}				
150 nm 240°C, O ₂	90	MgB _{0.8}	MgB _{0.6} C _{1.5} O _{2.2}	MgB _{1.2}	2.4	0.5	2.9
	20	MgB _{0.9}	MgB _{0.2} C _{2.0} O _{2.8}				
500 nm 240°C, O ₂	90	MgB _{1.4}	MgB _{0.7} C _{1.8} O _{2.7}	MgB _{2.2}	3.1	1.0	4.1
	20	MgB _{1.1}	MgB _{0.4} C _{2.1} O _{2.6}				
150 nm 400°C, O ₂	90	MgB _{0.8}	MgB _{0.1} C _{0.7} O _{1.5}	MgB _{1.3}	6.3		6.3
	20	MgB _{1.7}	MgB _{0.2} C _{1.0} O _{1.7}				
500 nm 400°C, O ₂	90		MgB _{0.1} C _{1.3} O ₄				
	20		MgB _{0.1} C _{2.1} O _{4.1}				

REFERENCES

- [1] J. Nagamatsu, N. Nakagawa, T. Muranaka, Y. Zenitani, and J. Akimitsu, Superconductivity at 39 K in magnesium diboride, *Nature* **410**, 63 (2001).
- [2] J. Kortus, I. I. Mazin, K. D. Belashchenko, V. P. Antropov, L. L. Boyer, Superconductivity of metallic boron in MgB₂, *Phys. Rev. Lett.* **86**, 4656 (2001).
- [3] S. L. Bud'ko, G. Lapertot, C. Petrovic, C. E. Cunningham, N. Anderson, and P. C. Canfield, Boron isotope effect in superconducting MgB₂, *Phys. Rev. Lett.* **86**, 1877 (2001).
- [4] A. Y. Liu, I. I. Mazin, and J. Kortus, Beyond Eliashberg superconductivity in MgB₂: Anharmonicity, two-phonon scattering, and multiple gaps, *Phys. Rev. Lett.* **87**, 087005 (2001).
- [5] J. M. An, and W. E. Pickett, Superconductivity of MgB₂: Covalent bonds driven metallic, *Phys. Rev. Lett.* **86**, 4366 (2001).
- [6] D. C. Larbalestier, L. D. Cooley, M. O. Rikel, A. A. Polyanskii, J. Jiang, S. Patnaik, X. Y. Cai, D. M. Feldmann, A. Gurevich, A. A. Squitieri, M. T. Naus, C. B. Eom, E. E. Hellstrom, R. J. Cava, K. A. Regan, N. Rogado, M. A. Hayward, T. He, J. S. Slusky, P. Khalifah, K. Inumaru, M. Haas, Strongly linked current flow in polycrystalline forms of the superconductor MgB₂, *Nature* **410**, 186 (2001).
- [7] H. J. Choi, D. Roundy, H. Sun, M. L. Cohen, and S. G. Louie, The origin of the anomalous superconducting properties of MgB₂, *Nature* **418**, 758 (2002).
- [8] P. C. Canfield, D. K. Finnemore, S. L. Bud'ko, J. E. Ostenson, G. Lapertot, C. E. Cunningham, and C. Petrovic, Superconductivity in dense MgB₂ wires, *Phys. Rev. Lett.* **86**, 2423 (2001).
- [9] D. K. Finnemore, J. E. Ostenson, S. L. Bud'ko, G. Lapertot, P. C. Canfield, Thermodynamic and transport properties of superconducting (Mg¹⁰B₂), *Phys. Rev. Lett.* **86**, 2420 (2001).
- [10] W. N. Kang, H. J. Kim, E. M. Choi, C. U. Jung, and S. L. Lee, MgB₂ superconducting thin films with a transition temperature of 39 kelvin, *Science* **292**, 1521 (2001).

- [11] D. Larbalestier, A. Gurevich, D. M. Feldmann, and A. Polyanskii, High- T_C superconducting materials for electric power applications, *Nature* **414**, 368 (2001).
- [12] J. M. Rowell, The widely variable resistivity of MgB_2 samples, *Supercond. Sci. Technol.* **16**, R17 (2003).
- [13] X. H. Zeng, A. V. Pogrebnyakov, A. Kotcharov, J. E. Jones, X. X. Xi, E. M. Lyszczek, J. M. Redwing, S. Y. Xu, J. Lettieri, D. G. Schlom, W. Tian, X. Q. Pan, and Z. K. Liu, In situ epitaxial MgB_2 thin films for superconducting electronics, *Nature Materials* **1**, 35 (2002).
- [14] D. Mijatovic, A. Brinkman, I. Oomen, G. Rijnders, H. Hilgenkamp, H. Rogalla, and D. H. A. Blank, Magnesium-diboride ramp-type Josephson junctions, *Appl. Phys. Lett.* **80**, 2141 (2002).
- [15] M. Naito, and K. Ueda, MgB_2 thin films for superconducting electronics, *Supercond. Sci. Technol.* **17**, R1 (2004).
- [16] H. Shimakage, K. Tsujimoto, Z. Wang, and M. Tonouchi, All- MgB_2 tunnel junctions with aluminum nitride barriers, *Appl. Phys. Lett.* **86**, 072512 (2005).
- [17] A. Saito, A. Kawakami, H. Shimakage, H. Terai, and Z. Wang, Josephson tunneling properties in $MgB_2/AlN/NbN$ tunnel junctions, *J. Appl. Phys.* **92**, 7369 (2002).
- [18] B. H. Moeckly, and W. S. Ruby, Growth of high-quality large-area MgB_2 thin films by reactive evaporation, *Supercond. Sci. Technol.* **19**, L21–L24 (2006).
- [19] M. van Zalk, A. Brinkman, A. A. Golubov, H. Hilgenkamp, T. H. Kim, J. S. Moodera, and H. Rogalla, Fabrication of multiband MgB_2 tunnel junctions for transport measurements, *Supercond. Sci. Technol.* **19**, S226 (2006).
- [20] T. H. Kim, and J. S. Moodera, Magnesium diboride superconductor thin film tunnel junctions for superconductive electronics, *J. Appl. Phys.* **100**, 113904 (2006).
- [21] S. A. Cybart, K. Chen, Y. Cui, Q. Li, X. X. Xi, and R. C. Dynes, Planar MgB_2 Josephson junctions and series arrays via nanolithography and ion damage, *Appl. Phys. Lett.* **88**, 012509 (2006).

- [22] Y. Cui, K. Chen, Q. Li, X. X. Xi, and J. M. Rowell, Degradation-free interfaces in MgB₂/insulator/Pb Josephson tunnel junctions, *Appl. Phys. Lett.* **89**, 202513 (2006).
- [23] K. Chen, Y. Cui, Q. Li, C. G. Zhuang, Z.-K. Liu, and X. X. Xi, Study of MgB₂/I/Pb tunnel junctions on MgO (211) substrates, *Appl. Phys. Lett.* **93**, 012502 (2008).
- [24] R. K. Singh, R. Gandikota, J. Kim, N. Newman, J. M. Rowell, MgB₂ tunnel junctions with native or thermal oxide barriers, *Appl. Phys. Lett.* **89**, 042512 (2006).
- [25] R. P. Vasquez, C. U. Jung, M. S. Park, H. J. Kim, J. Y. Kim, and S. I. Lee, X-ray photoemission study of MgB₂, *Phys. Rev. B* **64**, 052510 (2001).
- [26] K. B. Garg, T. Chatterji, S. Dalela, M. Heinonnen, J. Leiro, B. Dalela, R. K. Singhal, Core level photoemission study of polycrystalline MgB₂, *Solid State Commun.* **131**, 343 (2004).
- [27] R. P. Vasquez, Intrinsic Photoemission Signals, Surface Preparation, and Surface Stability of High Temperature Superconductors, *J. Electron Spectrosc. Relat. Phenom.* **66**, 209 (1994).
- [28] J. C. Fuggle, XPS, UPS and XAES Studies of oxygen adsorption on polycrystalline Mg at 100K and 300K, *Surf. Sci.* **69**, 581 (1977).
- [29] J. S. Corneille, J.-W. He, and D. W. Goodman, XPS characterization of ultrathin MgO films on a Mo(100) surface, *Surf. Sci.* **306**, 269 (1994).
- [30] D. Peterka, C. Tegenkamp, K.-M. Schroder, W. Ernst, and H. Pfnur, Oxygen surplus and oxygen vacancies on the surface of epitaxial MgO layers grown on Ag(100), *Surf. Sci.* **431**, 146 (1999).
- [31] P. Liu, T. Kendelewicz, G. E. Gordon, and G. A. Parks, Reaction of water with MgO(100) surfaces. Part I: Synchrotron X-ray photoemission studies of low-defect surfaces, *Surf. Sci.* **413**, 287 (1998).
- [32] W. E. Moddeman, A. R. Burke, W. C. Bowling, and D. S. Foose, Surface oxides of boron and B₁₂O₂ as determined by XPS, *Surf. Interface Anal.* **14**, 224 (1989).

- [33] Y. Wang and M. Trenary, Surface chemistry of boron oxidation. 2. The reactions of boron oxides B_2O_2 and B_2O_3 with boron films grown on tantalum(110), *Chem. Mater.* **5**, 199 (1993).
- [34] C. W. Ong, H. Huang, B. Zheng, R. W. M. Kwok, Y. Y. Hui, and W. M. Lau, X-ray photoemission spectroscopy of nonmetallic materials: Electronic structures of boron and B_xO_y , *J. Appl. Phys.* **95**, 3527 (2004).
- [35] W. K. Park, R. Wilken, K. Parkinson, L. Greene, B. H. Moeckly, and J. Rowell, Unpublished (2005).
- [36] J. F. Moulder, W. F. Stickle, P. E. Sobol, and K. D. Bomben, *Handbook of X-Ray Photoelectron Spectroscopy*, ULVAC-PHI, Inc. and Physical Electronics USA, Inc., Chigasaki, Japan (1995).
- [37] R. N. King, Esca binding energy calculator, Surface Science Laboratories, Mountain View, CA, USA (1984).
- [38] J. M. Hill, D. G. Royce, C. S. Fadley, L.F. Wagner, and F. J. Grunthaner, Properties of Oxidized Silicon as Determined by Angular-Dependent X-ray Photoelectron Spectroscopy, *Chem. Phys. Lett.* **44**, 225 (1976).
- [39] S. Tanuma, C. J. Powell, D. R. Penn, Calculations of Electron Inelastic Mean Free Paths (IMFPS).4. Evaluation of Calculated IMFPS and of the Predictive IMFPS Formula TPP-2 for Electron Energies between 50 and 2000 eV., *Surf. Interf. Anal.* **21**, 165 (1993).
- [40] X. Z. Liao, A. Serquis, Y. T. Zhu, J. Y. Huang, L. Civale, D. E. Peterson, F. M. Mueller, and H. F. Xu, $Mg(B,O)_2$ precipitation in MgB_2 , *J. Appl. Phys.* **93**, 6208 (2003).
- [41] C. Jariwala, A. Chainani, S. Tsuda, T. Yokoya, S. Shin, Y. Takano, K. Togano, S. Otani, and H. Kito, Comparative study of the electronic structure of MgB_2 and ZrB_2 , *Phys. Rev. B* **68**, 174506 (2003).
- [42] A. Goldoni, R. Larciprete, S. Lizzit, S. La Rosa, A. Bianco, and M. Bertolo, Occupied density of states in MgB_2 revealed by photoemission microscopy, *Phys Rev B* **66**, 132503 (2002).
- [43] A. Santoni, U. B. Vetrella, G. Celentano, U. Gambardella, and A. Mancini, X-ray photoemission study of MgB_2 films synthesized from in-situ annealed MgB_2/Mg multilayers, *Appl. Phys. A-Mater. Sci. Process.* **86**, 485 (2007).

- [44] Y. Cui, J. E. Jones, A. Beckley, R. Donovan, D. Lishego, E. Maertz, A. V. Pogrebnyakov, P. Orgiani, J. M. Redwing, and X. X. Xi, Degradation of MgB_2 thin films in water, *IEEE Trans. Appl. Supercond.* **15**, 224–227 (2005).

XPS STUDIES OF AlN TUNNEL BARRIERS

6.1 Introduction

Ultrathin films of Aluminum Nitride (AlN) are applicable as tunnel barriers in both superconducting Josephson Junctions (JJs) and in Magnetic Tunnel Junctions (MTJs). This material is potentially useful as a replacement for Aluminum Oxide (AlO_x) for two major reasons. AlN is composed of covalent Al-N bonds and when made stoichiometric should be unreactive at room temperature. In addition to this physical property, AlO_x is extremely difficult to make in its stoichiometric form (Al_2O_3) using conventional thermal oxidation techniques upon thin films of Al. Such thermally oxidized Al films are typically O deficient [1], which means there are O vacancies in the tunnel barrier layer which are sources of electronic noise [2], which is particularly detrimental to JJ performance, and may promote spin scattering which degrades MTJ device sensitivity.

With the discovery of extremely high TMR in MgO-based MTJs, AlO_x is no longer the tunnel barrier of choice for future MTJs. However, companies such as Everspin still use AlO_x as the tunnel barrier in some of their product lines since it is a more reliable material in terms of uniform performance in contemporary devices. [3] Although AlN is a candidate tunnel barrier material, several researchers have previously shown that it is very difficult to make pure AlN in any conventional thin film growth process because AlO_x , AlO_xN_y , and AlN all form during the deposition. Transport measurements of MTJs with AlO_xN_y barriers made by reactive sputtering and direct oxidation with barrier stoichiometries measured by Rutherford Back Scattering show that AlO_x performance is better than AlO_xN_y

performance, and that both of these tunnel barriers perform better than AlN. [4]

Although AlN has not been shown to be an ideal material for MTJs, it is still used widely in JJs. Nb / AlN / Nb [5–14], MgB₂ / AlN / MgB₂ [15] and NbN / AlN / MgB₂ JJs [16] have all been successfully fabricated. The ultimate goal of this project is to study the effect of O inclusions within the AlN tunnel barrier upon JJ device performance. The XPS studies discussed in this chapter represent the first step in this correlated materials and electronic transport research that aims to improve the understanding of how to form ideal AlN barriers for JJs. I started this study by developing the growth techniques for the film stacks, performing the XPS studies contained in this chapter, and by taking some initial STS data on AlN barrier layers. With the inclusion of more co-workers on the project, the scope of the investigation has grown such that currently Yun Li is exploring the behavior of AlN (AlO_xN_y) tunnel barriers. She is also working towards making film layers for patterning devices and for Pinshane Huang who is beginning an STEM/EELS investigation that should make further XPS studies unnecessary. Therefore, the data and discussion presented in this chapter serve to provide some feedback regarding the chemistry of the structures that form in the various growth processes. My goal is to provide some insight regarding which techniques are likely to be the best for growth of JJ structures that can be made by our team.

6.2 Experimental Details

The details of the spectrometer are the same as in Chapters 3 and 5. It was calibrated to the Au 4f_{7/2} line at 83.96 eV and the system has a resolution of \sim 0.5 eV. I grew the thin film samples using several different techniques in both Prep

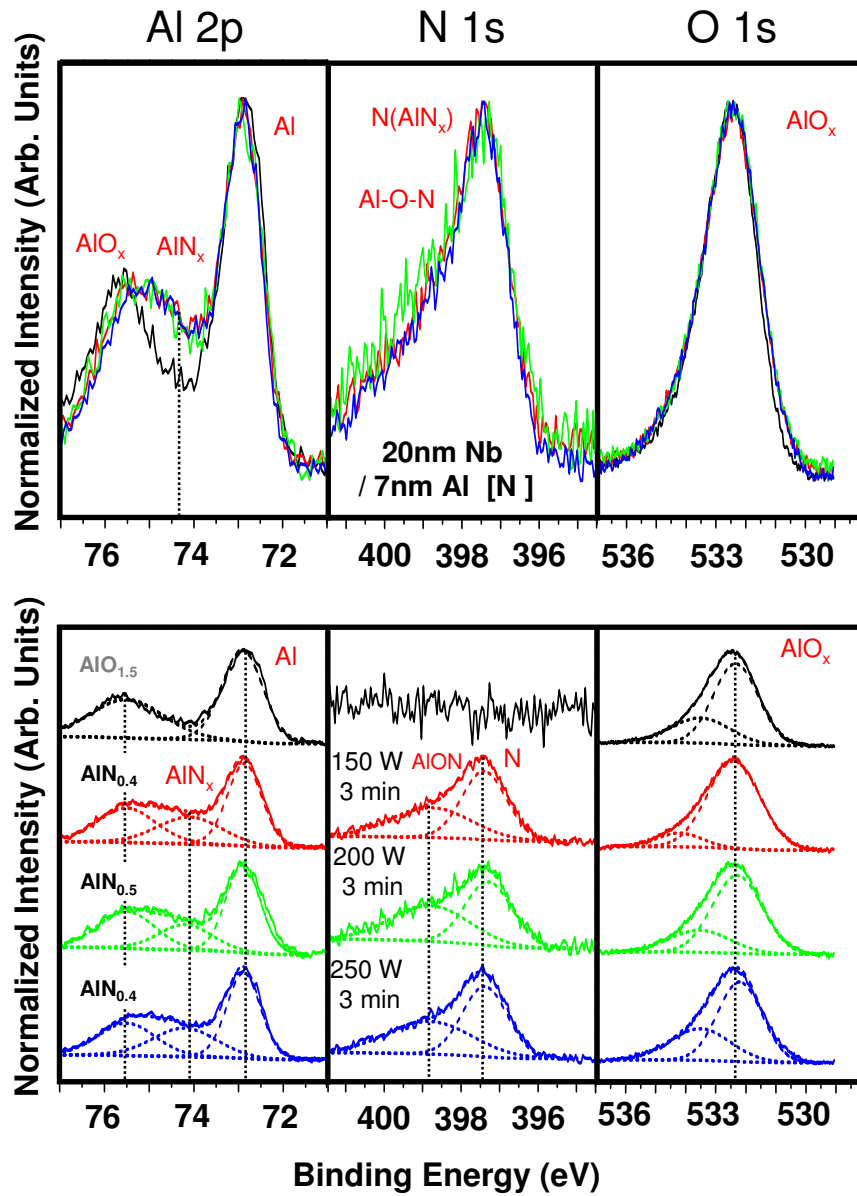


Figure 6.1: XPS data from Nb / Al films exposed to a N beam after in-situ vacuum transfer.

1 and Prep 2 and then vacuum transferred them to the XPS system for study. I performed the first set of experiments on 20 nm Nb / 7 nm Al bilayers that I e-beam (Nb) and thermally (Al) evaporated on thermally oxidized Si before exposing them to a beam of atomic N at various powers for different times. I vacuum transferred some samples from one deposition chamber to another in the interconnected film growth system before N exposure, and I exposed some samples to N directly after thin film growth without chamber transfer. I studied a second set of samples that included sputtered Nb / AlN bilayers grown on a Si / 8.5 nm Au Schottky barrier in the hopes of taking BEEM measurements. However, Nb scatters ballistic electrons substantially, so I could not obtain any BEEM current. I formed the 6.5 nm thick dc sputtered Nb base electrode on the thermally evaporated Au layer at 100 W sputtering power, and then I deposited the AlN layer with reactive rf sputtering under two different conditions. I deposited the AlN at 100 W rf power in either 100% Ar or in 100% N₂. [17, 18] These films are identical to several films studied by Yun Li with Scanning Tunneling Spectroscopy (STS) and her work continues at present to investigate the influence of O within the AlN upon the barrier bandgap. I made most of the samples in pairs where I annealed one of each pair in the oven in Prep 1 at 250 or 300°C for 1 hour and I normalized all of the data in this chapter to the highest intensity signal in each spectral region.

6.3 Nitrogen Beam Exposed Aluminum Films

The data presented in this section are from Al films that were exposed to a beam of atomic N at various power levels, either after in-situ vacuum transfer to an adjacent chamber or within the same chamber in which the films were deposited. The data in Figure 6.1 are from Si / SiO_x / 20 nm Nb / Al films that were first

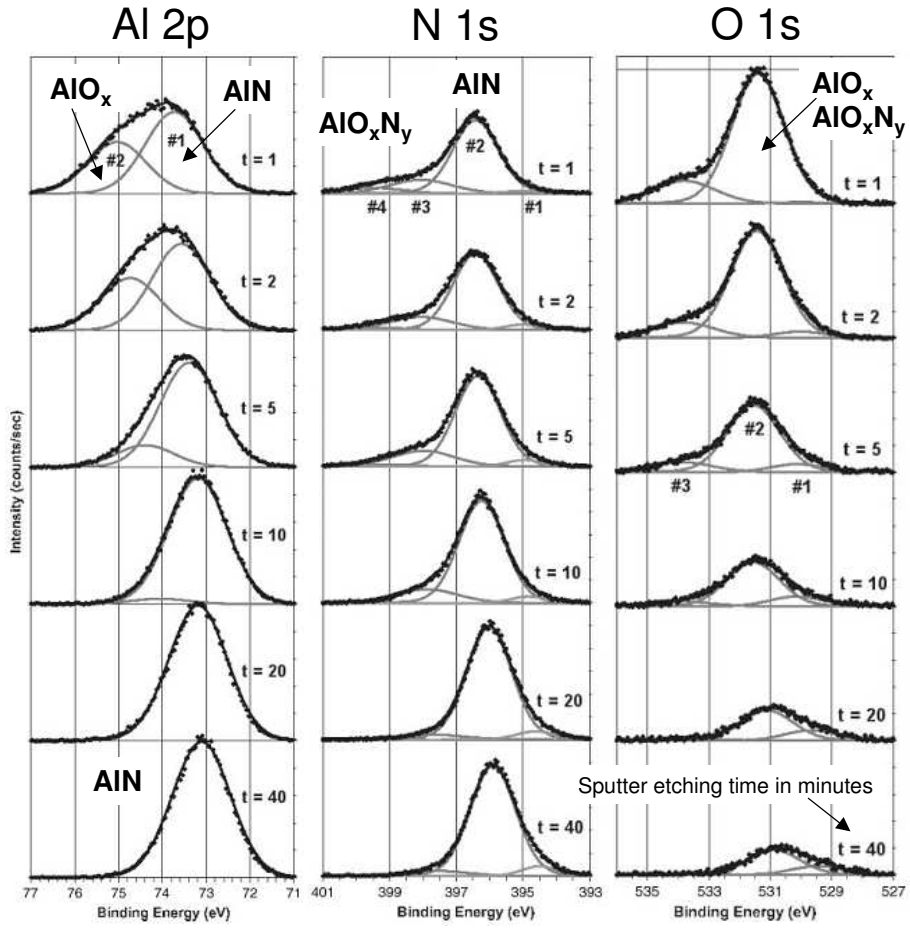


Figure 6.2: XPS data from sputter-etched, air-exposed PSMBE AlN films (from ref [19]).

vacuum transferred in-situ to an adjacent chamber for N beam exposure and then vacuum transferred to the XPS system for study. A bare Al film was also studied as a control sample to aid the identification of the Al 2p photoemission peak for AlO_x which appears at ~ 75.5 eV. The other samples in Figure 6.1 were exposed to the atomic N beam at 150, 200, or 250 W for 3 min. Each of these samples shows both AlO_x (~ 75.5 eV) and AlN (~ 74.5 eV) species in addition to the signature of metallic Al (~ 73 eV) in the Al 2p spectral region. The N 1s spectral region shows the presence of two peaks. The lower binding energy (BE) peak at ~ 397.5 eV is attributable to the N within the AlN film and the higher BE peak is due either to N that is bonded with both Al and O or to N chemisorbed on the film surface. The O 1s spectral region also contains two peaks. The lower BE peak is due to O in the AlO_x component because the peak location is the same for the control AlO_x sample and the test films (~ 532 eV). [1] The higher BE peak is likely due to O that is chemisorbed on the film surface. Estimates of film stoichiometry suggest that the films are nitrogen deficient ($\text{AlN}_{0.4-0.5}$) which is likely due to the partial film oxidation preventing nitridation. These peak assignments are similar to those measured by Rosenberger and co-workers (see Fig. 6.2) [19] who sputter-etched air-exposed plasma source molecular beam epitaxy grown AlN films, Perrem and co-workers (see Fig. 6.3) [20] who abrasive polished oxidized AlN films, and Liao and co-workers who studied air-exposed and heat treated AlN powders (see Fig. 6.4) [21].

The data from the samples in Figure 6.1 indicate that merely exposing the Al film to high vacuum conditions ($\sim 5 \times 10^{-7}$ Torr) is sufficient to lightly oxidize the film surface. Since the samples all receive the same vacuum transfer dose ($\sim 10^{-5}$ Torr-seconds) the data suggest that either the vacuum exposure before nitridation or the vacuum exposure during vacuum transfer is sufficient to partially oxidize

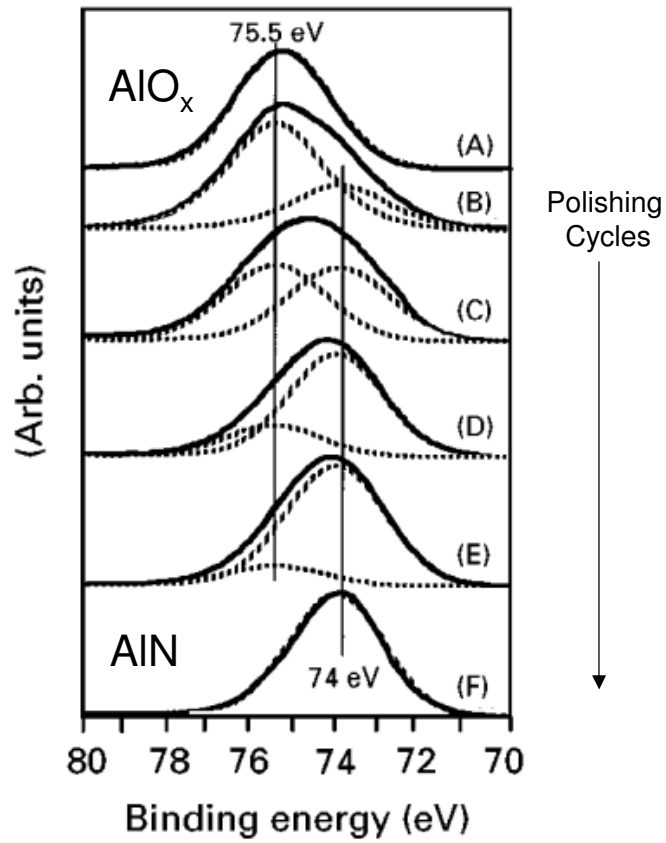


Figure 6.3: XPS data from abrasively polished oxidized AlN films (from ref [20]).

the film surface. These measurements show that the low power N exposure used to form these AlN films is insufficient to fully nitridize the film surface and that some Al is oxidized in this process. I carried out similar experiments at higher N beam power levels of 400 and 600 W for significantly longer times of 15 or 30 minutes. The XPS data from these films (not shown) have AlN Al 2p signal levels that are identical to the data from the samples shown in Figure 6.1, even after UHV annealing at 250°C. This suggests that the in-situ transfer process initially oxidizes the film, which makes the surface less reactive to the subsequent exposure to the atomic N beam.

The XPS data shown in Figure 6.5 are from films that I processed in a fashion similar to those discussed above with one major difference. I re-configured the deposition chamber for the growth of these films such that I grew the Al film in the same chamber where the N beam exposure process took place. These samples are similar to those in Figure 6.1 in terms of their photoemission spectra and estimated stoichiometry values ($\text{AlN}_{0.5-0.6}$). However, there is slightly more AlN Al 2p signature in these films in comparison to those on Figure 6.1. Annealing the samples to 300°C for 1 hour slightly changes the sample chemistry. The first notable change is that the AlO_x Al 2p peak increases in signal intensity relative to the AlN Al 2p peak. Also, the higher BE N 1s peak is reduced in signal intensity relative to the AlN N 1s peak and the estimated N film content increases. These changes suggest that annealing drives O which is bonded to both Al and N (higher BE N 1s peak) into the AlO_x , which is probably lower in the film stack and thus accounts for the apparent increase in the N film content. The O 1s spectra are very similar in shape and intensity to those in Figure 6.1 and do not change with sample annealing, suggesting that the AlO_x component is not reduced during the annealing process. These measurements of N beam exposed AlN (AlO_xN_y)

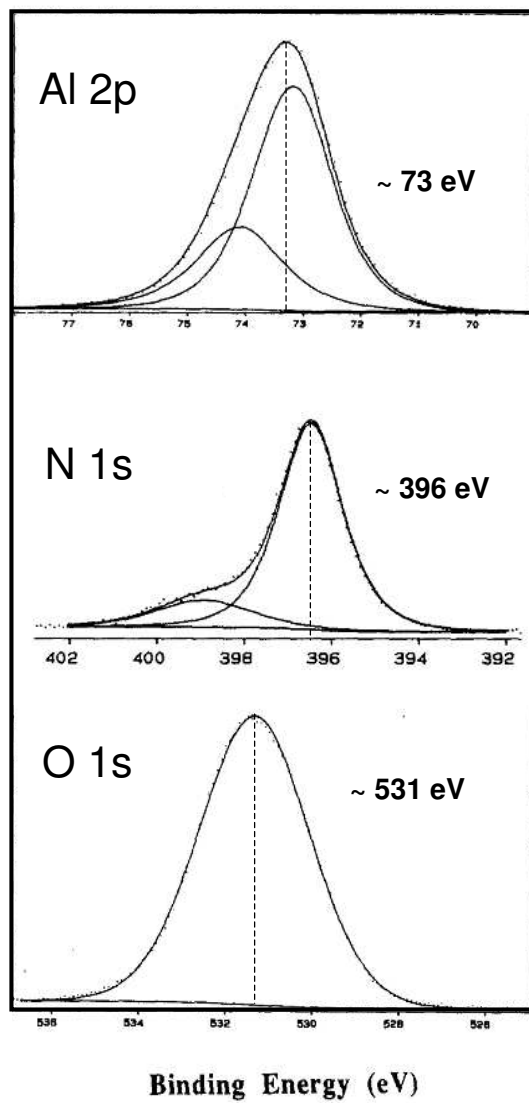


Figure 6.4: XPS data from air-exposed AlN powder from ref [21].

films clearly show that the films always contain both AlO_x and AlN which would certainly effect electron transport in a working device.

Nb / Al / AlN / Nb JJs with AlN tunnel barriers made with a similar N beam exposure process show very good device behavior. [22, 23] Given the high quality of the devices presented in these publications, it is unlikely but difficult to say for sure whether the films in these JJs contain some AlO_x . This points to an interesting extension of the gettering process during film growth described in chapters 2, 3, 4 and 7 of this dissertation. The vacuum chamber where the atomic N source is located also contains a Ti sublimation pump. A batch of test experiments utilizing this pump for its gettering properties during N beam exposure could substantially reduce AlO_x formation during film growth, which will likely make better AlN barrier materials.

6.4 RF Sputtered AlN Films

Sputtering is an effective way to make uniform thickness thin film structures over large area substrates. In an effort to explore an alternative approach to forming AlN with atomic N beam exposure and in an effort to develop deposition techniques suitable for making high quality AlN-based JJs, I investigated the growth of AlN barrier layers using reactive rf sputtering from an AlN target in either 100% ultra-high purity (UHP) Ar or 100% UHP N_2 . I grew all the AlN layers in this section directly on a Si / 8.5 nm Au / 6.5 nm Nb base structure as described above. In Figure 6.6, I compare XPS data from 2 nm thick AlN films grown in Ar with XPS data from 2 nm thick AlN films grown in N_2 . There are very significant differences between the films made with these two sputtering gasses. The Al 2p,

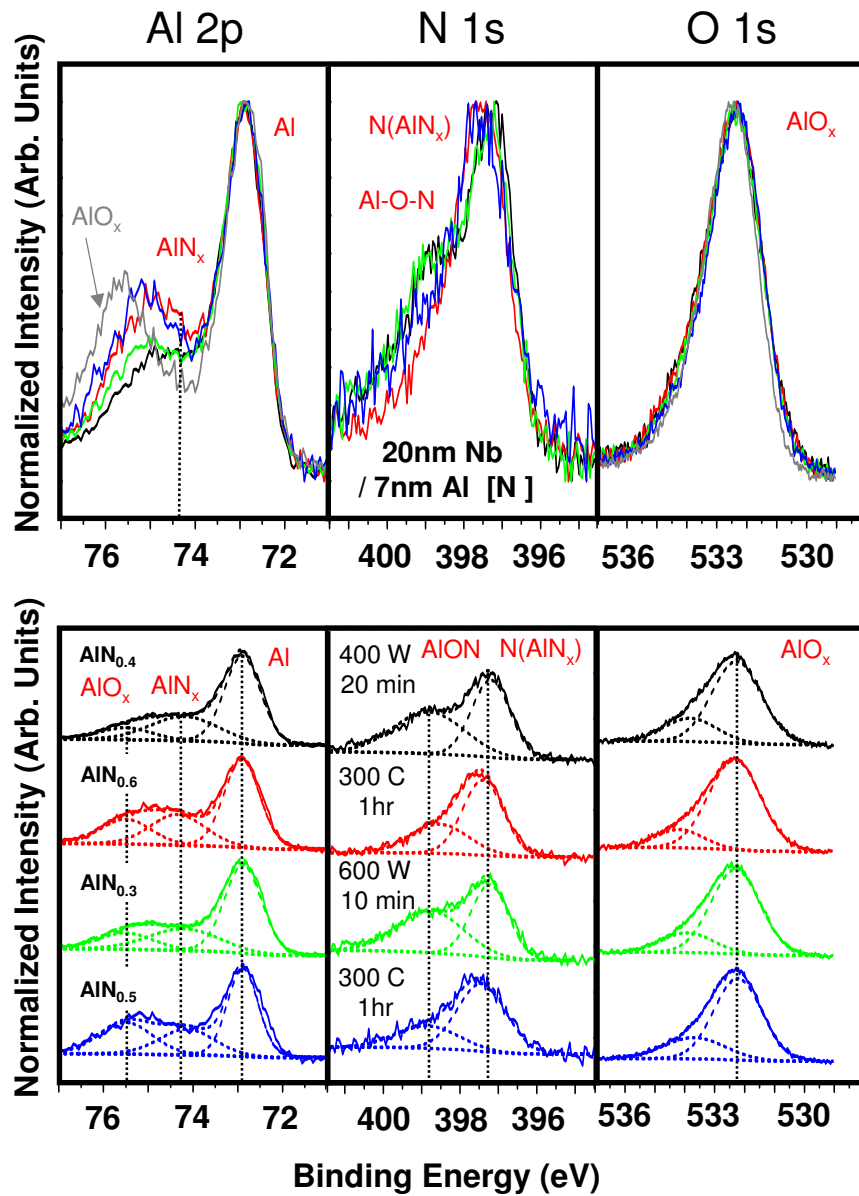


Figure 6.5: XPS data from Nb / Al films exposed to a N beam at high power before and after vacuum annealing.

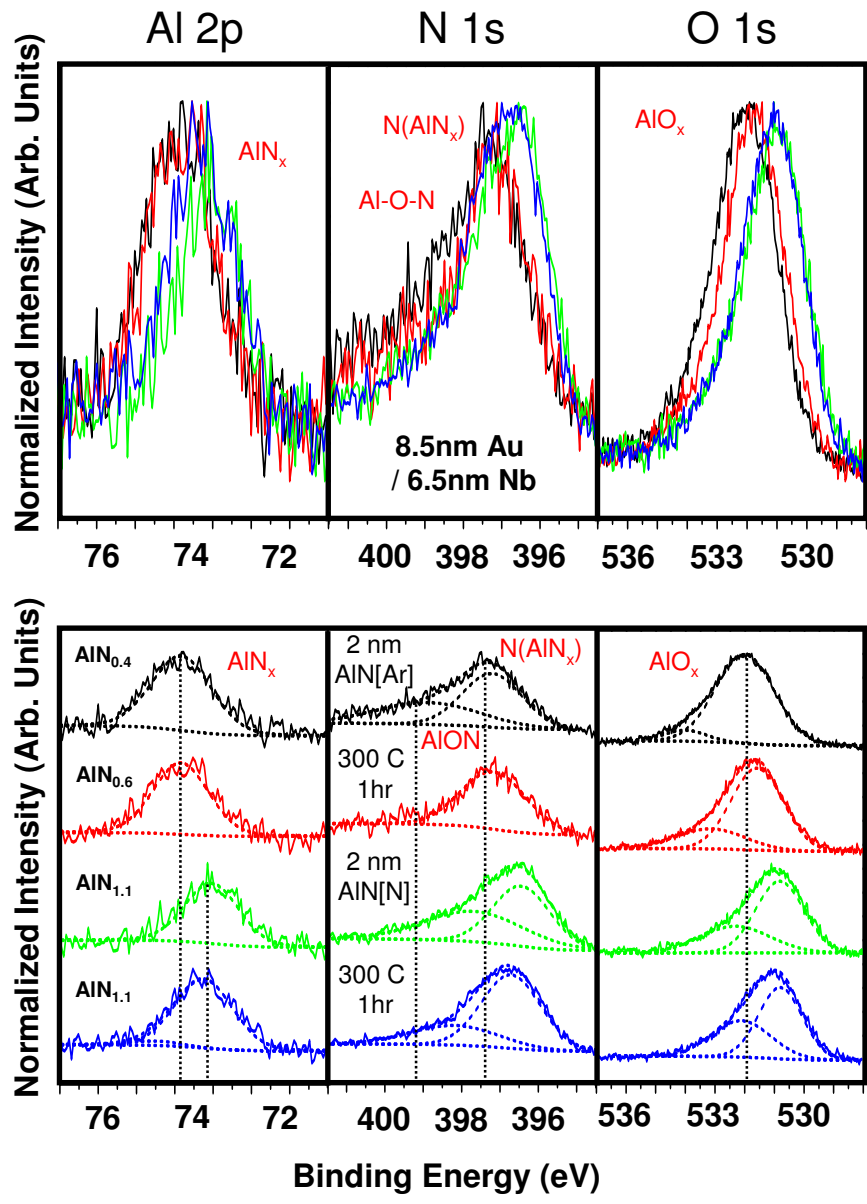


Figure 6.6: XPS data from AlN films rf sputtered on Nb in Ar or N_2 before and after vacuum annealing.

spectral region shows that the films sputtered in Ar have a higher peak BE than those sputtered in N₂. Comparison of the N 1s and O 1s spectral regions shows that the Ar sputtered films also have higher N 1s and O 1s peak BEs. These features suggest that rf sputtering AlN in Ar forms more AlO_x than rf sputtering in N₂. Also, in comparison with the AlN powder data in Fig. 6.4, the XPS data from the films sputtered in N₂ suggest the film surface is more AlN-like than the films sputtered in Ar. The estimated stoichiometry values for the Ar sputtered films are AlN_{0.4} before annealing and AlN_{0.6} after, behavior similar to the N beam exposed samples. The N₂ sputtered films appear to be roughly stoichiometric, but these numbers are misleading. The estimated stoichiometry is AlN_{1.1} before annealing and does not change after annealing, which could suggest a nonreactive AlN-AlO_xN_y film structure.

Close investigation of the Nd 3d spectra from these films, shown in Fig. 6.7, indicates that while the Ar sputtered films do not modify the Nb film chemistry, the N₂ sputtering process dramatically changes the Nb film surface as the AlN film grows. The Nb 3d peak structure is completely different for the N₂ sputtered film. Comparison with the data from the work of Lucci and co-workers (see Fig. 6.7) [24] on reactively dc-sputtered NbN films shows that increased peak intensity around ~ 207 eV is indicative of NbN and NbO_x formation. [24–27] A significant feature of the Nb 3d data is the increase in the relative intensity of the peak at ~ 207 eV after annealing. The relative intensity of N to Al is constant before and after annealing, and there is a slight decrease in the relative intensity of the higher BE N 1s peak after annealing. These peak intensity changes suggest that O that was bonded to Al and N bonds with Nb after the anneal. Therefore, it is very likely that the large increase in the N content in the estimated stoichiometry for these films is actually an overestimate because the N in the NbO_xN_y is counted

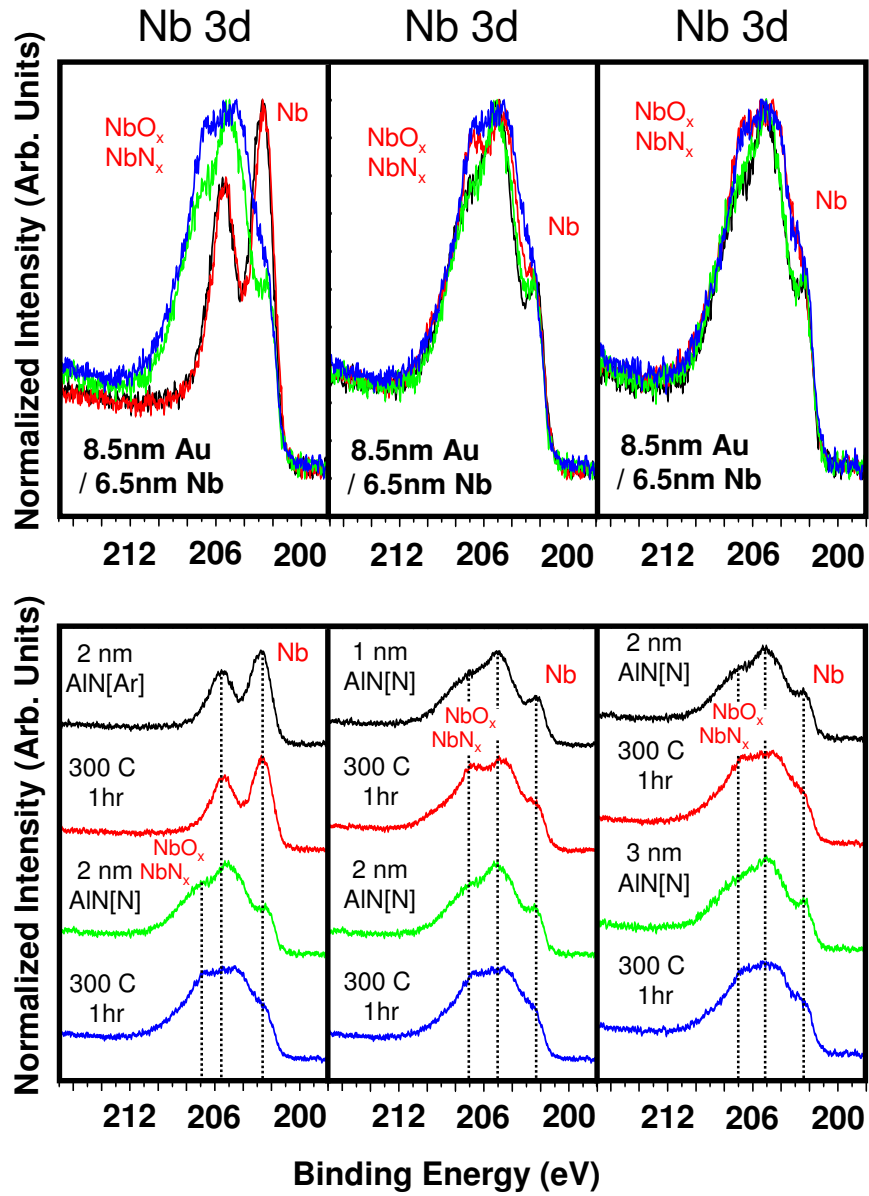


Figure 6.7: Nb 3d XPS data from AlN films rf sputtered on Nb in Ar or N₂ before and after vacuum annealing.

as being in the AlN layer. For the sake of consistency and comparison with the other films, these numbers are fine since they reflect a relative and not an absolute measure of stoichiometry. A more detailed peak fitting scheme will probably not help since the AlN and NbO_xN_y N 1s peaks appear to lie within ~ 0.5 eV of one another and thus cannot be de-convolved uniquely.

The data in Fig. 6.9 and Fig. 6.10 show the Al 2p, N 1s, and O 1s XPS data for a range of film thicknesses (1-3 nm) of N_2 sputtered AlN films. I show the Nb 3d XPS data from these samples in Fig. 6.7. All the XPS data are qualitatively the same for the entire thickness range. The Al 2p AlN peak shows a slight relative intensity increase as a function of thickness and both the higher BE N 1s and O 1s peaks also show slightly higher relative peak intensity as a function of thickness. The O 1s peak shifts slightly to higher BE as a function of thickness, perhaps suggesting there is a slight increase in the AlO_x content with increased sputtering time. As discussed previously, the N 1s peak changes slightly, decreasing with annealing. The largest changes appear in the Nb 3d data in Fig. 6.7 where the NbO_xN_y peak intensity increases after annealing for all cases. However, the relative intensity is roughly the same for the 2 and 3 nm thick films suggesting the NbO_xN_y layer is beneath the AlN as expected. The estimated relative stoichiometry values of $\text{AlN}_{1.7}$ for the 1 nm film, $\text{AlN}_{1.1}$ for the 2 nm film, and $\text{AlN}_{0.6-0.7}$ for the 3 nm film make more sense in light of these Nb 3d spectra. The reactive rf sputtering process in N_2 is forming NbN, and likely some NbO_x , at the Nb / AlN interface. This chemical process is similar to the CoFeB / MgO growth process discussed in Chapter 3 and provides a bit more resolution on the complexities of the chemical reactions driven by the reactive sputtering process. As in the case of the N beam exposed samples, the use of a getter material during sputtering may provide greater control over the O content in these reactively sputtered films. Study of the electrode and barrier

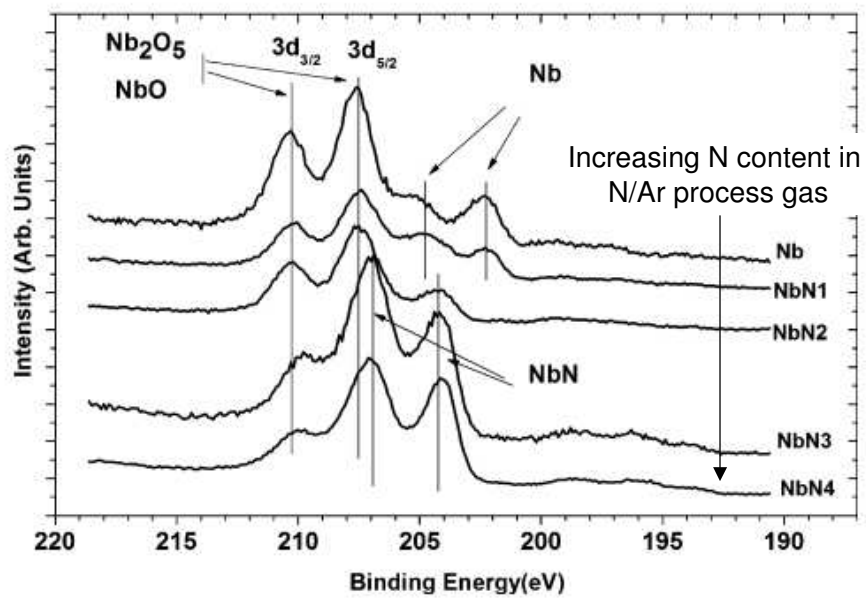


Figure 6.8: Nb 3d XPS data reactively dc sputtered NbN film using progressively higher N concentration in Ar/ N_2 process gas (from ref[24]).

composition for films sputtered in a mixture of Ar and N₂ may provide additional control over the barrier performance.

6.5 STM/STS Measurements of Nitrogen Beam Exposed Aluminum Films

In the course of these XPS studies, I also began a few STM/STS studies, which gave some initial measurements of the topography and electronic structure of the N beam exposed Al surface. I took the topographic image in Fig. 6.11 from the surface of a 7 nm Al film grown on 20 nm of Nb that I exposed to an atomic N beam at 400 W for 20 minutes, as described earlier in this chapter. I prepared this film identically to the sample measured in Fig. 6.5, but instead of being vacuum transferred to the XPS system, I in-situ transferred the sample to an STM system (Old BEEM). The surface appears amorphous, but relatively smooth. I took the STS data in Fig. 6.12 at several different spots on the sample surface and averaged them. Each trace represents the average of multiple individual traces from various spots of the surface. The data suggest that there are regions of wider or smaller bandgap behavior depending on the quantity of low energy defect states which smear together to form the bandtail shown on the right hand side of the top panel in Fig. 6.12. A possible explanation for this behavior is that the Al, O, and N that are present at or near the film surface are not uniformly mixed and thus have different bandstructure. XPS gives an average chemical behavior over a spot size of ~ 1 mm in diameter, while STM probes a spot size on the order of ~ 1 nm in diameter. Yun Li has since extended these measurements and is currently investigating the dependence of the AlN bandgap on O defects.

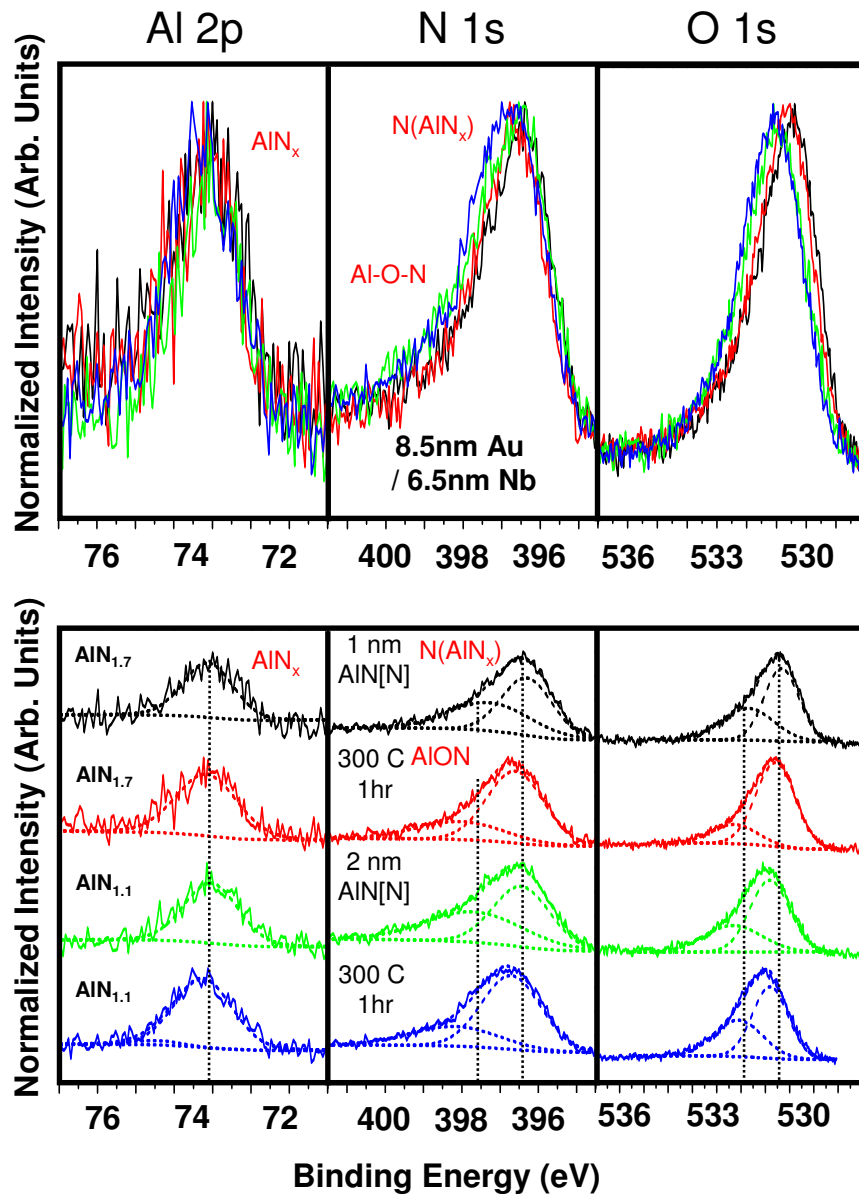


Figure 6.9: XPS data from 1-2 nm thick AlN films rf sputtered on Nb in N₂ before and after vacuum annealing.

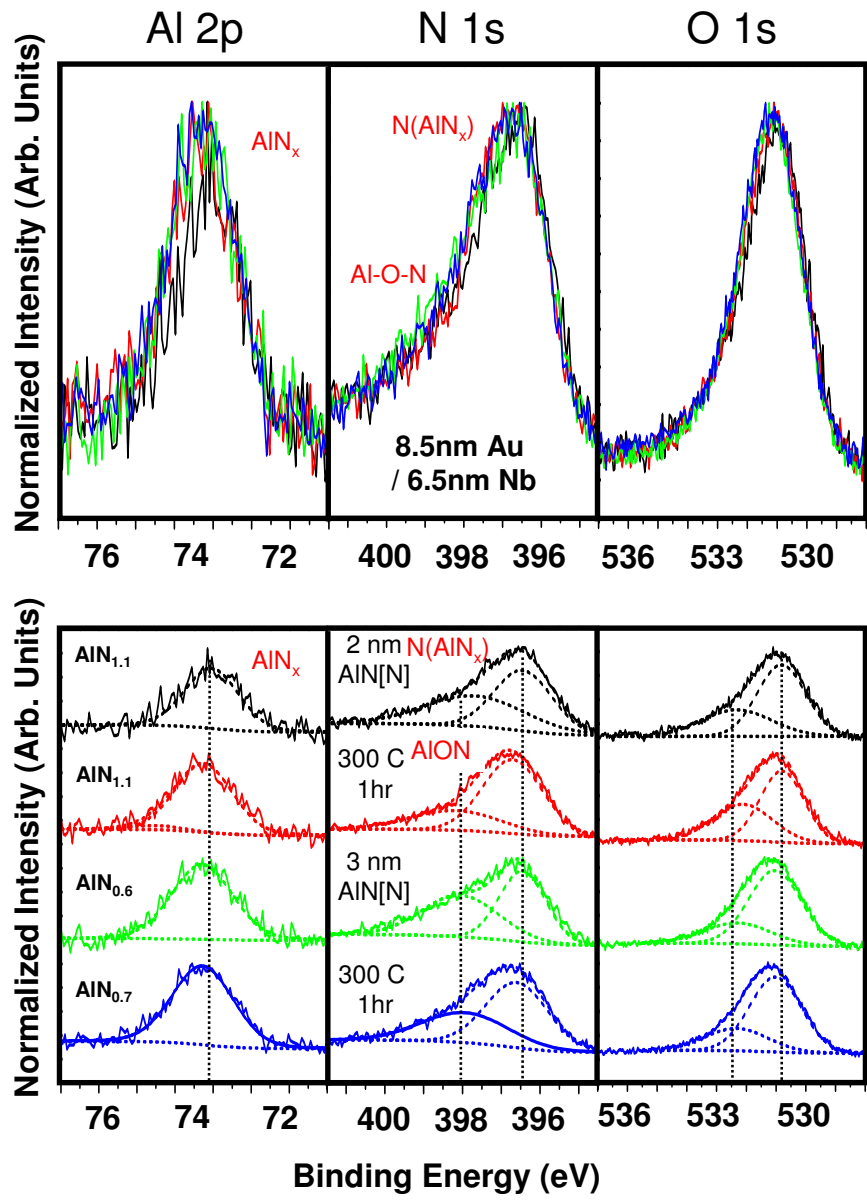
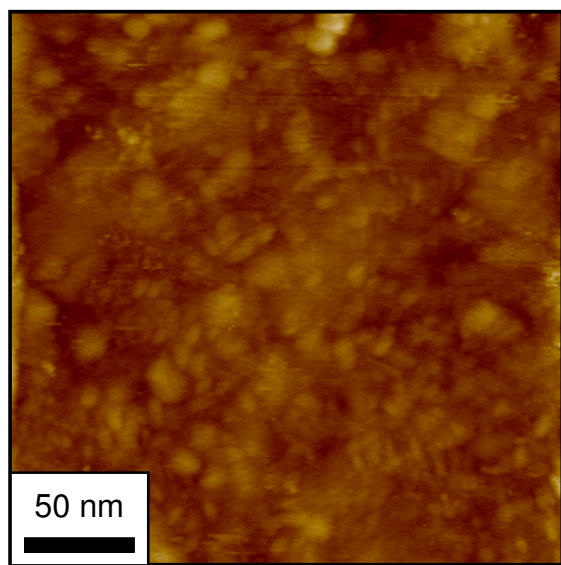


Figure 6.10: XPS data from 2-3 nm thick AlN films rf sputtered on Nb in N₂ before and after vacuum annealing.



$I_T = 150 \text{ pA}$
 $V_T = +2.5 \text{ V}$

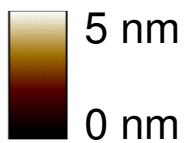


Figure 6.11: Topography of the surface of an Al film exposed to a beam of atomic N at 400 W for 20 minutes.

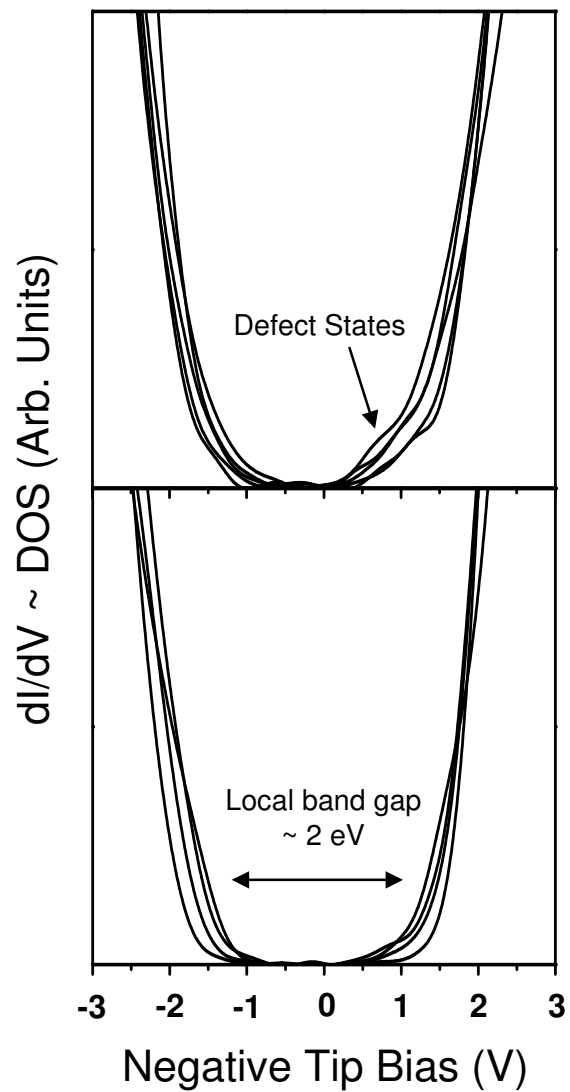


Figure 6.12: STS data from an Al film exposed to a beam of atomic N at 400 W for 20 minutes. The data in each panel were averaged from within two different 25 nm² film areas.

6.6 Summary

In summary, AlN films formed both by N beam exposure and by reactive rf sputtering inherently introduce O into the AlN film. The reactive rf sputtering process, when performed in an atmosphere of pure N₂, nitridizes the underlying Nb film. This behavior has also been observed in Co / AlN bilayers which confirms that the reactive rf sputtering process, when performed in N₂, acts to plasma nitridize the underlying film surface. The use of a getter before and during deposition may provide better control over the O content in N beam exposed and sputtered AlN films. These studies provide some clues as to barrier formation, however the full effect of O defects and barrier composition upon transport can only be addressed when correlated with STS measurements and transport measurements from JJ structures.

REFERENCES

- [1] E. Tan, P. G. Mather, A. C. Perrella, J. C. Read, and R. A. Buhrman, *Phys. Rev. B.* **71**, 161401 (2005).
- [2] C. T. Rogers, and R. A. Buhrman, Composition of 1/f Noise in Metal-Insulator-Metal Tunnel Junctions, *Phys. Rev. Lett.* **53**, 1272.
- [3] www.everspin.com.
- [4] M. M. Schwickert, J. R. Childress, R. E. Fontana, A. J. Kellock, P. M. Rice, M. K. Ho, T. J. Thompson, and B. A. Gurney, Magnetic tunnel junctions with AlN and AlN_xO_y barriers, *J. Appl. Phys.* **89**, 6871 (2001).
- [5] T. Shiota, T. Imamura, and S. Hasuo, Nb Josephson Junction with an AlN_x barrier made by plasma nitridation, *Appl. Phys. Lett.* **61**, 1228 (1992).
- [6] R. E. Miller, W. H. Mallison, A. W. Kleinsasser, K. A. Delin and E. M. Macedo, Niobium Trilayer Josephson Tunnel-Junctions with Ultrahigh Critical-Current Densities, *Appl. Phys. Lett.* **63**, 1423 (1993).
- [7] Z. Wang, A. Kawakami, Y. Uzawa, and B. Komiyama, High Critical-Current Density NbN/AlN/NbN Tunnel-Junctions Fabricated on Ambient-Temperature MgO Substrates, *Appl. Phys. Lett.* **64**, 2034 (1994).
- [8] A. W. Kleinsasser, W. H. Mallison, and R. E. Miller, Nb/AlN/Nb Josephson-Junctions with High Critical-Current Density, *IEEE Trans. Appl. Supercond.* **5**, 2318 (1995).
- [9] N. N. Iosad, D. V. Balashov, M. Y. Kupriyanov, S. N. Polyakov, and V. V. Roddatis, Characterization of NbN/AlN/NbN tunnel junctions fabricated without intentional heating, *IEEE Trans. Appl. Supercond.* **7**, 2805 (1997).
- [10] Z. Wang, A. Kawakami, and Y. Uzawa, NbN/AlN/NbN tunnel junctions with high current density up to 54 kA/cm², *Appl. Phys. Lett.* **70**, 114 (1997).
- [11] Z. Wang, Y. Uzawa, and A. Kawakami, High current density NbN/AlN/NbN tunnel junctions for submillimeter wave SIS mixers, *IEEE Trans. Appl. Supercond.* **7**, 2797 (1997).
- [12] N. N. Iosad, A. B. Ermakov, F. E. Meijer, B. D. Jackson, and T. M. Klapwijk, Characterization of the fabrication process of Nb/Al-AlN_x/Nb tunnel

- junctions with low $R_n A$ values up to $1 \Omega(\mu\text{m})^2$, *Supercond. Sci. Technol.* **15**, 945 (2002).
- [13] Z. Wang, A. Saito, A. Kawakami, and K. Hamasaki, Characterization of low frequency noise in epitaxial NbN/AlN/NbN tunnel junctions, *IEEE Trans. Appl. Supercond.* **13**, 131 (2003).
- [14] Z. Wang, H. Terai, A. Kawakami, and Y. Uzawa, Interface and tunneling barrier heights of NbN/AlN/NbN tunnel junctions, *Appl. Phys. Lett.* **75**, 701 (1999).
- [15] H. Shimakage, K. Tsujimoto, Z. Wang, and M. Tonouchi, All-MgB₂ tunnel junctions with aluminum nitride barriers, *Appl. Phys. Lett.* **86**, 072512 (2005).
- [16] H. Shimakage, K. Tsujimoto, Z. Wang, and M. Tonouchi, Characteristics of MgB₂/AlN/NbN Josephson junctions with optimized conditions, *Supercond. Sci. Technol.* **17**, 1376 (2004).
- [17] C. C. Cheng, Y. C. Chen, H. J. Wang, and W. R. Chen, Low-temperature growth of aluminum nitride thin films on silicon by reactive radio frequency magnetron sputtering, *J. Vac. Sci. Technol. A* **14**, 2238 (1996).
- [18] M. A. Auger, L. Vazquez, O. Sanchez, M. Jergel, R. Cuerno, and M. Castro, Growth dynamics of reactive-sputtering-deposited AlN films, *J. Appl. Phys.* **97**, 123528 (2005).
- [19] L. Rosenberger, R. Baird, E. McCullen, G. Auner, G. Shreve, XPS analysis of aluminum nitride films deposited by plasma source molecular beam epitaxy, *Surf. Int. Anal.* **40**, 1254 (2008).
- [20] R. Perrem, F. Henry, G. Peraudeau, B. Armas, R. Berjoan, and E. Beche, An XPS and thermogravimetric study of oxidized AlN and AlN-Si₃N₂ layers deposited by liquid-phase chemical vapour deposition, *J. Mater. Sci.* **32**, 1305 (1997).
- [21] H. M. Liao, R. N. S. Sodhi, and T. W. Coyle, Surface-Composition of AlN Powders Studied by X-ray Photoelectron-Spectroscopy and Bremsstrahlung-Excited Auger Electron Spectroscopy, *J. Vac. Sci. Technol. A* **11**, 2681 (1993).
- [22] A. B. Kaul, A. W. Kleinsasser, B. Bumble, H. G. LeDuc, K. A. Lee, Aluminum nitride tunnel barrier formation with low-energy nitrogen ion beams, *J. Mat. Research* **20**, 3047 (2005).

- [23] A. B. Kaul, A. W. Kleinsasser, B. Bumble, H. G. LeDuc, and K. A. Lee, Ion beam nitridation of Al for tunnel barrier applications, *IEEE Trans. Appl. Supercond.* **17**, 198 (2007).
- [24] M. Lucci, S. Sanna, G. Contini, N. Zema, V. Merlo, M. Salvato, H. N. Thanh, and I. Davoli, Electron spectroscopy study in the NbN growth for NbN/AlN interfaces, *Surf. Sci.* **601**, 2647 (2007).
- [25] F. Malengreau, V. Hautier, M. Vermeersch, R. Sporcken, and R. Caudano, Chemical Interactions at the Interface Between Aluminum Nitride and Iron-Oxide Determined by XPS, *Surf. Sci.* **330**, 75 (1995).
- [26] K. S. Havey, J. S. Zabinski, and S. D. Walck, The chemistry, structure, and resulting wear properties of magnetron-sputtered NbN thin films, *Thin Solid Films* **303**, 238 (1997).
- [27] L. Kang, P. H. Wu, J. R. Sh, W. X. Cai, S. Z. Yang, Z. M. Ji, and Z. Wang, Fabrication and characterization of NbN, AlN and NbN/AlN/NbN on MgO substrates, *Supercond. Sci. Technol.* **16**, 1417 (2003).

CHAPTER 7

FOLLOW-UP EXPERIMENTS, FUTURE DIRECTIONS, AND DISSERTATION SUMMARY

In this chapter I propose experiments that are extensions of the research described in this dissertation. My hope in writing them all down here is that these ideas may be explored by current or future researchers on the materials physics side of the Buhrman Group which could provide extremely useful developments for device structures for measurement by both the Buhrman and Ralph Groups. Several of these ideas, particularly those that involve device measurements, were substantially aided by discussions with Pat Braganca, Mark Tseng, Yun Li, Praveen Gowtham, Judy Cha, Pinshane Huang, Ozhan Ozatay, Luqiao Liu, Oukjae Lee, Dan Ralph, Bill Egelhoff, and of course, Bob Buhrman.

7.1 MgBO Tunnel Barrier Growth

The experiments discussed in Chapter 3 and Chapter 4 clearly show that rf sputtering of MgO on a B-alloyed electrode forms MgBO through the reaction of O ions from the sputtering plasma with the alloy B. It appears that MgO does not sputter as a molecule but rather as O and Mg ions, likely Mg^{2+} and O^{2-} , or some variation. I grew the sputtered barriers for the XPS studies discussed in Chapter 3 at low power (100 W, 2" target $\sim 4.9 \text{ W/cm}^2$), and I grew the tunnel barriers in the MTJ samples discussed in Chapter 4 at higher power (300 W, 2" target $\sim 14.8 \text{ W/cm}^2$). Although I grew the structures at different power densities, both barrier materials are MgBO. There are a few significant differences in the barrier preparation techniques. One is the use, or lack of use, of a getter material during the barrier deposition. The other is the chamber pressure at which I lit the MgO

sputtering gun. Both of these conditions effect the initial barrier deposition and could play a substantial role in the barrier formation. Deeper understanding of the mechanisms at work during the barrier deposition could provide more control over the RA and TMR of the MTJ formed, and could ultimately lead to more robust MTJ device structures.

The studies performed to date that investigate the chemical composition of the MgBO tunnel barrier materials described in this dissertation suggest that the tunnel barriers formed with rf sputtering include upwards of 5-10 % B content, and exploration of the naturally occurring phases of magnesium-borates suggests $\text{Mg}_3\text{B}_2\text{O}_6$ because of its cubic crystal structure, low B content, and trigonal coordination of B to O. Stoichiometry estimates using XPS have two complications. One is that the structure measured is a bilayer and not a full MTJ. This may generate a potential difference across the barrier which could enhance the diffusion of B towards the surface of the tunnel barrier. Also, the XPS measurement is not well resolved in terms of sample depth. Since it is likely that B reacts with surface O, and since XPS is a surface sensitive measurement, any XPS stoichiometry estimate is probably an overestimate of the B concentration in the MgBO. Angle dependent XPS measurements could provide some better estimates, but EELS is a stronger technique for these experiments since it can be used to investigate full MTJs. However, the EELS measurement has the issue of background subtraction from the signal. Since the B K-edge is a low intensity feature, it is difficult to achieve exact values for the B composition, making stoichiometry estimates a little inaccurate. Although this is a challenge, the uncertainty is significantly smaller for EELS than for XPS in terms of stoichiometry estimates.

The experiments outlined in the next paragraphs describe a body of research

that aims to fully understand and further control MgBO tunnel barrier formation. The initial presumption is that MgBO barriers are more beneficial than MgO barriers because they have a smaller bandgap and thus a smaller energy barrier height. This allows for the possibility that MgBO barriers could be more electrically thin (smaller RA product) for a given physical barrier thickness in comparison to MgO barriers. Also, it is possible that MgBO barriers are more thermally stable (less reactive) and are therefore less sensitive to the heating effects caused by extended current wear in a working MTJ. While these contentions may not be correct, they provide a starting point for investigating MgBO barriers as a benefit as opposed to a detriment, which is how these materials have been presented and perceived by the MTJ community to date.

7.1.1 MgO Sputtering Power, Chamber Pressure, and Getter Use

One important follow up experiment is the systematic study of the barrier chemical composition and junction TMR and RA as a function of sputtering power, chamber pressure, and getter use. Some studies of this already exist in the MgO MTJ literature, but a detailed investigation of the electrode-barrier interfaces, barrier chemistry, and subsequent as-grown and annealed device performance using the correlated measurement (XPS, STS, EELS, CIPT, and magnetics measurements) approach outlined in Chapter 4 will certainly provide a great deal of interesting and useful information regarding optimal barrier growth conditions for achieving thermally stable, robust tunnel barriers for STT and sensor devices. There are several limitations to consider. One is the range of rf power that can be used. The rf power supply for the AJA system can reach 500 W, however, this makes the

target and the sputtering gun extremely hot. This is not necessarily a problem for short barrier depositions, but for making thickness calibration samples it could cause some problems. If such a high power is to be used, then another thickness calibration method besides the standard liftoff and profilometry approach should be used. Lower power promotes very slow film growth and requires an extended time to get a film thick enough to measure by profilometry (typically I make a FM / MgBO / FM / Cu structure 50 nm thick where the MgBO layer is \sim 1-10 nm thick). With this in mind, it is advisable to find a more accurate way to measure the growth rate of thin MgBO barriers for these experiments.

Another consideration is the number of targets. The AJA system in its current configuration allows 7 targets. If the layers are going to be patterned, then it is not essential to include a Ta / CuN seed layer. A different seed layer, such as Ta / Ru or Ta / TaN, can be used instead. Therefore, the use of both Mg and Ta getters during barrier deposition can be studied if the chamber is setup (for example) with Ta (gun 1), MgO (gun 2), Mg (gun 3), FeCoB (gun 4), $\text{Py}_{80}\text{B}_{20}$ (gun 5), IrMn (gun 6), Ru (gun 7). An additional adjustment is getter sputtering power. For the samples discussed in this dissertation, I used 50 W, but higher powers may be more beneficial since the getter material will deposit faster and will likely have a greater gettering effect during deposition.

With these two conditions addressed, one can carry out careful experiments that adjust sputtering power, chamber pressure during the lighting of the MgO target, and use of Mg, Ta, or other getter materials during the MTJ layer growth. Then one can pattern samples for transport studies and characterize them with EELS and magnetometry. Also, the prep 2 system in the D7 lab can make nearly identical samples. Here there are 4 sputtering guns, so if one used (for example)

MgO, Mg (or Ta), FeCoB, and $\text{Py}_{80}\text{B}_{20}$, then one can investigate the electronic structure of the MgO. While these barriers are not exactly the same as the barrier grown in the AJA (no seed layers or IrMn pinning layer), they would provide more insight regarding the nature of defect states in the tunnel barrier, tunnel barrier bandgap changes with deposition conditions (and annealing), and band offset as a function of electrode composition and deposition conditions.

7.1.2 MgBO Target Sputtering

Although careful estimation of the barrier stoichiometry is important, a relative measurement of the MgBO barrier is all that is really required to investigate the use of tunnel barriers grown from an MgBO target of a particular composition in comparison with MgBO barriers formed as described in Chapter 3 and Chapter 4. XPS and EELS measurements both show that B from the electrodes enters the barrier when MgO is sputtered, so a natural question is whether this is enhanced or suppressed by starting with a MgBO sputtering target. The primary reasons to attempt such barrier formation are to study the effect on the electrodes, particularly on electrode crystallization as a function of annealing and the resultant magnetic performance of the electrodes. Also, if the sputtered MgBO material does not oxidize the base electrode, or oxidizes it differently than the MgO deposition does, this could provide a more robust or less noisy barrier material. In addition, one can conduct another set of experiments that compares the use of an MgBO target with both the MgBO barrier formation and the growth of MgBO by co-sputtering MgO with metallic B. While this may not be an ideal barrier material [1], investigating the material formed could provide some clues about what aspects of MgBO barriers are non-ideal or need improvement. Obviously, one can

adjust all of the experimental parameters discussed in the previous paragraphs for the MgBO target and MgO-B co-sputtering depositions.

7.2 Glassy Magnetic Electrodes

Previous studies show that one of the major benefits of using glassy magnetic electrodes in MTJs that incorporate MgO tunnel barriers is that as the MTJ is annealed the MgO imprints its crystal structure on the electrodes as they change from amorphous materials into polycrystalline materials. The work in this dissertation shows that these B-based alloys have another benefit in terms of sample chemistry. The alloy B reduces transition metal oxides during annealing which effectively decreases the quantity of antiferromagnetic interfacial oxides in the MTJ which degrade device performance. The templating and oxide reducing characteristics of B-based alloys make them prime candidates for further study in MgO MTJ structures.

7.2.1 New B-based Alloys

The work in chapter 4 demonstrates that Ni-Fe-B alloys can be successfully incorporated in high TMR, low RA MTJ structures. One interesting extension of this investigation is to study the possible incorporation of other alloy materials designed with specific magnetic properties to see if the inclusion of glass forming B is beneficial to making MgBO-based MTJs with carefully engineered electrodes. One set of experiments is to study the incorporation of a wider range of Ni-Fe-B alloys, like $\text{Py}_{90}\text{B}_{10}$ or $\text{Py}_{85}\text{B}_{15}$. Another interesting candidate alloy is Conectic

(Ni₇₇Fe₁₄Cu₅Mo₄). [2] This extremely soft alloy is highly useful in sensor structures and could possibly be incorporated into MgBO based MTJs with the addition of 20 %B in the alloy (Ni₆₂Fe₁₁Cu₄Mo₃B₂₀). The metallurgy of this system should first be investigated to ensure that such an alloy target can even be made, then a study of the device performance and magnetism can proceed.

7.2.2 Out of Plane Magnetized Free Layers

The use of out of plane magnetized electrodes has shown some encouraging results with regards to possibly lowering the critical current density required for STT switching. In addition, out of plane magnetized electrodes are interesting for oscillator studies. The layers used for this purpose that typically show up in the literature are usually composed of multilayers of Ni and Co, both of which will form detrimental antiferromagnetic oxides when in contact with MgO. Study of the use of a thin ($\sim 1-4 \text{ \AA}$) layer of CoFeB, NiFeB, or another B-based alloy, upon which is grown the Ni / Co multilayer could prove beneficial for out of plane magnetized free layers without the formation of antiferromagnetic interfacial oxides. [3] This structure has the additional benefits of forming a locally epitaxial Fe / MgBO / Fe MTJ since the MgO barrier will imprint its structure on the B-based alloy and the alloy B will be incorporated into the tunnel barrier.

7.3 MTJ Device Fabrication and Transport Measurements

The previous paragraphs describe materials studies geared towards understanding the physical and chemical properties of MgO and MgBO based MTJ structures.

Although the materials physics is of great inherent interest, it is ultimately the fabrication and study of working MTJ devices that is of broader interest to the research community. To fully correlate the materials studies with transport measurements and thus understand more deeply the impact of the various materials considerations upon device behavior, we need a reliable device fabrication process to form working MTJs for transport measurements.

7.3.1 MTJ Transport Measurements

Once the device fabrication process is complete, a wide range of transport studies is possible. I should note here that Mark (Hsin-Wei) Tseng is already hard at work on developing this process and is likely to have completed it by the time this dissertation is available to anyone in the Buhrman Group who cares to consider the experiments I propose here. One reasonable place to start the device measurements is with TMR scans. A simple measurement of V/I as a function of applied field will give a first glimpse of the device quality. This should give a measurement of TMR ($\frac{\Delta R}{R}$) and the device resistance times the patterned area will give the device RA product. This provides a comparison with CIPT measurements of unpatterned layers which will indicate if patterning has changed the device properties. Another interesting study is the behavior of TMR as a function of applied bias. This measurement is a good test bed for comparing MgBO barriers of different MgBO compositions to see if there is any change in device performance. As the bias voltage is increased, the energy landscape of the electrodes changes, so in some sense TMR vs. V is a probe of the electrode density of states and spin polarization as a function of energy. This measurement may also be a window to differences in defect states within the tunnel barrier, although measuring the derivative of

differential conductivity $\frac{dI^2}{dV^2}$ is a more direct approach. With patterned junctions in hand, one measurement of great interest is the 1/f noise of different barriers. [4] Careful investigation of the 1/f noise for various MgBO compositions will provide useful information regarding the utility of the MgBO barrier in sensor applications and may also point to the physical nature of barrier defects.

From an engineering and reliability standpoint, measurements of breakdown voltage and current wear out are important for the long term behavior of a device. With patterned devices it would be highly useful to compare the breakdown voltage of, for example, Mg/MgO bilayer barriers with the breakdown voltage of MgBO barriers. This is one way to determine if MgBO barriers are more robust than MgO barriers. Also, a measurement of TMR as a function of time for a particular current bias will provide a direct measurement of the current wear out properties of various barrier materials. Considering that the MTJs of interest for STT applications are on the order of 1 nm thick and that the voltage applied across the barrier necessary to excite STT is on the order of 0.5 V, the electric field applied across the barrier is on the order of what is applied in electrochemistry experiments. This raises the question as to whether any electrochemical reactions are taking place during typical device usage. The work of Houssameddine and co-workers shows significant changes in MTJ performance after current wear out which suggest possible barrier modifications. [5] Voltage breakdown and current wear out properties in conjunction with chemical analysis will be very useful in determining optimal barrier composition.

7.3.2 STT MTJs and FIB EELS Studies

The STT behavior of devices with different barrier compositions is of great interest. This is the natural progression of the project and the reason why I began developing an MgO MTJ growth process to begin with. Once the device patterning process is complete and working devices are routine, the next step is to push towards measuring STT switching in MgBO MTJs. Provided this is achievable, there are a number of exciting studies that can be explored. Obviously, study of the switching behavior and thermal stability of different free layer materials used with different MgBO barrier compositions is one interesting investigation. Another obvious extension is to study the microwave power emitted by MTJs that are fabricated in either a conventional sense (free layer on top) in the "inverted" sense (free layer on bottom) [6] or fabricated with thick bottom electrodes for study of vortex formation. [7] Each of these is worthy of study and could lead to many more exciting experiments.

In keeping with the theme of correlated transport, electronic, chemical, and magnetic studies, an experiment of particular interest to me is to pick a particular device parameter to study, for example breakdown voltage, or current wear out. Then identify two nominally identical working devices (meaning just TMR is measured) from a wafer with a particular barrier chemistry and electrode configuration. Then put one of the two devices through a series of measurements of the device parameter in the study (i.e. breakdown voltage) until the device fails. Finally cut out both the control sample and the destroyed sample using focused ion beam (FIB) for cross-sectional TEM / STEM / EELS investigations.

7.3.3 Double Barrier Junctions

Perhaps the most interesting proposal is the formation of double barrier MTJs (Figure 7.1). The key component is the free layer, sandwiched between two barrier layers. If this material can be made crystalline then many interesting device properties should emerge. The results of the studies on PyB free layers discussed in Chapter 4 suggest that crystallization of a PyB free layer sandwiched between two MgBO layers is probable, and I am currently conducting experiments with Judy Cha and Mark (Hsin-Wei) Tseng on these structures. The results of these initial studies should give a better idea of what free electrode thicknesses are likely to work. The major challenge is to form a layer that is thick enough to maintain thermal stability while thin enough to fully crystallize.

Double barrier MTJs are beneficial for increasing $V_{1/2}$, the bias voltage value for which the device TMR decreases by a factor of 1/2 from its low bias value. [8] Double junction structures have substantial benefits for STT devices if the two fixed layers are pinned such that they are oriented in an antiferromagnetic arrangement. This provides twice the STT since both the transmitted and reflected spin-polarized tunnel currents impart a torque on the free layer. [9] In addition to these enhancements, a thin, crystalline free layer between two tunnel barrier layers can create spin-filtering states within the tunnel barrier. [10] This should improve the effective spin-polarization of the tunneling currents and thus the STT efficiency. [11] Such a structure has the possibility of decreasing both the current required for switching and the time required to make a switch in a STT device.

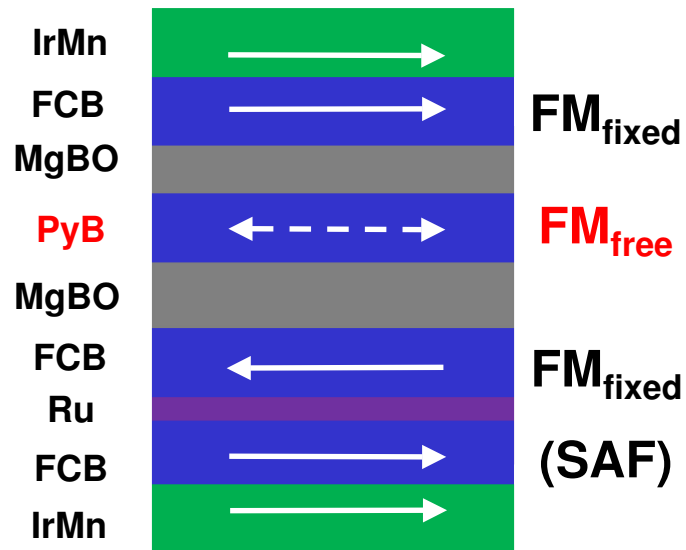


Figure 7.1: Cartoon of a double barrier junction incorporating MgBO barriers and a PyB free layer.

7.4 MgB₂ / MgBO / MgB₂ Josephson Junction Development

Since the discovery of superconductivity in MgB₂ and the development of high quality thin film growth processes many research groups have worked towards the development of all-MgB₂ JJs. As mentioned in Chapter 5, to date all-MgB₂ JJs have not demonstrated the performance necessary for useful devices. The experiments outlined in this section provide some ways to study the materials physics in these systems that may be helpful in determining the best approach to forming successful, high quality all-MgB₂ JJs.

7.4.1 MgB₂ / MgBO Annealing Studies

In order to form high quality all-MgB₂ JJs two important details must be addressed. One is the formation of good tunnel barrier materials that do not degrade the quality of the base electrode. The other is the subsequent formation of a good MgB₂ top electrode on this tunnel barrier material. The experiments in Chapter 5 address the first issue and the second issue is addressed by work that Mark (Hsin-Wei) Tseng and I did on annealing MgB₂ / MgBO bilayers. Since the required deposition temperature for good MgB₂ growth is between 500 and 700°C depending on the deposition technique we investigated the effect of annealing on both the electrode and the tunnel barrier with XPS. This work is on-going, but the initial results are that reactively evaporated films with barrier layers formed by exposure to oxygen do not substantially degrade for anneals up to 500°C for 30 minutes. The barriers do not get dramatically thicker, but the effect of the anneal upon film T_C is unknown at present. In addition to chemical analysis and barrier

thickness estimates as a function of annealing, measurements of film T_C before and after annealing will be helpful in determining film quality. These studies can be correlated with transport studies performed by our collaborators to fully inform which procedures are likely to form the best all-MgB₂ structures.

7.4.2 MgB₂ / MgBO Barrier Thickness Studies

The experiments discussed in Chapter 5 provide some baseline measurements of the MgB₂ films and their surface oxides formed by a variety of oxidation techniques. One crucial step in the formation of high quality JJs is the control of the tunnel barrier and one missing piece in the investigations performed by our team to date is an accurate thickness estimate. While XPS is excellent at chemical identification and is good at chemical quantification, the power of the technique gets significantly weaker when dealing with a mixed oxide material like MgBO. Also, while thickness estimation with XPS is often very accurate in systems like Si / SiO_x, a multilayer sample like the samples discussed in Chapter 5, especially one that has been exposed to atmosphere, makes for a difficult time in getting accurate numbers. With this in mind it would be very helpful to find an appropriate technique, perhaps TEM, for generating accurate thicknesses for the tunnel barriers formed by specific growth and post-growth oxidation techniques. With this calibration, one will yield more reliable thickness estimates from XPS studies.

7.5 Nb / AlN / Nb and Nb / NbN / AlN / NbN / Nb Josephson Junction Growth

The investigations of AlN tunnel barriers in Chapter 6 provides a good starting point for developing a process for making AlN-based JJs. These structures should be sputtered to form full wafers that can be processed with techniques similar or identical to those used to fabricate micron-sized MTJs. The first step in the development of AlN-based JJ thin film growth is to sputter Nb and NbN layers for resistivity versus temperature measurements. This can be easily started by growing Nb, NbN, or Nb/AlN on thermally oxidized Si wafers or chips and capping the layers with Cu. Then, using the van der Pauw dipper described in Chapter 2, sheet resistance versus temperature can be measured which can easily be converted to resistivity versus temperature provided the thickness of the thin film is known. The effects of the Cu layer, which is used as a cap to prevent Nb oxide formation, will need to be included in this calculation to get a precise measurement, but this should be reasonably done by measuring Cu thin films by the same process. The XPS measurements of the various AlN samples shows that for some deposition processes (reactive rf sputtering of AlN in N) the Nb electrode is actually nitridized and oxidized, so the film layer is Nb / NbO_xN_y / AlN_z. One study that should be done in conjunction with the transport measurements is to vary the Ar:N ratio during reactive rf sputtering. These films can then be studied with both EELS and ρ vs. T measurements to get a good idea of T_C as a function of electrode and barrier composition. With this knowledge in hand, one can then incorporate Ta / CuN seed layers for smoothing and top Nb layers to form complete JJ structures for patterning and ultimately for low temperature transport studies.

7.6 Hybrid Magnetic Tunnel Junction - Josephson Junction Film Layer Growth

The final proposed structure is a hybrid MTJ-JJ device. This is far and away the most difficult structure to make, but with the other techniques and studies described in this dissertation, and provided the Nb / AlN / Nb JJ process becomes reality, then it is my opinion that there is only one crucial step that would need to be worked out to allow the development of the hybrid device film layers. This device structure is interesting for a number of reasons. First, superconductivity and ferromagnetism are natural enemies, so any device that can include them both successfully is of broad scientific interest. However, in terms of applications, this device structure allows the low temperature operation of an interconnected JJ and MTJ and could be the basis of a very fast memory technology. [12]

The next paragraphs propose a multi-step process that could provide the means to making the film layers for this hybrid device concept. The idea is to load the AJA sputtering system with 7 targets (Ta, Cu, MgO, FeCoB, IrMn, AlN, Nb) which will allow first the growth of the JJ structure, then removal from the chamber to deposit the spacer layer / superconducting ground plane / spacer layer stack, then re-introduction into the AJA to grow the MTJ. Step one of the device layer growth is the formation of the Ta / CuN seed layers for smoothing, which is described in Chapter 2. The next step is the growth of a Nb / AlN / Nb JJ with a Cu capping layer to prevent oxidation. Provided the process (or some variation of the process) describe in the previous section is successful, then this step should be easily incorporated onto the Ta / CuN layers.

Then the wafer is taken out of the chamber and a Cu spacer layer / Nb super-

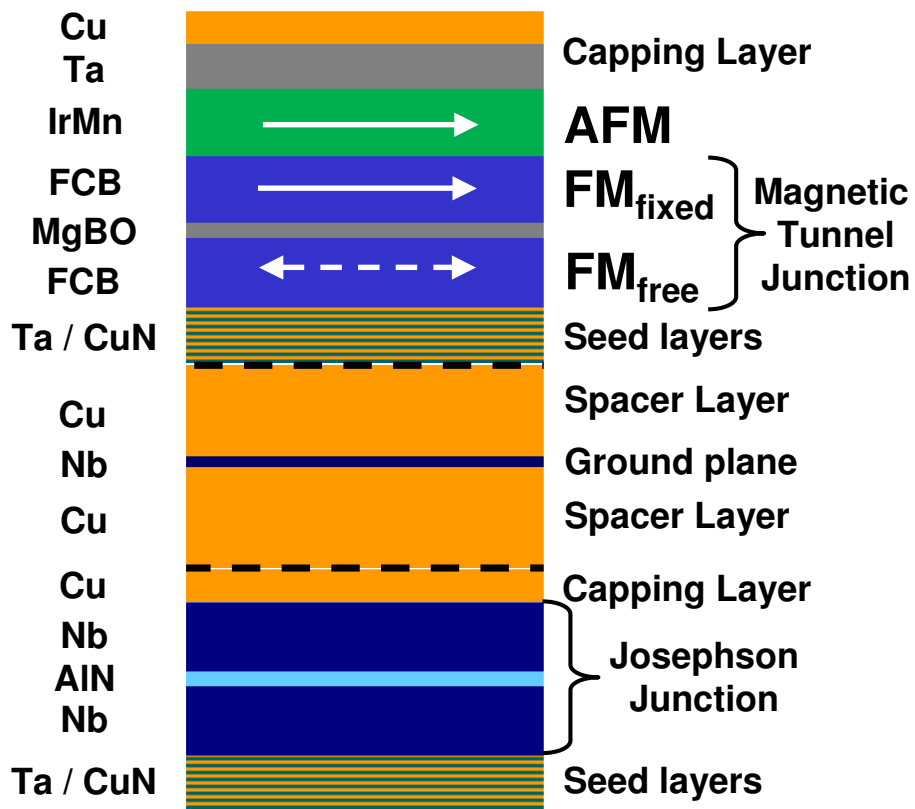


Figure 7.2: Cartoon of hybrid MTJ - JJ device film layers. The dashed lines indicate breaks in the deposition when the wafer is removed from vacuum and placed in a different deposition chamber.

conducting ground plane / Cu spacer layer structure is deposited by high power sputtering. The purpose of the ground plane is to make a diamagnetic film plane that will prevent the field from the MTJ layers from influencing the JJ performance without dramatically changing the MTJ performance. A few Oe field may be enough to disturb the JJ performance, but exactly how much field magnitude is currently unknown. The location of the Nb ground plane in the stack may prove to crucial to the performance of this device and this is one of the most important open questions regarding the development of this device structure. In addition, these sputtered Cu / Nb / Cu layers must be smooth enough to grown a good MTJ structure on top of them. AFM studies of surface smoothness will provide a means to optimize the post growth processing required to get a film smooth enough to successfully deposit the MTJ on top of these sputtered layers. After this step, the wafer is re-introduced in to the AJA and another stack of Ta / CuN seed layers is deposited. It is possible that rf back-sputtering to etch and clean the film surface will be beneficial for this step. Then the MTJ layers and finally a Ta / Cu capping layer are deposited. The MTJ must be annealed to activate high TMR and the studies in Chapter 6 show that the AlN barriers get some additional benefit from annealing as well. This will not be an easy or straightforward process to develop, especially since it is difficult to know just how thick the spacer layers need to be, and it may also be very difficult to successfully smooth the spacer layers enough to get good MTJ growth. Also, annealing may diffuse Cu throughout the structure, so low temperature, long time annealing procedure are probably best. In addition, the device fabrication will be very challenging. I propose to put the JJ on the bottom since its device area should be larger. This should allow the fabrication steps to proceed as a hybrid between nano-pillar and micro-pillar fabrications. It will not be easy, but it could be a very exciting, and highly fundable project for

one or more future students.

7.7 Dissertation Summary

The research presented in this dissertation investigated the development of thin film growth processes for fabrication of both MTJ and JJ structures focused primarily on the chemical, electronic, and structural properties of tunnel barrier materials and the interfaces they make with the electrode materials to which they are adjacent. I developed a process that is capable of making MgO (MgBO)-based MTJ thin film device layers that have TMR, RA, and magnetic characteristics that are comparable to several industrial research groups. I studied the materials properties of these junction structures along with MgB₂ oxidation processes and AlN tunnel barrier formation. While the work presented in this dissertation is capable of standing alone as a body of research, there is little doubt the the greatest accomplishment of my research efforts of these past years is developing techniques and procedures that will allow my colleagues to make new MTJ and JJ device structures with few limitations.

I conducted XPS studies on CoFeB / MgO bilayer samples which show that MgO barrier growth can be controlled in such a way as to either prevent or promote electrode oxidation. If the electrode is protected with a Mg layer, then stoichiometric, crystalline MgO forms. Alternatively, if the plasma formed in rf sputtering oxidizes the electrode, then a MgBO material with promising physical and chemical properties forms. In both cases, the post-growth annealing that is required to activate high TMR in MgO-based MTJs reduces Fe and Co oxides formed in the deposition process through a reaction of B from the electrode with O in the

transition metal oxides. In the case of MgBO barriers, annealing causes an atomic rearrangement of the Mg, B, and O species, and the formation of a different barrier oxide material adjacent to a crystalline CoFe electrode. Increased control over the barrier composition by including an Mg layer, or through use of getter materials during the rf sputtering deposition of MgO is due to the capture of oxygen liberated from the MgO target in the early stages of sputtering. However, reaction between B from the electrode and sputter deposited MgO is an inherent part of the formation of rf sputtered MgO-based MTJs and the ability to intentionally make MgBO barriers provides an opportunity to fabricate MTJ devices that potentially have more robust transport characteristics due to the increased thermal stability of MgBO in comparison to MgO.

In conjunction with Judy Cha and Bill Egelhoff, I studied the correlated results of STEM/EELS, STS, CIPT, and magnetics research which shows that MgBO-based MTJs have several advantages over MgO-based MTJs. As-grown MgBO-MTJs exhibit a TMR which increases with decreasing barrier thickness and as-grown MgBO barriers have fewer low energy defect states than MgO barriers. There is also no substantial increase in these defect states in MgBO barriers after annealing. Comparison of MTJs with MgBO barriers with MTJs with Mg/MgO bilayer barriers shows that MgBO barriers yield higher TMR values and lower RA values than MgO barriers of comparable thickness. $\text{Py}_{80}\text{B}_{20}$ alloy top electrodes are capable of forming MgBO MTJs with high TMR ($\sim 150\%$) and low RA ($\sim 15 \Omega(\mu\text{m})^2$) values after annealing. These MTJs also show desirable magnetic characteristics of low M_S and H_C , and the coupling in these layers decreases dramatically after annealing due to interfacial oxide reduction by the B content in the MgBO and in the interfacial region of the electrode. B is not only important for the formation of ultra-thin, low-resistance, highly spin-filtering tunnel barriers, but is

also the crucial component for enabling the use of superior ferromagnetic, Py-based electrode materials for spin torque MRAM and magnetic sensor applications.

I also studied MgBO barriers in a different material system through an exploration of the oxidation of MgB₂ thin films. The highly reactive nature of Mg dominates the oxidation of the MgB₂ film surface, but the surface oxide is composed of both Mg and B components and is similar to the MgBO materials I observed in MTJ structures. Exposure to N₂ or O₂ promotes formation of MgO on the MgB₂ film surface and the surface becomes completely composed of MgO if the oxidation process is carried out at elevated temperatures for an extended time. If the oxidation occurs at lower temperatures, then the surface oxide formed is a mixed MgBO, similar to the native MgB₂ surface oxide. The oxidation process depletes the film surface of Mg, forming MgO_x, and promotes development of elemental B, and B sub-oxide near the film surface. The degree of formation of the elemental B, and B sub-oxide species is dependent upon the method of delivery of O to the film surface as well as the sample temperature during oxidation. These B species are likely to effect MgB₂ / MgBO / MgB₂ JJs formed with these oxidation processes. Ion milling and water exposure oxidize and etch the MgB₂ film surface in similar ways to different extents. These chemical studies provide insights into optimal MgBO barrier formation techniques for future MgB₂-based JJ devices.

I started another project developing the growth processes for AlN tunnel barriers formed both by N beam exposure of Al films and by reactive rf sputtering of AlN in either Ar or N₂ process gas for use in Nb / AlN / Nb or Nb / NbN / AlN / NbN / Nb JJs. Both AlN growth processes introduce O into the AlN film, which could possibly be controlled with getter material in a manner similar to the way these getter materials are used in MgO and MgBO-based MTJ growth.

These XPS studies show that when one uses a pure N₂ atmosphere for reactive rf sputtering of AlN, the film growth nitridizes the underlying Nb film, similar to the way MgO oxidizes CoFeB. These studies provide some insights regarding optimal AlN barrier formation for JJ structures that can now be further developed by other researchers.

Finally, I constructed a list of experiments ranging from systematic and guaranteed to produce interesting materials studies to complicated with a high risk of failure. I did my best to make the descriptions detailed enough as to provide direction and encouragement, and vague enough as to allow modification, improvement, or rejection if need be. My hope in assembling these experiments is that my outstanding colleagues may choose to investigate some of my ideas, and with a little work, eclipse everything I have accomplished in my time here. I wish you good luck, well-behaved vacuum systems, and piles of publications.

REFERENCES

- [1] S. S. P. Parkin, Comment regarding work done by the team at IBM Almanden, RIEC 2nd annual Symposium on MgO, Tohoku University, Sendai, Japan (2007).
- [2] W. F. Egelhoff, Jr., R. D. McMichael, C. L. Dennis, M. D. Stiles, A. J. Shapiro, B. B. Maranville, and C. J. Powell, Suppression of orange-peel coupling in magnetic tunnel junctions by preoxidation, *Appl. Phys. Lett.* **88**, 162508 (2006).
- [3] D. C. Ralph, This idea came from a comment Dan made during a discussion about the MMM conference regarding out of plane magnetized free layers. (2008).
- [4] C. T. Rogers, and R. A. Buhrman, Composition of 1/f Noise in Metal-Insulator-Metal Tunnel Junctions, *Phys. Rev. Lett.* **53**, 1272.
- [5] D. Houssameddine, U. Ebels, B. Delaet, B. Rodmacq, I. Firastrau, F. Pontonnier, M. Brunet, C. Thirion, J.-P. Michel, L. Prejbeanu-Buda, M.-C. Cyrille, O. Redon, and B. Dieny, Spin-torque oscillator using a perpendicular polarizer and a planar free layer, *Nature Materials* **6**, 447 (2007).
- [6] P. M. Braganca, O. Ozatay, A. G. F. Garcia, O. J. Lee, D. C. Ralph, and R. A. Buhrman, Enhancement in spin-torque efficiency by nonuniform spin current generated within a tapered nanopillar spin valve, *Phys. Rev. B* **77**, 144423 (2008).
- [7] V. S. Pribiag, I. N. Krivorotov, G. D. Fuchs, P. M. Braganca, O. Ozatay, J. C. Sankey, D. C. Ralph, and R. A. Buhrman, Magnetic vortex oscillator driven by d.c. spin-polarized current, *Nature Physics* **3**, 498 (2007).
- [8] T. Nozaki, A. Hirohata, N. Tezuka, S. Sugimoto, and K. Inomata, Bias voltage effect on tunnel magnetoresistance in fully epitaxial MgO double-barrier magnetic tunnel junctions, *Appl. Phys. Lett.* **86**, 082501 (2005).
- [9] G. D. Fuchs, I. N. Krivorotov, P. M. Braganca, N. C. Emley, A. G. F. Garcia, D. C. Ralph, and R. A. Buhrman, Adjustable spin torque in magnetic tunnel junctions with two fixed layers, *Appl. Phys. Lett.* **86**, 152509 (2005).

- [10] T. Nozaki, N. Tezuka, and K. Inomata, Quantum oscillation of the tunneling conductance in fully epitaxial double barrier magnetic tunnel junctions, *Phys. Rev. Lett.* **96** (2006).
- [11] I. Theodonis, A. Kalitsov, and N. Kioussis, Enhancing spin-transfer torque through the proximity of quantum well states, *Phys. Rev. B* **76** (2007).
- [12] R. A. Buhrman, This idea was proposed by Bob for a prototype low temperature, high speed MRAM. (2008).